MICROSTRUCTURAL INFLUENCE ON THE EFFECTS OF FORWARD AND REVERSE MECHANICAL DEFORMATION IN HSLA X65 AND X80 LINEPIPE STEELS

John-Paul Tovee

For the degree of:

DOCTOR OF PHILOSOPHY

Department of Metallurgy and Materials
School of Engineering and Physical Sciences
University of Birmingham

Abstract

Where operating conditions allow, high strength low alloy (HSLA) steels are the preferred option for materials selection across the oil and gas industry for the transportation of hydrocarbon liquids and natural gas. Demand for higher strength grades which show optimum performance in aggressive environments is increasing with the advance of deep water projects, extraction of shale gas, drive to increase hydrocarbon output and save costs by avoidance of stainless steel grades. The mechanical properties are obtained through complex thermo-mechanical controlled rolling schedules of steel slabs microalloyed with small additions of C, Mn, Nb, Ti and / or V. A wide variety of microstructural phases and constituents can be produced, which match the criteria for high strength American Petroleum Institute (API) grades, including pearlite, bainite, acicular ferrite, martensite and / or ferrite. The rolling history and wt % additions of alloying elements will determine how the microstructures perform under reverse deformation schedules commonly seen during large diameter linepipe fabrication as steels can undergo work softening in the reverse direction of deformation, otherwise known as the Bauschinger effect. The Bauschinger effect is known to be dependent on the initial forward pre-strain, volume fraction (VF) of carbo-nitride particles and initial dislocation density. The effects of grain size and solid solution strengthening are a matter of debate in the literature and the combined effects of all five strengthening mechanisms have rarely been quantified.

This body of research has studied five API (X65 - X80) grade steels designed for linepipe applications produced using different processing routes to obtain differing single phase ferritic / bainitic microstructures and dual phase ferrite microstructures containing pearlite and martensite austenite (MA) constituents. The aim is to study the influence of strengthening mechanisms within a variety of different microstructures and their effect on the mechanical properties of steel and how this will affect the final mechanical properties of large diameter linepipe through cold forward deformation and Bauschinger tests. To do this five API grade steels designed for linepipe applications produced using different processing routes and with varying microstructures were studied to quantify the contributions to yield strength arising from solid solution, grain size, dislocation density and precipitation of carbo-nitride particles which have correlated against differences in work hardening and work softening behaviour obtained from mechanical data.

Volume fraction of precipitates analysed using scanning electron microscopy (SEM) and transmission electron microscopy (TEM) compare well to thermodynamic software predictions (using Thermo-Calc) and ranged from 0.00066 - 0.00158 in the studied steels. Area % of second phase pearlite and MA islands was between 8 - 12 % in the studied steels which was found to alter the mechanical behaviour significantly in comparison to single phase microstructures. TEM investigations determined the dislocation densities to be between $2.2 \times 10^{14} \text{ m}^{-2}$ - $5.8 \times 10^{14} \text{ m}^{-2}$ in the as received condition. Dislocation density increase and evolution of structure was also examined with increasing deformation up to 0.04 strain. This study of work has discovered a dramatic difference in dislocation structure which tend to adopt low energy states consisting of regular, straight line structures in as received and 0.02 strained materials containing high amounts of Ni ▄▄▄

- ███████ Bauschinger tests conducted on the studied steels found greater drops in yield strength during reverse loading to occur in steels containing dual phase microstructures, high microalloying additions and high dislocation densities due to back stresses from dislocation pile ups, residual stresses from secondary phase / ferrite interfaces, dislocation bowing and masking from particle interaction. The relationship between the Bauschinger stress parameter and microstructure is complicated by the presence of second phase and low energy dislocation structures (LEDS) arising from prior processing and presence of Ni which cause differences in the incremental increase of the Bauschinger parameter at various pre-strains (an increase of 0.2 for Ni bearing steels and increase of 0.1 for non-Ni bearing steels from 0.01 - 0.04 pre-strain). Long range recovery (of initial forward flow stress properties) is greater for steels containing lesser amounts of particles but only MA bearing steels recovered work hardening rates during reverse deformation comparable to that of forward loading. Ferritic, bainitic and pearlite bearing microstructures experience lower rates of reverse work hardening which is transient at lower pre-strains, this has been previously attributed to dissolution of cellular structures during forward loading but in this study these were not seen at low pre-strains and therefore attributed to saturation of back stress from annihilation of mobile dislocations. The observed trends have given a greater insight into the influence microstructure has on the mechanical properties across a wide range of HSLA steels of similar strength grades which are of important consideration for future development of low carbon steels designed for the petrochemical industry.

Table of Contents

1 Microstructural characteristics of linepipe steels

1.1 Overview of linepipe

Large diameter linepipe is defined as having a diameter between 16 - 64'' (0.4 – 1.6 m) and can be fabricated from steel plate or sheet. These must have excellent mechanical properties to ensure the linepipe has:

- Good toughness in low temperature environments;

- Good weldability;

- Sufficient strength to withstand high internal and external pressures during service;

- The ability to withstand stress corrosion cracking, hydrogen sulphide attack and CO_2 corrosion.

HSLA (high strength low alloy) steels subject to TMCR (thermo-mechanical controlled rolling) schedules are the only materials that can deliver these required properties at competitive cost. Achievement of the required strength is through a combination of solid solution strengthening, grain refinement, phase balance, precipitation strengthening and work hardening. The magnitude of the contribution that these various mechanisms make

to the net yield stress of a material is limited for solid solution (due to the limitation that the steel cannot exceed a specified carbon equivalent value to ensure weldability) and phase balance as high percentages of particular phases or constituents such as pearlite may have detrimental effects on toughness. Arguably the most effective means of enhancing steels properties for a given composition is the refinement of microstructure through controlled rolling and continuous cooling schedules to refine grain size, provide precipitation strengthening and careful alteration of the phase balance.

Differing linepipe strength grades are categorised predominantly by the American Petroleum Industry (API) under standard API 5L [1]. The higher the strength grade of a material, the higher the numerical value to the grade given i.e. X65, X80, X100 and X120, the latter having the higher yield stresses. Table 1.1 lists the yield stress criteria required to satisfy the requirements set out by standard API 5l relating to mechanical properties for linepipe steels.

Table 1.1 API 5l yield stress (YS) requirements for X42 − X120 linepipe steel derived from [1]

Grade	Min YS, MPa	Max YS, MPa
X42	280	500
X46	310	510
X50	350	510
X56	370	510
X60	390	550
X65	410	590

X70	460	610
X80	550	705
X100	758	800
X120	827	931

The offshore oil and gas industry is driving demand for higher strength linepipe, which has been a trend since the middle of the last century (Figure 1.1). Motivations for materials selection for linepipe grades are predominantly influenced by the depth below sea level where the linepipe will be in service and its weldability in harsh environments. Deeper subsea conditions obviously demand a higher collapse pressure, which is obtained either through greater wall thicknesses or higher strength grade linepipe.

The obvious benefits of higher strength linepipe are a potential reduction in wall thickness and / or increase in pipe diameter and thus cost savings related to welding and transportation; in the case of increased pipe diameter a greater level of output can be expected yielding a faster payback for a given project. Thinner wall thickness will benefit linepipe in terms of improved weldability and reduced weight; however increased strength can also introduce problems in terms of fabricating linepipe with existing equipment designed for lower strength grades [2,3].
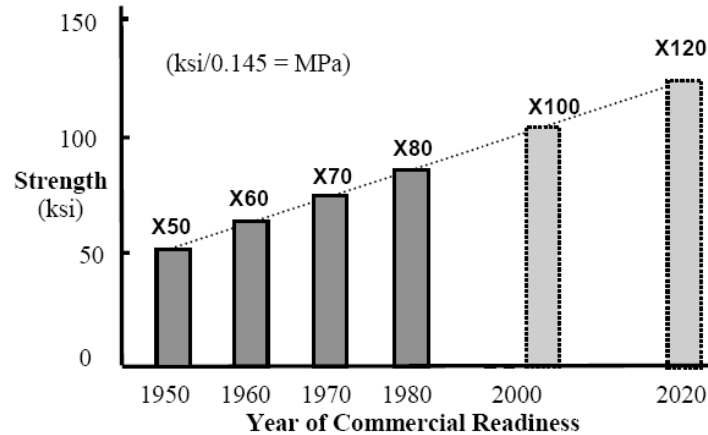
Figure 1.1 Linepipe strength grade trends for offshore projects [4]

The materials selection process for onshore projects is more complicated due to the potential presence of hydrogen, CO_2 and chlorides which are highly corrosive to carbon steel and can initiate sudden failure from stress corrosion cracking (SCC), embrittlement of microstructure leading to hydrogen induced cracking (HIC) and / or hydrogen induced blister cracking (HIBC). The presence of certain microstructural features can promote these failure mechanisms with potentially catastrophic consequences. Banded microstructures of pearlite [5] or hard phases such as martensite and bainite [6,7] can increase the susceptibility to attack from hydrogen sulphide (H_2S) therefore softer ferritic or acicular microstructures are preferred [6]. Precipitates present in the steel microstructures can also have a significant influence on the susceptibility to stress corrosion cracking. For example, an increase in volume fraction of carbides and nitrides in linepipe has been found to increase its susceptibility to SCC [6] (Figure 1.2, a and b). Hard particles and phases at grain boundaries can act as initiation sites for SCC and should be avoided in steels for use in sour service [6]. However, additions of Ti have also been found to be beneficial in reducing SCC due to the high binding energy of

Ti(C,N) with hydrogen providing trapping sites [8] and, provided the Ti(C,N) precipitates are sufficiently refined (< 0.1 µm) and dispersed throughout the matrix, hydrogen embrittlement can be reduced. Higher strength steels, as a result of their microstructures typically including dual phase constituents and relatively large volume fractions of precipitates, are generally acknowledged as being more prone to cracking under sour service environments [9].
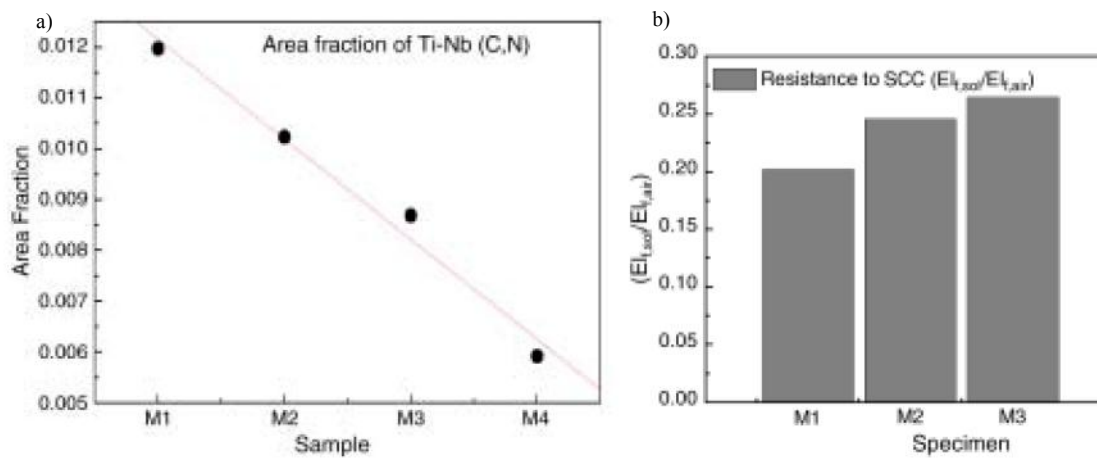
Figure 1.2 (a) Area fraction of carbo-nitride particles in four 0.053C-1.22Mn-0.1V+Nb+Ti steels subjected to different TMCP schedules and (b) the respective resistance to SCC [6]

For higher strength grade materials, satisfying corrosion requirements is not always possible and thinner wall thicknesses may not be a major motivation for increases in strength grades as increased thicknesses are usually required to compensate for corrosion allowances in mild - moderately sour environments to comply with NACE (National Association of Corrosion Engineers) and ISO (International Organisation for Standardisation) standards such as NACE MR0175 and ISO 15156. Traditionally onshore engineering does not demand high external collapse pressure for linepipes, instead

materials selection is motivated to use steels capable of delivering high toughness in severe temperatures and an increase of linepipe diameter to maximise output, which develops a different set of challenges to fabricators. Recent developments in the extraction of shale gas are setting new challenges for petrochemical engineers as the injection of water, aggressive chemicals and proppant at high pressure and high velocity requires high erosion - corrosion resistance which would obviously be more suited to harder, dual phase microstructures rather than softer single phase / acicular microstructures.

1.1.1   Development of steel plate and sheet

HSLA plate / sheet start as continuous cast slabs which are re-heated prior to rolling and are subject to carefully considered processing parameters including: re-heat (soaking) temperature and time, rolling schedules i.e. number of passes, reduction % per pass, hold temperatures and time, finish rolling temperature and cooling rate after rolling to obtain the desirable microstructure and properties for a given application. Typical practice is to first re-heat the slab to ensure that the microalloying elements are taken into solution through dissolution of existing precipitates formed during slow cooling of the as-cast slab. For simple C-Nb alloyed steels this temperature is calculated using Irvine's formula (Equation 1) to ensure dissolution of the microalloying elements whilst making sure the soaking temperature is not too high as this results in excessive grain growth, which is undesirable [10,11]. More complex commercial steels require the use of thermodynamic

software, such as Thermo-Calc, to predict dissolution temperatures with any real accuracy.

$$\log[Nb]\left[C + 12\frac{N}{14}\right] = 2.26 - \frac{6770}{T} \qquad (1)$$

The rolling process for reheated slabs is split into two stages - roughing and finishing, for which there is a holding time between the two whilst the plate is cooled (Figure 1.3). Table 1.2 shows the typical range of rolling variables for a C-Mn-Nb steel subject to TMCR processing. Roughing is carried out between 1050 and 950 $^{\circ}$C with slab reduction of up to 13 % per pass and finishing is carried out between 800 and 770 $^{\circ}$C with slab reduction of up to 18 % per pass.
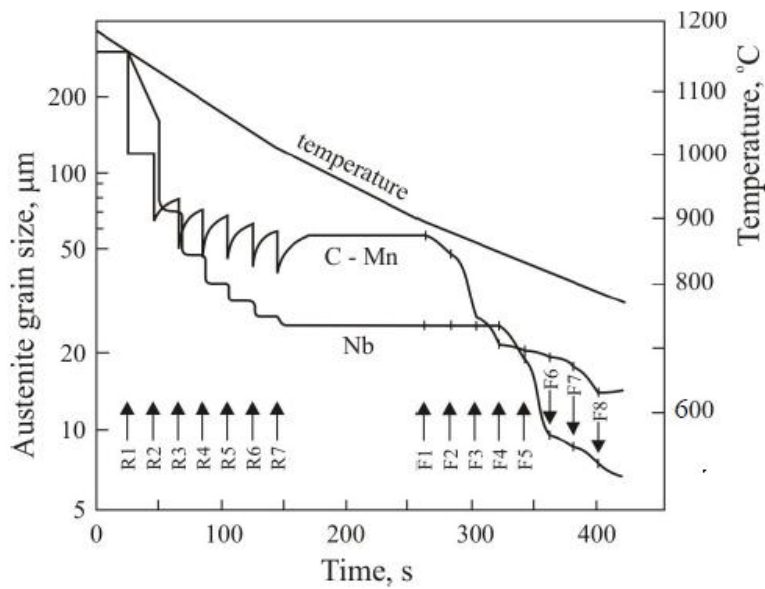
Figure 1.3 Rolling schedule for a C-Mn and C-Nb bearing steel showing the subsequent change in austenite grain size during slab reduction from 200 mm to 20 mm during roughing (passes designated as R) and finishing (F) passes [12,13]

Table 1.2 Roughing and finish rolling schedules for a 0.12C-1.4Mn-0.025Nb steel [14]

	Roughing	Finishing
Number of passes	11	9
Temp range (°C)	1050 - 950	800 - 770
Finish plate thickness (mm)	67	20
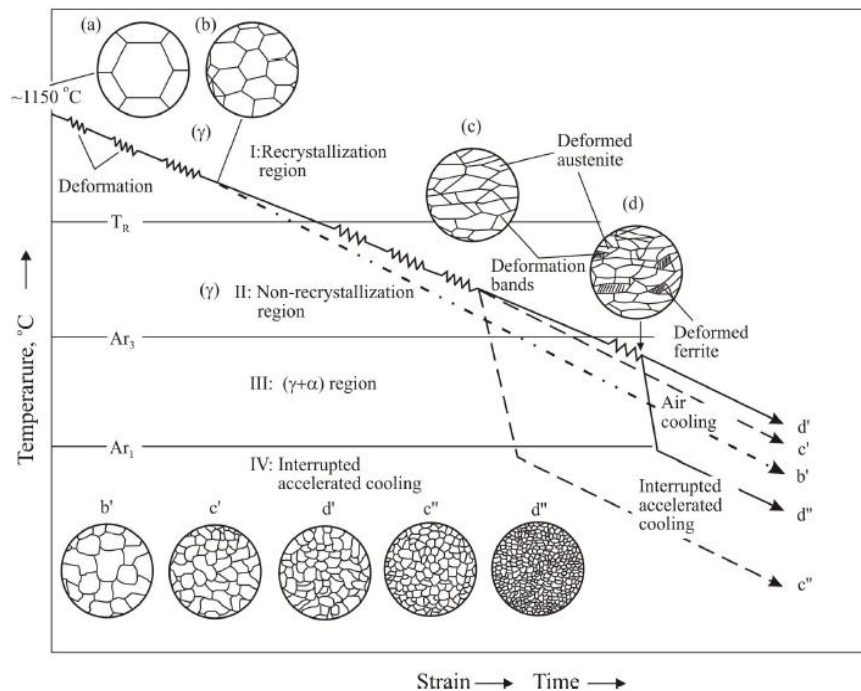
Figure 1.4 Change in grain structure after different TMCR cooling schedules and corresponding microstructures [15]

Figure 1.4 shows how rolling schedules during TMCR affect the grain structure during rolling and in the finished product when different cooling schedules are used. Rolling within the austenite recrystallisation region can occur for several passes during which significant austenite grain refinement will result [16]. If rolling occurs in the non-recrystallisation region then deformation bands can be observed and austenite grains will become 'pancaked'. Ferrite grains nucleate on the deformed austenite grain boundaries hence a more refined austenite grain structure aids the refinement of ferrite grains due to a greater number of nucleation sites and more rapid impingement of ferrite grains across a prior austenite grain [16,17]. It has also been observed that rolling within the austenite non-recrystallisation region introduces dislocations into the austenite grains, which can act as a driving force for the formation of acicular ferrite upon transformation [18-21]. There is a limit to the refinement of average grain size in industrial TMCR steels due to recalescence, which is calculated to be 1 μm [22]. When rolling in the $\gamma + \alpha$ region (below Ar_3) deformation bands of austenite are observed surrounded by a deformed ferrite substructure. The final microstructure after cooling consists of a mixed grain size of equiaxed ferrite grains (from austenite) and ferrite subgrains (from the deformed ferrite) [23]. Experimental data from low carbon X52 steel plates rolled in this region showed a mixed grain size with a high dislocation density attributed to ferrite formed during deformation which did not fully undergo recovery and recrystallisation [24].

In practice not many HSLA steels are rolled into the intercritical region. Figure 1.5 shows how bainitic, martensitic and dual phase steel microstructures have been obtained, using

different deformation schedules, that satisfy the strength and toughness criteria for X120 [25]. The parameters for soaking, start / finish rolling temperatures and reductions per pass have a significant influence on the yield stress and tensile strength of the final product. Lowering of the finish rolling temperature (FRT) results in refinement of the grain size and increase in strength (Figure 1.6) but can be detrimental to the impact transition temperature [26]. Studies in the literature [27] compared the mechanical properties of a C-Nb-V microalloyed steel which was soaked at 1100 ^{o}C and 1000 ^{o}C then subjected to high and moderate rolling reductions at different temperatures between 900 and 700 ^{o}C. It was found that higher soaking temperatures resulted in only a slight improvement in the yield stress whilst lower soaking temperatures improved the yield stress considerably; however the higher soaking temperature resulted in greater improvements in UTS (ultimate tensile strength) at higher rolling temperatures. The steel that was subjected to a lower soaking temperature only showed considerable improvement after lower rolling temperatures, which was attributed to straining of the ferrite grains. Similar synergistic trends were also observed in a C-Nb steel [24]. The effects of soaking and rolling temperatures on the mechanical properties for the C-Nb-V steel are shown in Figure 1.7.
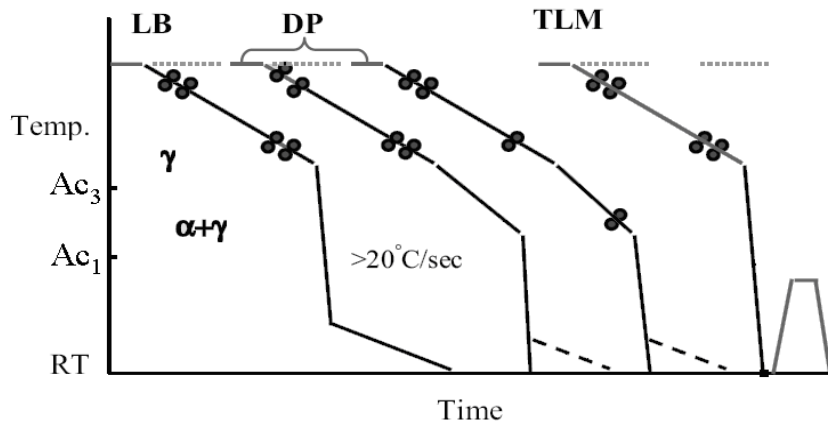
Figure 1.5 Rolling schedules predominantly above A_{R3} for X120 grade steel lower bainite (LB) = 0.06C-1.5Mn-0.02Nb, dual phase (DP) = 0.07C-1.7Mn-0.04Nb, tempered lath martensite (TLM) = 0.08C-1.00Mn-0.08Nb, all wt % [25]
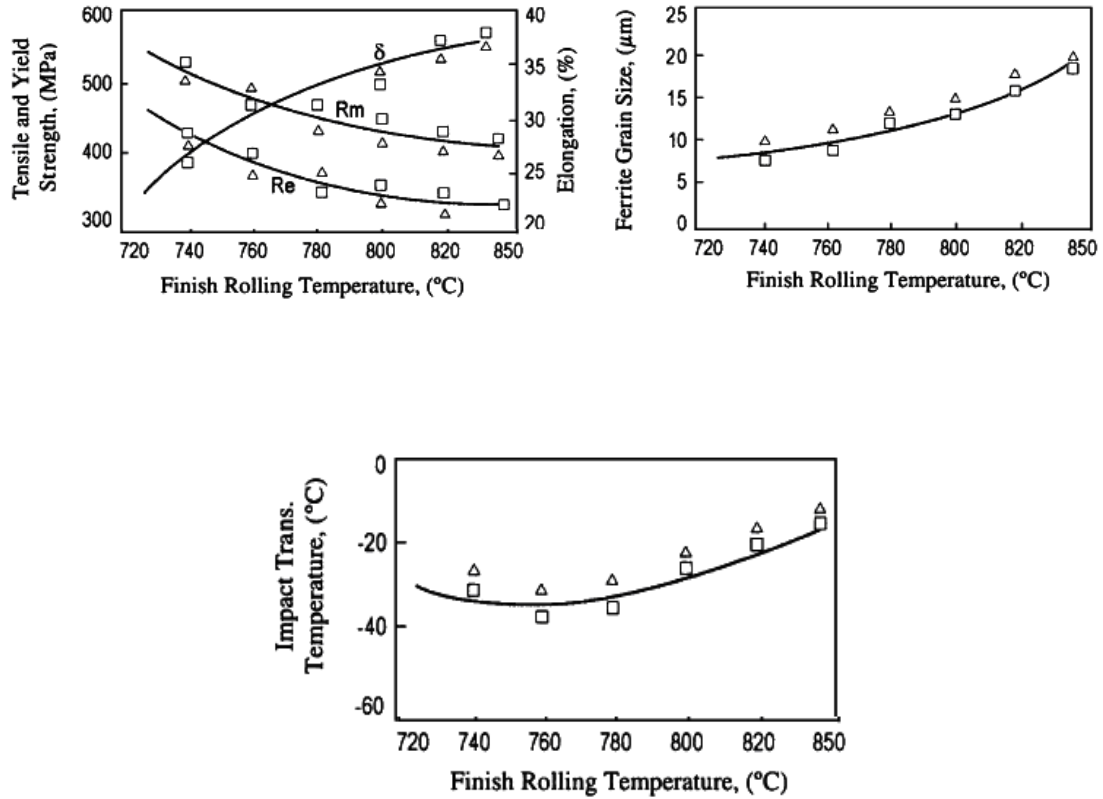
Figure 1.6 Influence of finish rolling temperature (FRT) for a 0.20C-1.03Mn-0.054Nb-0.046V microalloyed steel on mechanical properties (a) increase in UTS (b) decrease in ferrite grain size and (c) decrease in impact transition temperature (ITT) in a low carbon steel [24]
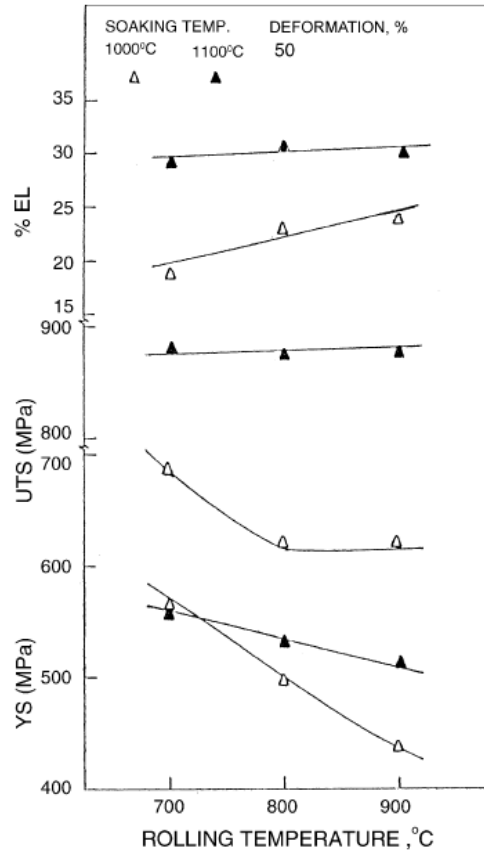
Figure 1.7 Mechanical properties of a 0.10C-0.036Nb-0.010V microalloyed steel subject to soaking at 1100 / 1000°C and 700 - 900°C rolling temperatures. [27]

The FRT and the cooling rate after rolling both affect the microstructure and hence mechanical properties of steel plate, but of the two the cooling rate typically has the greater influence. Increasing the cooling rate will increase the volume fraction of a given phase (e.g. martensite, bainite) and refine the grain size but this can be detrimental to the mechanical properties if the cooling rate is too rapid as low toughness can result. In the case of grain size it has been found that there is little benefit in a cooling rate > 10 ^{o}C / s [20] (Figure 1.8). Specimens cooled at lower rates contained ferrite - pearlite microstructures, whilst for cooling at over 10 ^{o}C / s the microstructures became ultrafine

12

grained with small amounts of bainite and MA phases. The authors did not speculate as to the mechanisms by which the cooling rate refined the grain size / microstructure. Work by Esmailian et al. conducted on 0.11C-1.38Mn-0.03Nb steel found refined grain size to be attributed to a slower ferrite nucleation rate which becomes more prominent with large austenite grain size [28]. Prior austenite grain size was found to be a significant factor in the formation of refined microstructures as a greater number of carbo-nitride particles were found within large austenite grains providing nucleation points for acicular and intergranular ferrite. Many other studies have also determined the cooling rate to have considerable influence on the phase transformation behaviour. For a Mo-free HSLA (Figure 1.9), acicular and polygonal ferrite microstructures are associated with accelerated cooling schedules and conversely, pearlite in steels will be the product of a slower cooling rate and so microstructures with pearlite would be expected to have coarser grain sizes compared to those containing acicular ferrite.
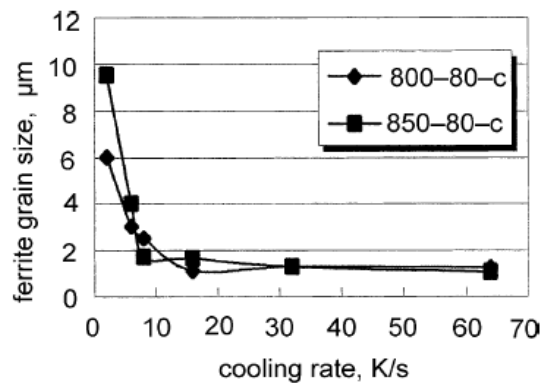
Figure 1.8 Effect of cooling on grain size, which ceases to become effective in grain size refinement > 10 K/s in an 0.29C-0.005M-08Nb steel cooled from 800 ^{o}C and 850 ^{o}C [20]
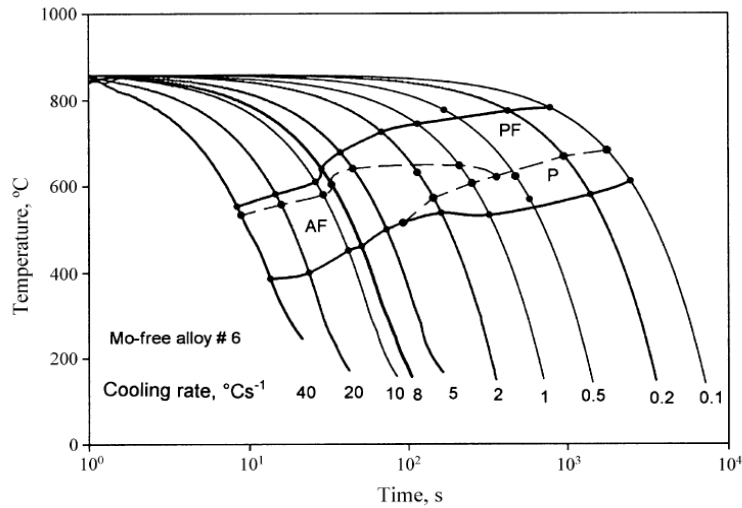
Figure 1.9 Continuous cooling transformation (CCT) diagram for Mo-free HSLA steel with AF (Acicular Ferrite), PF (Polygonal Ferrite) and P (Pearlitic) microstructures [18]

After TMCR the steel will be in the form of plates or if the steel has been reduced to a thickness of under about 12 mm then may be in the form of coils. The overall effect of coiling is reported to be effective in annealing out transformation dislocations associated with rapid cooling i.e. bainitic phases, acicular ferrite, martensite etc. and is not sensitive to small changes in coiling temperature [18].

1.1.2 Ferrite

Ferrite / proeutectoid ferrite will form during slow cooling from austenite at the highest transformation temperature. Increasing the cooling rate will result in differences in phases formed and in the character of the ferrite phase [26] (Figure 1.10). At slow cooling rates ferrite grains will precipitate on austenite grain boundaries and this will yield a polygonal or equiaxed morphology.

At higher cooling rates ferrite can lose its polygonal characteristics as elongated crystals of ferrite form. This type of ferrite is classified as Widmanstätten ferrite (WF). Increasing the cooling rate further can cause the growth of massive ferrite (MF) or quasi-polygonal ferrite (QPF). These microstructures are achieved by suppressing the partitioning of carbon during the $\gamma \rightarrow \alpha$ transformation resulting in a change in crystal structure with no change to composition [29,30]. Studies on these microstructures have shown them to possess high dislocation densities and demonstrate high rates of work hardening [31,32].
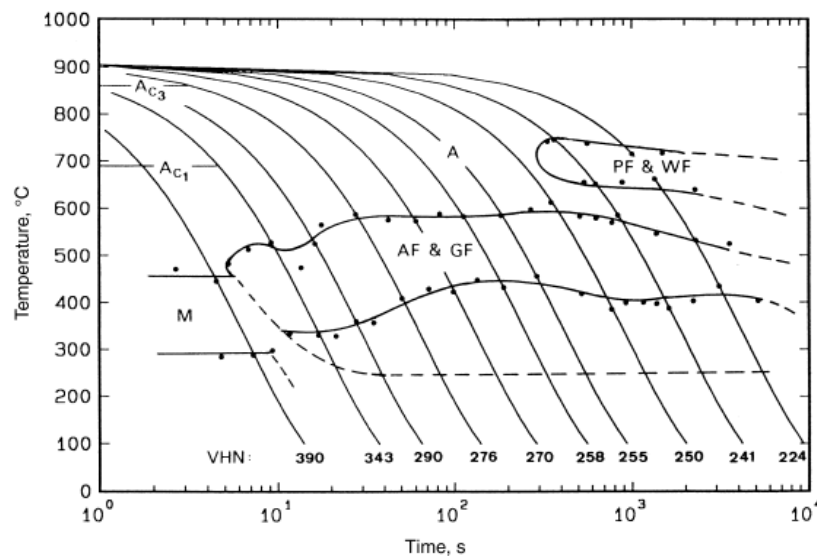
Figure 1.10 Continuous cooling-transformation plot for a 0.06C-1.25Mn-0.42Mo steel showing the influence of cooling rate on microstructural phases - accelerated cooling yields M (martensite), AF (acicular ferrite), as cooling time increases GF (granular ferrite), PF (polygonal ferrite) and WF (Widmanstätten ferrite) are produced [26]

15

1.1.3   Pearlite

Pearlite is perhaps the most established microstructural constituent in carbon steels. Its appearance has been likened to 'mother of pearl', from where the name derives and has been of interest to metallurgists as far back as the 18th Century [33,34]. The occurrence of pearlite is a eutectoid transformation and consists of lamellae of Fe_3C (cementite) and ferrite giving a striped appearance within the microstructure, the carbon present in the austenite phase is given sufficient time to diffuse and form Fe_3C. The cooling rate through the eutectoid temperature region controls the levels of pearlite and thus rapid cooling will not yield this phase. If sufficient levels of pearlite are present then bands of pearlite can be observed parallel to the rolling direction, which become less continuous as the volume fraction of pearlite reduces. Figures 1.11, a - c show 3 pearlitic steel plate microstructures in the quarter thickness position with varying amounts of pearlite, it can be seen that the area fraction reduces with a decrease in carbon content (Table 1.3), and the reduced volume fraction of pearlite makes bands more difficult to resolve [35].
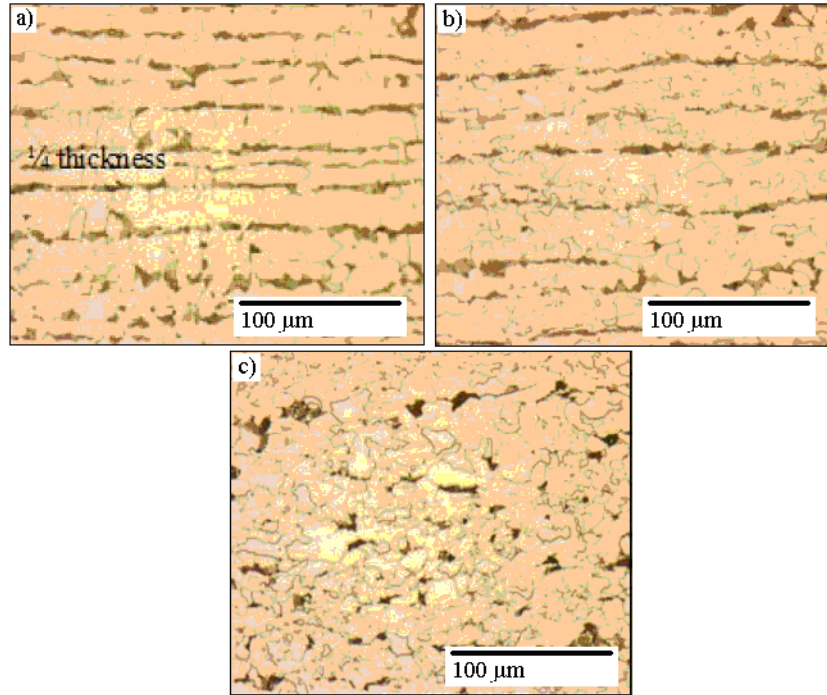
Figure 1.11 Ferrite-pearlite steels showing reduced pearlite content in (a) X52 0.12C-1.09Mn (b) X65 0.1C-1.36Mn-0.034Nb and (c) X65 0.08C-1.47Mn-0.046Nb steel [35]

Table 1.3: Carbon-manganese contents and corresponding pearlite percentage for ferrite-pearlite microalloyed linepipe steels [35]

Steel (w t%)	Pearlite %
0.12C-1.09Mn	15.4
0.10C-1.36Mn	9.7
0.08C-1.47Mn	4.7

Generally an increase in the amount of pearlite in carbon steels raises the yield strength [36] however there are conflicting reports for low pearlite content with one report stating that when the amount of pearlite present in material is < 30 % the yield strength is not affected [37] whilst another report stated that when large amounts of ferrite are present refining the grain size and varying the volume fraction of pearlite both affect the lower yield stress [38].

1.1.4 Bainitic phases

Bainite, named after work by Davenport and Bain [39] has many classification systems, six were proposed in the work [40] of which two of the most widely acknowledged are schematically presented in Figure 1.12. Bainite consists of laths or sheaves of ferrite. Cementite will form inside the bainitic ferrite at lower temperature (lower bainite), alternatively at higher temperatures the carbon will be partitioned into the remaining austenite forming carbides between the laths (upper bainite).

(a)   (b)
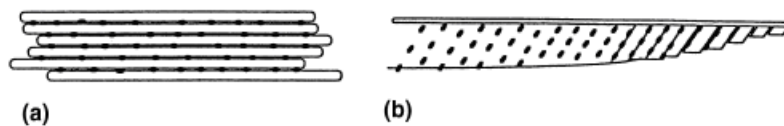
Figure 1.12 Schematic drawings of ferrite-bainite microstructures where black represents cementite: (a) upper bainite (b) lower bainite [40]

Granular bainite / granular ferrite (GB / GF) features a small distribution of cementite and / or martensite austenite islands which outline prior austenite grain boundaries. The

18

microstructure within sheaves of bainitic ferrite gives a granular appearance [41]. Characteristically MA islands in granular bainite microstructures are at low angle boundaries between ferrite regions giving a distinct appearance on etched micrographs.

1.1.5   Acicular ferrite

Acicular ferrite (AF) was first characterised in the early 1970s in work conducted by Smith et al. [42] and noted for its high dislocation density and fine grained nature yielding its mechanical properties; good strength, toughness at low temperatures and resistance to corrosion. AF has an arrangement of ferrite plates facing in multiple directions within prior austenite grains [43,44]. AF is formed upon rapid cooling of low carbon steels whereby nucleated ferrite plates are small and have a narrow, elongated morphology far different from that of typical polygonal ferrite grain structures. The cooling rate and amount of deformation in the finishing rolling passes dictate the volume fraction of AF produced, the larger the deformation, the higher the transformation temperature which leads to greater amounts of AF in a microstructure (Figures 1.13, a and b). In the case of plate production AF will precipitate in areas of high dislocation density when the austenite is subject to deformation in the non-recrystallisation region [44-46]. During subsequent cooling the AF may coarsen and polygonal ferrite will form near prior austenite grain boundaries.
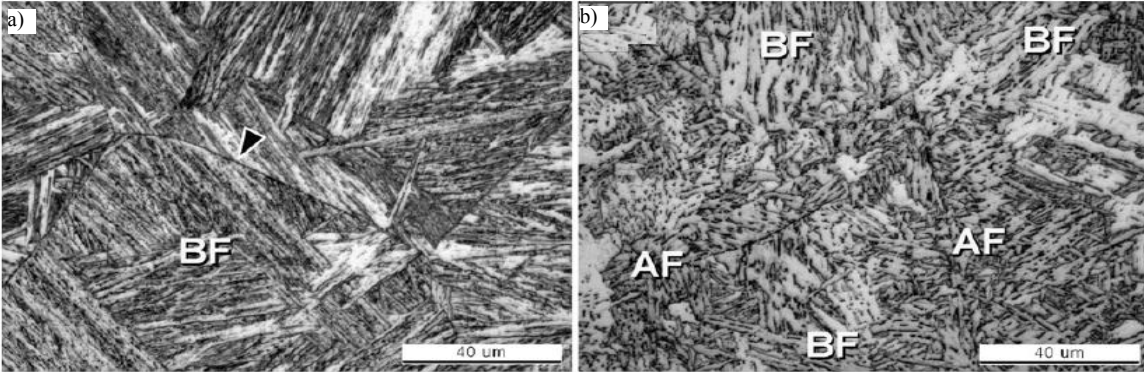
Figure 1.13 Example of microstructures arising from (a) no deformation during the TMCR and (b) deformation in the austenite region where BF is bainitic ferrite and AF is acicular ferrite [44]

The amount of AF formed is therefore not greatly dependent on carbon content but heavily dependent on the amount of deformation in the prior austenite grains and hence finish rolling temperature, cooling rate and alloying elements such as Cu, Ni and Mo which suppress the transformation to pearlite. The additions of Mo also delay the precipitation of polygonal ferrite and enhance the formation of AF [26,46,47].

1.1.6 Martensite - austenite constituents (MA islands)

MA constituents are typically found in higher strength linepipe steels (> X80 grade steels). Upon cooling, carbon-rich austenite can transform to pearlite but with an increase in cooling rate can form small amounts of martensite with or without retained austenite. The formation of martensite involves no diffusion of carbon and so the levels will be the same as the parent austenite phase [48]. After rolling, accelerated cooling is applied on the run out table, faster cooling rates increases the amount of MA these steels exhibit, (as

shown in Figure 1.14, a) however a lower finish cooling temperature has a greater effect on the observed volume fractions of low temperature transformation constituents such as MA (Figure 1.14, b) due to accelerated cooling through the AF start-finish temperature regions which conversely encourages the formation of greater levels of GB and MA [49,50].
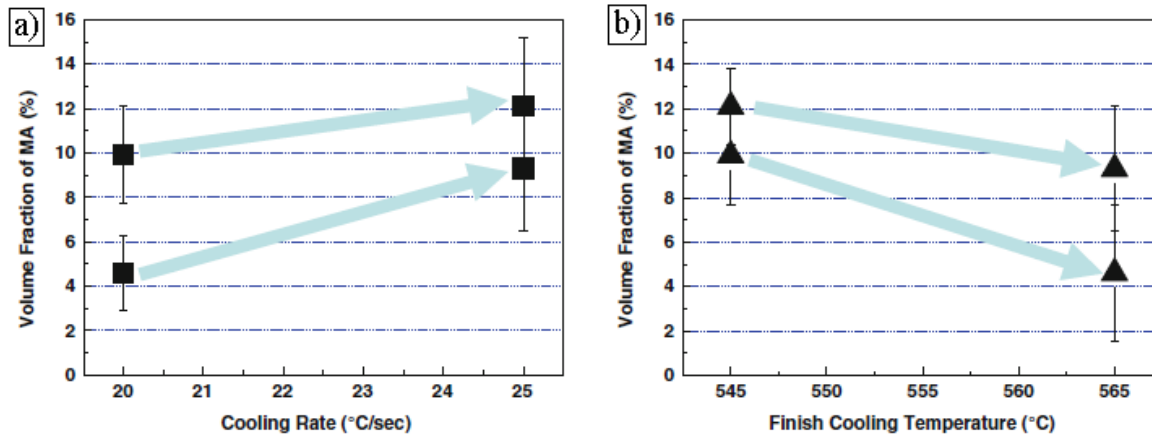
Figure 1.14 Observed volume fraction of MA as a function of (a) cooling rate and (b) finish cooling temperature in a 0.08C-1.9Mn-2Mo-0.25Ni-0.06Nb steel [51]

The presence of MA in small amounts (< 3 %) promotes strength increase however studies have shown the improvements in strength to decrease or even reduce when the volume fraction of MA increases to over 5 %, tensile strength is acknowledged to increase with increasing MA content [51,52].

1.2　Precipitation strengthening

HSLA steels typically use small additions of carbo-nitride forming elements Ti, Nb and V (< 0.1 wt %) to increase strength. This is achieved in two ways; refining the austenite grain size by grain boundary pinning during reheating (primarily Ti(C,N)) and through recrystallisation control during TMCR (primarily Nb(C,N) via strain induced precipitation and solute drag) and by forming small precipitates (primarily VC) which hinder dislocation motion during cold deformation thereby raising the yield stress.

1.2.1　Formation of carbo-nitride precipitates

There is a hierarchy for formation of carbo-nitride particles in steel during cooling due to the different thermodynamic stability of the various precipitates. Nitrides form at higher temperatures than carbides, titanium has the strongest affinity for nitrogen and its precipitates have a higher dissolution temperature than those formed from niobium, with vanadium showing the lowest temperature of formation as shown in Figure 1.15.
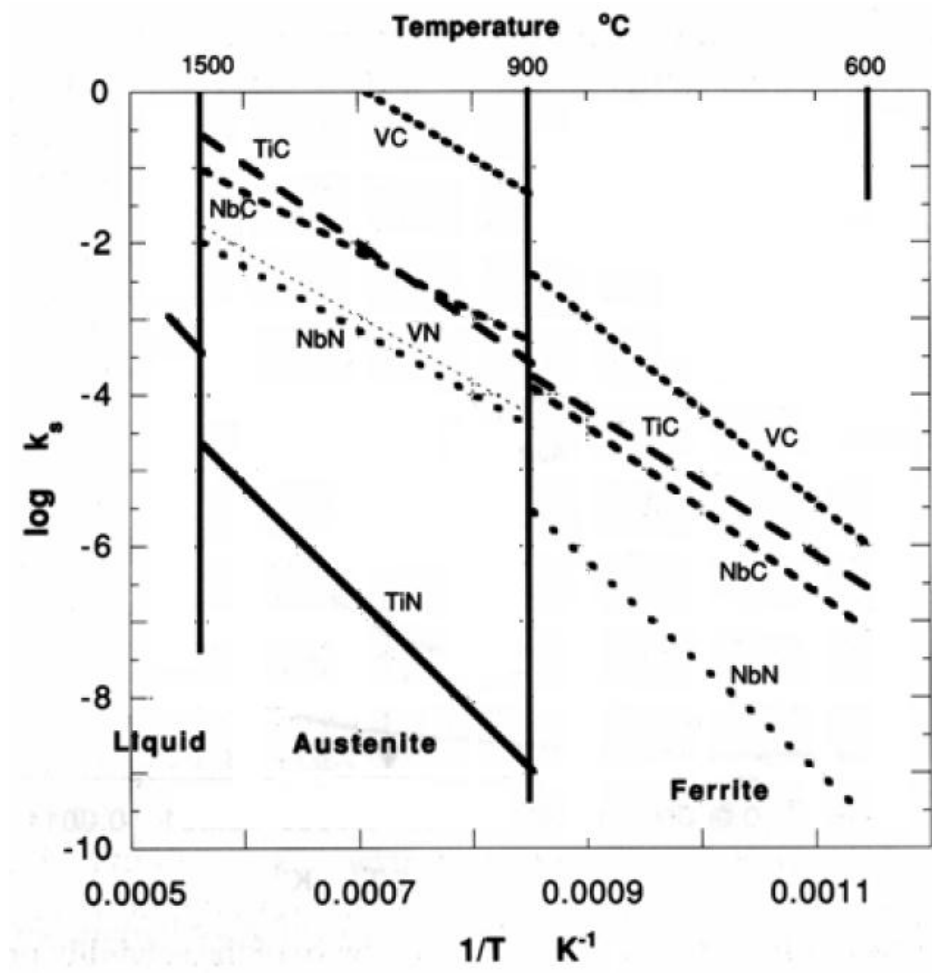
Figure 1.15 compound precipitation of elements (Ti,Nb,V)(C,N) and their temperature dependence derived from the Arrhenius relationship: Log k_s = log [M] [X] = A − B/T Where k_s is the equilibrium constant, [M] = microalloying additions (wt %) [X] = additions of C and N (wt %), A and B are constants and T is absolute temperature

1.2.2   Titanium, niobium and vanadium rich carbo-nitride phases:

Titanium, niobium and vanadium rich carbo-nitride precipitates have been extensively studied and are generally classified into 3 categories:

Coarse Ti-rich nitrides

Coarse TiN particles have been reported to range up to several microns in diameter due to their formation in the liquid phase and have a cuboidal morphology; generally their chemistry is mostly made up of Ti with only trace amounts of Nb [54,55]. Formation in the solid phase refines their size to < 500 nm [56] which can act to pin austenite grain boundaries at high temperature, for example during slab reheat prior to TMCR [57,58], whilst the coarse (Ti,Nb)-rich particles are too large, and too few in number, to contribute to grain refinement and can also be detrimental to toughness [54,59].

Intermediate (Ti,Nb)-rich particles

(Ti,Nb)(C,N) particles can be observed in HSLA steels with sizes >10 nm that formed after solidification, but prior to rolling. The formation temperature depends on the levels of Ti, Nb, C and N in the steel (and can be predicted using thermodynamic software). Generally TiN precipitate first then Nb(C,N) form on the TiN particles to give complex (Ti,Nb)(C,N) particles, with further small Nb(C,N) particles forming on cooling. It has been found that the ratio of Ti – Nb is lower for smaller particle sizes, this relationship is shown in Figure 1.16 for a low carbon X100 grade steel [60]. Often these mixed particles

24

are of ellipsoid, round or polygonal morphology depending on the Ti content. There are large size ranges reported for this type of precipitate between 10 – 700 nm, precipitates < 50 nm are generally Nb(C,N) and take on a spherical / ellipsoid / lens / needle or cuboidal morphology [61-72]. Cuboidal particles have been observed of Nb(C,N) composition [54].
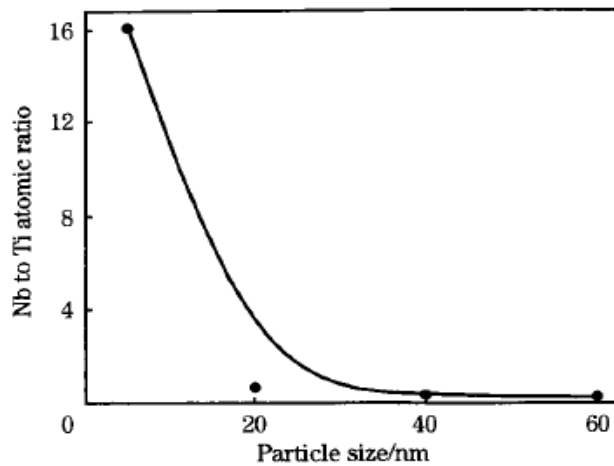
Figure 1.16 effect of the Nb:Ti atomic ratio and particle size in a 0.005C-1.7Mn-0.041Nb-0.01Ti X100 grade steel [60]

VC precipitates

Vanadium carbides are usually the last precipitates to form in low C-Ti-Nb microalloyed steels, particularly in the presence of Ti whereby most of the free nitrogen is taken up before the point at which V starts to precipitate. Vanadium carbo-nitrides will precipitate behind moving γ→α interfaces at higher temperatures; at lower temperatures precipitation can occur randomly in the α matrix [73]. The lower the precipitation

temperature the finer the particle size which has been shown by fine dispersions of V(C,N) dispersed at incoherent interphase boundaries such as those between γ and α, pearlite lamellae and upper bainite laths [74,75]. Interparticle spacing within rows of interphase precipitates is also observed to decrease with lower isothermal transformation temperatures [76].

Strain induced particles

Strain induced particles are generally carbides (VC, TiC, NbC) and predominantly of spherical morphology in HSLA steels, ranging from 2 – 50 nm in diameter depending on the strain and temperature at which they are formed [54,67,72].

Strain induced precipitates (SIP) benefit microstructures by restricting the recrystallisation of austenite after interpass deformation. Accelerated diffusion of Ti, Nb and V along dislocation lines will leave solute depleted regions, precipitates will then nucleate on high energy points such as dislocation nodes and pin austenite grain boundaries (provided the driving force for recrystallisation is lower than that of the pinning forces) [78]. There are a range of studies into strain induced precipitates and the various roles that carbo-nitride forming elements play. In the case of titanium, nitrogen will be taken up in the formation of TiN at high temperatures and so strain induced precipitation of Ti has been observed to be TiC [79], For NbTi microalloyed steels, NbC was reported to be the predominant particle to arise from strain induced precipitates and were frequently found to precipitate on existing (Nb,Ti)(C,N) particles that remained

undissolved during reheating. NbC would be expected as the dominant phase to precipitate as it has a large temperature range in which there is driving force for precipitation in comparison to other carbo-nitrides as shown in Figure 1.17. Precipitation of V mostly occurs in the ferrite phase due to its high solubility in austenite however strain induced precipitates can be effective in taking some V out of solution in austenite to form V(C,N) or (Nb,V)(C,N) if Nb is present [80]
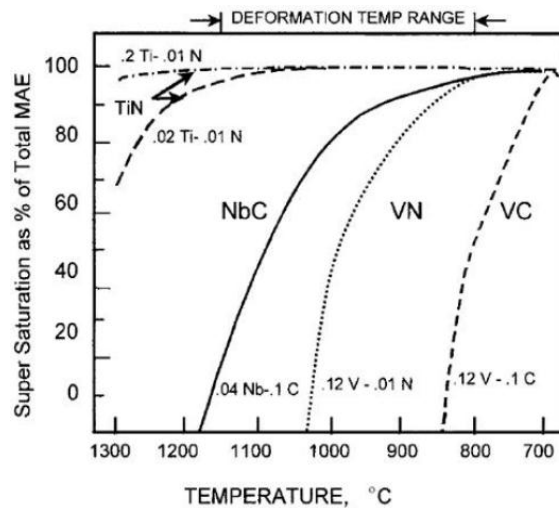
Figure 1.17 Graph depicting the supersaturation typical of carbo-nitride forming microalloying elements (MAE) in the hot deformation temperature regions [81]

Distribution of VC precipitates

Because precipitation of carbo-nitrides will vary through the different stages of production (solidification, reheating, TMCR and cooling) for plate and sheet steels, the nature of their distributions will vary, which can bring advantages or disadvantages to the overall strength of a material.

Particles (e.g. VC) precipitated in supersaturated ferrite have shown a random, dense distribution of fine particles (Figure 1.18, a), which will provide a uniform contribution to strengthening. Giving sufficient time whilst cooling (< 5 °C/min) precipitates will form on interphase boundaries which can be easily identified by their linear formation within the ferrite matrix [82] (Figure 1.18, b).
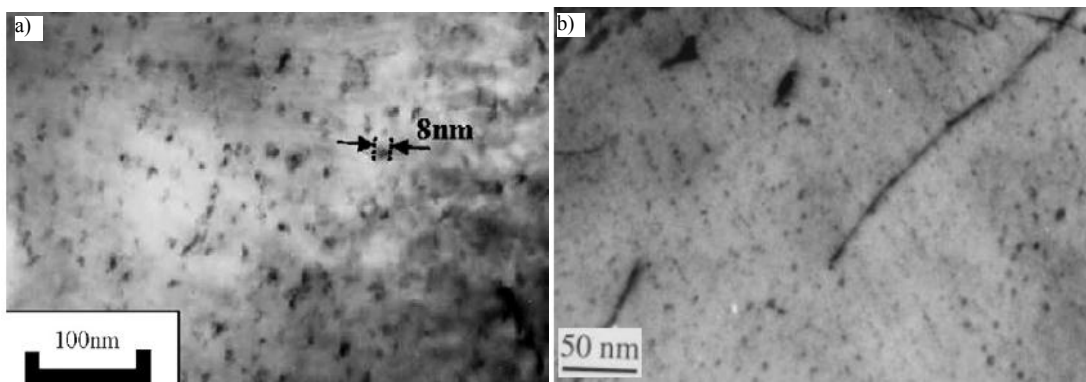
Figure 1.18 TEM images of carbo-nitride precipitates formed in (a) ferrite and (b) interphase boundaries [82]

1.2.3 Precipitate contributions to yield stress

The range of contribution vanadium and niobium rich particles have on the yield stress for HSLA C-Mn steels is reported to be between 40 – 150 MPa [63,66,83]. Studies on two X65 C-Nb / C-Nb-V bearing steels [35] classified the particles as being coarse or fine, having an effective circle diameter (ECD) > 50 nm and < 50 nm respectively. Contributions attributed to coarse precipitates (predominantly related to Nb-Ti rich particles) were reported as between 5 and 15 MPa, whilst the smaller carbides (mainly

(Nb,V)C, and, in annealed specimens, CuS particles) were reported to give much greater values between 20 and 75 MPa owing to their higher number densities and reduced inter-particle spacing [35]. The most effective strengthening size range for precipitates is reported to be between 5 and 20 nm to allow for optimal size and spacing to block dislocations without being too widely dispersed or too small to obstruct dislocations [84].

Precipitates will either be of a coherent nature to the matrix i.e. all crystallographic planes are constant throughout them and the matrix or have an incoherent / semi-incoherent interface. If the particle is small enough to be coherent with the matrix a cutting mechanism will operate and larger particles with semi-coherent interfaces with the matrix will demonstrate a blocking mechanism when a dislocation tries to bypass it. It is a common assumption that the majority of strengthening comes from non-deformable particles. This is described by the Ashby-Orowan mechanism and quantitative contributions to the yield stress of a material can be calculated from equations taking into account the average particle spacing, size and number density of precipitates (Figures 1.19, a and b). It is widely accepted that strengthening from particles which allow themselves to be sheared by dislocations only contributes marginally to the strength of a material but by a completely different mechanism from that of non-deformable particles; either by increased energy expended by the dislocation during particle shearing or by stress fields surrounding particles [85]. It is not well recorded from what size range different types of precipitates become hard obstacles; studies by Kostryzhev [35] found CuS particles in X65 grade steels were partially bisected by mobile dislocations when their diameter was less than 12 nm. Another effect of particle shearing is the channeling

of dislocations into a small number of slip planes; as dislocations cut through particles, the particle cross section reduces which requires a lower critical shear stress from an already active slip plane for subsequent dislocations to move through. This creates high shear strains and local concentration of slip on favourable slip planes [85].
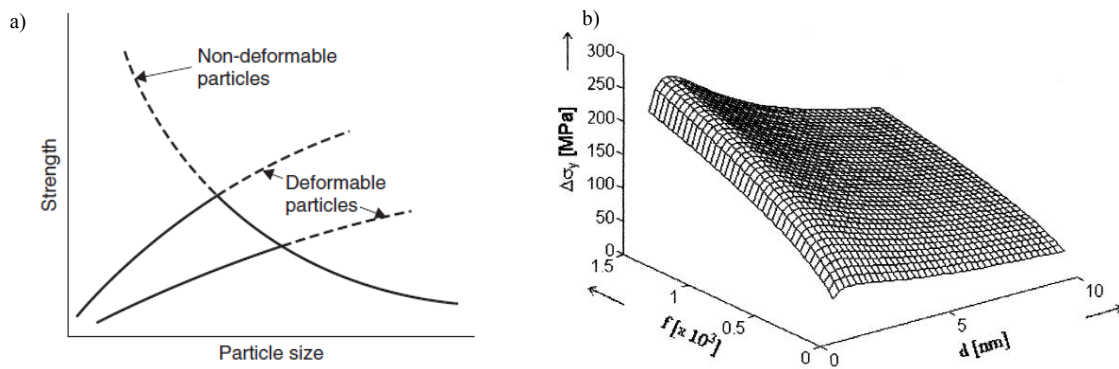
Figure 1.19 (a) Effect of particle size taking into account the deformation mechanism [86] (b) effect of particle diameter and volume fraction on the strengthening based on Ashby-Orowan theory [87]

For spherical particles down to 5 nm diameter the following equation is well established for obtaining the contributions to yield stress of a material containing a precipitate volume fraction of between 0.0003 and 0.0015.

$$\Delta \sigma y = \frac{10.8\sqrt{f}}{X} \ln \left[\frac{X}{6.125.10^{-4}} \right] \tag{2}$$

Where f is the volume fraction of precipitates and X is the mean diameter in μm.

To stop over compensation in the prediction of yield stress arising from the size effect of smaller particles (< 5 nm) in the Ashby-Orowan model the following equation was proposed [88].

$$\sigma_i = \frac{3.56Gb}{4\pi l_r}\left[\frac{1+v-\frac{3v}{2}}{1-v}\right]ln\left[\frac{l_r}{b}\right]\left[\frac{ln\left[\frac{2D_g l_r}{b(D_g+l_r)}\right]}{ln\left[\frac{l_r}{b}\right]}\right]^{3/2}$$ (3)

Where v = Posisson's ratio, G = the shear modulus, b = the Burgers' vector $l_r = \left(\frac{\pi D_g^2}{6f}\right)^{\frac{1}{2}}$ = mean distance between obstacle centres in the glide plane in µms. D_g = mean particle diameter (µm) and f = particle volume fraction.

Coarse precipitates > 50 nm in diameter formed in the γ + α phase field have been frequently observed on grain boundaries in C-Nb-V steels [35]. In addition higher number densities of precipitates were also observed, using SEM, in second phase pearlite regions than in the adjacent ferrite grains, which was linked to microalloying element segregation during solidification. This may result in non-uniform strengthening.

1.3 The role of microalloying elements and grain size on strength in HSLA steel

1.3.1 Microalloying elements

Typical industry practice for HSLA linepipe steels is to limit the wt % of alloying elements to a carbon equivalent under 0.32 % which must be precisely balanced as per equation (4) since increasing the amount of carbon increases the risk of hard phases forming during welding of linepipes, which would be detrimental to toughness within the heat affected zone (HAZ).

$$CE \text{ (wt \%)} = \text{wt \%C} + \text{wt \%Mn}/6 + \text{wt \%(Cr+Mo+V)}/5 + \text{wt \%(Ni+Cu)}/15 \qquad (4)$$

Where low temperature toughness and resistance to hydrogen induced cracking are major concerns formulae for carbon equivalent such as equation (5) are applied [89,90].

$$CE \text{ (wt \%)} = \text{wt \%C} + \text{wt \%Si}/25 + \text{wt \%(Mn+Cu)}/20 + \text{wt \%(Cr+V)}/10 + \qquad (5)$$
$$\text{wt \%Ni}/40 + \text{wt \%Mo}/15$$

Where CE is limited < 0.12 wt %.

Microalloying additions serve three purposes in microalloyed steel –

- Substitution of iron atoms to increase strength and hardness

- Suppression of phase formation at lower temperatures and cooling rates.

- Formation of carbo-nitride particles

Carbon and nitrogen act as interstitial elements and are the two most effective elements for solid solution strengthening, they have extremely high strengthening coefficients comparative to other elements but have limitations as to how much strengthening they can contribute. The solubility at 723 ^{o}C for C and N is 0.02 wt % and 0.1 wt % respectively which decreases to $< 5 \times 10^{-5}$ wt % at ambient temperatures. Formation of carbo-nitride precipitates further reduces the free carbon and nitrogen in solution. Table 1.4 summarises the solid solution strengthening coefficients for various alloying elements in steel.

Table1.4 Strengthening coefficients for a number of solutes [53]

Element	C & N	P	Si	Mn	Mo	Cu	Cr	Ni
Strengthening co-efficient (MPa per 1 wt % addition)	5544	678	83	32	11	39	-31	0

From the values given in Table 1.4 it is possible to calculate the total solid solution strengthening contributed to a material given the wt % composition, this equation does not take into account the alloying elements which may be used for the formation of precipitates / inclusions. The stress required for a dislocation to move through a crystal lattice (Peierls / friction stress) is widely accepted to be 56 MPa for iron but authors such as Morrison et al. have reported the friction stress of iron to be as high as 70 MPa [91].

$$\sigma_y = \sigma_I + \sum_{i=1}^{n} k_i.c_i + k_y d^{-1/2} \tag{6}$$

Where σ_i is the friction stress of iron, c_i is a concentration of ith solute and k_i is the coefficient of strengthening as per Table 1.4.

The other alloying elements added to HSLA steel do not create interstitial atmospheres, as they cannot fit into the spaces within the iron matrix. Instead they substitute themselves for an iron atom and cause strain fields as the lattice is distorted. P, Si and Mn are the most effective elements in terms of this; Figure 1.20 shows the effect of Mn on tensile strength.
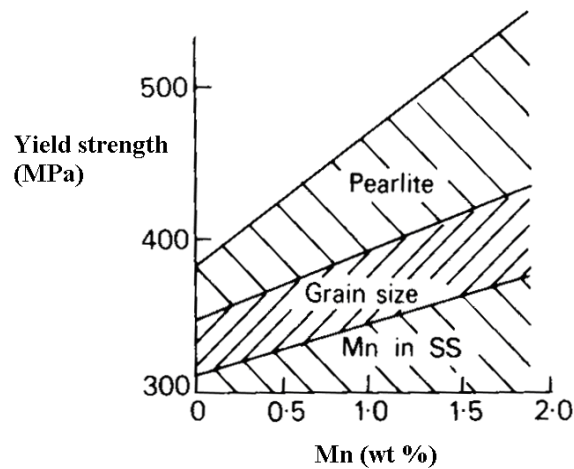
Figure 1.20 Effect of solid solution strengthening of Mn additions, after [92]

The elements copper, molybdenum, nickel and chromium do not provide as large a contribution to strengthening per wt % addition as C and N (Cr has a slightly negative effect on strength).

Mo, Ni, Cu and Cr combined with Mn are added to promote toughness by grain refinement through lowering the austenite-ferrite transformation temperature; V, Nb and Mo will slow down recrystallisation of austenite but have little effect on solid solution strengthening. Kasugai and Titherand et al. found Cr and Mo to increase the A_{r3} temperature, suppressing the formation of pearlite, lowering the transformation temperature of bainite and martensite and promoting acicular ferrite formation [93-94] thereby increasing the weldability of microstructures and reducing the susceptibility to HIC [95-96].

Ni has a strong effect on the suppression of the $\gamma \rightarrow \alpha$ phase transformation. Strengthening levels are not directly influenced by its presence, as there is a small misfit parameter but it is used in X80 grade linepipe in relatively small amounts to ensure the formation of martensitic, bainitic and acicular phases (Figure 1.21).
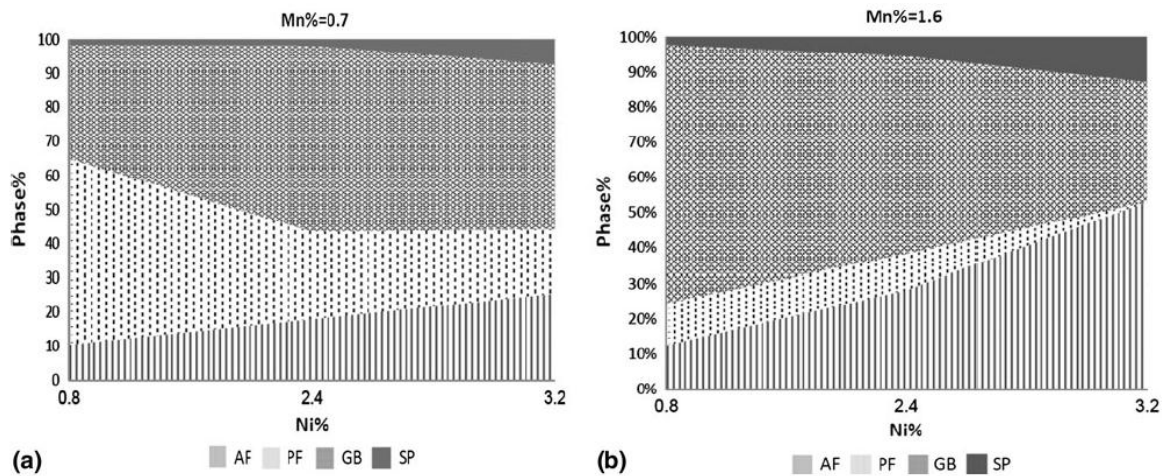
Figure 1.21 Influence of Ni and Mn on the phase compositions: acicular ferrite (AF), polygonal ferrite (PF), granular bainite (GB) and side plate ferrite (SP) in X80 Linepipe steel for (a) 0.07C-0.7Mn-0.40Mo and (b) 0.07C-1.6Mn-0.40Mo [96]

1.3.2 Grain size strengthening

A decrease in grain size leads to an increase in the total area of grain boundaries which act as obstacles to dislocation motion when they are at high angles to one another [97]. A widely held definition of what constitutes a low angle grain boundary (LAGB) and a high angle grain boundary (HAGB) is under or over 15° misorientation between two grains respectively [98,99] although some authors report the differentiating angle to be as low as 10° [100].

The effect of grain size on strength has been quantified by the Hall-Petch equation:

$$\sigma_y = \sigma_0 + k_y \mathrm{d}^{-1/2} \tag{7}$$

Where σ_0 is the friction stress of iron and k_y represents a constant reported to be between $21 - 24$ in carbon steels [53,101-104].

The Hall-Petch relationship is plotted for a low carbon steel in Figure 1.22. Studies on the influence of grain size on yield stress in ultrafine grained steels have shown strength to increase down to a grain size of 20 nm until a grain boundary sliding mechanism operates [105].
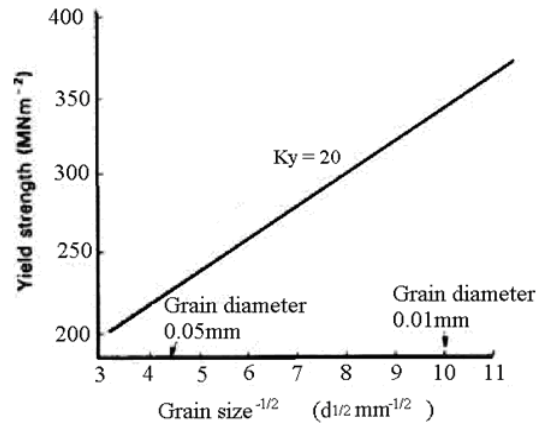
Figure 1.22 Effect of grain size on yield stress for a 0.17C-0.85Mn steel [105]

2   Mechanical behaviour of low carbon steels

2.1.1   Yield and work hardening behaviour in steels

When steels are subject to an external force, which exceeds the elastic limit of the material, yielding occurs which is the initiation of crystal slip of the lattice structure. Once slip has been initiated then the stress required to continue deformation is termed the flow stress of the material. Flow stress is the stress required to continue movement of mobile dislocations which must overcome obstacles such as other dislocations, Cottrell atmospheres from solute atoms dispersed in the matrix and coherent / incoherent particles in the matrix. As deformation continues the number of dislocations increases requiring greater stresses to continue slip and this is known as work hardening. During work hardening there is an increase in dislocation density, which, in turn, leads to an increase in the material's hardness [106]. The concept of work hardening by crystal imperfections was first put forward in 1934 [107] and despite still being the subject of widespread research and models, there is a distinct absence of a universally accepted criterion for work hardening behaviour in steels.
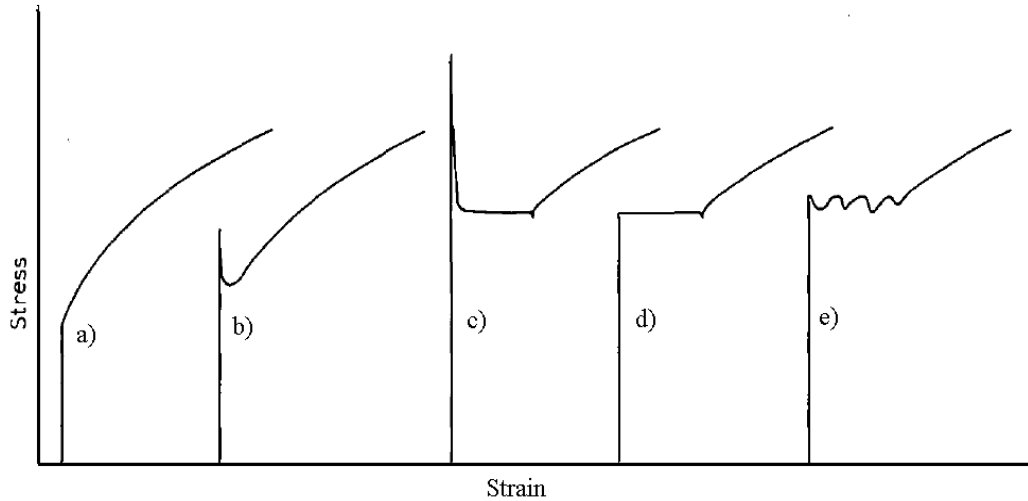
Figure 2.1 Typical stress strain curves for low carbon steels (a) represents continuous yielding, (b) upper yield and lower yield points with no Lüders strain, (c) upper yield point with Lüders strain, (d) no upper yield point with Lüders strain, (e) Portevin–Le Chatelier effect during Lüders strain [108]

One of the main differences in the tensile stress-strain behaviour of many carbon steels is the nature of the yield point, which can be observed in the stress strain curves represented in Figures 2.1 a-e. Figures 2.1 b-e have clearly identifiable yield points (upper and lower yield stresses) but some steels behave in manner similar to Figure 2.1 a in which no sharp yield point phenomenon exists and an offset is required (usually 0.001 - 0.002 strain) to define the proof stress (which is taken to be equivalent to the yield stress), this is known as continuous yielding. The yield behaviour shown in Figure 2.1 b, where there is a yield stress drop, occurs as the flow stress is lowered slightly after dislocation motion is activated, due to the dislocations escaping from pinning (Cottrell) atmospheres. Not all specimens homogenously work harden after yielding (Figure 2.1 c-d) and propagation of

Lüders bands are common below 0.02 strain in many carbon steels. Lüders banding has also been observed up to 15 % strain in some fine-grained material [108].

The Lüders strain region occurs when the work hardening rate at the lower yield stress fits equation (8). In practice work hardening in the Lüders range is never exactly zero but the closer d_σ/d_ε is to this value at the lower yield stress, the more prolonged the Lüders strain region is [109] (Figure 2.2).

$$\varepsilon_L \times \left(\frac{d\sigma}{d\varepsilon} \right)_{LYS} = \Delta$$

(8)

where ε_L = Lüders elongation, $(d_\sigma/d_\varepsilon)_{LYS}$ = the work hardening rate at the LYS and Δ is a constant depending on test temperature, carbon content, strain rate, microstructure and grain size.
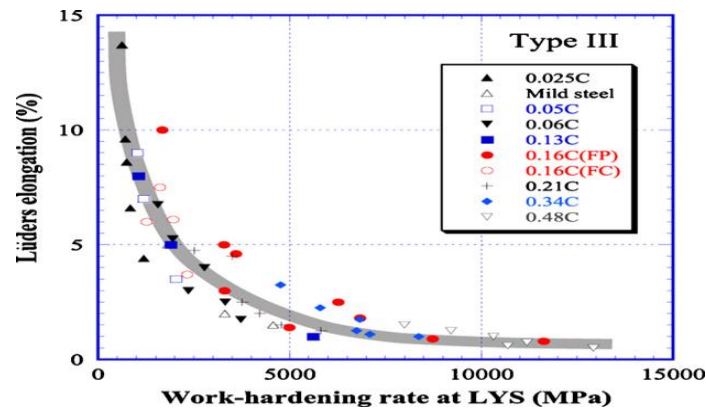
Figure 2.2 Relationship between Lüders elongation and work hardening rate using data from experiments on various low carbon, FP (ferrite-pearlite) and FC (ferrite-cementite) steels with differing carbon content and grain sizes [91, 109,110]

Lüders bands are the result of elastic material interacting with plastically deformed regions, where the dislocations move away from pinning points. During deformation stress concentrations form as these glissile dislocations are mobilised, rapidly multiply and the elastic portion of the material takes the majority of the load [108]. Serrations can occur in the Lüders strain region (Figure 2.1 e); this is termed the Portevin–Le Chatelier effect and is characterised by sharp increases and decreases in the stress strain curve caused by the repeated pinning and release of mobile dislocations by interstitial elements such as carbon and nitrogen.

Flow stress begins to increase with increasing strain after any yield phenomenon and Lüders strain, and this is known as work hardening. There are five distinct stages to work hardening, with the three initial work hardening stages for carbon steels being significant for linepipe fabrication and are therefore discussed here, these are shown schematically in Figure 2.3.
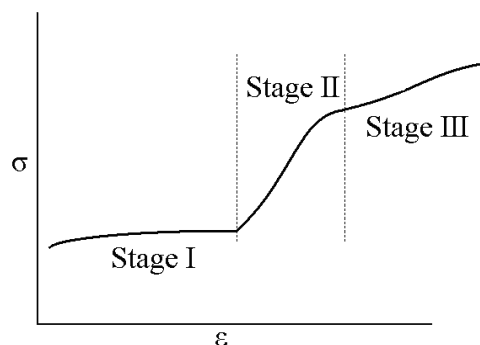
Figure 2.3 Schematic diagram of post-yield stress-strain behaviour in fcc and bcc crystal lattices showing the initial 3 stages of work hardening

During stage I work hardening dislocations accumulate at a rate inversely proportional to the mean slip distance between obstacles [111]. The distribution of dislocations is generally not homogeneous throughout the ferrite grains due to prior processing / residual stresses. During this initial stage of deformation un-deformed grains of low dislocation density will accumulate dislocations. Dislocations, which are present generally, in these grains have fewer and less effective obstacles in their path such as strain fields from other dislocations; these weak interactions do not significantly raise the yield stress thus a low rate of work hardening is observed. Dislocations during stage I hardening only act on one slip plane and structures such as Orowan loops and pile-ups may be observed [112]. If work hardening during stage I is negative or not linearly increasing i.e. Lüders region, then dislocations may be suddenly relieved of obstacles blocking their path - typically in carbon steels this mechanism would be dislocations escaping from Cottrell atmospheres due to solute atoms or elastic interaction with plastically deformed regions (as covered in the previous section). This is still considered as stage I hardening. When the dislocation distribution throughout neighbouring grains becomes relatively uniform then the work hardening rate increases sharply in a linear fashion and can be identified as stage II work hardening; during this stage a small degree of annihilation occurs but this is insignificant compared to the overall net effect of the generation of more dislocations (by the Frank Read mechanism) and the increased dislocation-obstacle interaction operating due to the increase in dislocation density and decrease in slip distance between obstacles. Slip will occur on multiple systems at this stage resulting in strong dislocation-dislocation interactions and the formation of forrest dislocations, tangles, pile-ups, nodes and jogs [112,113]. At the end of stage II work hardening cellular structures begin to develop

Eventually the work hardening behaviour becomes parabolic and this is known as stage III work hardening, the same mechanisms as in stage II are still occurring but an increase in cross slip and subsequent annihilation of dislocations results in a reduced rate in the number of dislocations being created, and hence reduced work hardening rate characterised by a parabolic stress strain curve. Not all authors are in agreement with this explanation of parabolic hardening at this stage - Bassim and Klassen have concluded that the decreased rate in work hardening behaviour is due to the reduction in diameter and eventual cessation of formation / growth of cellular structures during stage III which was experimentally proven with a C-Mn low alloy steel [114]. Kuhlman proposed that the cause of parabolic stage III hardening is more likely to be caused by increased mobility of dislocations due to increased cross slip during stage III [112]. The latter stages IV and V of work hardening see cellular structures become sub-grain structures and impede the movement of dislocations between cells in much the same way as HAGB's [115].

At the time of writing, literature on steels containing MA constituents does not comment on the effect of interstitial carbon on the work hardening rate, one reason being the presence of MA constituents influences work hardening rates by acting as a source of dislocations [117]. The authors of [118] found that the work hardening rate is dependent on the cementite content in dual phase ferrite-pearlite steels due to the increase in dislocation density from the interfacial area between ferrite and cementite (Figure 2.4). Work hardening was attributed to the lamellar ferrite at small strains where there is assumed to be no deformation of cementite. Although the average work hardening rates

for each composition fit well with the equations used, it is questionable whether carbon wt % alone can be responsible for the work hardening rate as the cementite volume fraction was used as a function of the carbon content in the equations.
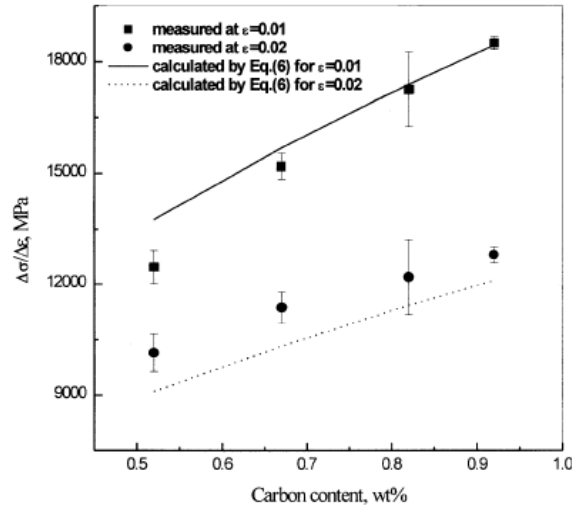
Figure 2.4 Work hardening rate as a function of carbon content in four ferrite - pearlite steels of 0.52C/0.67C/0.82C/0.92C-0.3Si-0.4Mn compositions [118]

Studies have failed to accurately predict the relationship between the rate of work hardening or the yield stress and hardness of steel to the same degree of accuracy as the relationship between tensile strength and hardness [119]. As Figure 2.5 a shows, a linear relationship exists between the tensile strength and hardness (generally the strength is 3.5 times higher than the hardness) but when plotted against yield stress or the rate of work hardening the plots show a large amount of scatter below 400 Hv (Figure 2.5 b and c). Despite this, a general trend can be observed in dual phase low carbon steels consisting of ferrite and levels of martensite up to 60 % where the higher the Hv of a material, the greater the strength and the lower the rate of work hardening.
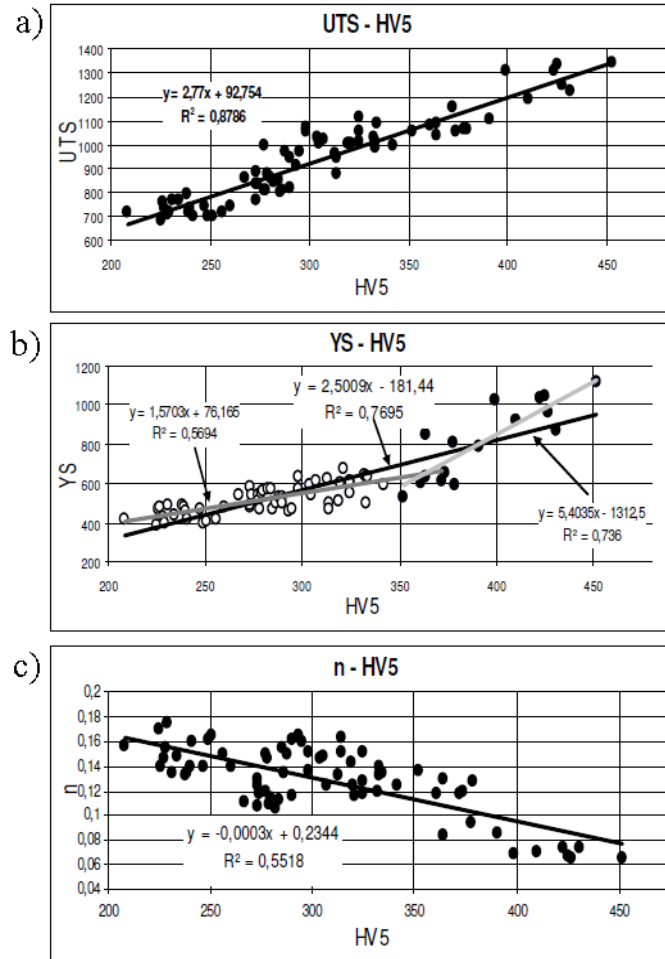
Figure 2.5 Relationship between hardness value and (a) ultimate tensile strength (b) yield stress and (c) work hardening rate in intercritically annealed dual phase ferrite-martensite 0.07-0.15C-1.0-1.8Mn steels [119]

Grain size has more of an effect on the rate of work hardening at small plastic strains, < 0.02 strain, than at higher strains (Figure 2.6). Studies on the plastic behaviour of polycrystalline materials showed that the strain hardening behaviour up to 0.02 strain decreases with an increase in average grain size over 2.5 µm. Strain hardening ceased to be dependent on grain size when the average grain size was below 2.5 µm [120].
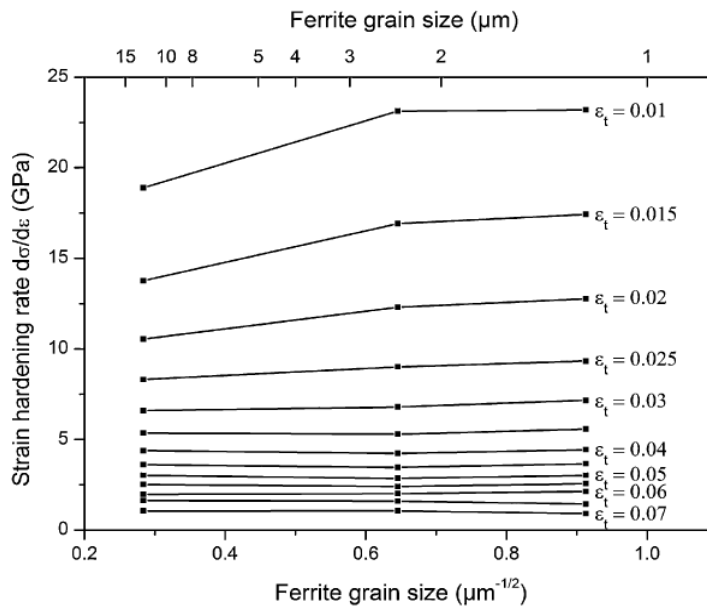
Figure 2.6 Graph depicting the effect of grain size on the rate of work hardening at small strains for a 0.17C-1.49Mn steel. For strains above 0.02 strain the grain size ceases to have any significant effect [120]

Two other features in the microstructure have a profound effect on the rate of work hardening; particles and dislocations, which are discussed in detail in sections 2.1.1.

2.2 Role of dislocations in HSLA steel plate

Crystals deform by means of crystal slip via dislocation motion, which requires a certain level of stress to initiate. The stress required for dislocation slip to initiate and continue moving through the matrix is raised when their motion is hindered and this forms the basis for the five strengthening mechanisms operating in metals.

2.2.1 Evolution of dislocation structures in steel during plastic deformation

The dislocation density in a polycrystalline material gives an accurate overview as to how much deformation the specimen has undergone (assuming no recovery or recrystallisation processes have occurred) as an increase in plastic deformation will give rise to a greater number of dislocations per unit volume.

There is a set hierarchy of structures in bcc metals that evolve with plastic deformation and these are split into 2 categories: high energy dislocation structures and low energy dislocation structures (HEDS and LEDS respectively). The majority of dislocation structures in steel are classified as LEDS, i.e. when a dislocation is no longer able to lower its energy then it falls into the latter category and these encompass Orowan loops, tangles, bows and dislocation pileups [112].

In a metal which has been subject to TMCR and slow cooled to ferrite and pearlite, dislocations are given sufficient time to become low energy dislocation structures (LEDS) comprising regular straight line structures which are generally separated in a

heterogeneous fashion within ferrite grains. In annealed steels the dislocations are sometimes seen to adopt a sub-structure comprising of regular networks / 'nets' (Figure 2.7 a), even though dislocations intersecting the individual dislocation segments still appear relatively straight (Figure 2.7 b and c) [121].
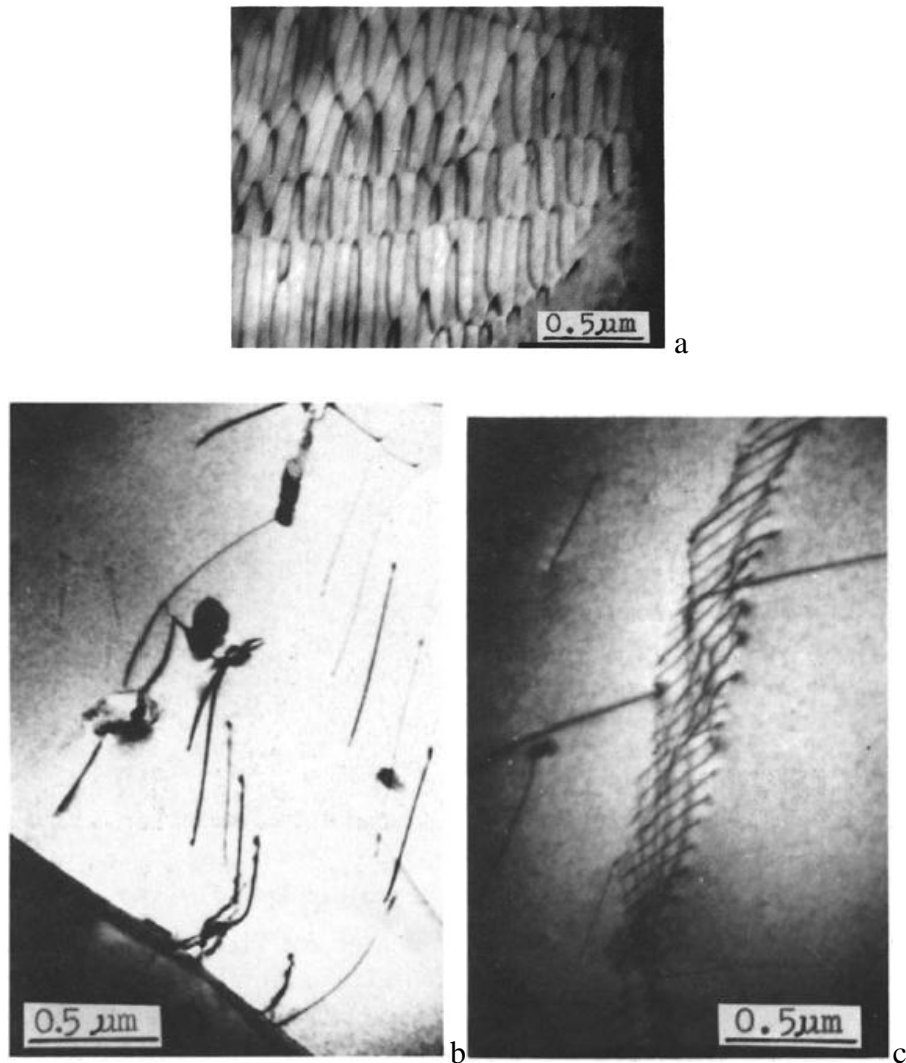
Figure 2.7 (a) low energy dislocation sub structure network in an annealed CrMo-containing ferritic steel (b) relatively straight dislocation lines intersecting and (c) running parallel with one another [121]

Work by Pal'a et al. and Dingly and Mclean [122,123] has documented the evolution of dislocation structures in low carbon structural steels with coarse grain sizes ranging from 25 - 200 μm. There is a well established pattern of how dislocations arrange themselves as strain hardening increases. In the early stages of deformation dislocations are still relatively straight, homogeneously distributed and piled up along favourable slip planes. Dislocations will eventually become immobilised by grain boundaries, which then requires generation of more dislocations to continue the process of slip. Dislocations will become high energy dislocation structures (HEDS) with increasing strain, comprising of jogs and tangles which act as obstacles to glissile dislocations. Dislocations will also bow against these obstacles and particles.

On further straining dislocations lose their ability to re-arrange themselves in an orderly fashion and become clusters, the distribution becomes ever more heterogeneous throughout the grains and areas of high and low dislocation density within ferrite grains become apparent. At this point dislocations become locked, acting as anchoring points for other dislocations and generation sources for new dislocations as per the Frank-Read mechanism.

As more dislocations are generated they become absorbed into fine bands up to 20 times greater in dislocation density than the adjacent areas [124,125], these bands interconnect taking on a cellular morphology that surround areas relatively free of dislocations. With further strain the cell structure size decreases [114] (Figure 2.8). Eventually the cells attain a stable size and develop into sub grains within ferrite grains with their own misorientation (Figure 2.9).
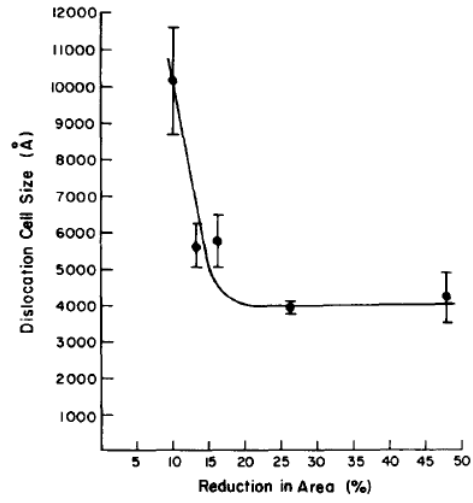
Figure 2.8 Dislocation cell size with increasing strain in a 0.12C-1.15Mn-0.01Nb steel
[114]
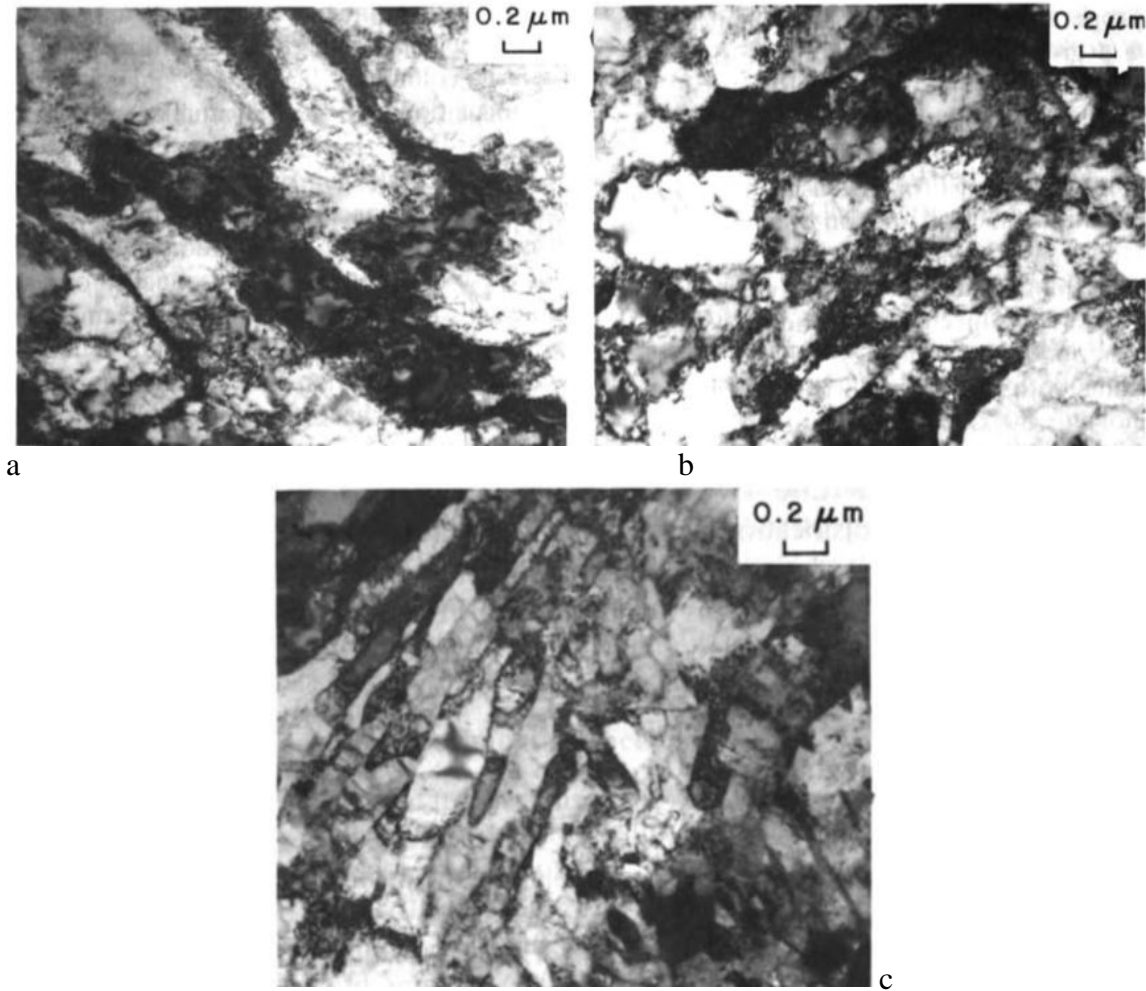
Figure 2.9 Evolution of dislocation cell structure, with increasing deformation the cell size is seen to decrease and substructure develop in a 0.40C-0.75Mn steel through the range of (a) 0.12 strain (b) 0.18 strain and (c) 0.70 strain [114]

The initial dislocation density increase with strain is greater with grain refinement [124]. Work by Kostryzhev et al. [35] reported dislocation tangles and interactions with precipitates in as-received (TMCR processed) and annealed C-Mn, C-Mn-Nb steel samples with grain sizes in the range of 2.0 - 2.8 μm. However, in work by Pal'a et al. on low carbon steels this was not seen in samples with grain sizes of approx 50 μm until > 0.04 strain has been applied [122]. Although it is not uncommon to see HEDS such as

tangles and pile ups in as received and even annealed steels [121], this would suggest that dislocation structures in fine grained HSLA steels subject to TMCR schedules have a more evolved structure and therefore these steels would require less strain to develop dislocation structures otherwise seen with significant levels of deformation in large grain sized low carbon steels. This requires further investigation given the lack of literature reporting the effects of deformation during the initial stages of plastic deformation up to 0.04 strain on dislocation structures in HSLA steels.

For microstructures containing MA constituents, high dislocation densities are reported in the areas of ferrite grains adjacent to the second phase in comparison to the grain interior, which arises from the volume displacement during formation of martensite [126,127]. These dislocations are also observed to be of a glissile nature [129]. On deformation martensite constituents release dislocations into adjacent ferrite grains, therefore the dislocation density of the martensite reduces as they accumulate in the ferrite [129]. These dislocations transfer via stress concentrations at the interface between ferrite and MA constituents which are the source of dislocations during the early stages of plastic strain where the softer ferrite matrix undergoes hardening whilst MA phase softens [130, 131].

Bainite and acicular ferrite (AF) have similar mechanisms for formation and the shear strains involved give them an inherently high dislocation density, which is mostly described qualitatively within the literature in comparison to adjacent ferrite and polygonal ferrite (PF) grains [39,132,133,134]. Poruks et al. have given quantitative

values for the dislocation densities in as-supplied X80 grade 0.04C-1.77Mn-0.08Nb steels containing AF and bainite, of which bainite was found to contain the higher density (2.1 x10^{15} m^{-2} in AF and 6 x10^{15} m^{-2} in bainite) [133]. This agrees with other studies on X80 grade 0.05C-1.8Mn-0.1Nb steels which report the dislocation density of predominantly AF microstructures to be lower than that of predominantly granular bainite microstructures [51]. Quantitative measurements of dislocation densities in as-rolled ferrite-pearlite steels by Kostyzhenov [35] reported values between 1.2 and 4.0 x10^{14} m^{-2}. In these steels the distribution of dislocations was varied throughout the ferrite grains but was not reported to be higher in adjacent areas to the second phase pearlite (unlike that observed in ferrite-MA microstructures). Dislocations in bainitic phases are reported to be glissile, which can give rise to continuous yielding as also seen in dual phase steels [135]. For dual phase ferrite-pearlite steels, deformation will cause ferrite to deform plastically whilst the cementite will elastically deform before hardening but high internal stresses will occur at the cementite-ferrite interface which can act as the source of dislocations and as a sink [118].

The dislocation density increases with plastic deformation, for metals this can be written as

$$\rho = k.10^{15}.\varepsilon \tag{9}$$

Where ρ is the dislocation density and k is the dislocation generation rate. The rate at which dislocations are generated is much higher for fcc metals than for bcc metals due to the difference in slip systems. For body centred tetragonal structures such as martensite the dislocation generation rate has been observed to increase linearly up to 0.07 strain and then increase exponentially from 0.07 - 0.11 strain [136, 137].

The contribution to yield stress from dislocation density, ρ, is calculated from equation (10)

$$\sigma_d = \alpha Gb\rho^{0.5} \qquad\qquad (10)$$

Where α = a constant between 0.38 and 1.33, G = the shear modulus for iron (8.1 x 10^4 MPa) and b = the Burgers vector of ferrite (0.243 nm).

Studies have found that, in carbon steels there is a higher density of dislocations within ultrafine ferrite grains ($<$ 1 µm) compared to microstructures containing comparatively coarser grains, which had a more heterogeneous distribution of dislocations. Under deformation rapid dislocation interaction caused high rates of strain hardening and back stresses were exerted on coarser, neighbouring ferrite grains due their plastic incompatibility [120, 135,138]

2.2.2 Transformation dislocations

The dislocation density and arrangement / structure in steel plates and strip depends on the transformation product that forms and the cooling rate, as this will affect whether recovery mechanisms operate, volume expansion occurs or thermal stresses develop. For a steel that transforms to predominantly ferrite the dislocation structure consists of straight lines in stable arrangements, these are the result of a gradual transformation from austenite to ferrite and the difference in their respective volumes which cause thermal stresses in the ferrite phase upon cooling [121]. Where two phases occur transformation dislocations are usually seen at matrix / second phase interfaces such as between ferrite and cementite lamellae, MA islands and large precipitates (Figure 2.10).
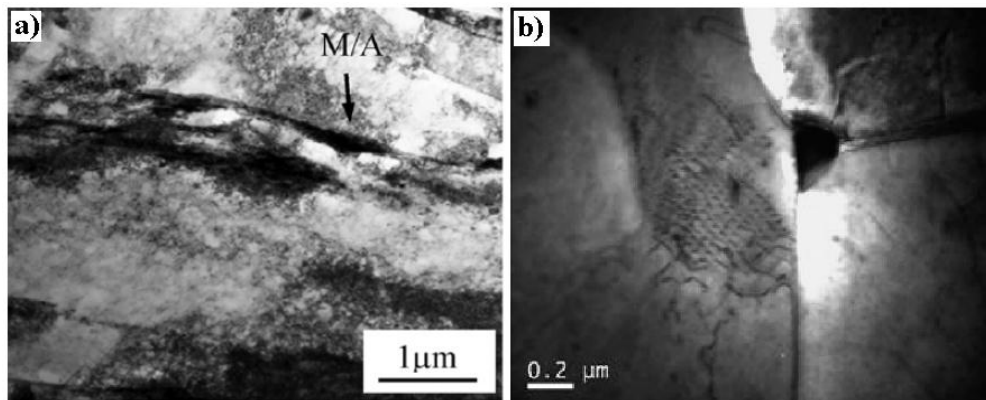
Figure 2.10 High dislocation density at MA - ferrite interface in (a) hot rolled 0.07C-1.43Mn-0.035Nb steel and (b) dislocation sub structure at the ferrite - grain boundary / second phase constituent interface in a 0.04C-0.50Mn-0.05Nb X52 grade steel [140]

Interfacial boundaries will either be of a coherent, semi-coherent or incoherent nature. In the case of incoherent interfaces a misfit strain is present at the interface boundary, which

requires atoms to rearrange themselves to lower the energy of the system (Figure 2.11),
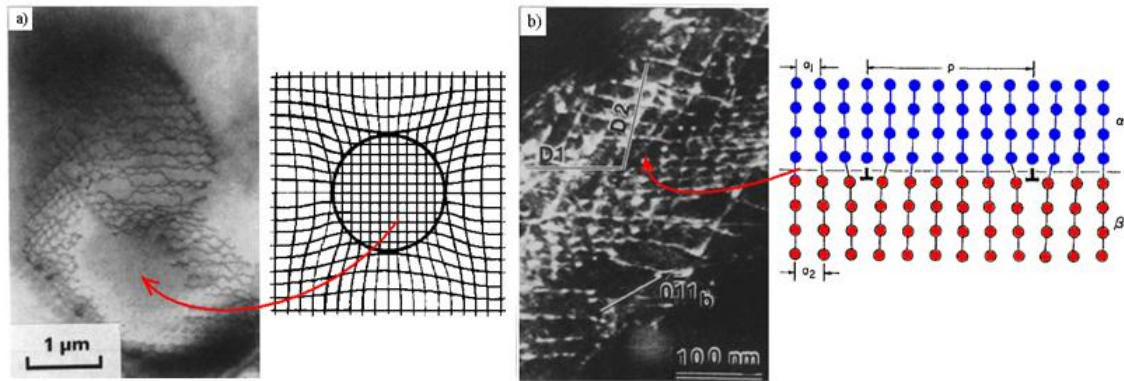
Figure 2.11 Interfacial dislocation structure surrounding precipitates in (a) Ni-Cr-Mo alloy with corresponding schematic of small negative misfit from a coherent particle and (b) misfit dislocation network between martensite laths in Fe-20Ni-5Mn Alloy and corresponding schematic of misfit dislocations between two semi coherent phases [141]

Extensive research by Shiflet into dislocation structures [141] found all phase boundaries across a range of alloys and steels including ferrite-austenite, bainite and particle interfaces to be of a semi-coherent or completely coherent nature. Constituents that cause this behaviour in metals can be precipitates or second phase constituents, such as MA phase or pearlitic regions. As with most low energy dislocation structures misfit dislocations have regular structures in a 'carpet' fashion across the interfacial boundary. The majority of studies detailing misfit dislocation structures centre around alloys where misfit dislocations are spaced between 8 and 200 nm thus easily imaged as opposed to misfit dislocations observed between lamellae interfaces in a pearlitic steel where the dislocation spacing is observed to be in the order of 1.2 nm (Figure 2.12).
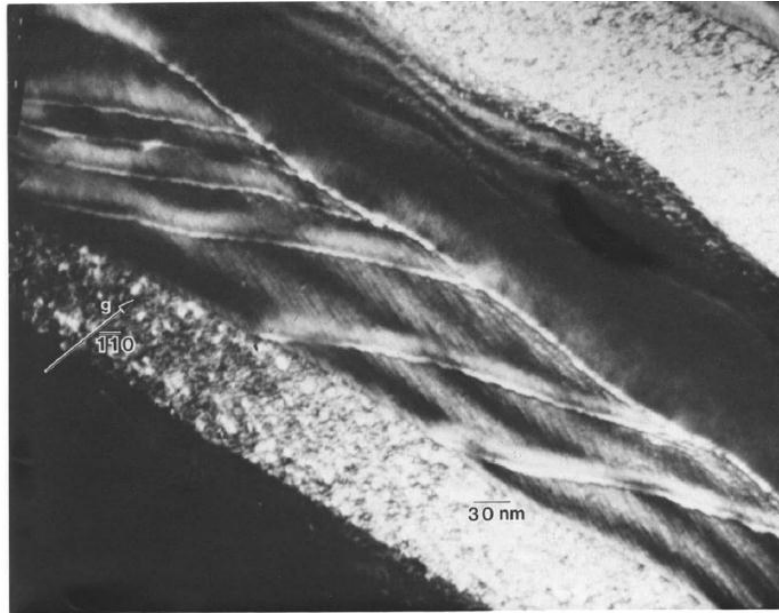
Figure 2.12 Misfit dislocations between steps within lamellae cementite - ferrite interface [141]

2.2.3 Dislocation evolution during reverse loading

Deformation of polycrystalline materials requires dislocations to rearrange themselves to stabilise the system and their structure is dependent on the loading path. The net effect is an immediate devolution of the dislocation structure during load reversal / change in strain direction due to annihilation before the re-establishment of a new dislocation structure as reverse deformation continues.

Dual phase ferritic steels with MA constituents subject to reverse shear loads exhibited a partial dissolution of dislocations observed within cell domains and break down in the cell structure after reverse loading suggesting a dislocation density decrease, as plotted in

Figure 2.13 [142]. This would be due to dislocation annihilation within the cell walls and has been a recorded phenomenon in other studies which observed dissolution of the cell structure during the early stages of reverse deformation in both fcc and bcc materials [142,143,144] (Figure 2.14).
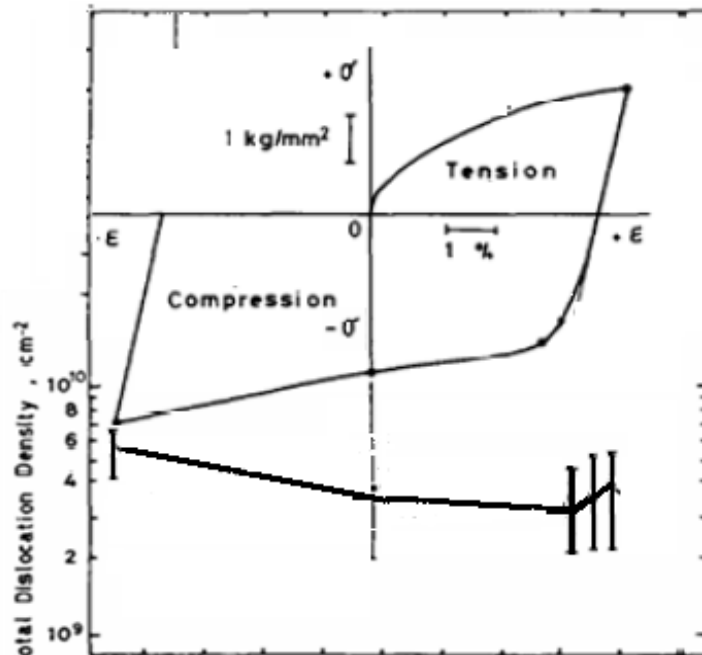
Figure 2.13 Stress strain curve and dislocation density (determined by TEM) taken at various points during the reverse deformation cycle in polycrystalline aluminium. The first three dislocation density readings (on the far right) were taken during unloading, shortly after reverse yield, dislocation density shows a slight decrease followed by an increase as reverse strain passes through the original point of 'zero strain' [142]
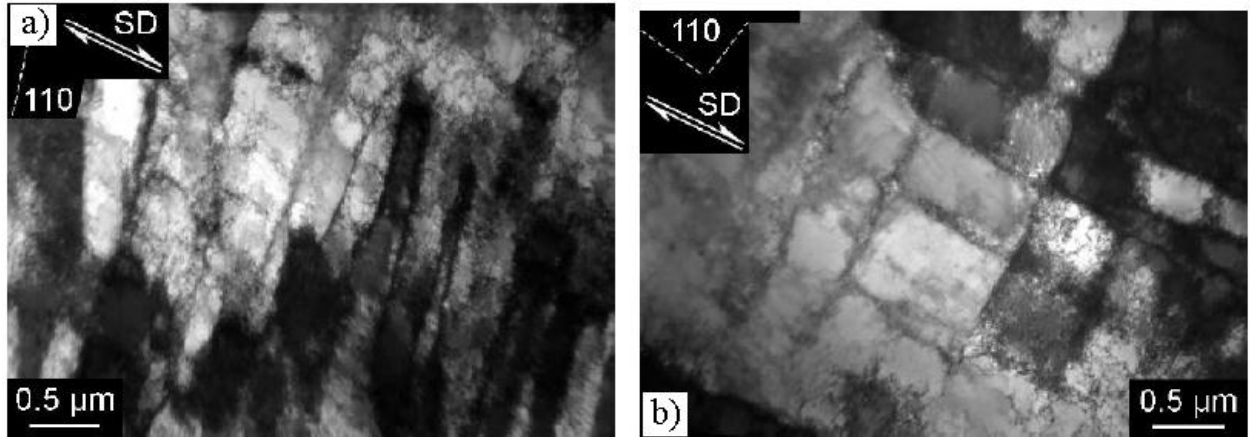
Figure 2.14 Dislocation cell structures in a 0.12C-1.39Mn DP ferritic steel with MA constituents subject to (a) 0.30 shear strain and (b) 0.30 reverse shear strain [145]

Recent studies applying computational modelling of dislocation behaviour have shown dislocation mechanisms during reverse deformation to follow the process of creation, annihilation, mobilisation, and remobilisation. More specific behaviour of dislocations within cell walls, thought to be immobilised by forward pre-strain, showed that they actually migrated from the cell walls to the interior cell boundaries as remobilisation was activated by strain reversal [145].

At the time of writing, studies into the dislocation structure during reverse yield are primarily concerned with the dissolution of cell structures where annihilation within cell walls will happen on a large scale and can be quantified by the difference in cell diameter. Work done by Queyreau and Devincre showed, through computational simulations (discussed later on), that, at small pre-strains, bowing of dislocations and masking of precipitates is the dominant factor [146], therefore annihilation would not be expected to occur after unloading and shortly after loading in the reverse direction

dislocations would therefore display their earlier characteristics. Where annihilation is the dominant mechanism, a transient hardening can be observed in the early part of the reverse stress strain curve as a result of fewer dislocations being present [145]. Therefore a comparable or higher rate of work hardening in reverse-strain curves (against forward stress-strain) could be evidence of dislocation density and structure remaining relatively unaffected during reverse yield following a small pre-strain.

2.3 Plate to pipe deformation cycles.

2.3.1 Plate to pipe forming

Linepipe with a diameter > 16'' (0.406 m) is classified as large diameter linepipe and is generally fabricated using a process known as 'UOE'. Each letter describes the three major deformation schedules known as U-ing, O-ing and expansion. Large diameter linepipe can also be fabricated from helical-welded (spiral-welded) pipe at a reduced cost and to a much greater range of dimensions and lengths. These types of linepipe are accepted for transportation of water, low-pressure hydro-carbons and dry gas service but fall foul of API-5l regulations for higher strength grades required for more demanding applications as fabrication limitations cannot yield the required thicknesses, circumferential roundness or mechanical properties governed by API-5L to withstand high-pressure, low temperature, corrosive environments. Electric resistance welded pipe (ERW) can be fabricated to a smaller range diameters than UOE but benefits from considerable cost savings from an interrupted fabrication schedule of uncoiling, forming, welding, heat treatment, sizing and cutting. These pipes are generally used in non-corrosive environments and are not subject to high stresses in service [147]. As shown in Figure 2.15, UOE is the only process available to satisfy size and mechanical property requirements for LNG (Liquefied Natural Gas) service. This chapter will give a brief overview of the fabrication of large diameter linepipe, why it is relevant to the Bauschinger effect and current issues surrounding the fabrication process.
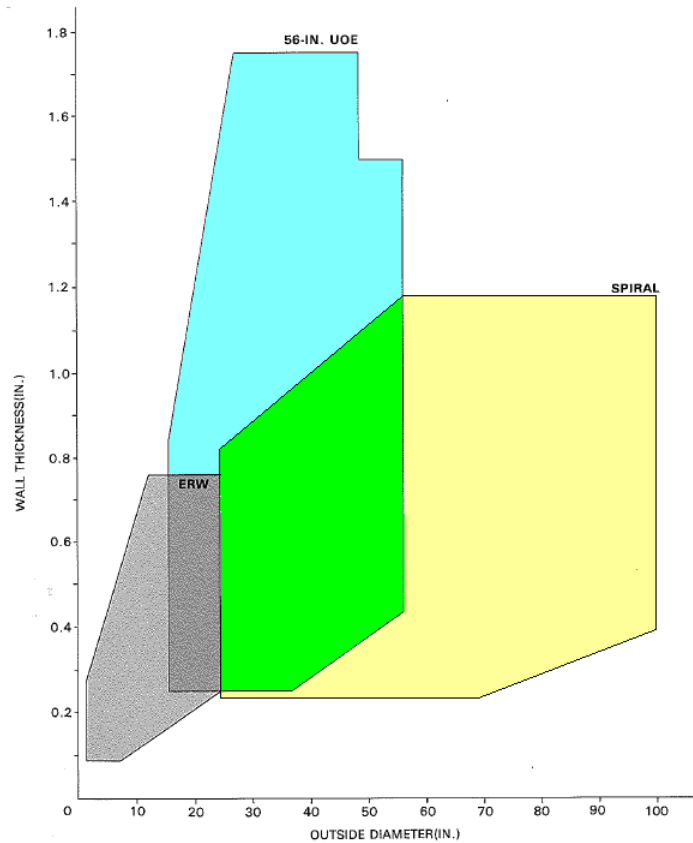
Figure 2.15 Basic size ranges for line pipe showing the limitations of UOE, spiral and electric resistance welded (ERW) pipes at the NKK Ohgishima Complex [148]

2.3.2 UOE process

The first stage of the UOE process is to cut the plate down to the required size and dress the edges by edge milling and beveling. Fabricators and API 5l use 12 m as a standard maximum length for linepipe. The first mechanical deformation is crimping of the plate edges (Figure 2.16) – this creates a curvature profile on the longitudinal seam of the pipe and ensures that a sound connection can be made between the two face edges which eases the welding process after the O-ing stage is complete [149].
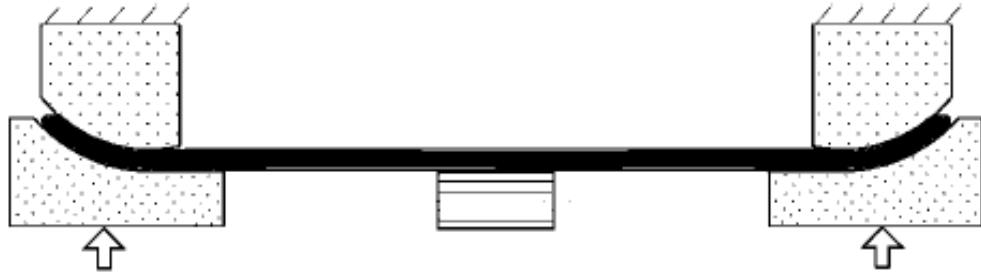
Figure 2.16 Schematic of edge crimping [144]

The next stage is for a U-bulb to press down on the central axis region of the plate and turn the plate into a U-shape otherwise know as a *skelp* (Figure 2.17, a)– the mid axis of the plate now has a radius similar to that of the finalised linepipe and the edges are pushed inwards by horizontal rollers which force the plate edges to face vertically upwards. During this stage of deformation the outside region of the plate undergoes tensile strain and the inside region experiences compressive strain (Figure 2.17 b).
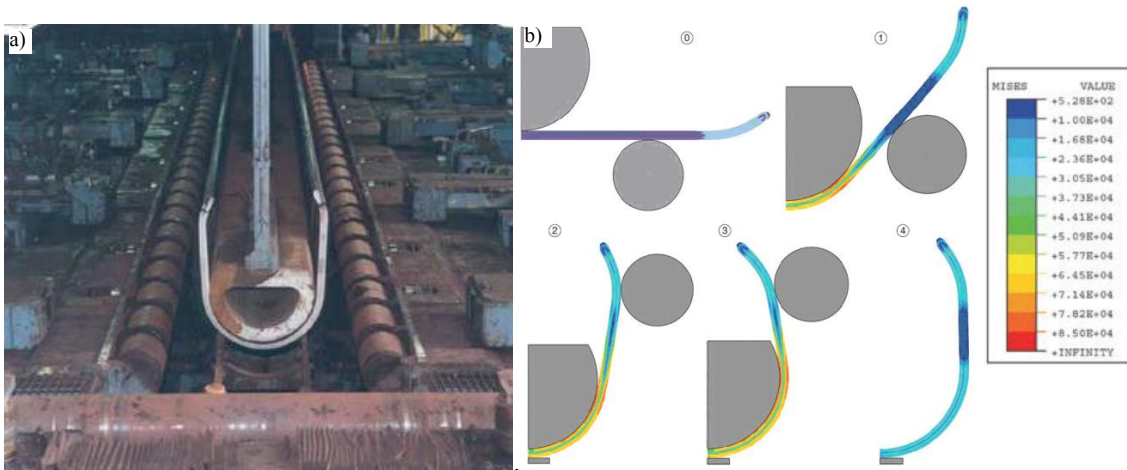
Figure 2.17 (a) U-press courtesy of Corus (now Tata) Tubes (b) FEA simulation of the U process showing regions of high stress [147]

The O-ing stage involves an O-press to manipulate the longitudinal faces of the skelp ends together and gives the linepipe its cylindrical form (Figure 2.18 a). The strain distribution across the outer and inner plate surfaces is reversed, compared to the U process, as the inside surface region of the plate now undergoes tension as the inside diameter is increased and the outside surface region is compressed (Figure 2.18 b). After completion, a residual stress of around 0.2 – 0.4 % of the yield stress can be expected to remain [150]. If the pipe is to be used for sour service then large strains during expansion are avoided due to the dependence of hydrogen diffusivity on strain and an increase in trapping sites due to a greater number of dislocations [150,151]. After O-ing is complete SAW (Submerged Arc Welding) is carried out along the longitudinal length of the pipe [147].
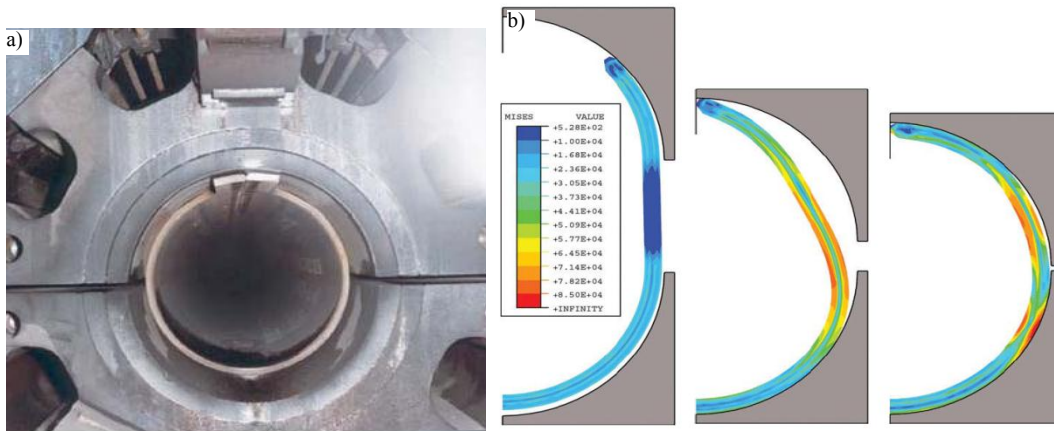
Figure 2.18 (a) Photograph of an O-press and (b) FEA simulation of O-pressing showing highly stressed regions [147]

The final stage prior to inspection and testing is mechanical expansion (Figure 2.19 a) – this ensures strain is distributed through all regions of the pipe (Figure 2.19 b) as not all areas will have undergone the same magnitudes of deformation. Expansion of the UO

pipe is achieved by running an internal mandrel with 8, 10 or 12 segments through the pipe to expand a length of one half to one diameter [147]. Ovality of the linepipe and thickness diameter ratio is reduced to satisfy API-5L standards. The expansion process is a very important part to ensure the structure does not buckle or collapse from external pressure, this is of particular concern if the linepipe is to be used in subsea conditions where the external pressures exerted are likely to be very large. Industry practice is to increase the pipe diameter after O-ing by 0.8 – 1.3 %. Studies have shown that < 0.3% is sufficient to decrease the ovality, and > 0.3 % has a positive impact on the pipe collapse pressure but to a much lesser extent than the initial 0.3 % [147].
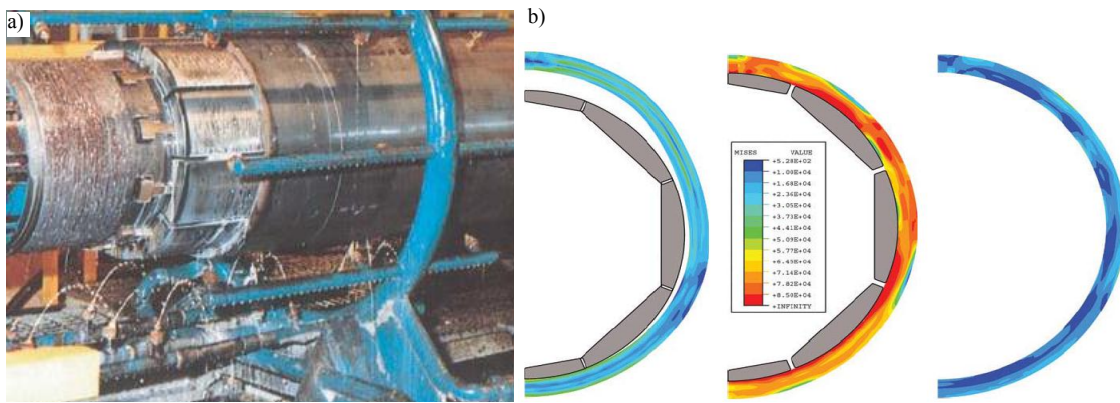
Figure 2.19 (a) Photograph of expander and (b) FEA simulation of the expansion process [147]

2.3.3   Diameter / thickness ratio

The diameter wall thickness ratios is an important aspect of pipeline manufacture both in terms of the mechanical properties of the pipe and the demands placed on the pipe mill (Figure 2.20).
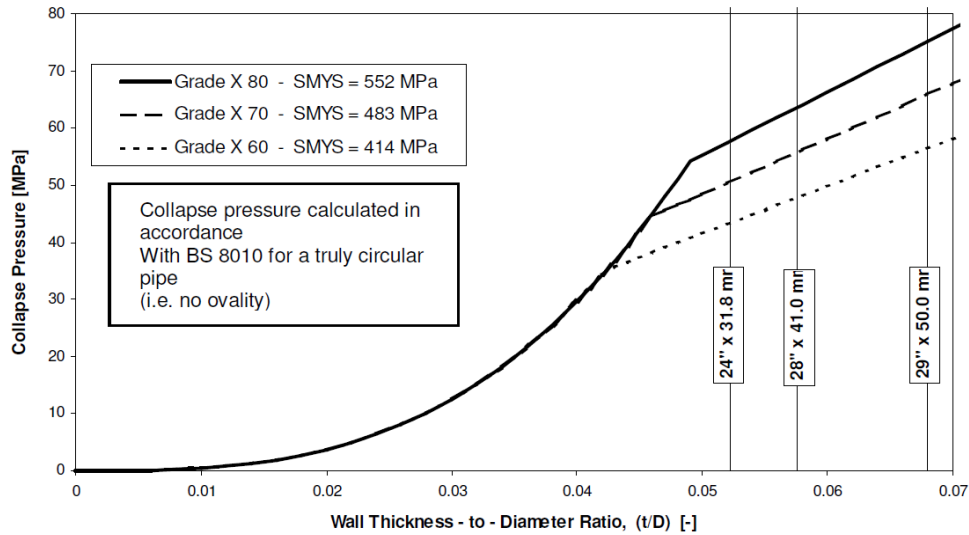
Figure 2.20 Graph showing the correlation between the wall-thickness diameter ratio and collapse pressure [152]

For deep-water applications wall thickness is of particular concern to provide suitable corrosion allowance over the service life or to cope with the rise in external pressure, which increases 1 bar for every 10 m of depth [152]. This in itself presents a problem to the pipe fabricators because, to increase the compressive strength a smaller diameter is favoured. It is not always practical to subject pipe mills to the large loads required for small t/D (thickness/diameter) ratios due to the risk of overloading the presses and a compromise must be reached to acquire the desired ovality % and ensure strength properties are evenly distributed throughout the linepipe [147,152] and, as Figure 2.15 shows, this limits the size range for pipe manufactured using the UOE process. Table 2.1 presents five deep-water projects at various water depths and the chosen thickness diameter ratios and API grades.

Table 2.1 Thickness (wall thickness, WT) – diameter (outside diameter, OD) ratio of major sub-sea pipeline projects in the past decade [152]

.Project	Pipe Size (OD x WT)		API grade	Pipeline length, km	Maximum water depth, m
	OD	WT			
Oman-India	7112 mm (28'')	41 mm	X70	1200	3500
Russia - Turkey	6096 mm (24'')	32 mm	X65 (sour)	374	2200
Libya-Sicily	8128 mm (32'')	30 mm	X65	560	800
Gulf of Mexico	7112 mm (28'')	38 mm	X65	712	2000
Iran-India	7366 mm (29'')	50 mm	X70 / 80	1500	3500

A second problem with the wall thickness-diameter ratio relates to susceptibility to hydrogen induced cracking (HIC). It was found that the susceptibility for HIC increased with an increase in pipe wall thickness due to the increased strain required for the expansion process when the thickness is increased [151]. Microstructural features also increase the HIC susceptibility such as large non-metallic inclusions, which are found in thicker plates. It is reported that a coarser grain structure reduces the diffusion path for hydrogen atoms and therefore increases HIC resistance [153]. This is pushing against the trend for thinner plates with more refined microstructures which will inherently be higher in strength.

2.3.4 Calculation of strain distributions in UOE pipe

To calculate the stains imposed on the inner and outer regions of the linepipe walls during the UOE fabrication process then equations can be utilised to represent simple bending (U-ing) and expansion of a diameter (O-ing and the expansion process).

Taking the simple bending of a beam, with no shift in the neutral layer (taken as mid thickness) then the strain of the outer region subject to tension can be calculated using equation (11).

$$\varepsilon_{out} = \frac{l_0 - l_n}{l_n} = \frac{aR_0 - a\left[R_0 - \frac{t}{2}\right]}{a\left[R_0 - \frac{t}{2}\right]} = \frac{t}{2\left[R_0 - \frac{t}{2}\right]} \tag{11}$$

Where l_o and l_n represents the outer layer and the neutral layer (taken as mid-thickness for low strains) respectively, α = the curvature angle of the beam, R_0 = is the outer radius and t = the thickness of the plate.

The compressive strain in the inner region is calculated using equation (12).

$$\varepsilon_{in} = \frac{t}{2\left[R_0 - \frac{t}{2}\right]} \tag{12}$$

Expansion (or reduction due to change in diameter reduction during the O-stage) of the pipe is not a simple bending action and the equations used to calculate the strains are:

$$\varepsilon_r = \frac{2\pi r - 2\pi R}{2\pi R} = \frac{r-R}{R} \tag{13}$$

Where $\varepsilon_r =$ strain from reduction and $r =$ the inner radius of the plate, $R=$ outer radius of the plate.

$$\varepsilon_e = \frac{2\pi R - 2\pi r}{2\pi r} = \frac{R-r}{r} \tag{14}$$

Where $\varepsilon_e =$ strain from expansion.

Comparison between the calculated strains using these equations [35] and measured strains derived from [154-157] found that the calculations output representative levels of strain in comparison with FEA models and physical measurements during the UO process as shown in Table 2.2.

Table 2.2 Comparison of measured and calculated strain after the UO process and after expansion for a 914 mm diameter pipe with wall thickness of 25 mm

Thickness / diameter(mm)	Cumulative strain during UO		Expansion Strain	
	Measured [158,159]	Calculated [35]	Measured [158,159]	Calculated [35]
25 / 914 mm	0.032	0.028	0.011	0.011

Calculations of the deformation stages does not vary for inner and outer surfaces, the U-ing process is found to exert the most strain on the plate at the 180° position (0.046 strain) whilst the O-ing is calculated to exert lesser strains in the region of (0.018 strain) for a 25 x 914 mm pipe [35]. Measured strain however, shows greater variation for inner and outer surfaces of the pipe and cumulative strain after the UO stage was found to be 0.032 strain for the outer surface and 0.0464 strain for the inner surface, this is attributed to compression during closure of plate edges during the fabrication process [155]. For the expansion stage the measured data were found to be significantly higher than calculations for the outer surface where metal flow is unconstrained, for the inner surface where expansion shoes are in contact with the pipe the measured strain was reported to be much less, possibly due to the retarded metal flow and shift in the neutral layer. For a range of plate thicknesses (9.5 mm - 50.8 mm) and pipe dimensions largest strain recorded was 0.082 strain recorded in the pipe with largest wall thickness. [158,159].

Therefore during the UOE process different regions of the pipe circumference experience reverse straining with initial strain values in the order of around 0.045 where wall thickness is < 25 mm. The effects of these reverse loading schedules are discussed in the next section.

2.4   The Bauschinger effect in metals

2.4.1   Quantification of the Bauschinger effect:

The phenomenon of the reduction in yield strength in the opposing direction of the initial pre-strain was first recorded by John Bauschinger in 1881 and is still a widely researched subject across a range of materials and applications.

A typical stress strain diagram helps visualise how a material can display a lower yield stress upon reverse loading as seen in Figure 2.21.
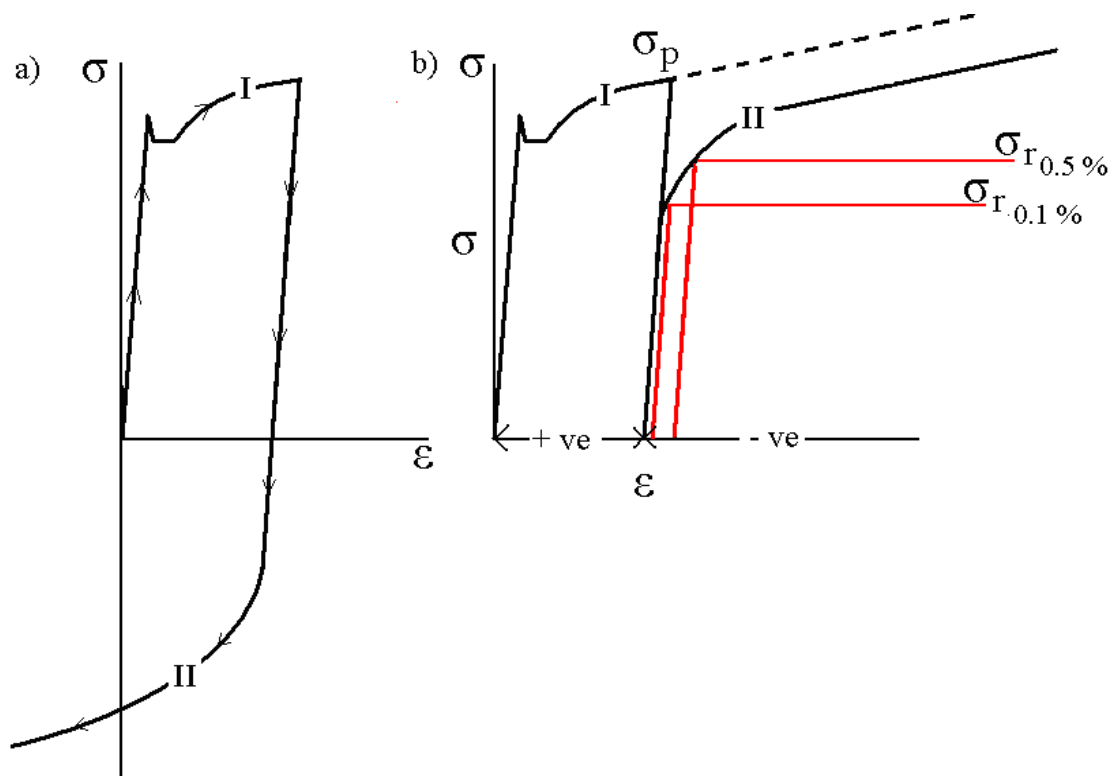
Figure 2.21 Forward-reverse stress strain plot showing the decrease in reverse yield stress σ_r compared to the maximum pre-stress, σ_p (a) shows the path of the stress strain curve as seen during testing, (b) shows the same curve with the reverse loading (stage II) plotted in the same direction as the forward loading curves. The effect of permanent softening

can be observed between the extrapolated forward stress strain curve. $\sigma r 0.1$ % and $\sigma r 0.5$ % represent the offset strain taken to define the Bauschinger stress parameters

The Bauschinger stress parameter ($\beta_{\sigma 1}$) can be quantified by dividing the difference between the stress at maximum pre-strain (σ_p) and reverse yield (σ_r) by the stress at maximum pre-strain:

$$\beta_{\sigma 1} = \frac{\sigma_p - \sigma_r}{\sigma_p} \tag{15}$$

The offset yield point taken for the reverse strain can give an indication of the rate at which material will recover its previous properties as it strain hardens after yielding. The most common values reported in the literature are 0.001, 0.002 and 0.005 (0.1, 0.2 and 0.5% respectively) offset strain. 0.001 offset strain reveals the short range (temporary) work softening and 0.005 the long range (permanent) work softening the material undergoes upon reverse yielding. These Bauschinger stress parameters are represented in the equations below:

$$\beta_{\sigma 3} = \frac{\sigma_p - \sigma_{r0.5}}{\sigma_p} \tag{16}$$

$$\beta_{\sigma 2} = \frac{\sigma_p - \sigma_{r0.2}}{\sigma_p} \tag{17}$$

$$ß_{\sigma5} = \frac{\sigma_{r0.5}}{\sigma_p} \qquad (18)$$

Permanent softening ($\Delta\sigma_s$) can be quantified by taking the difference in stress between the reverse and forward stress strain curves once the reverse stress has reached the level of pre-stress (Figure 2.22).

In the case of materials which reach reverse stress at the equivalent level of maximum pre-strain (i.e. reverse stress reaches maximum forward pre-stress) in the reverse direction the Bauschinger strain parameter is used to determine the magnitude of plastic deformation in the reverse direction to achieve this:

$$ß_{\varepsilon} = \frac{\varepsilon_r}{\varepsilon_p} \qquad (19)$$

Where ε_p is the plastic pre-strain and ε_r is strain in the reverse direction where the stress is equal to the stress at maximum pre-strain (Figure 2.22).

The amount of energy required to achieve the pre-strain stress level during reverse deformation is determined using:

$$\beta_E = \frac{E_S}{E_p} \qquad (20)$$

Where E_P is the energy required to pre-strain the material and E_S is the energy saved in the reverse direction due to work softening behaviour (Bauschinger effect) (Figure 2.22).
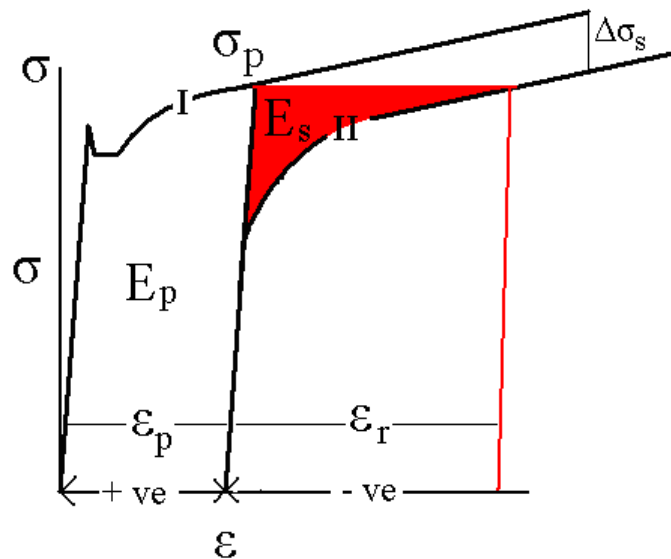
Figure 2.22 Bauschinger stress strain curves showing permanent softening ($\Delta\sigma_s$), points ε_p and ε_r required for the Bauschinger strain parameter and E_p and E_s required to calculate the Bauschinger energy parameter

2.4.2 Theory behind work softening

Orowan offered the first explanation for the Bauschinger effect in 1966, which was further expanded on by Brown and Stobbs in 1976 [160] and relates the back stress to Orowan looping and bowing of impenetrable obstacles. Another well-established theory

74

by Abel and Muir in 1972 [161] suggests that dislocation pile ups also contribute significant back stress after forward pre-loading. It is now widely accepted that the cause of work softening behaviour in materials, which exhibit a Bauschinger effect, is the impedance of dislocation movement caused by randomly dispersed obstacles present in a material which help aid deformation in the opposing direction (reverse) to the forward pre-strain. These obstacles can occur from any of the strengthening mechanisms which give the metal its strength; solute atoms which create stress fields by distorting the iron matrix, high angle grain boundaries, precipitates, second phase constituents and other dislocations. These will be discussed in this section.

Dislocations of similar signs which encounter large obstacles such as high angle grain boundaries, second phase constituents and other (sessile and glissile) dislocations during plastic deformation will pile up when their motion is blocked creating a stress field around the source of the pile up, which in turn creates a back stress in the opposing direction. This back stress will lower the reverse flow stress and consequently the reverse yield point. Dislocations generated from the same source of slip can also be of the opposing sign in the same plane and annihilate in the reverse direction, which also results in a drop in the reverse flow stress. As the back stress is a function of the accumulation of dislocation pile ups the dislocation density naturally has an influence on the amount of back stress generated i.e. the more dislocations present in a material, the higher the potential back stress generated. This is provided that dislocations do not become immobilised by other dislocations in the form of jogs and tangles and the effect of this has not been approached in studies due to the complexity of the dislocation dynamics and

the second mechanism which contributes to back stress generation during forward deformation, Orowan theory.

Arguably the more dominant mechanism in the Bauschinger effect is the Orowan theory as illustrated in Figure 2.23, which shows a material after forward loading (a) and (b) shortly after unloading and subsequent reverse loading.
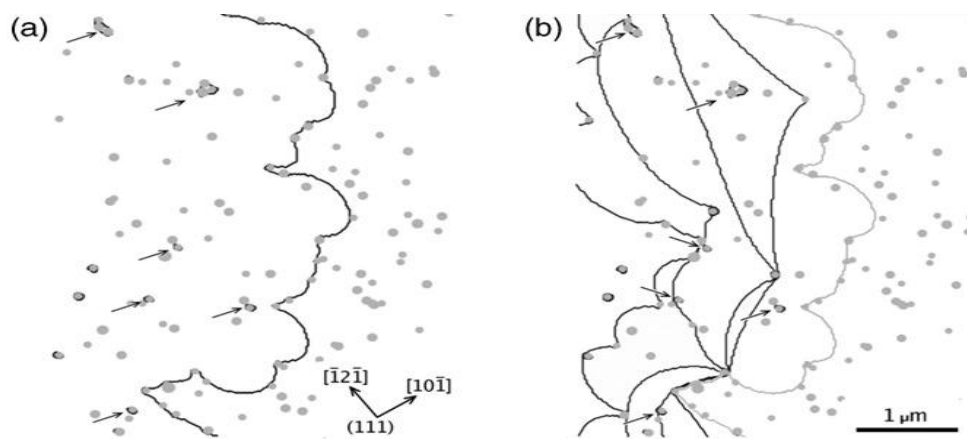
Figure 2.23 Schematic representation of dislocation-particle interaction (a) during forward loading (dislocation line moves from left to right), arrows highlight Orowan loops / islands formed during forward deformation, and (b) the resulting masking effect from precipitates during reverse deformation (dislocation line moves from right to left and only interacts with precipitates which do not have Orowan loops left behind after forward deformation [146]

In Figure 2.23 a mobile dislocation has travelled through the matrix and past obstacles leaving Orowan loops in its path. Once reverse loading has occurred the dislocation line is elastically attracted to the Orowan loops and absorbs the dislocations in the reverse direction. Where Orowan looping does not occur but bowing exists between particles, the dislocation will try to arrange itself into a lower energy state thus aiding reverse straining.

76

A small amount of back stress is produced in the form of elastic attraction and line tension as the dislocation is drawn towards the loop but the majority of flow stress reduction comes from the masking effect of features that acted as obstacles in the forward direction. Studies investigating the effect this has on the work softening behaviour have shown the masking effect to be the primary mechanism for short range work softening [146]. When computer simulations have been run to a 'perfect Orowan' scenario, i.e. all obstacles interact with dislocations, the reverse flow stress reaches zero and long range internal stresses such as pile ups do not have any influence until long after dislocations travel beyond their original point before forward loading [146]. In physical metallurgy this scenario will never exist but it highlights the basis for softening behaviour and theoretically establishes a hierarchy of mechanisms responsible for back stress and the stages at which they operate.

2.4.3   Observed trends in the Bauschinger effect in different microstructures

The Bauschinger effect has been widely researched across a variety of metals as it is of great concern to industries subjected to strict standards for mechanical behaviour of components after fabrication or whose fabrication processes can be affected by manifestations of the Bauschinger effect, such as spring back and change in mechanical properties post deformation. The exact mechanisms behind the Bauschinger effect in specific materials is still the subject of much academic research but rarely are the studied materials subject to quantitative analysis of the five strengthening mechanisms that

contribute to the initial yield strength. Nevertheless if one is to take a look at the existing data for a range of computer models, microstructures and strength grades then qualitative trends can be observed.

The first trend generally accepted is that the Bauschinger stress parameter increases with an increase in pre-strain as back stresses become larger from increased dislocation density and obstacle interaction. It has been reported that the Bauschinger parameter increases linearly with increasing pre-strain and that the work hardening co-efficient of the material is proportional to the rate of increase in the Bauschinger parameter [162]. In addition the literature gives examples of increased initial yield stress giving larger Bauschinger parameters [35,162,163]. These observations have typically been explained through the presence of residual stresses arising from work hardening during processing or from the presence of dual phase constituents, which will add to the initial dislocation density or that generated during forward pre-strain. Contributions to yield stress arising from the five strengthening mechanisms, which if increased will lead to greater contributions to back stresses, are overlooked in most of the literature and so data differentiating the mechanisms are not readily available either due to the complexity of quantifying the separate mechanisms or because the research has gravitated towards specific mechanisms such as second phase content and strain rate, ignoring or making general assumptions as to the behaviour stemming from other factors.

Solid solution strengthening contributions are a problematic variable to assess as different steels grades will typically vary the wt % of alloying additions of microalloying elements

and so a higher strength grade will be more dependent on the processing parameters (and hence phase balance or precipitates) rather than the wt % of e.g. Mn or Si. It was concluded that the Bauschinger parameter is dependent on impurity elements when two 0.57 C and 0.9C steels containing different levels of Mn and Si were compared since the higher alloyed material demonstrating a higher Bauschinger parameter [162]. In this study the microstructures were not quantitatively measured in terms of grain size, volume fraction of pearlite or dislocation density. Subsequent heat treatments to spheroidise the lamellae pearlite reduced the Bauschinger parameter in both the steels, with the Bauschinger parameters following the same trend, i.e., higher values for the samples with greater wt % of C, Mn and Si. Therefore conclusions as to the effects of impurity elements, or any single factor for that matter, should be balanced against other microstructural features contributing to the yield strength and acting as sources of back stress / work softening.

The Hall-Petch relationship has shown that yield stress is proportional to a decrease in grain size due to the increased area of grain boundaries for dislocations to cross. Theoretically it follows that an increase of dislocation pile-ups caused by a greater number of grain boundaries would result in higher back stress thus a greater Bauschinger parameter. Studies on C-Mn steels however show that this is not true for grain sizes ranging from 72 – 15 microns [154], although further details regarding the specific microstructures for each respective grain size were not given in the paper to determine if other factors were also varied. Not all studies gravitate towards the widely held belief that the Bauschinger effect has no dependence on grain size, for example Danilov et al.

studied the Bauschinger effect in heat treated copper, magnesium, steel and zinc samples and found a clear link between the proportional drop in yield strength and decreased grain size leading the author to conclude that a decrease in surface area of grains leads to a decrease in area where micro stresses occur [163]. More recently, researchers are suggesting that grain size does in fact play a crucial role in the Bauschinger effect. Balint et al. [164] used two dimensional computational models of copper crystals with varied grain sizes and using loading simulations found the Bauschinger parameter to be independent of grain size down to 2 µm. Below this the work softening behaviour showed a direct correlation to the decrease in grain size due to the build up of stresses at the grain boundaries which at small strains resulted in a back stress to occur. Ultrafine grains < 1 µm in a 1.49C-0.22Mn dual phase steel were reported to be responsible for an increase in the rate of work hardening arising from back stresses exerted from early dislocation interactions [120].

The predominant phase in HSLA linepipe steel is ferrite and to enhance yield stress microstructures often have second phase present e.g. pearlite, bainite or martensite / retained austenite. Studies on dual phase ferritic microstructures have reported larger Bauschinger parameters in steels with second phase associated with higher strength materials e.g. martensite, and an increase in volume fraction of second phase to increase the magnitude of work softening [165, 166].

There have been different mechanisms reported for this observation - Han et al. [165] attributed the large Bauschinger parameters to residual stresses occurring around the

harder second phase MA in the softer ferrite matrix during plastic deformation increasing dislocation density thus increasing back stress. Studies by Zhonghua and Haicheng [131] into the mechanical behaviour of martensite and ferrite during reverse loading suggested that the residual stresses contribute to short range softening where pile ups occurring at the hard phases resulting from increased dislocation density lead to early yielding during reverse loading. Once back stress from these pile ups reaches zero then the material residual stress is returned to pre-forward strain levels and rapid work hardening in the reverse direction (the characteristic roundhouse curve) returns the material to its original properties. In the case of pearlite, similarities arise in that levels under 30 % have no significant contribution to the yield stress but Kumakura [162] found that an increased volume fraction of pearlite led to a greater Bauschinger parameter in low carbon steel. Studies on the Bauschinger effect during the UOE process in pearlite reduced (low carbon steels with predominantly fine ferrite grain structure and small amounts of pearlite) and acicular ferrite bearing microstructures observed a trend in the yielding behaviour and amount of permanent softening after forming. The pearlite reduced steels, which showed discontinuous yielding behaviour, exhibited lower final yield strengths in comparison to the steel which contained acicular ferrite [89]. Studies by Kostreyzhev [35] showed the higher Bauschinger parameters to be independent of pearlite volume fractions (in the range 5 – 15 %) but this was due to differences in the dislocation density and particle volume fraction between the microstructures. The same study extensively studied the role of precipitation on the Bauschinger parameter and by comparing the level of precipitation and dislocation density in as-rolled (TMCR) and annealed specimens (heat treated so as to not effect the grain size and levels of second phase, but change the

dislocation density and precipitates) found that CuS particles < 12 nm were ineffective obstacles to dislocation motion. Particles > 50 nm were found not to contribute any significant work softening as the interparticle spacing exceeded that of the average dislocation length. Increasing the particle number density (particles in the size range 12 - 50 nm) increased the Bauschinger parameter but the main contribution to the Bauschinger parameter was found to be the initial dislocation density (effect reported to be 2.7 times greater than that of particle number density). It is accepted that an increase in dislocation density increases the Bauschinger stress parameter but little focus is made on the dislocation structure and how this may influence back stress. Computer simulations showed that the masking of obstacles to dislocations acts as the main driver for reduced flow stresses [146], whilst other authors [131,155,166] suggest that immobilised dislocations in the form of tangles did not contribute to back stresses. Studies into the effects of slip in Hadfield steel single crystals (fcc structure) [166] managed to correlate greater decreases in yield strength during reverse loading to specific [111] and [001] orientations where dislocation pile ups were observed adjacent to twins acting as impenetrable obstacles. Where twinning was the main deformation mechanism, a greater numbers of twins acting as barriers to dislocations resulted in lower reverse yield stresses from greater back stresses acting at the twin boundaries. This was particularly effective at lowering the reverse yield stress at small pre-strains and demonstrated higher Bauschinger parameters when compared to precipitation hardened Cu crystals where Orowan mechanisms were the main source of back stress.

Previous research, which related the Bauschinger stress parameter to dislocation density, made little comment on the dislocation structure present, which contributes to back stress [35], instead concentrating on the dislocation density. Both are important factors to consider as the dislocation structures in the as received condition (prior to Bauschinger testing) may vary and should be taken into account to explain the work hardening and work softening behaviour.

2.5   Objectives of the present study

There is an increased worldwide demand for higher strength grades of steel plate and sheet obtained through complex dual phase microstructures with refined grain size and containing carbo-nitride precipitates. For fabrication of large diameter linepipe the UOE process is the only method which can be used to give pipe with the range of properties needed to meet both on-shore and sub-sea applications. This introduces strain path changes throughout different regions of the plate / sheet and subsequent work hardening and work softening behaviour can be observed after mechanical deformation. The different strengthening mechanisms employed to achieve the desired strength levels have a direct influence on the forward and reverse deformation behaviour of a material.

The aim of the present study is to investigate the microstructural properties of five different grades of X80 and X65 steel sheets / plates and determine the influence their microstructures have on the mechanical behaviour, in particular the Bauschinger parameters. The following objectives have been set out to achieve this.

1. Characterisation and quantification of the features of the five steel microstructures (grain size, second phase %, thermodynamic prediction, and direct observation, using SEM for >50nm, carbo-nitride precipitates, TEM analysis of dislocation density and <50nm carbo-nitride precipitates).

2. Determination of the mechanical properties of the five steels, in particular measurement of the yield stress, tensile strength, work hardening and work softening behaviour.

3. Quantification of nano-structures i.e. fine precipitates and dislocations at various levels of pre-strain using TEM.

4. Consideration of the role of the coarse and fine scale microstructural features on the mechanical behaviour of the studied steels and comparison to previously studied steels.

5. Quantitative and qualitative determination of the influence of the different strengthening mechanisms on the mechanical behaviour and how this relates to industrial development and materials selection based on likely dimensions of linepipe.

3 Materials and experimental techniques

3.1 Materials

Three commercial X65 grade steel plates were provided by Tata Steel plc of around 19.0 mm thickness. Two 'trial' X80 grade steel sheets, of 11.0 mm thickness, were provided by Arcelor Mittal. All materials meet the relevant API 5l mechanical requirements for linepipe steel, Table 3.1, and the compositions are given in Table 3.2.

All microstructural characterisation (with the exception of dislocation characterisation) and mechanical testing were conducted on samples in the as-received state.

Table 3.1 Mechanical properties in the longitudinal orientation from data supplied by Arcelor Mittal for the X80 steels and Tata Steel plc for the X65 steels

Steel	Grade	Process	Yield Stress, MPa
			Tata / Arcelor Mittal data
X65 (I)	X65	TMCR + Acc cooled	489
X65 (II)	X65	TMCR + Acc cooled	492
X65 (III)	X65	TMCR	498
X80 (I)	X80	not reported	612
X80 (II)	X80	not reported	645

Table 3.2: Plate compositions by wt %

	C	Si	Mn	P	N	Al	Cu	Mo	Ni	Cr	V	Nb	Ti
X65 (I)	0.032	0.329	1.537	0.007	0.005	0.037	0.015	0.002	0.016	0.167	0.001	0.043	0.013
X65 (II)	0.037	0.288	1.399	0.011	0.003	0.032	0.129	0.018	0.191	0.037	0.001	0.044	0.014
X65 (III)	0.075	0.38	1.47	0.01	0.006	0.047	0.01	0.005	0.01	0.01	0.074	0.036	0.002
X80 (I)	0.054	0.2	1.77	0.013	0.005	0.04	<.01				0.001	0.08	0.001
X80 (II)	0.049	0.2	1.85	0.011	0.005	0.05	0.28				0.001	0.08	0.002

3.2 Experimental techniques

a. Thermodynamic modelling

Thermodynamic modeling was conducted on versions L and Q of Thermo-Calc to predict the levels of expected second phase and the type, amount and formation temperature of micro-alloy precipitates expected. The average wt % compositions of the studied steels were entered into the software and the equilibrium phase balances and compositions between 600 and 1600 K were calculated. With a decrease in temperature the amount of nitrogen in the carbo-nitride phase is reduced and the carbon content increases due to their respective thermodynamic stabilities at elevated temperatures. Likewise, plotting the Ti, Nb and V content in the carbo-nitride phases of the studied steels shows the chemical composition of the carbo-nitride phase to change with decreasing temperature, allowing the precipitation sequence to be divided into sections where Ti, Nb or V were dominant in the carbo-nitride phase.

b. Optical microscopy analysis

Specimens for optical analysis were extracted > 20 mm from the plate edge and machined to maximum dimensions of (15mm x 15mm x 10mm) or (15mm x 15mm x 15mm) depending on the thickness of the plate / sheet. These were then mounted in conductive Bakelite with the inspection surface parallel to the rolling plane, ground, polished down

to a 1 μm finish and etched with 2 % nital. The best results were obtained from etching by swabbing for 5 - 8 seconds using cotton wool soaked in the etch.

Optical microscopy was conducted on the Leica DMRX and Zeiss Axioskop-2 microscopes utilising Axiovision 4.6.3 software. Grains for the X65 grade specimens were successfully measured as an equivalent circle diameter (ECD) for an average of 1000 - 1500 grains. The grain size in the X80 steels was too fine for optical measurement, therefore SEM techniques were used (described below). Second phase pearlite volume fraction was measured using 5 images of each point using a 50 X objective lens in 0.5 mm steps covering a total area of approximately 30,000 μm^2 through sub-surface (< 1000 μm from plate edge), quarter-thickness and mid thickness regions of the steel plate.

c. Scanning Electron Microscopy (SEM)

SEM imaging of second phase MA constituents in the X80 grade steel plates was conducted using a Jeol 6060 SEM operating at 10 - 20 kV across the plate thickness taking 20 representative random areas in the mid-thickness, quarter-surface and sub-surface region covering approximately 54,000 μm^2.

Grain size for X80 specimens was measured using the linear intercept method parallel and perpendicular to the rolling direction to determine the distance between grain boundaries (i.e. diameter). This was done for 600 grains for each specimen and results presented as per ASTM E3182.

For precipitates > 50 nm in diameter (TiN, and (Nb,V)(C,N)) the Jeol JSM 7000F field emission gun SEM was used operating at 20 kV with an Oxford INCA energy dispersive X-ray (EDS) probe for characterisation of particle composition at a working distance of 10 mm. EDS spectra of precipitates were compared against those acquired from the surrounding steel matrix where no apparent precipitates were present. To determine number density and volume fraction 200 - 400 particles were analysed over 100-150 fields of view (each field of view covers approximately 50 μm^2) from a total area of 5000 – 9000 μm^2 for each steel. Volume fraction has been considered equal to area fraction and calculated by dividing the total area of particles (determined from measured particle diameters) by total area analysed.

EBSD (electron backscattered diffraction) analysis was carried out in the Jeol 7000 SEM using the Oxford Crystal software to calculate the average ECD grain size and 'effective' grain size by neglecting boundaries with misorientation values below 1.9^o and 15° respectively. 15° was selected as reports suggest that grain boundaries with misorientations below this value do not provide effective barriers to crack propagation [168-170]. Specimens for EBSD were prepared by polishing down to a 1µm diamond finish as per all other optical microscopy samples and etched with 2 % nital. Re-polishing at 1 µm and subsequent etching was repeated 3 - 4 times to remove any work hardened surface layers which enhanced the results from EBSD.

d. Transmission Electron Microscopy (TEM) investigation

i. Specimen preparation

Thin foils were prepared from the quarter-thickness region of as-rolled steel samples or from deformed cylindrical samples parallel to the compression face (also taken from the quarter thickness region). Samples were cut to approximately 0.5 mm thickness using an Accutom 5 then ground down to < 150 μm using grade 400 SiC grinding papers, mechanically punched into 3 mm diameter discs then further ground down to < 100 μm by hand on SiC grinding papers (grades 800, 1200, 2500). Samples at this stage were super-glued to flat metal polishing blocks and detached frequently by electro cleaning in neat acetone to alternate the face being polished and to check thickness. For electro-polishing a Struers Tenupol 3 twin jet electro polisher was used with a mixture of 1 part of perchloric acid to 9 parts of acetic acid. Polishing conditions were optimal at slightly below room temperature (5 – 10 ^{o}C) with a flow rate between 8 - 9 and a closed circuit potential of 45 V (with current set to 150 – 200 mA).

i. TEM examination

Thin foils were investigated on the Jeol 2100 and EDS spectra obtained with an Oxford INCA EDS probe. Specimen foil thickness was measured between 70-110 nm which was carried out using the convergent-beam electron diffraction (CBED) method [171] in the

two-beam condition with excited hkl reflections to obtain Kossel-Mollenstedt (K-M) fringes (as shown in Figure 3.1).
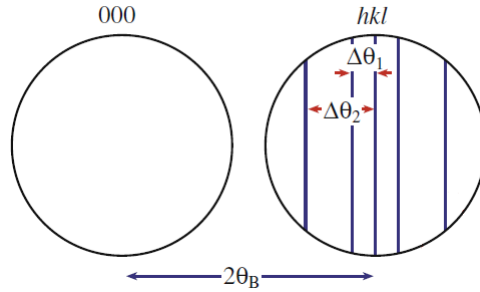
Figure 3.1 Schematic showing separation of 000 and hkl discs ($2\theta_B$) and K-M fringes $\Delta\theta_1$ - $\Delta\theta_2$ [171]

The Spacing deviation parameter (S_i) is calculated using Equation (21):

$$S_i = \lambda \frac{\Delta\theta_i}{2\theta_B d^2} \tag{21}$$

Where λ = wavelength of incident electrons, θ_B = Bragg angle for diffracted (hkl) plane, d = (hkl) interplanar spacing and $\Delta\theta_1$ = measured spacing of central bright fringe (exact Bragg condition).

Foil thickness t is then determined from:

$$\frac{s_i^2}{n_k^2} + \frac{1}{\xi_g^2 n_k^2} = \frac{1}{t^2} \tag{22}$$

Where n_k is an integer assigned to fringes (n=1 for first fringe, k = identical to i or a consistent integer), t = foil thickness and ξ_g = extinction distance taken from Table 3.3.

By plotting $\left(\frac{s_i^2}{n_k^2}\right)^2$ against $\left(\frac{1}{n_k^2}\right)^2$ from equation (22) and extrapolating a straight line, the

foil thickness is given at the point where the $\left(\frac{s_i^2}{n_k^2}\right)^2$ axis is intercepted (Figure 3.2):
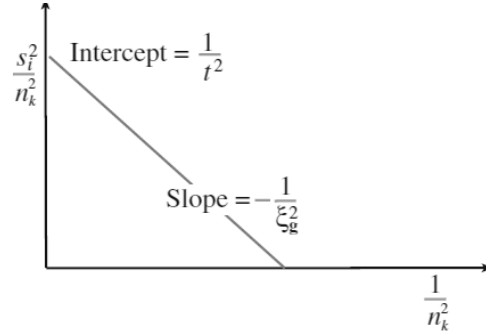
Figure 3.2 graphical plot of $\left(\frac{s_i^2}{n_k^2}\right)^2$ vs. $\left(\frac{1}{n_k^2}\right)^2$ for which thickness, t is extrapolated from the intercept [171]

Table 3.3 Extinction distances ξ_g used and corresponding (hkl) planes [172]

(hkl)	ξ_g (nm) at 100kV	ξ_g (nm) at 120 kV
110	27	28.9
200	39.5	42.3
211	50.3	53.8
220	60.6	64.8
222	82	84.2
310	71.2	76.2
321	92.7	96.5

Dislocation density (ρ) was calculated using equation (23) using measurements of dislocations taken across 10 – 30 fields of view (each field covers an approximate volume of 0.016 μm^3) for each specimen in each condition. In plastically deformed materials it was not possible to measure individual dislocations within cellular structures; in these

instances dislocation density has been described as cellular. Dislocations were imaged using the two beam imaging technique from the [001] zone axis, **g** vectors used were 200, 110 and 211 of which a proportion are invisible (as shown in Table 3.4):

$$\rho = (L / V^3) \ \text{m}^{-2} \tag{23}$$

Where L = total length of dislocations and V = total volume of material.

Table 3.4 Proportion of Burgers Vectors which are invisible under two-beam imaging of ferrite [172]

Diffraction condition	Proportion of a/2 <111> Burgers Vectors Invisible	Proportion of a/2 <100> Burgers Vectors Invisible	Proportion of a/2 <110> Burgers Vectors Invisible	Potential Error
g=<110>	0.5	0.33	0.17	- 26 %
g=<200>	0	0.67	0.33	- 20 %
g=<211>	0.25	0	0.17	+ 7 %

Particles studied in TEM were determined using EDS analysis and compared against a corresponding spectra for the surrounding steel matrix. Volume fraction of particles was calculated by dividing the volume of particles (determined from measured diameter) by the unit volume of material. The total number of particles measured to determine volume fraction ranged between 100 - 150 over 20-30 fields of view per specimen (each field of view covers approximately 0.012 μm^3).

e. Hardness testing

Hardness tests were conducted across the thickness of samples and the average taken from 10 readings for each indentation location (sub-surface, quarter-thickness and mid-thickness) on a Vickers Hardness Testing machine using a load of 20 kg for samples in the as-received and compressed conditions.

f. Mechanical testing

Compression slugs, measuring 6 mm in diameter, were extracted from the quarter thickness position (middle of the cylinder centered at the quarter thickness position) for X65 plates and as close to quarter thickness as possible for X80 grade specimens. Due to the thickness of X80 plates, areas of sub-surface and mid-thickness could not be avoided (Figure 3.3). Cylindrical samples were extracted from plates/sheets using EDM that were then sliced using the Accutom 5 to samples of 10 mm height. These samples were compressed to different levels of strain to allow characterisation of the dislocation structures after deformation.
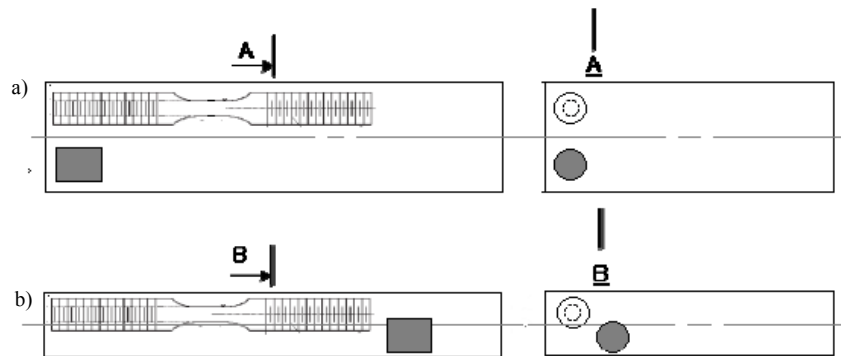
Figure 3.3 Schematic diagram which demonstrates the locations of where compression and tensile test samples were extracted in relation to the supplied (a) X65 and (b) X80 grade steel plates

Samples prepared for reverse deformation (Bauschinger tests) were taken from quarter thickness position in the three X65 steel plates and as close to quarter thickness as possible in the X80 plates, as with the compression slugs, sub-surface and mid-thickness areas could not be avoided (Figure 3.3). These were machined into typical tensile test piece specimens of 4.5 mm diameter and 13 mm gauge length (Figure 3.4). Strain gauges were attached after surface preparation; grinding with 1200 SiC grinding paper and subsequent cleaning with acetone to remove any excess oil. Kyowa Loctite Cement was used to affix strain gauges which were left to dry for 24 hours.
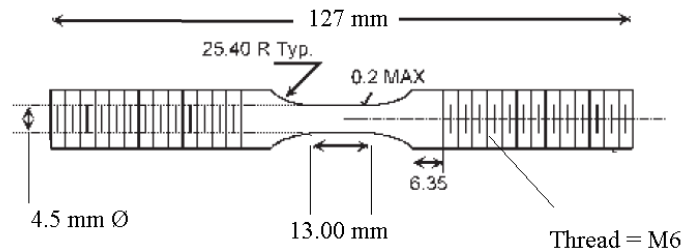
Figure 3.4 Machined tensile test piece specimen showing critical dimensions

Compression was carried out using an ESH 250 kN servo-hydraulic twin column ramp universal testing machine at ambient room temperature at a strain rate of 1.6 x 10^{-4} with samples being compressed to 0.01, 0.02 and 0.04 strain (measured from strain gauge readings and physical measurements in sample height before and after compression). Tensile tests were conducted at the same strain rate as compression tests to failure, strain at UTS was not recorded as specimens failed outside the limits of the strain gauge equipment (> 0.05 strain).

Compression-tension tests were conducted at the same strain rate as the compression tests. Forward loading was in the compressive direction to 0.01, 0.02 and 0.04 strain for each specimen, loads were held at this strain to change ramp settings then subsequently reverse, tensile loaded to failure at the same strain rate.

All specimens were tested at least once for each strain regime and repeat tests showed a standard deviation ±1.5 for measured strength values. Experimental parameters for plastically induced strain and number of tests carried out at each strain regime for forward compressive / tensile tests (required for strength and work hardening behaviour) and pre-strain regime (level of forward compressive strain preceding reverse tensile loading required for work softening behaviour) shown in Table 3.5.

Data output from the ESH universal testing machine was set to a maximum of 5 V corresponding to 100 kN force. Strain gauge outputs were measured using an AC/DC converter which also output a maximum of 5 V corresponding to 0.02 strain. Labview (Version 9.1) was used to process the data.

Table 3.5 Experimental matrix of plastic deformation tests carried out for all steel specimens

X65 (I)			
	loading schedule / number of tests		
induced strain / *pre-strain	compression	tensile	compression - reverse tensile to failure (*Bauschinger test)
1%	2	2	1
2%	2	2	2
4%	2	2	1
X65 (II)			
	loading schedule / number of tests		
induced strain / *pre-strain	compression	tensile	compression
1%	2	2	2
2%	2	2	1
4%	2	2	1
X65 (III)			
	loading schedule / number of tests		
induced strain / *pre-strain	compression	tensile	compression - reverse tensile to failure (*Bauschinger test)
1%	2	2	1
2%	2	2	1
4%	2	2	2
X80 (I)			
	loading schedule / number of tests		
induced strain / *pre-strain	compression	tensile	compression - reverse tensile to failure (*Bauschinger test)
1%	2	2	1
2%	2	2	1
4%	2	2	1
X80 (II)			
	loading schedule / number of tests		
induced strain / *pre-strain	compression	tensile	compression - reverse tensile to failure (*Bauschinger test)
1%	2	2	2
2%	2	2	1
4%	2	2	1

4 Microstructural characterisation

4.1 Thermo-Calc modeling of microstructure phases

Thermo-Calc Software [173] was utilised in this project to predict the carbo-nitride phases present in the studied steels. Previous research into HSLA steels has shown the volume fraction of carbo-nitride particles predicted by Thermo-Calc to be comparable to measured data for steels in the as-rolled and reheated conditions [35, 174].

Full steel wt % compositions from Table 3.2 were used for the data input with Fe as the remainder. Phase balances and the levels of the microalloying elements in the carbo-nitride phase were plotted as a function of temperature (600 - 1600 K) every 2.5 K, (Figure 4.1) and the Ar_1 / Ar_3 temperatures were also determined, Table 4.1. X65 (II) which has a higher Ni content than other comparative grades has a lower A_{r3} temperature and a much smaller temperature range down to A_{r1}. X80 (II) which also has a high Ni content does not show this trend but this is most likely due to high additions of Mo which give a lower A_{r1} temperatures in both X80 steels compared to the X65 grades, more so for X80 (II) (604°C).

Table 4.1 Thermo-Calc predictions of Ar_1 and Ar_3 temperatures (^{o}C)

Steel	$\gamma \rightarrow (\alpha + \gamma)$ (Ar_3)	$(\alpha + \gamma) \rightarrow \alpha$ (Ar_1)
X65 (I)	863	678
X65 (II)	771	682
X65 (III)	859	678
X80 (I)	845	657
X80 (II)	830	604

Thermo-Calc did not separate the volume fraction of each carbo-nitride phase predicted to be present in the studied steels i.e. TiN, Nb(C,N) and VC, but gave a combined volume fraction. It was possible to determine the separate volume fractions by plotting the content of C, N, Ti, Nb and V in the carbo-nitride phase across the temperature range (Figure 4.1) and the mole fraction of carbo-nitride phase against temperature.
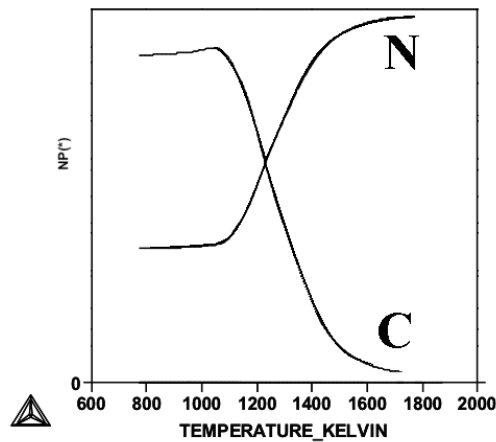
Figure 4.1 Typical plot for nitrogen and carbon content in the carbo-nitride phase with decreasing temperature in studied steels

Figure 4.2 allows the temperature ranges to be determined for when the carbo-nitride phase will be C-, N-, Ti-, Nb- or V-rich. To obtain the volume fraction of inclusions and

precipitate phase the densities of each phase present in the steel (Fe, MnS, Fe_3C, TiN, Nb(C,N), VC, AlN) were divided by their respective mass and converted into a percentage. The properties listed in Table 4.2 were used for these phases.

Table 4.2 Molecular mass, lattice parameter, molecules per unit cell, density and molar volume of predicted phases at room temperature after Gladman [53]

Compound Structure	Molecular mass	Density (Mg m^{-3})	Molar volume (cm^3)
NbC	105	7.84	13.39
NbN	107	8.41	12.72
VC	63	5.83	10.81
VN	65	6.18	10.52
TiC	60	4.89	12.27
TiN	62	5.42	11.44
AlN	41	3.27	12.54
MnS	87	3.99	10.7
Fe3C	179	7.43	9.21
Fe-α	56	8.15	6.85

X65 I and II carbo-nitride phases are predicted to consist of TiN from solidification down to 1030 ^{o}C, after which Nb(C,N) precipitates down to 710 ^{o}C; below this temperature VC adds marginally to the total second phase (Figure 4.2).
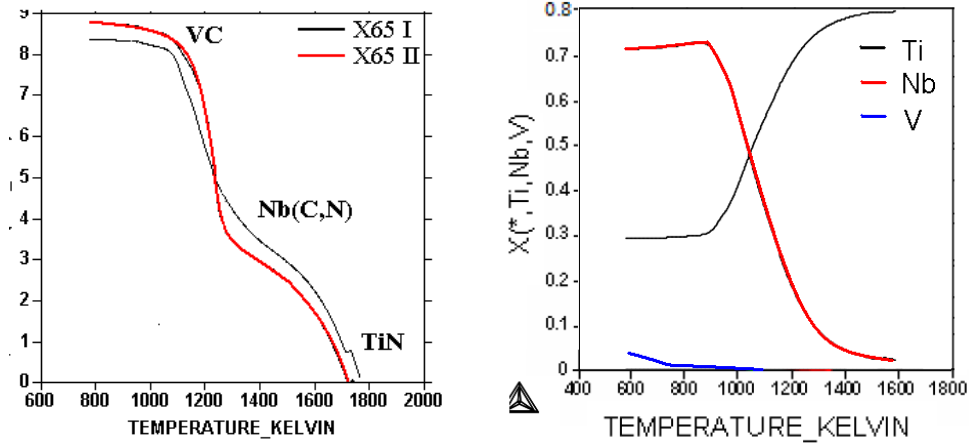
Figure 4.2 (a) Dependence of the carbo-nitride phase mole-fraction in X65 (I) and X65 (II) against temperature (b) content of Ti, Nb and V in the carbo-nitride phase for X65 (II)

For X65 III precipitation down to 1227 °C is attributed to TiN with Nb(C,N) forming between 1200 and 677 °C, and precipitation of VC occurring below 927 °C and contributing significantly to the overall amount of carbo-nitride phase, as would be expected as the steel has large additions of V (0.074 wt %) (Figure 4.3).
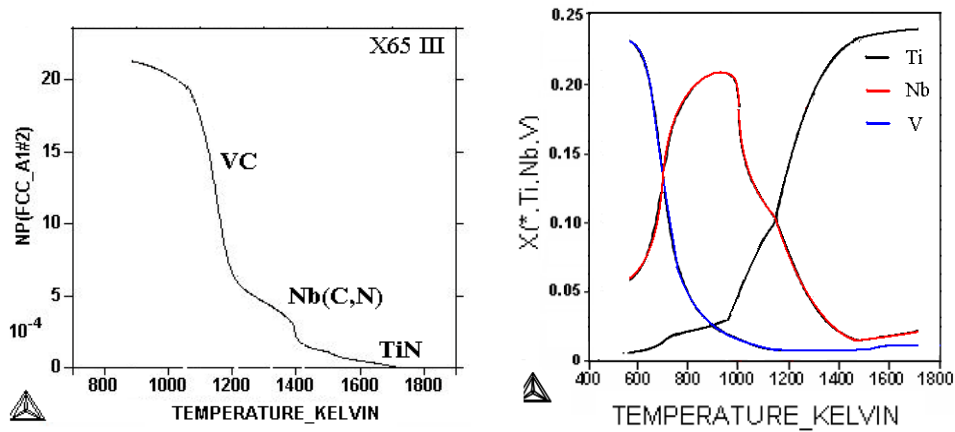
Figure 4.3 Mole fraction of carbo-nitride phase against temperature in X65 (III)

In both the X80 grade steels precipitation of TiN is predicted to finish on cooling at approximately 1130 °C followed by Nb(C,N). For these steels (which both have higher Nb contents than the X65 steels) the Nb(C,N) phase has been separated as NbC and NbN by Thermo-Calc, thus Nb(C,N) forms over the temperature range of approximately 1200 – 760 °C with a very small amount of VC predicted to form due to the low levels of V (0.001 wt %) in these steels below 700°C (Figure 4.4).
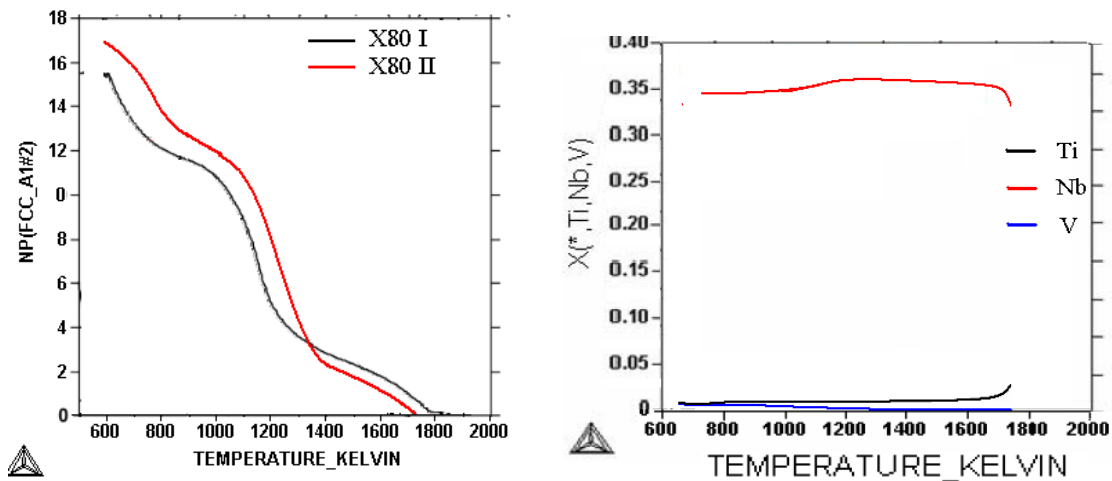
Figure 4.4 Mole fraction of carbo-nitride phase against temperature in X80 (I) and (II)

The total volume fraction of carbo-nitride phases predicted to form and their corresponding formation temperatures are presented in Table 4.3.

Table 4.3 Predicted precipitation finish equilibrium temperatures (^{o}C) and corresponding volume fractions (VF).

Steel	Ti-rich		Nb-rich		V-rich	
	ppt finish (^{o}C)	VF		VF	ppt finish (^{o}C)	VF
X65 (I)	1027	0.00011	717	0.00054	327	
X65 (II)	1033	0.00011	710	0.00063	327	<0 .00005

X65 (III)	1127		677	0.00038	327	0.0012
X80 (I)	1133	< 0.00005	747	0.00144	527	< 0.00005
X80 (II)	1127		770	0.00139	527	

4.2   SEM analysis of (Ti,Nb)-rich carbo-nitride phases

Microalloy carbo-nitride precipitates of a coarse nature (in this study these are classified as particles > 50 nm in diameter) are formed at higher temperatures (above Ar_3); typically these are Nb- and Ti-rich, initially as nitrides due to their higher driving force for precipitation. These types of particles generally have too low a number density (and are therefore too widely spaced) [36, 40-44] to produce any significant strengthening by means of the Orowan mechanism [175,176], instead they act as grain refiners by pinning austenite grain boundaries [177]. SEM analysis was used to quantify the area fraction of these precipitates. This was used in combination with the Thermo-Calc predictions of total volume fraction of microalloy precipitates expected at equilibrium to estimate how many fine particles (< 50 nm) might be present, for subsequent TEM analysis. All reverse loading tests were conducted in the quarter thickness region of the steel plates and therefore particle analysis was concentrated in that region of the plates.

4.2.1   Particle composition and morphology

The observed particle size in SEM analysis was between 20 and 300 nm. Particles under 50 nm have been disregarded for SEM analysis as it could not be guaranteed that all fine

precipitates would be observed, and particles in this size range were investigated using TEM. The particles observed in the SEM were predominantly Nb-rich and had a spherical morphology. X65 (I) and (II), which have high microalloying additions of Ti, had a substantial number of cuboidal precipitates mostly > 100 nm side length but were also observed down to 60 nm in size. Finer (< 80 nm) Ti-rich particles were also observed in the other steels (X65 (III), X80 (I) and X80 (II)), which have small additions of Ti. Traces of V were detected in particles < 90 nm in the X65 (III) grade steel (which has a higher V content than the other steels) in Nb- and Ti-rich particles, this may be due to the formation of VC co-precipitated on larger Nb-rich particles.

It was found that there was a higher number density of precipitates within pearlitic regions or immediately adjacent ferrite for steel X65 (III) (Figure 4.5, a and b). This is similar to the observations reported in [35] for an X65 grade ferrite + pearlite steel where the inhomogeneous distribution was related to microalloying element segregation during casting. The remaining steels showed a homogeneous distribution of particles throughout the ferrite grains (Figure 4.5 c and d). Particles were not observed within MA constituents and the presence of MA did not appear to have any influence on the number of particles seen in the adjacent grains in comparison to the rest of the microstructure. Precipitates were not observed in the MA phases in the X80 grade steels (X80 (I) and (II)) (Figure 4.5, e and f). Moderately sized particles, > 100 nm, were frequently observed on ferrite grain boundaries in X65 (I), X65 (III) and X80 (I) (Figure 4.6).
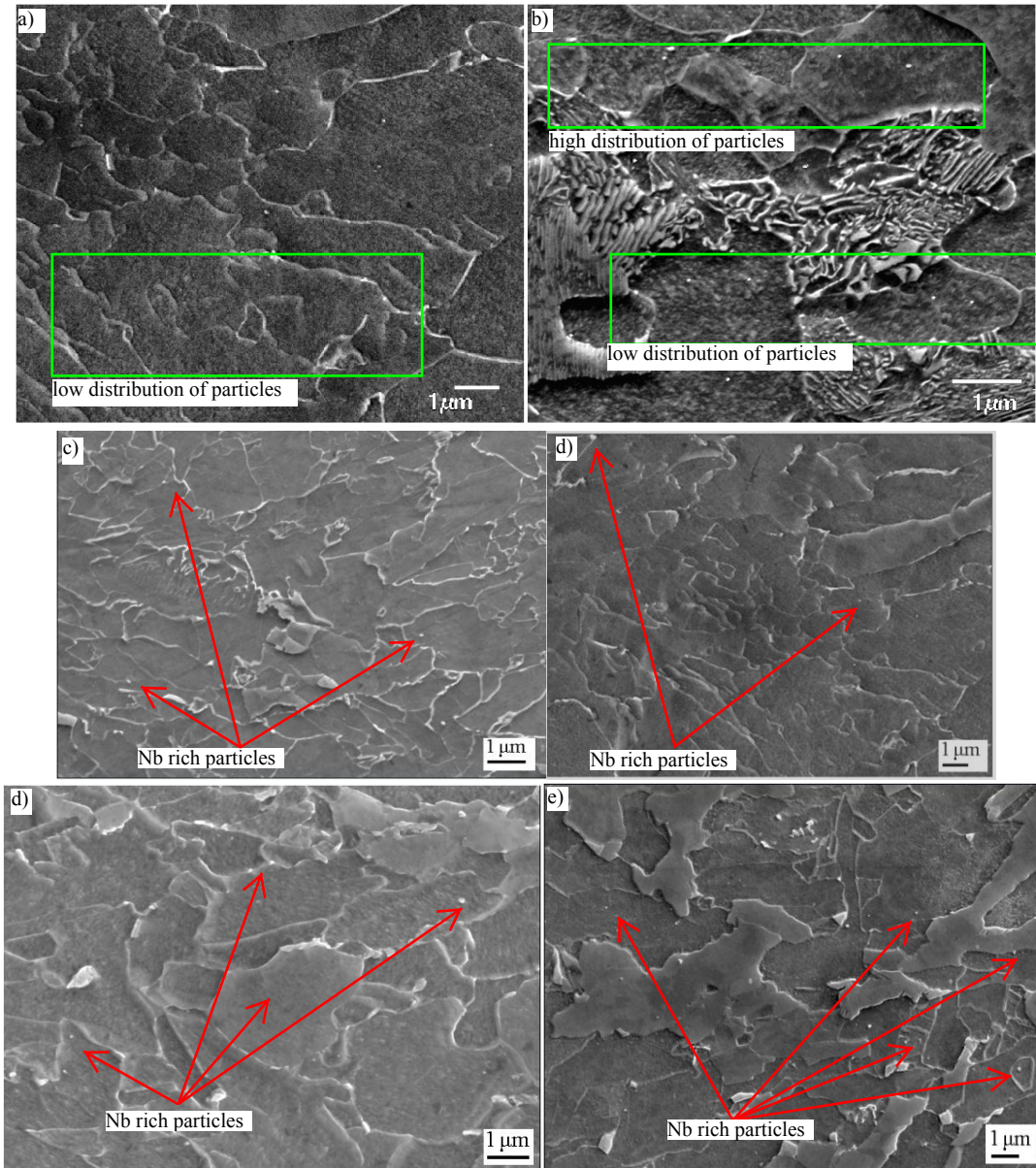
Figure 4.5 SEM micrographs showing (a) X65 (III) low distribution of coarse Nb-rich

particles typically observed in ferritic regions, (b) X65 (III) pearlitic region showing a

greater number density of smaller Nb-rich particles responsible for the skewed

distribution of carbo-nitride precipitates (c) typical homogeneous distributions of coarse

Nb- and Ti-rich X65 particles X65 (I) and (d) X65 (II (e) distribution of predominantly

Nb-rich particles within the ferrite grains and adjacent to MA constituents in X80 (I) and

f) X80 (II) typical distribution of fine and coarse Nb-rich particles in X80 (II)
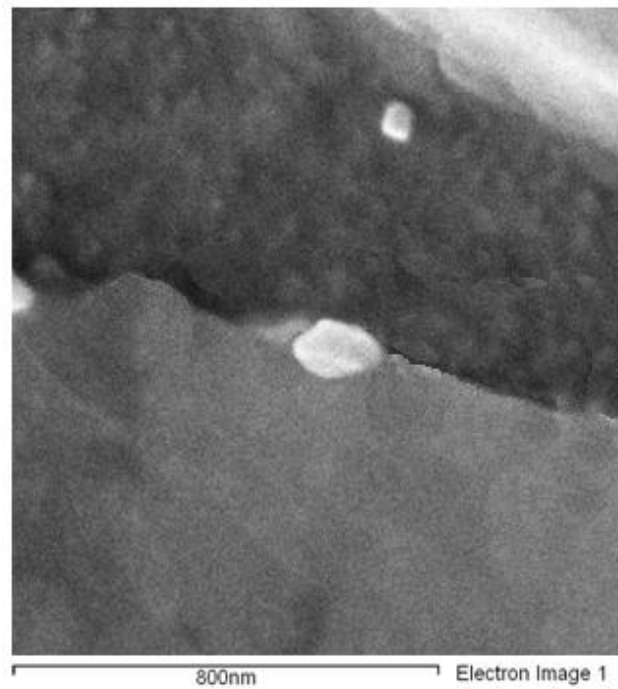
Figure 4.6 Coarse Nb-rich precipitate on ferrite-ferrite grain boundary in X65 (III);

frequently observed in X65 (I), X65 (III) and X80 (I) which increase the risk of

intergranular corrosion, stress corrosion cracking and detrimental to the toughness

properties of steel
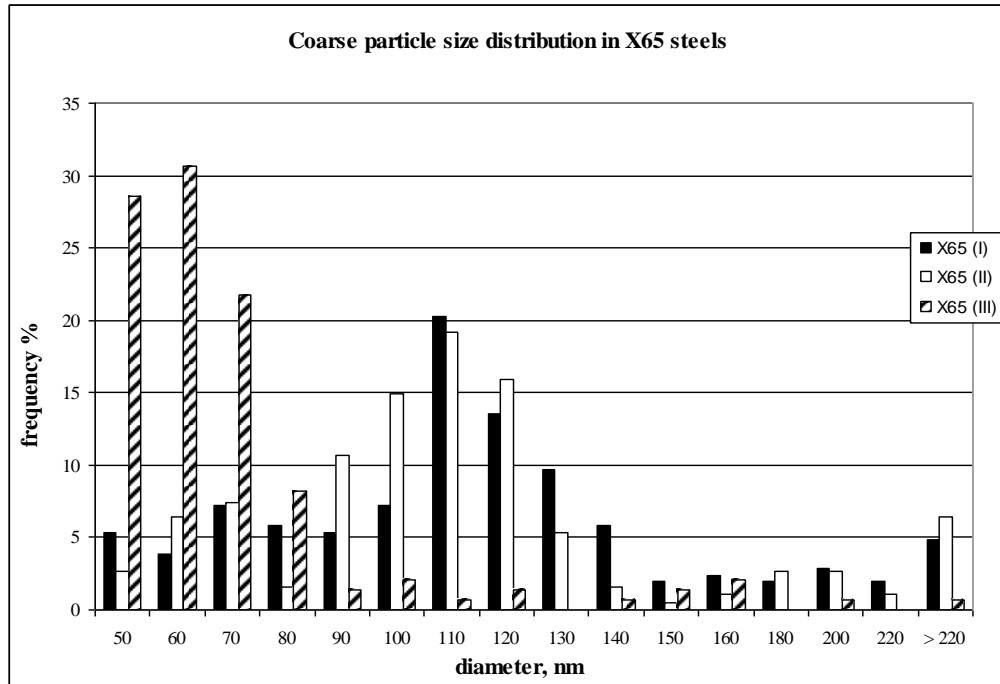
Figure 4.7 Frequency % distribution of 50 – 220 nm size range precipitates in X65 (I),

(II) and (III)
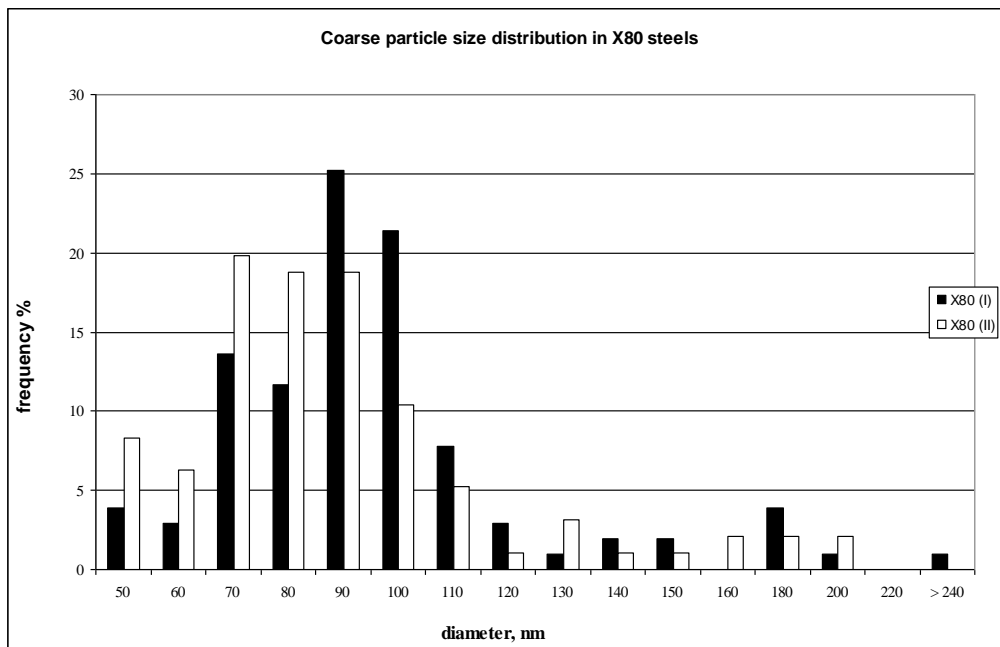
Figure 4.8 Frequency % distribution of 50 – 220 nm size range precipitates in X80 (I) and

(II)

The frequency percentage graphs for the coarse (> 50 nm) microalloy precipitates are shown in Figures 4.7 and 4.8 for the X65 and X80 steels respectively. The five steels show different particle size frequency distributions. X65 (I & II) show similar distributions generally consisting of a large percent of particles > 100 nm, this would be expected as the formation temperatures and volume fractions for TiN and Nb(C,N) are similar. X65 (III) size distribution was skewed to the right, no TiN particles were present; owing to the fact that the additions of Ti are very small (<0.002 wt %) which gives a higher start temperature, Table 4.3, but an absence of nucleation sites decreases the size whilst precipitation continues to a lower temperature for the majority of Nb-rich particles and therefore particle sizes were smaller than those seen in X65 (I) and (II). Both X80 steels showed a similar distribution of particles between 70 and 110 nm with X80 (II) showing relatively more particles between 50 and 60 nm and fewer between 90 and 120 nm in diameter suggesting that the particles are slightly smaller in size than X65 (I) and (II). Larger particles are expected to occur in X80 (II) given the start and finish precipitation temperatures but this was not observed possibly due to the broadness of the distribution peaks masking this effect.

SEM-EDS analysis showed size and composition relationships across the range of carbo-nitride particles for the studied steels. Coarse particles > 100 nm were (Ti,Nb)-rich for both X65 (I) and (II). Polygonal particles were generally in the region of 100 - 300 nm and predominantly Ti-rich with small amounts of Nb (Figure 4.9 a). Analysis of finer particles in these steels < 100 nm were usually spherical and Nb-rich with trace amounts

of Ti present (Figure 4.9 b); as particle size reduced Ti ceased to be present in the particles (Figure 4.9 c). SEM-EDS undertaken on particles in all other steels were found to contain mostly Nb with trace amounts of V in fine particles < 70 nm in X65 (III) owing to co-precipitation of Nb and V (Figure 4.9 d). Trace amounts of Ti were detected in coarse particles for the X80 grade steels (Figure 4.9e).

a

b

c
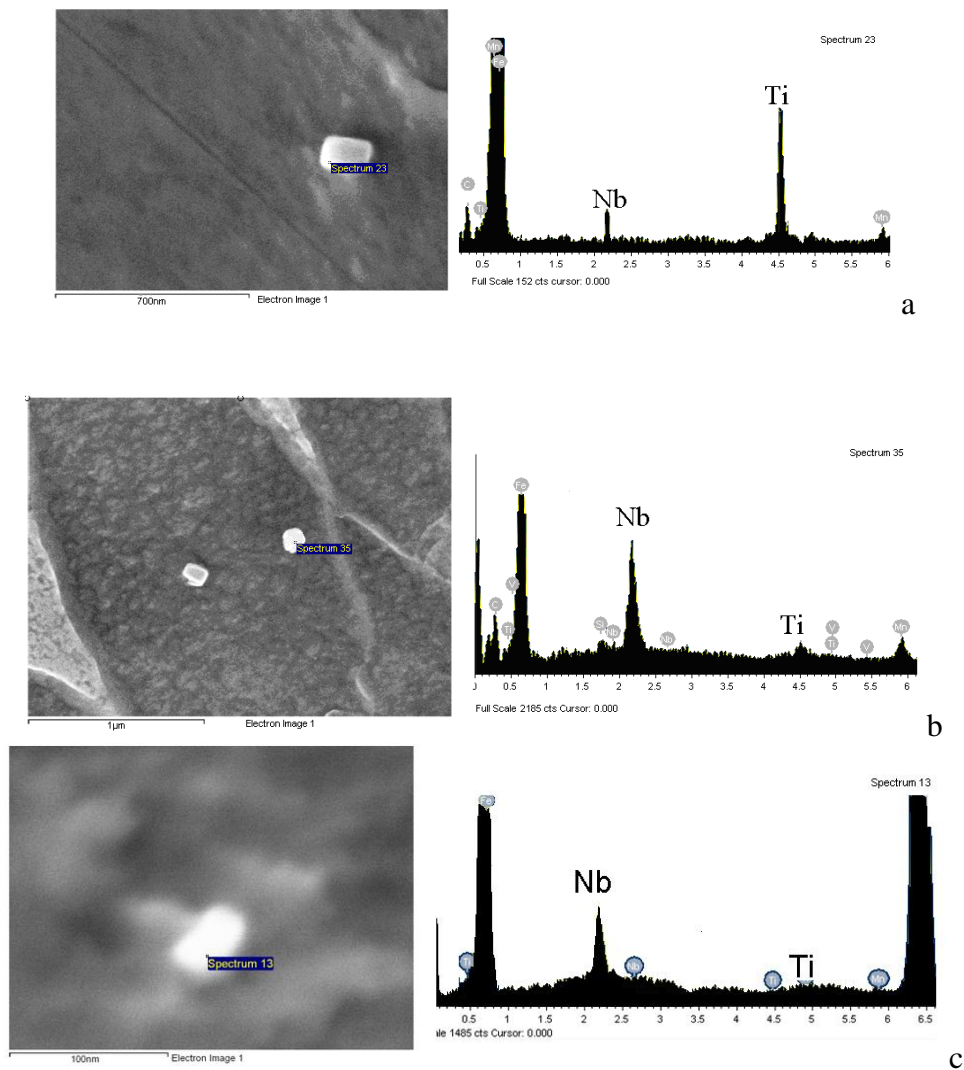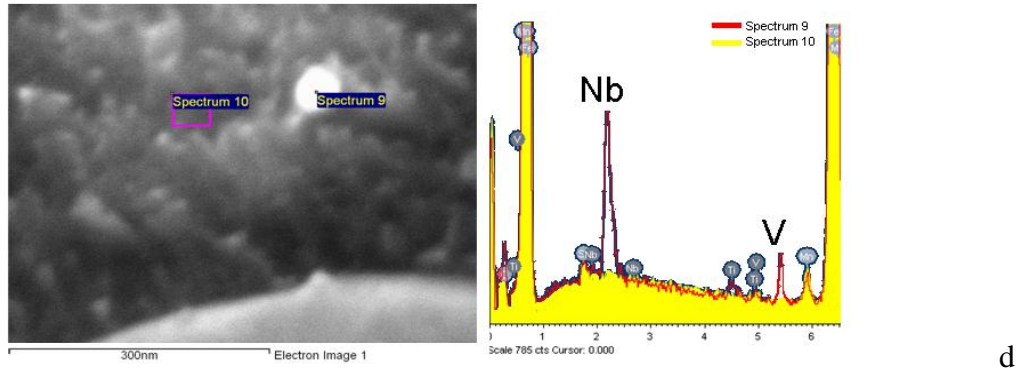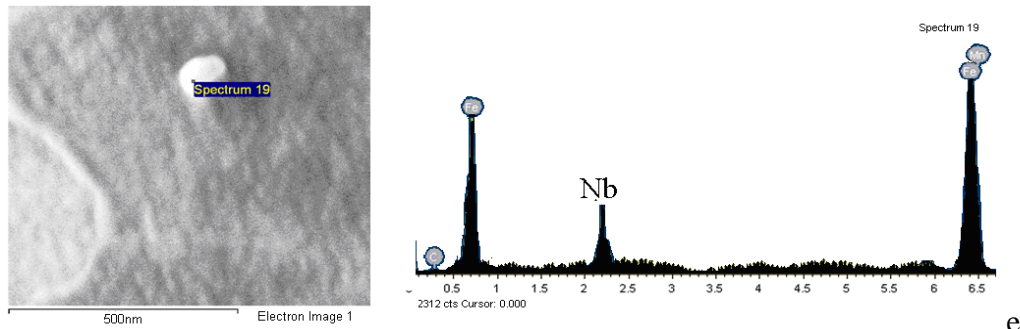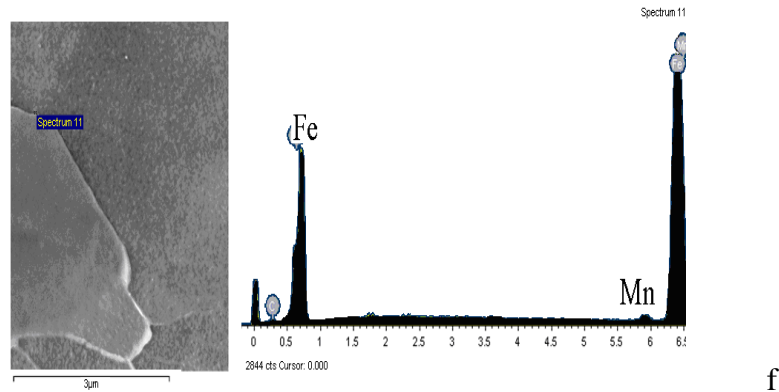
Figure 4.9 Typical SEM images and corresponding EDS spectra of (a) TiN in X65 (II)
(b) (Nb,Ti)-rich particle in X65 (II) (c) (Nb,V)-rich precipitate and EDS spectra of
particle and matrix (d) (Nb,Ti)-rich particle in X80 (II) and (e) typical ferrite matrix
spectrum

The measured particle volume fractions are presented in Table 4.4. Comparing the
measured volume fractions of these carbo-nitrides against the predicted Thermo-Calc
volume fraction values for (Ti,Nb)-rich phases there is a notable difference between X65

and X80 grade materials. X65 (I) and (II) show 23 % and 31 % (negative) difference from Thermo-Calc predictions respectively. These steels have large additions of Ti which are predicted to finish precipitating as TiN at lower temperatures than the Ti-free steels, whilst the Nb(C,N) phase is predicted to finish precipitating at higher temperatures, Table 4.1. These showed a wider range of formation temperatures so the volume fraction unaccounted for in SEM was analysed via TEM. X65 (III) showed reasonable agreement with Thermo-Calc predictions for the Nb-rich phase with a (negative) difference of 13 %. After free nitrogen and Nb have formed NbN particles then precipitation of NbC occurs across the same temperature range as VC is expected to precipitate. Thus, (Nb,V)-rich particles and complex precipitates may have increased the volume fraction determined from SEM measurements. Particles which were not observed in SEM are expected to be predominantly V-rich carbides and a fraction of particles that are still Nb-rich to account for the difference between the measured and predicted volume fractions of Nb-rich particles. Measured volume fraction of precipitates measured by SEM for X80 (I) and (II) were half the predicted amount but were still higher than the measured volume fractions of the X65 grade materials. Only trace amounts of Ti were seen in small particles < 100 nm and the remaining particles were Nb-rich. The only phase predicted to precipitate from these materials is Nb(C,N) and so TEM was used to quantify the remaining precipitates as, although Nb-rich particles are predicted to start and finish forming at higher temperatures than in the X65 grades, the SEM-determined size distributions are smaller, Figures 4.7 and 4.8; this suggests that some of the ~50 % discrepancy from the predicted values comes from precipitation of finer particles than resolvable using SEM.

Table 4.4 Summary of characterisation of coarse particles (> 50 nm) from SEM analysis

Steel	number of particles quantified	average particle size (nm)	volume fraction	number density (x 10^{-4} mm^{-2})	Volume fraction (TC prediction)
X65 (I)	260	94	0.00042	54	0.0007
X65 (II)	280	83	0.00049	56	0.00079
X65 (III)	250	66	0.00033	48	0.01243
X80 (I)	360	76	0.00064	89	0.00154
X80 (II)	310	71	0.00072	102	0.00149

4.2.2   TEM analysis of fine particles

TEM analysis was employed to quantify precipitates < 50 nm in diameter in the studied steels. It was observed that the particles were not evenly distributed throughout the microstructures of X65 (I) and (III) with certain regions showing higher number densities of particles which is consistent with microalloying segregation during processing (Figure 4.10). This was accounted for during the measurement of fine scale precipitates by taking measurements either side of an equivalent area to give a more representative figure. In X65 (III) particles were present on dislocation lines (Figure 4.11) which is possibly from strain induced precipitates but characteristic linear formation associated with this type of particle was not observed. Particles in X65 (III) and both X80 grades showed greater number densities within ferrite grains owing to their higher microalloying content and higher predicted volume fractions of carbo-nitride phases which can be seen when

comparing Figure 4.12 for X65 (I) and Figures 4.13 and 4.14 for X65 (III) and X80 (I) respectively.
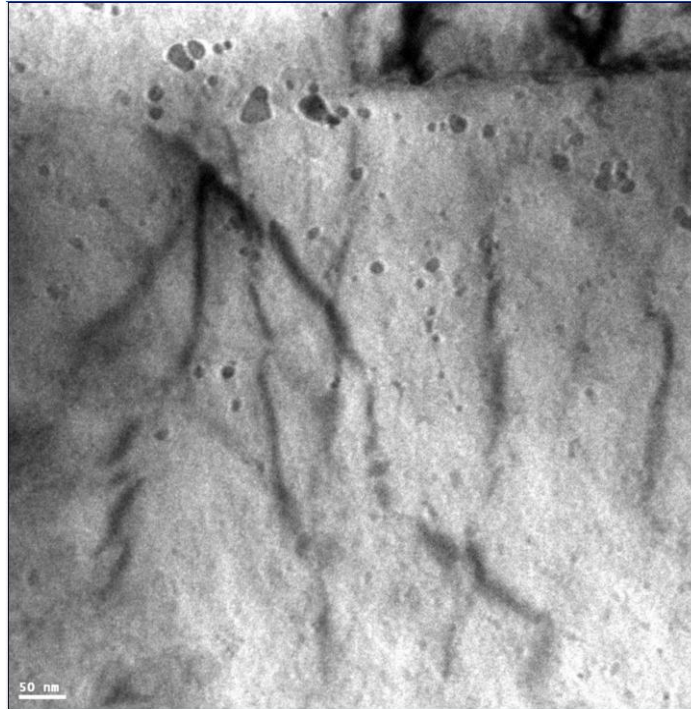
Figure 4.10 (Nb,Ti)-rich particles heterogeneously dispersed in a row within a ferrite

grain in X65 (II). The immediate area parallel to the particles is solute-depleted and

shows a low number density of particles
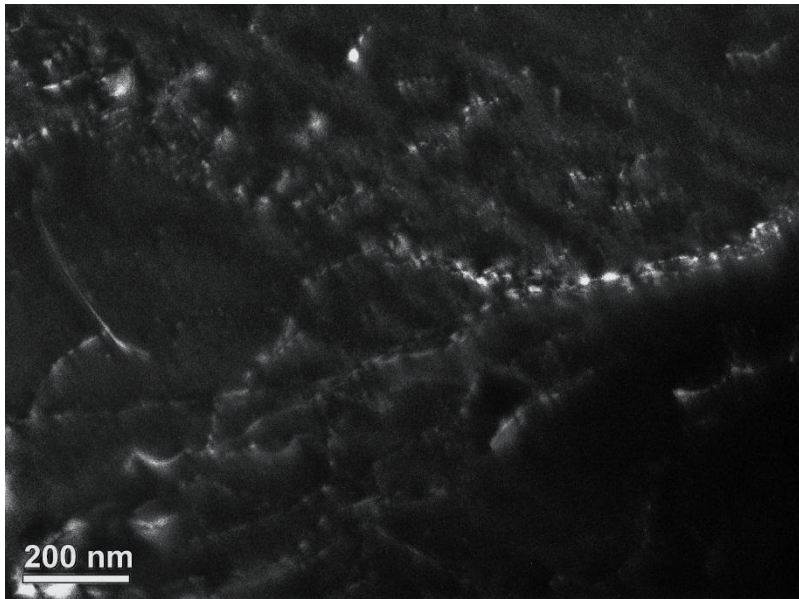
Figure 4.11 Dark field image of precipitates on dislocation lines in X 65 (III) quasi-linear formations suggests these are strain induced precipitates
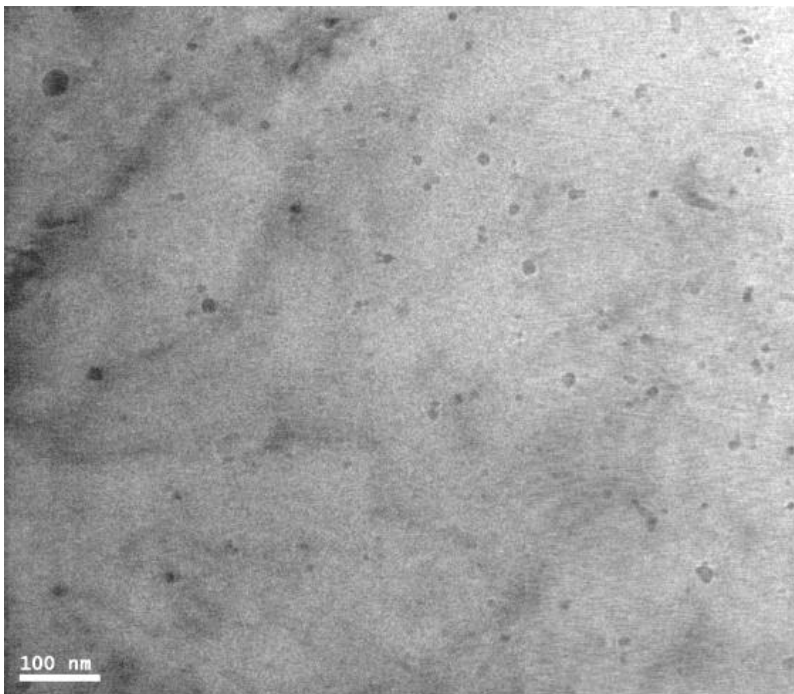
Figure 4.12 Typical TEM micrograph of Nb-rich precipitates in X65 (I) which are relatively low in number density in comparison to X65 (III) and X80 grades
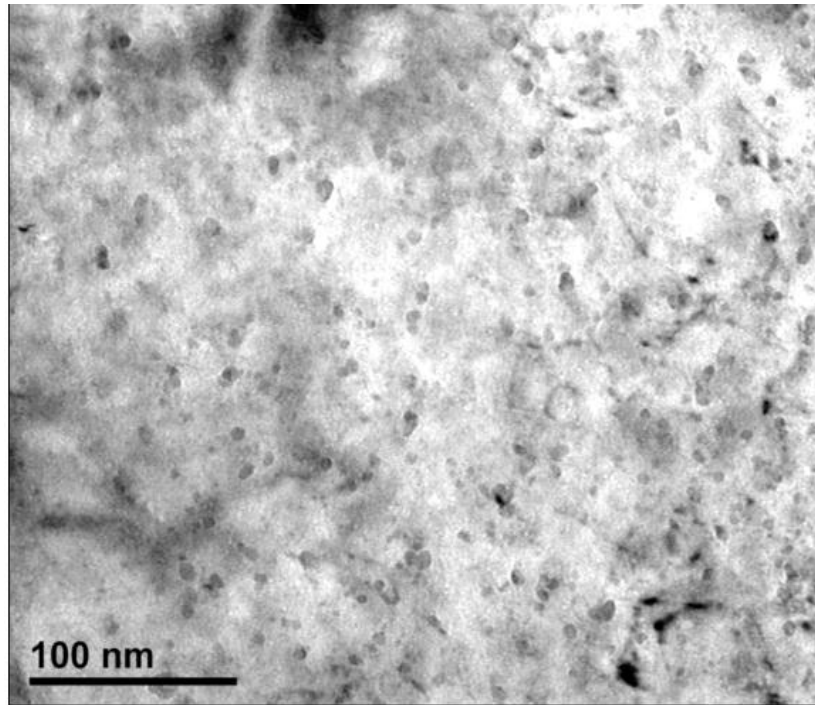
Figure 4.13 Typical TEM micrograph of fine Nb and V-rich precipitates in X65 (III) which have the highest number density of all studied steels owing to the high additions of vanadium
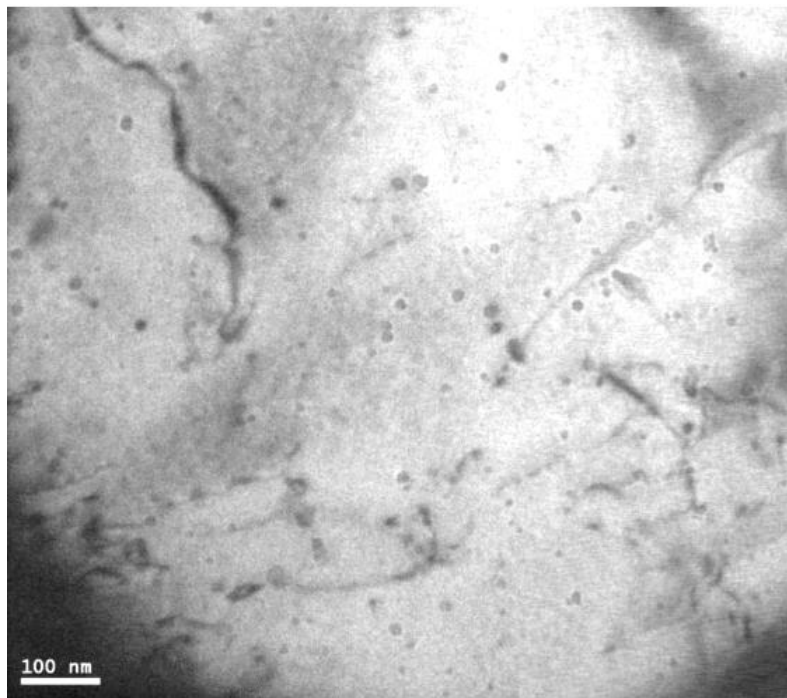
Figure 4.14 Typical TEM micrograph showing a high number density of Nb-rich precipitates in X80 (I) within a ferrite grain

When larger particles, > 50 nm, were observed they were usually Nb- and/or Ti-rich and located far from grain boundaries, smaller particles were observed typically outside the radius of larger particles as the immediate vicinity would be solute depleted (Figure 4.15). Particles < 10 nm in diameter were more frequently observed in X65 (III) and both the X80 grades due to the relatively large addition of vanadium in X65 (III) and the accelerated cooling processing used for the X80 steels. Morphology was typically spherical for fine carbides of VC, NbC or ellipsoid for (Nb,V)C (Figure 4.16). Some cuboidal precipitates were still observed in the sub 50 nm size range in X65 (I) (Figure 4.17).
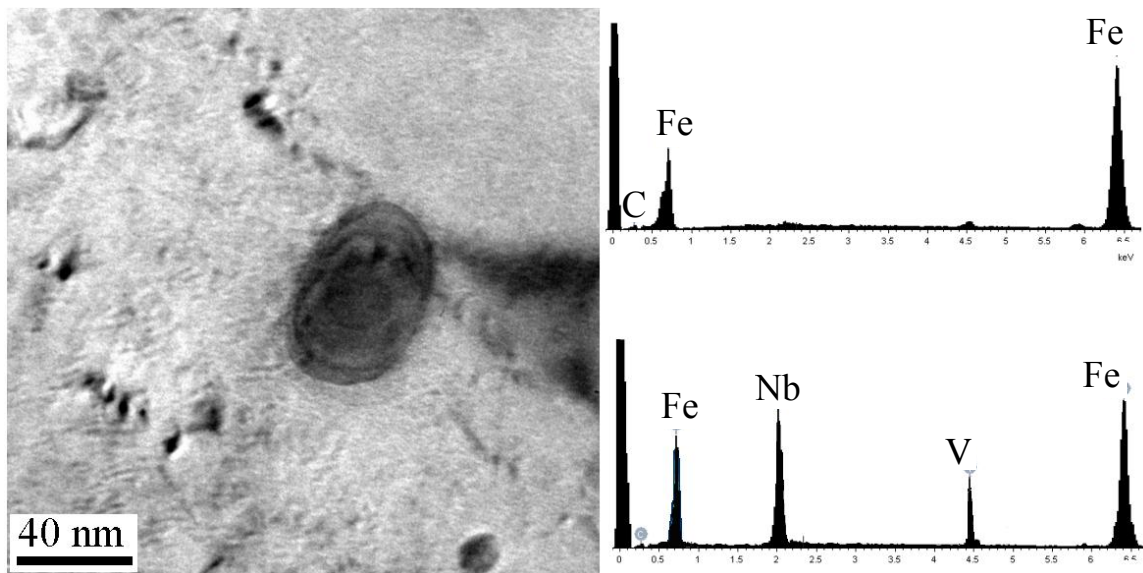
Figure 4.15 (Nb,V)-rich particle in X65 (III) and corresponding EDS spectra of particle and the surrounding matrix. A smaller VC particle is seen outside the region which would be solute-depleted
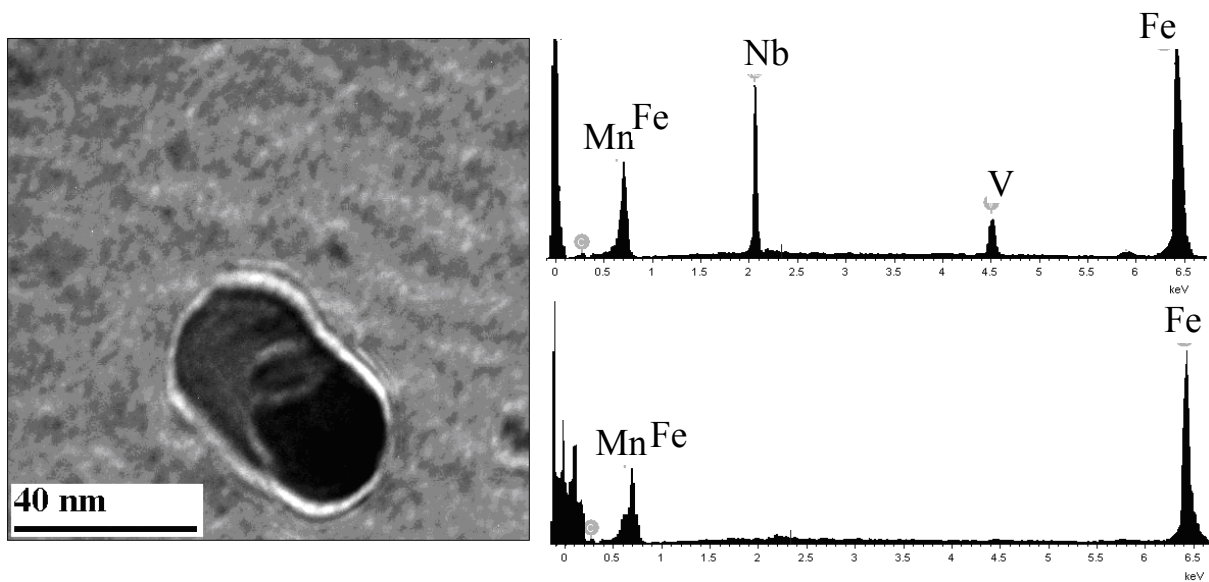
Figure 4.16 (Nb,V)-rich particle in X65 (III) and corresponding EDS spectra of particle
and the surrounding matrix
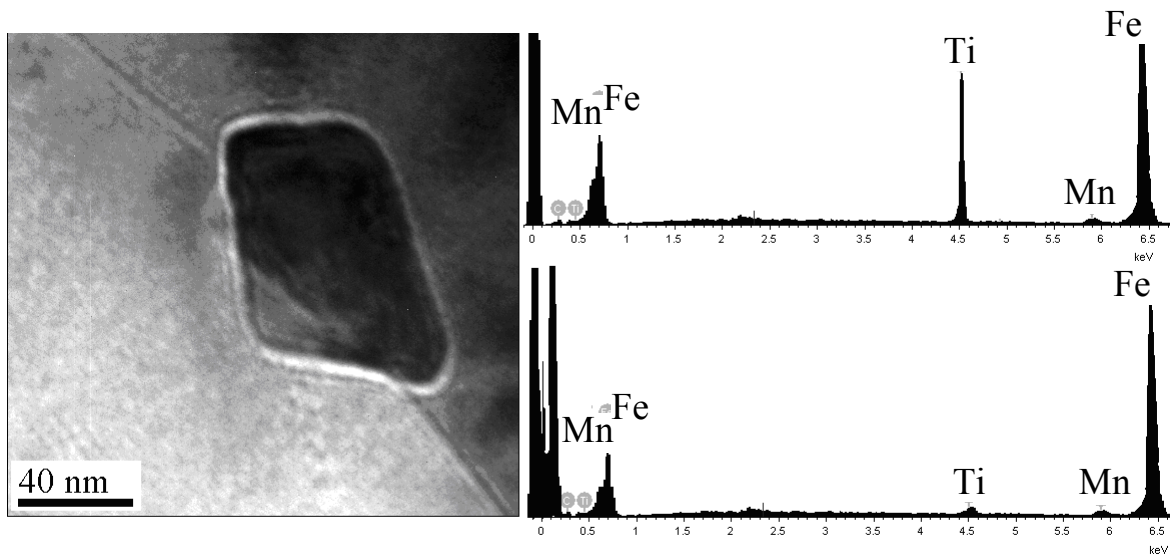
Figure 4.17 (Ti,Nb)-rich particle on grain boundary in X65 (I) and corresponding EDS
spectra of particle and the surrounding matrix. This is very unusual and detrimental to
toughness in HSLA steel

Frequency % distributions are shown in Figures 4.18 and 4.19. Both X65 (I) and (II) had particle size distributions skewed to the right (more so for X65 (II)) which were predominantly Nb-rich which would suggest that, assuming that Ti has taken up most of the free nitrogen, the majority of niobium has precipitated as NbC. A clear difference in the size distribution of particles can be observed between X65 (III) and X65 (I) and (II) as the majority of particles are finer in X65 (III), which is as expected from the high additions of vanadium and lower precipitation range for VC which typically forms as small precipitates (approx 5 - 10 nm) in low carbon TMCR steels [67, 70, 178]. The size distribution for X80 (I) is skewed to the right (smaller particles) of that for X80 (II) due to the higher levels of carbon present and the lower precipitation finish temperature expected Nb-rich carbo-nitrides.
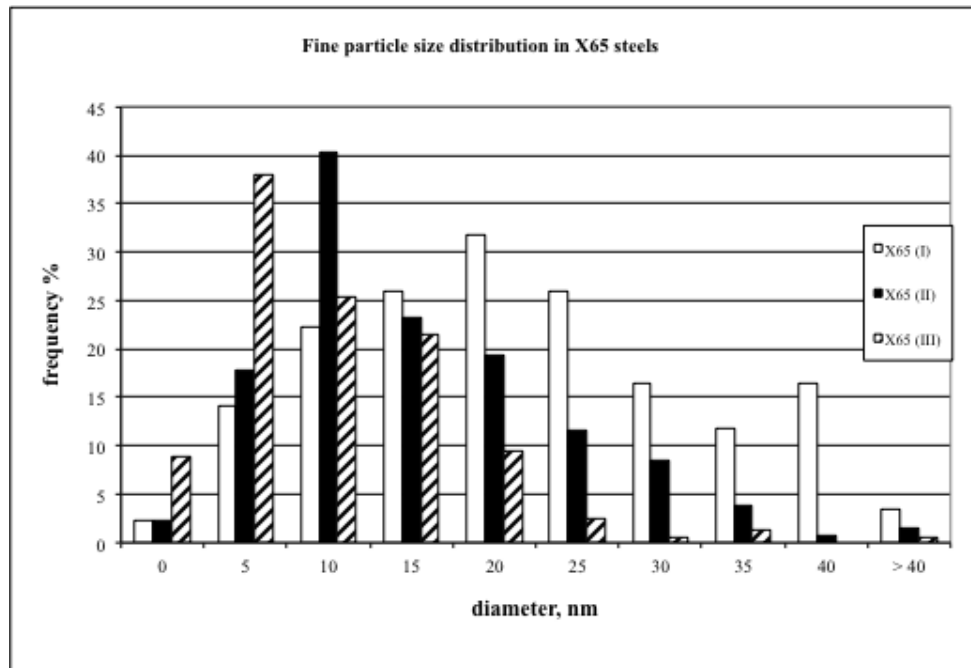
Figure 4.18 Frequency % distribution of particles up to 50 nm in diameter in the X65 grade steels. X65 (I) shows a broad distribution whilst the remaining specimens are skewed to the right
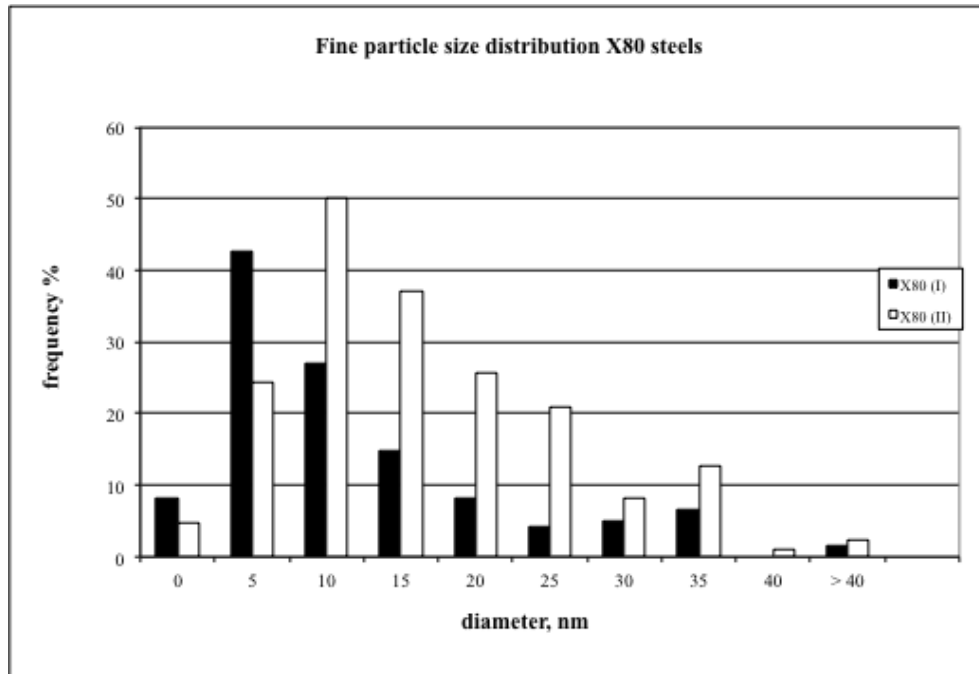
Figure 4.19 Frequency % distribution of particles up to 50 nm in diameter in the X80 grade steels, X80 (I) is skewed heavily to the right

Measured TEM particle data are summarised in Table 4.5. The combined measured TEM and SEM volume fraction values of precipitates agree well with Thermo-Calc predictions (Table 4.6) with the exception of X65 (III). The volume fraction of particles for this steel did not account for 8 % of the predicted carbo-nitride phase, a possible reason for this discrepancy could be due to difficulties in imaging fine-scale VC particles < 5 nm and accounting for these during measurement which requires a reasonable field of view to capture the entire size range of particles.

Table 4.5 Summary of characterisation of fine particles (<50 nm diameter) from TEM analysis

Steel	number of particles quantified	average particle size (nm)	volume fraction	number density (x10^4 / mm^2)
X65 (I)	420	25	0.00026	1356
X65 (II)	490	19	0.00021	1732
X65 (III)	690	9	0.00115	4271
X80 (I)	720	11	0.00093	3652
X80 (II)	580	14	0.00066	2354

Table 4.6 Summary of characterisation of all measured particles and Thermo-Calc predictions

Steel	Measured VF (SEM)	Measured VF (TEM)	Total measured VF	Thermo-Calc predicted VF
X65 (I)	0.00042	0.00026	0.00068	0.00059
X65 (II)	0.00049	0.00021	0.0007	0.00068
X65 (III)	0.00033	0.00115	0.00148	0.00163
X80 (I)	0.00064	0.00093	0.00157	0.00154
X80 (II)	0.00072	0.00066	0.00138	0.00149

4.3 Optical microscopy

4.3.1 X65 (I) & (II)

Typical micrographs for X65 (I) and (II) taken in the longitudinal orientation at quarter thickness position are shown in Figure 4.20 and Figure 4.21.

Figure 4.20 Optical micrograph of X65 (I) in the longitudinal orientation taken from the quarter thickness position
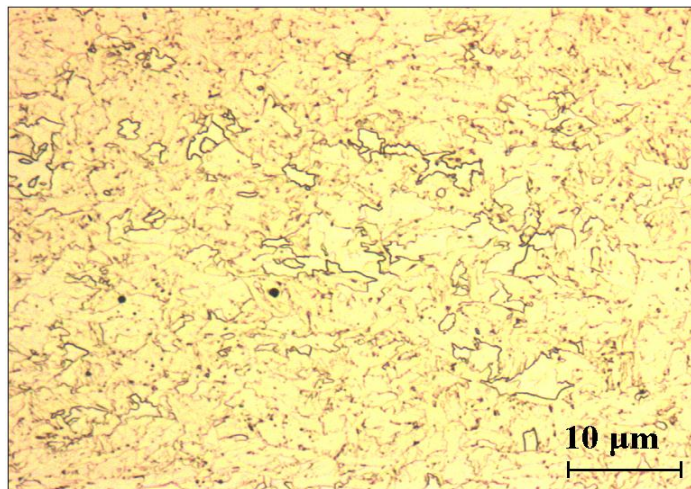
Figure 4.21 Optical micrograph of X65 (II) in the longitudinal orientation taken from the quarter thickness position

The measured ferrite grain sizes (equivalent circle diameter, ECD) were 1.9 μm and 2.1 μm for X65 (I) and X65 (II) respectively. These steels were produced at high load capacity rolling mills and therefore may have experienced multiple recrystallisation stages and then significant deformation below the recrystallisation stop temperature, (as discussed in section 1.2) and have been subjected to accelerated cooling schedules. They also contain titanium which, when present at TiN particles, can pin the prior austenite grain boundaries during the reheating stage prior to rolling. These factors result in a refined grain structure. The steels contain different bainitic and ferrite structures, which are also consistent for accelerated cooling of steels with low carbon content [18,26]. X65 (I) consists of polygonal ferrite and acicular ferrite as seen in Figure 4.22 a and b.
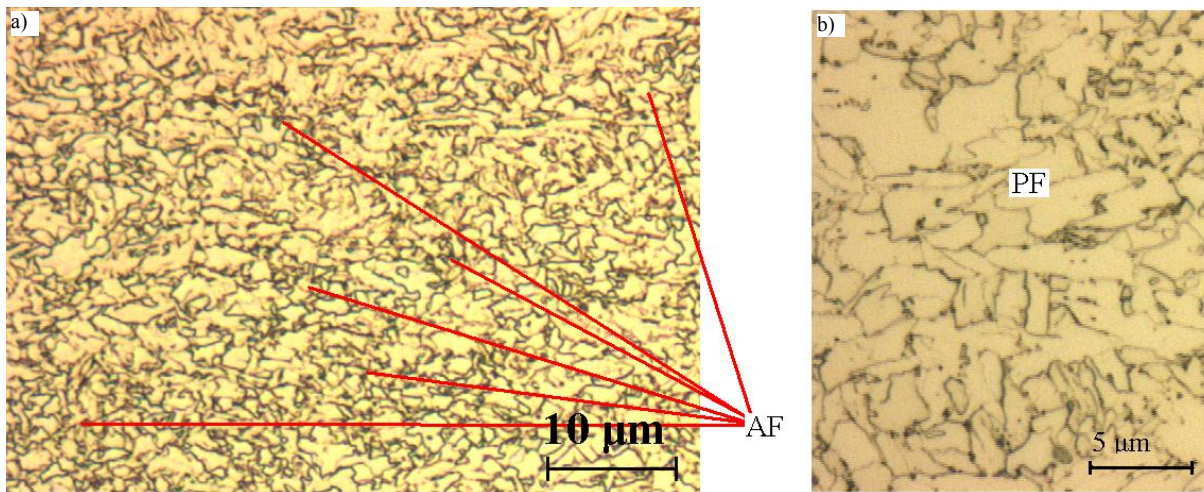
Figure 4.22 Optical micrographs of X65 (I) showing (a) regions of acicular ferrite (AF) are observed around coarse ferrite grains and (b) higher magnification image showing polygonal ferrite (PF) grains with adjacent regions of bainite and acicular ferrite

X65 (II) mostly consists of polygonal ferrite and granular bainite, cementite can be observed at grain boundaries and within ferrite grains. Areas of massive ferrite / quasi-polygonal ferrite were frequently observed in the microstructure as shown in Figure 4.23 a) and b). The grain size distributions for both steels are presented in Figure 4.24 and Figure 4.25.
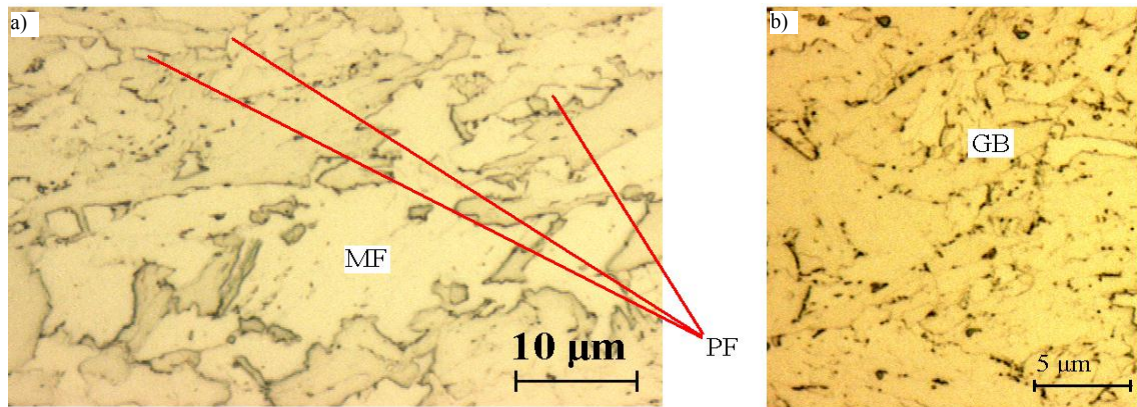
Figure 4.23 Optical micrographs of X65 (II) showing (a) regions of massive ferrite (MF) which characteristic evidence of sub-structure and (b) micrograph of granular bainite (GB), characteristic regions of cementite outline prior austenite grain boundaries
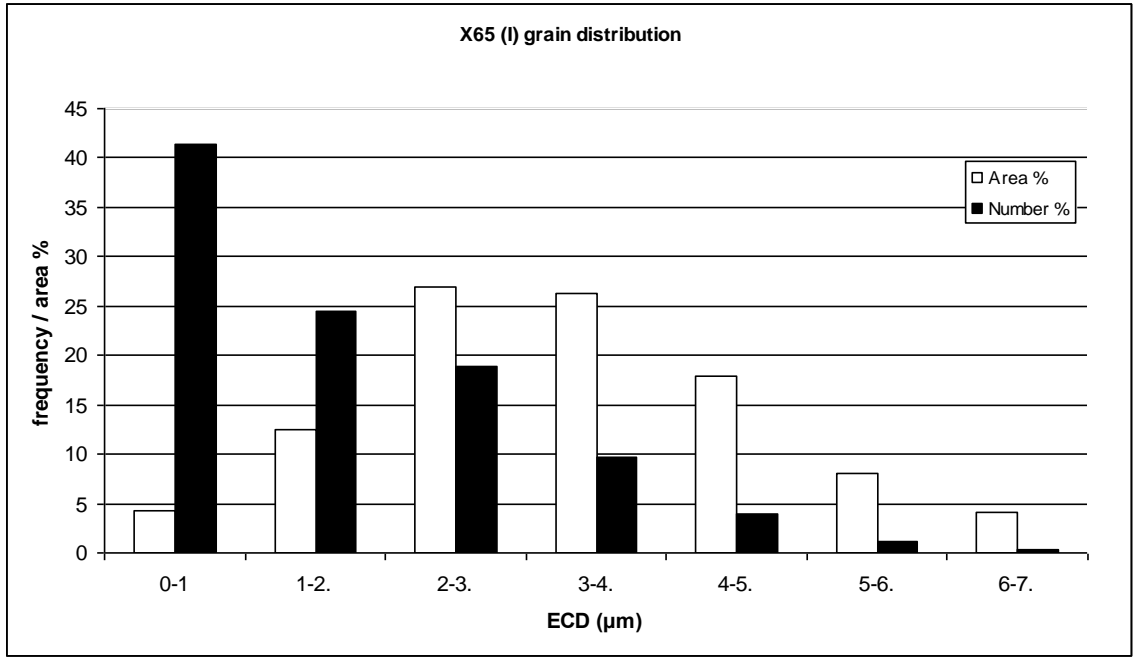
Figure 4.24 X65 (I) area % and frequency % distribution of grain sizes at the quarter
thickness position
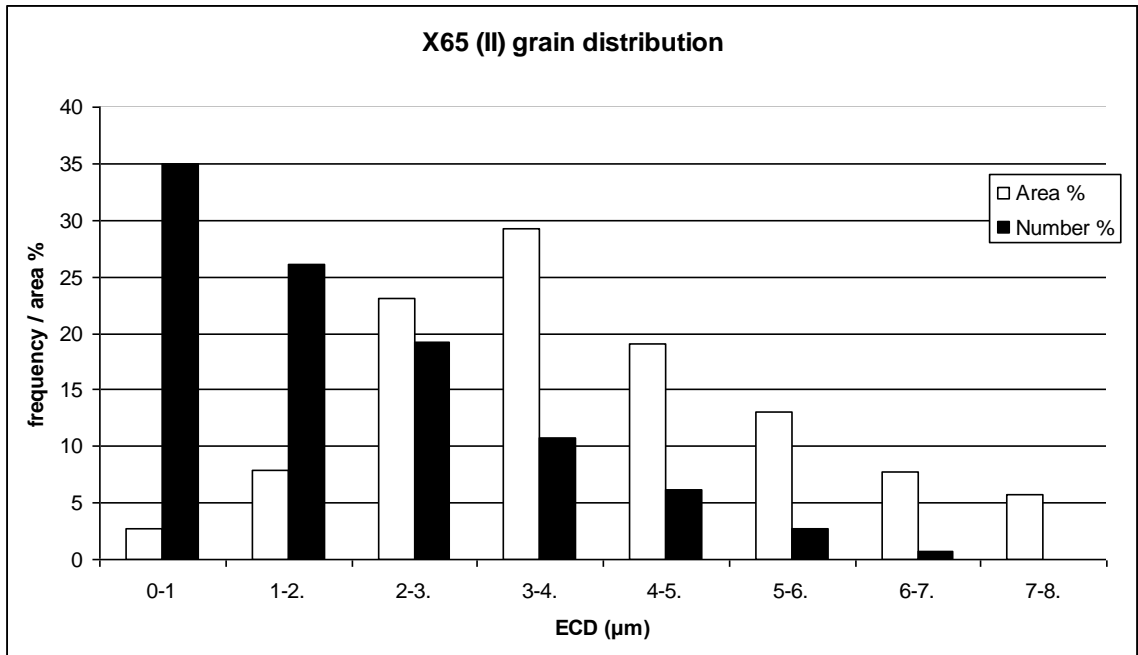
Figure 4.25 X65 (II) area % and frequency % distribution of grain sizes at the quarter
thickness position

4.3.2   X65 (III)

Figure 4.26 presents a micrograph of X65 (III) steel, which shows a dual phase microstructure predominantly consisting of ferrite and pearlite generally in bands parallel to the rolling direction. The average grain size determined for X65 (III) was 2.3 μm and the grain size distribution is shown in Figure 4.27.
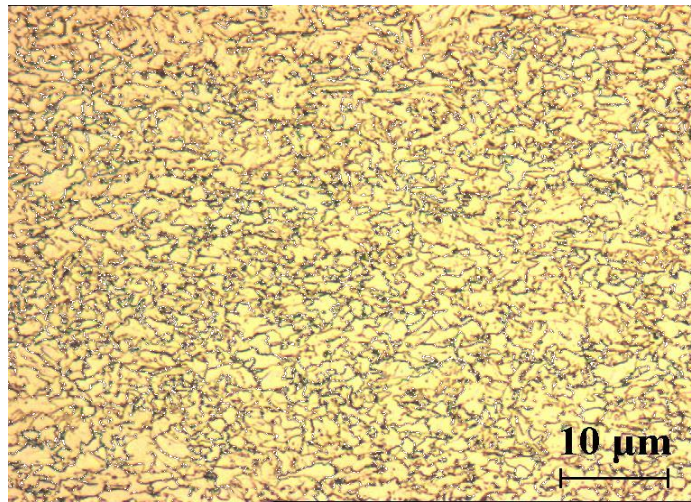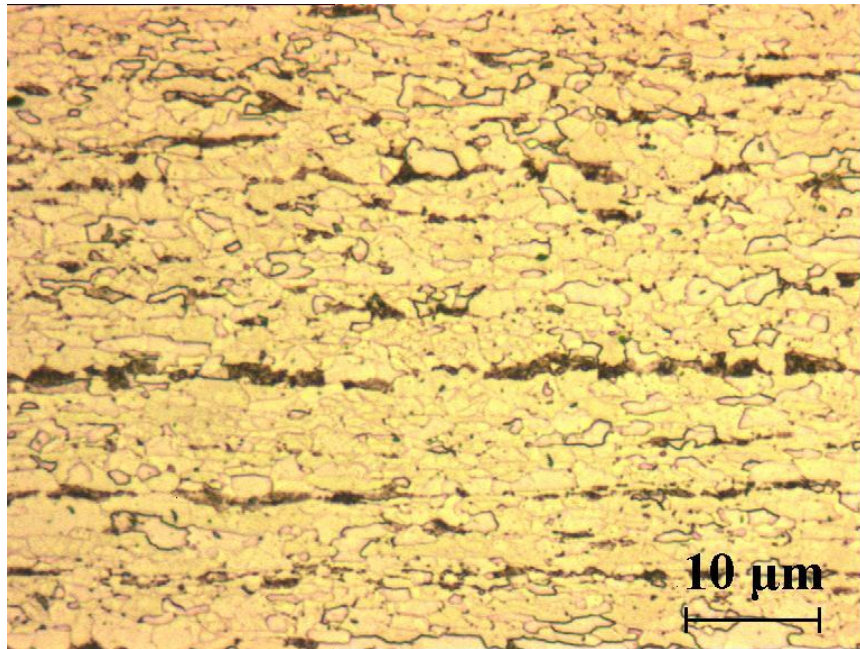

Figure 4.26 Optical micrograph of X65 (II) in the longitudinal orientation taken from the quarter thickness position
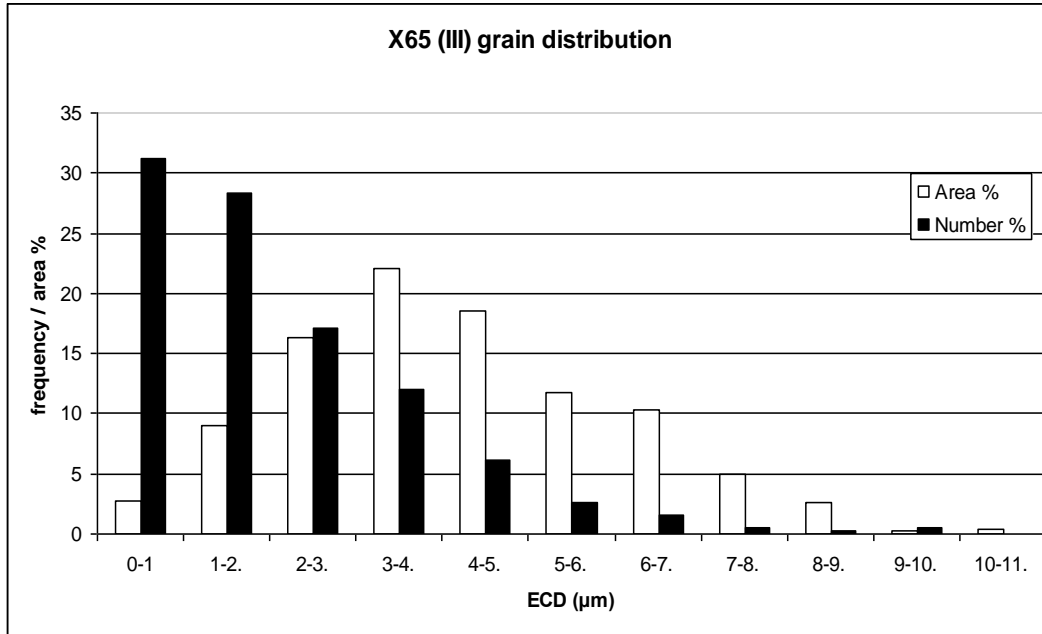
Figure 4.27 X65 (III) area % and frequency % distribution of grain sizes at the quarter

thickness position

The area % of pearlite in X65 (III) was variable through the thickness of the plate as

shown in Table 4.7. The pearlite percent was found to increase towards the central region

of the plate. This is consistent with previous studies [35] as carbon gets segregated during

the solidification process towards the centre region of the plate, which is the last part to

solidify prior to the rolling process.

Table 4.7 Pearlite % through plate thickness

Position	Pearlite %	
	Average	Standard deviation
Sub-surface	4.4	1.3
Quarter thickness	8.9	3.1
Mid-thickness	17.0	1.7

4.3.3   X80 (I) & (II)

X80 (I) consists of a predominantly ferrite microstructure, the ferrite grains had an elongated morphology suggesting that the steel may have been deformed below the non-recrystallisation temperature (Figure 4.28). The microstructure for X80 (II) is presented in Figure 4.29. It is generally similar to that of X80 (I), however the grain structure is more refined and a larger proportion of grains are equiaxed. Both steels contain second phase regions that appeared to be martensite austenite (MA) islands, which were frequently observed and generally had a small size (typically less than 1 µm) as shown in Figure 4.30. Confirmation that the second phase was MA constituent was carried out using TEM by obtaining diffraction patterns from the austenite phase and the ferrite, the orientation relationship was determined to be $[111]_\alpha$ // $[110]_\gamma$ (Figure 4.31). Both X80 steels showed degeneration of the MA constituents after annealing for 4 hours at 350 $^\circ$C as would be expected as martensite and retained austenite transform into ferrite and cementite (Figure 4.32).
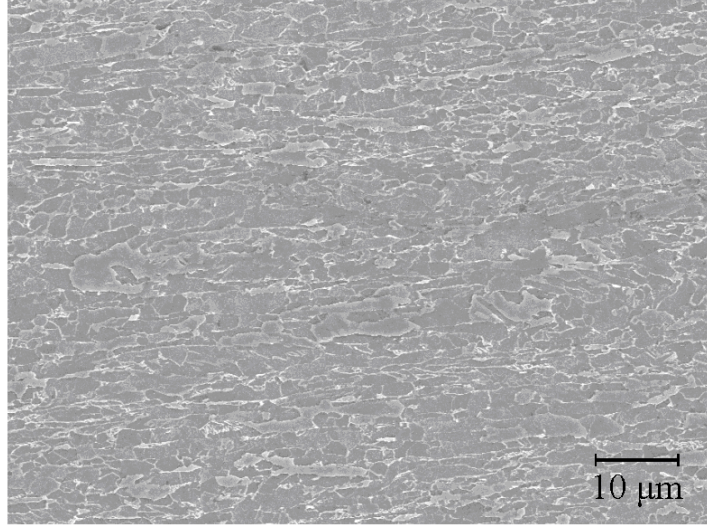
Figure 4.28 SEM micrograph X80 (I) in the longitudinal orientation taken from the
quarter thickness position
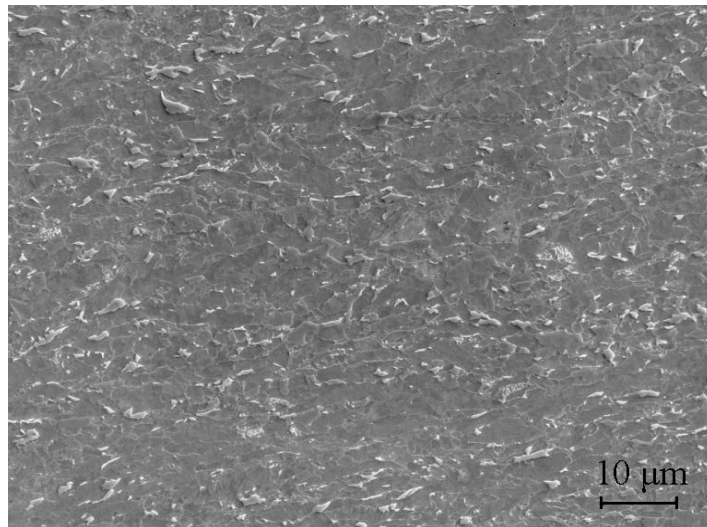
Figure 4.29 SEM micrograph X80 (II) in the longitudinal orientation taken from the
quarter thickness position
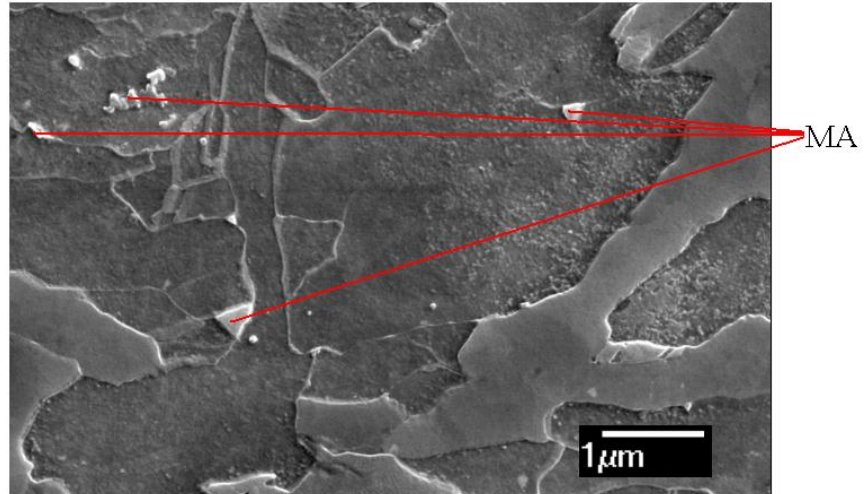
Figure 4.30 Typical SEM micrograph of MA Islands in X80 (II) distinguishable from ferrite grains by their blocky / jagged morphology
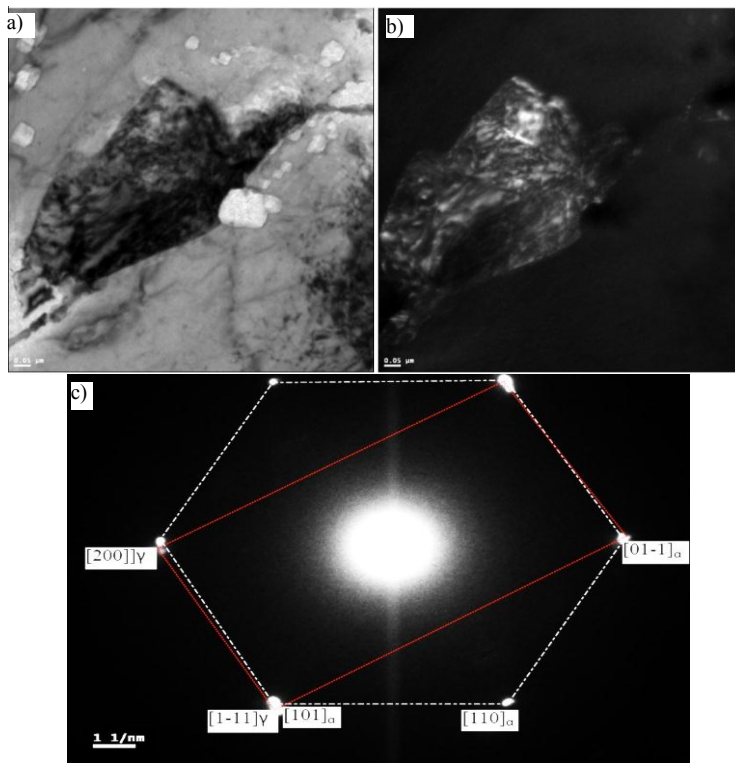
Figure 4.31 MA island in X80 (I) showing (a) bright field image (b) dark field image of retained austenite region within MA island taken from the [200] diffraction spot c) diffraction pattern $[111]_\alpha$ // $[110]_\gamma$

The percentage of MA islands was measured to be 8 % in X80 (I) and 12 % in X80 (II), which correlates well with the increased amount of Ni and Mn in X80 II, known to stabilise austenite.
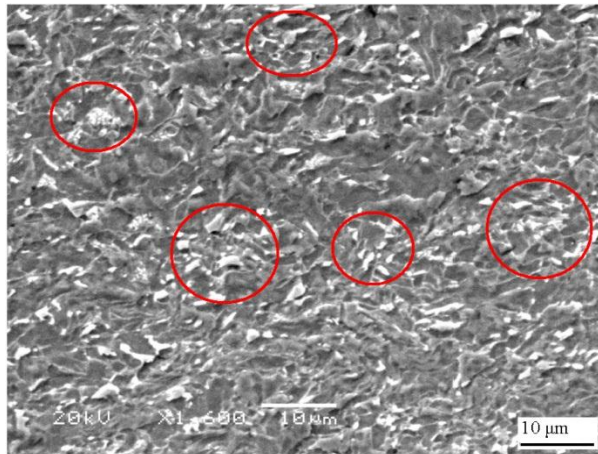
Figure 4.32 X80 (II) microstructure of X80 (II) after annealing for 4 hours at 350 $^{\circ}$C showing classical degeneration of MA which has lost its blocky morphology and started to spheroidise

X80 microstructures were too fine scale to accurately determine their respective grain sizes using the same automated image analysis on optical micrographs as for the X65 grade steels so the linear intercept method was used to determine the grain size of all studied steels. This method showed consistently lower grain sizes for all steels than optical measurements as shown in Table 4.8.

EBSD was used to determine the effective grain size (by considering boundaries with misorientations between 1.9^o and 15° for low angle boundaries, and above 15°, for high angle boundaries) in X65 (I), (II) and X80 (I). The measured ECD for boundary misorientations $< 1.9^o$ was larger than that recorded using optical micrographs for all three steels, possibly due to some very small angle boundaries between grains ($< 1.9^o$) being revealed by etching. However the order of the grain size for the steels was consistent (i.e. X65 (II) consistently had the largest grain size). Increasing the misorientation threshold angle from 1.9° to 15° increased the grain sizes by around 2 - 3 μm. This value is likely to give a more realistic representation of the contribution grain size has on toughness [179] and strength [173-176] and therefore effective grain sizes for X65 (III) and X80 (II) were determined by multiplying the linear intercept grain sizes by a factor of 2.7. Micrographs comparing the effective grain sizes in X65 (I) and X65 (II) are presented in Figure 4.33 and Figure 4.34 and a summary of the measured grain sizes is listed in Table 4.8.
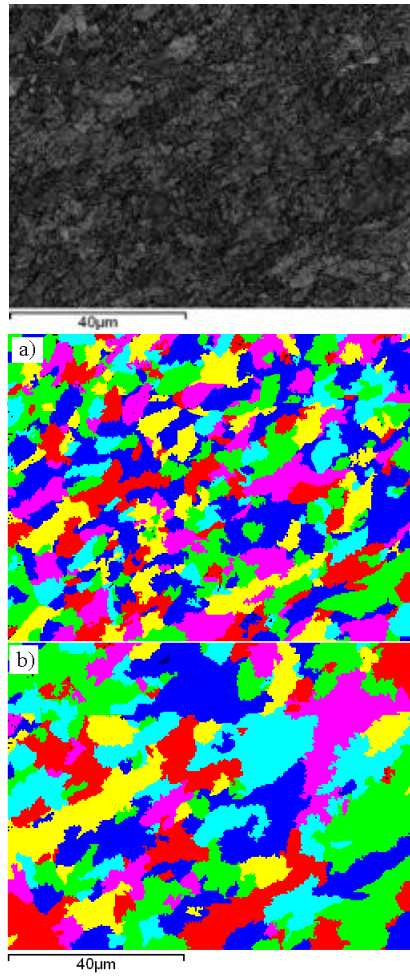
Figure 4.33 EBSD images showing an increase in average grain size X65 (I) with the grain angle misorientation threshold set at (a) 1.9^{o} and (b) 15°
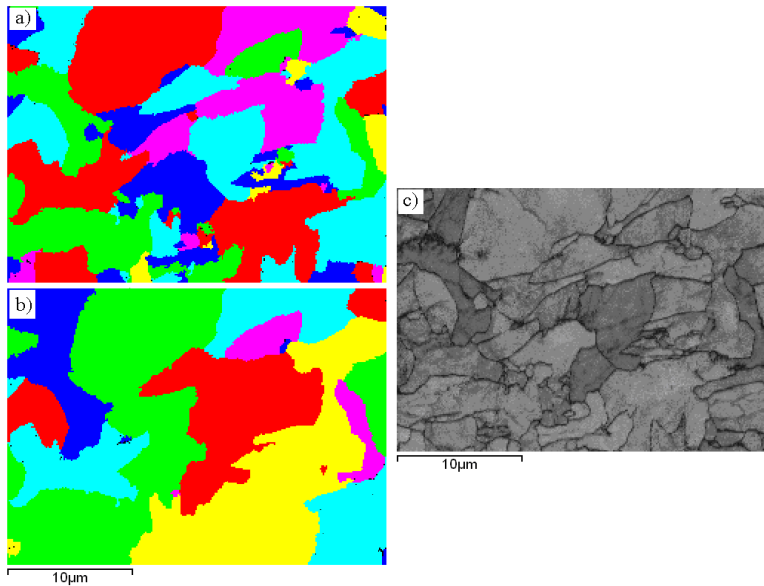
Figure 4.34 Close up EBSD micrograph of X65 (II) showing the difference in grain size with boundary misorientation set at (a) 1.9^o and (b) 15°. Comparing the grain structure set at 15° misorientation against the SEM image in (c) individual grains / grain boundaries revealed by etching which do not contribute significantly to the strength of the material can be identified

Table 4.8: Average grain sizes measured using ECD, linear intercept and EBSD methods with misorientation of 1.9 and 15° (for EBSD)

Steel	Average grain size (µm)			
	Akiovision 4.6.3 average ECD	Linear intercept	EBSD	
			$(1.9^o$ misorientation)	$(15^o$ misorietnation)
X65 (I)	1.9	1.8	3	5
X65 (II)	2.1	1.8	3.3	6
X65 (III)	2.3	2.1	-	6.2
X80 (I)	Not measured	1.4	2.6	4.5
X80 (II)	Not measured	1.6	-	4.3

4.4   Analysis of dislocations (TEM)

4.4.1   Dislocation densities

The dislocation density was analysed for all steels in the as-received condition and in specimens compressed to 0.02 and 0.04 strain to determine the evolution of dislocation density with plastic deformation.

The dislocation density increased in all specimens with an increase in pre-strain and a significantly higher dislocation density was observed in all conditions for both X80 grade specimens compared to the X65 grade steels. The dislocation structure varied significantly between the high Ni bearing (X65 (II) and X80 (II)) and low / non Ni bearing steels (X65 (I), X65 (III) and X80 (I)) for the as-received and 0.02 strained samples (and will be presented in depth later), which has not been previously reported in literature for HSLA steels. Therefore the analysis of dislocations has been split into two sections; the first giving a quantitative analysis of the dislocation densities between grades and the second detailing the differences in dislocation structures observed in the Ni / non-Ni bearing steels.

The dislocation density values are summarised in Table 4.9. X65 (III) had the lowest average dislocation density of all studied steels (2.2 x 10^{14} m^{-2}) in the as-received condition consistent with pearlite (present in this steels microstructure) being a diffusional transformation product. X65 (II) had the highest dislocation density of all

three X65 grade specimens (3.5×10^{14} m^{-2}). The dislocation density for X65 (I) was measured to be 2.9×10^{14} m^{-2}. Dislocation density measurements for the X65 grade steels in the as-received condition are as expected for the microstructures present (assuming similar TMCR schedules with all deformation carried out above A_{R1}) i.e. bainitic microstructures typically achieved during accelerated cooling schedules are displacive transformations which explains the higher dislocations densities compared with that of X65 (III) and bainitic ferrite / granular bainite has been observed to have higher dislocation densities than AF microstructures from the volume displacements during transformation from austenite [180].

Both X80 (I) and (II) steel strips in the as-received condition were found to have slightly different initial dislocation densities (5.8 and 5.4×10^{14} m^{-2} respectively), which were higher than in the X65 grade as–received plates. Both X80 steels have a fine ferrite structure with MA constituents, which are generally associated with a high dislocation density in adjacent ferrite grains [52, 181]. The X80 grade material was produced as strip that was hot coiled, therefore the cold uncoiling would be expected to result in some plastic deformation, which may contribute to the high dislocation density seen in these steels.

After 0.02 strain the dislocation density increase was smallest for X65 (I), 0.02 strain is still within the Lüders strain region for this steel and a small increase in dislocation density is expected during this stage of deformation consistent with previous reports on steels which exhibit Lüders strain behaviour [112]. A larger increase in dislocation

density for X65 (II) and (III) strained to 0.02 strain was observed which is just before the onset of stage II work hardening in these steels. The increase in dislocation density for X65 (III) is more rapid than that in X65 (II) which can be attributed to a high number density and volume fraction of fine VC precipitates (< 50 nm) acting as obstacles and sources for a Frank-Read mechanism to operate at this stage [181-183].

X80 grade specimens showed significantly higher dislocation densities than X65 steels at 0.02 strain and in the case of X80 (I) areas of high dislocation density were observed (discussed later in section 4.4.1) comprising of clusters. Areas adjacent to these clusters had a relatively low dislocation density suggesting that dislocations are being absorbed into the high density areas consistent with the evolution of cellular structures. The average measured dislocation density in X80 (I) after 0.02 strain was 7.3×10^{14} m^{-2}. In X80 (II) after 0.02 strain the dislocations adopted a more linear structure and a marked increase in dislocation density was observed as they became more homogeneously distributed throughout ferrite grains; the calculated average dislocation density was 7.7×10^{14} m^{-2} and hence a greater increase in dislocation density was observed from 0 - 0.02 strain in X80 (II) compared with X80 (I).

The 0.04 strained material revealed the start of cell structures and clusters in X65 (III) (as discussed later) and dislocation density increased significantly to 9.5×10^{14} m^{-2}. It was not possible to determine from the micrographs any influence that fine particles had on the dislocation structure as they could not be observed in the areas of high dislocation density. All steels showed evidence of increased dislocation interaction with obstacles

and other dislocations leading to an increase in dislocation density (discussed in Chapter 2.2.1). The dislocations were generally more homogeneously distributed throughout the microstructure in agreement with the onset of stage II work hardening. X65 (II) showed an increase in dislocation density in a more homogeneous fashion, discussed in the next section, and was measured to be 9.1 x 10^{14} m^{-2} in ferrite grains which did not contain cell structures.

X80 (I) showed the highest dislocation density at this stage with heavily deformed grains and cell walls frequently observed throughout the foils. Cell structures were also observed in X80 (II) but far less frequently than in X80 (I), accurate determination of overall dislocation densities was problematic at this stage given the chaotic arrangement of dislocations. The higher dislocation density / increased cell structure in X80 (I) is in agreement with the dislocation generation rate being higher for steels containing a higher number density of fine particles (as is the case with X65 (III)).

Table 4.9 Measured dislocation density in all studied steels for as-received (AR), 0.02 and 0.04 compressive strain conditions

Condition		Average dislocation density x 10^{14} m^{-2}									
		X65 (I)		X65 (II)		X65 (III)		X80 (I)		X80 (II)	
AR	min	0.9		1.9		1.2		4.2		3.4	
	max	3.6	**2.9**	5.2	**3.5**	3.5	**2.2**	7.6	**5.8**	7.2	**5.4**
0.02 strain	min	1.4		3		3.4		4.5		4.1	
	max	5.3	**3.5**	6.8	**4.6**	7	**4.2**	cell	**7.3**	cell	**7.7**
0.04 strain	min	5		4.2		6.5		6.3		5.1	
	max	9.2	**6.2**	cell	**9.1**	cell	**9.5**	cell	**cell**	cell	**cell**

4.4.2 Dislocation structures

TEM investigations revealed dislocations to be present in areas with high number densities of fine VC precipitates (< 5 nm) (Figure 4.35 a). TEM analysis also revealed unexpected results for X65 (II) and X80 (II); these specimens contain higher levels of Ni (████████ wt % respectively) compared to the other three steels (<0.05 wt %) and demonstrated ordered low energy dislocation structures in the as-received and 0.02 strained conditions in contrast to higher energy dislocation structures in the low-Ni bearing steel, as described below.

In the as-received condition, dislocations in the low-Ni bearing steels were randomly distributed throughout the grains, often pinned or interacting with the small precipitates

present. The vast majority of these dislocations were in a high energy state i.e. showed evidence of bowing (Figure 4.35 b). Dislocation - dislocation interactions were observed mostly in X65 (I) (Figure 4.35 c), dislocations were generally quite widely separated in X65 steels with long line lengths in the region of 200 – 600 nm frequently trapped and pinned by particles (Figure 4.35 d). Dislocation clusters were seen throughout X80 (I) (Figure 4.35 e) which could arise from plastic strain during uncoiling [184,185] and therefore having a more evolved dislocation structure than the X65 steels. Areas adjacent to MA constituents had high numbers of dislocations in the region of 7×10^{14} m^{-2} frequently in clusters in contrast to a more evenly spaced arrangement of dislocations with measured density in the region of 4×10^{14} m^{-2} away from MA constituents (Figure 4.35 f).
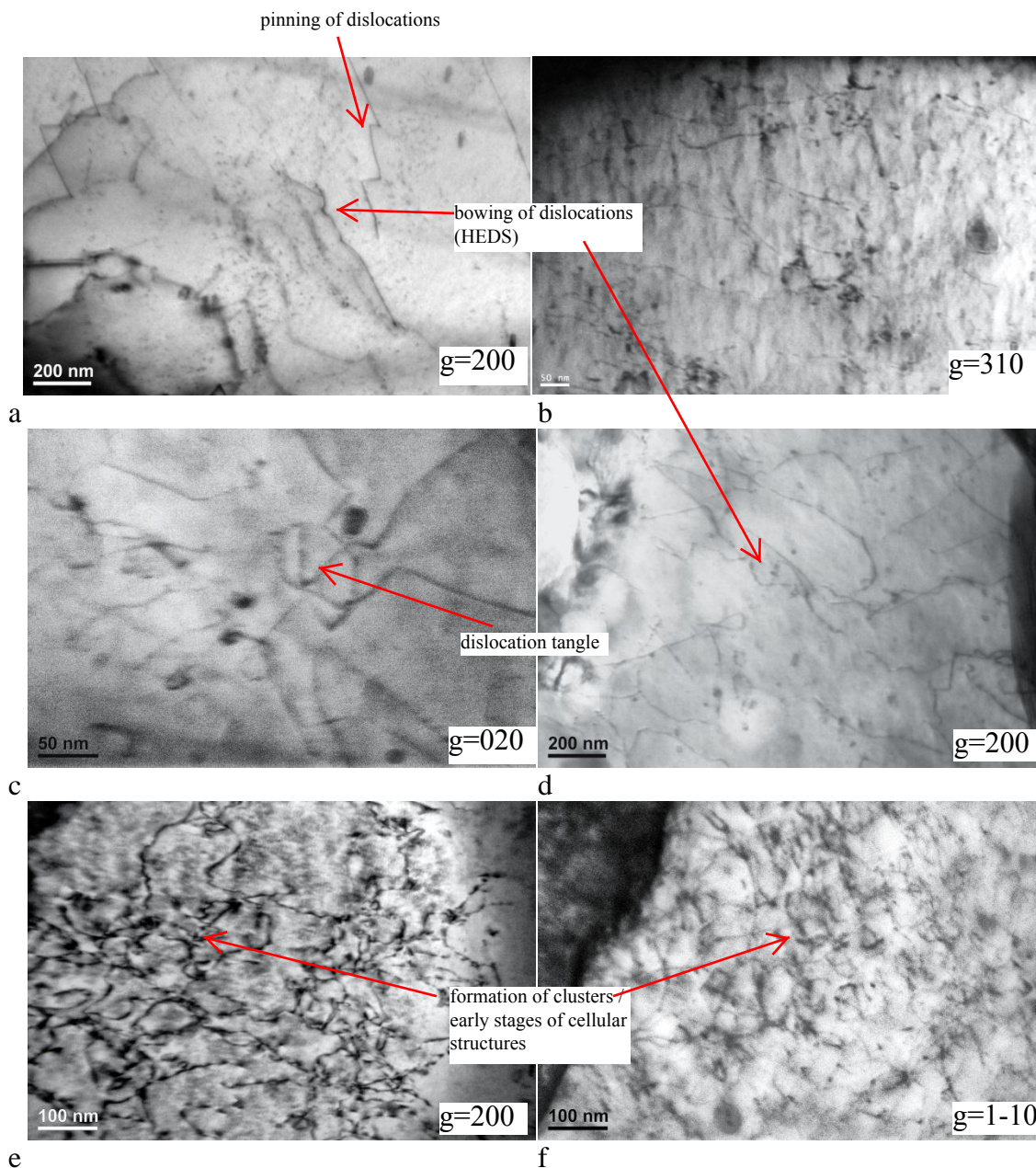
Figure 4.35 TEM micrographs showing dislocation structure in as-received condition for (a) X65 (III) dislocations accumulating in areas containing high number density of VC, (b) typical dislocation distribution in X65 (I), (c) dislocations in X65 (I) showing a tangle and interaction with Nb(C,N) particles, (d) typical dislocation distribution in X65 (III) showing evidence of dislocation pinning, (e) X80 (I) dislocation structure clusters and high dislocation interaction rate with other dislocations and (f) ferrite grain adjacent to MA island showing high dislocation density and pinning of precipitates

As deformation is introduced (0.02 strained materials) dislocations become less homogeneously dispersed in the non-Ni bearing steels; the dislocations become concentrated into areas of parallel running dislocations, tangles (Figure 4.36 a) and regions of high and low dislocation density within ferrite grains can be identified (Figure 4.36 b). Dark field images of the dislocation structure within MA regions show a chaotic structure of high dislocation density (Figure 4.36 c) and ferrite regions adjacent to MA appear to contain dislocations in relatively straight sets which can be distinguished further away from the interphase boundary where spacing between dislocations increases (Figure 4.36 d). Areas of X65 (III), which had high number densities of VC precipitates, showed high dislocation densities (Figure 4.36 e).

For the high Ni-bearing steels the dislocation structures in the as-received and after 0.02 strain conditions were frequently observed to have sub-structures much different to those observed in the non-Ni steels. Typically these were identified as LEDS observed throughout grains in the form of parallel, straight line dislocation networks, arrowheads and misfit dislocations surrounding particles > 50 nm and near grain boundaries (Figure 4.37, a-c).

.
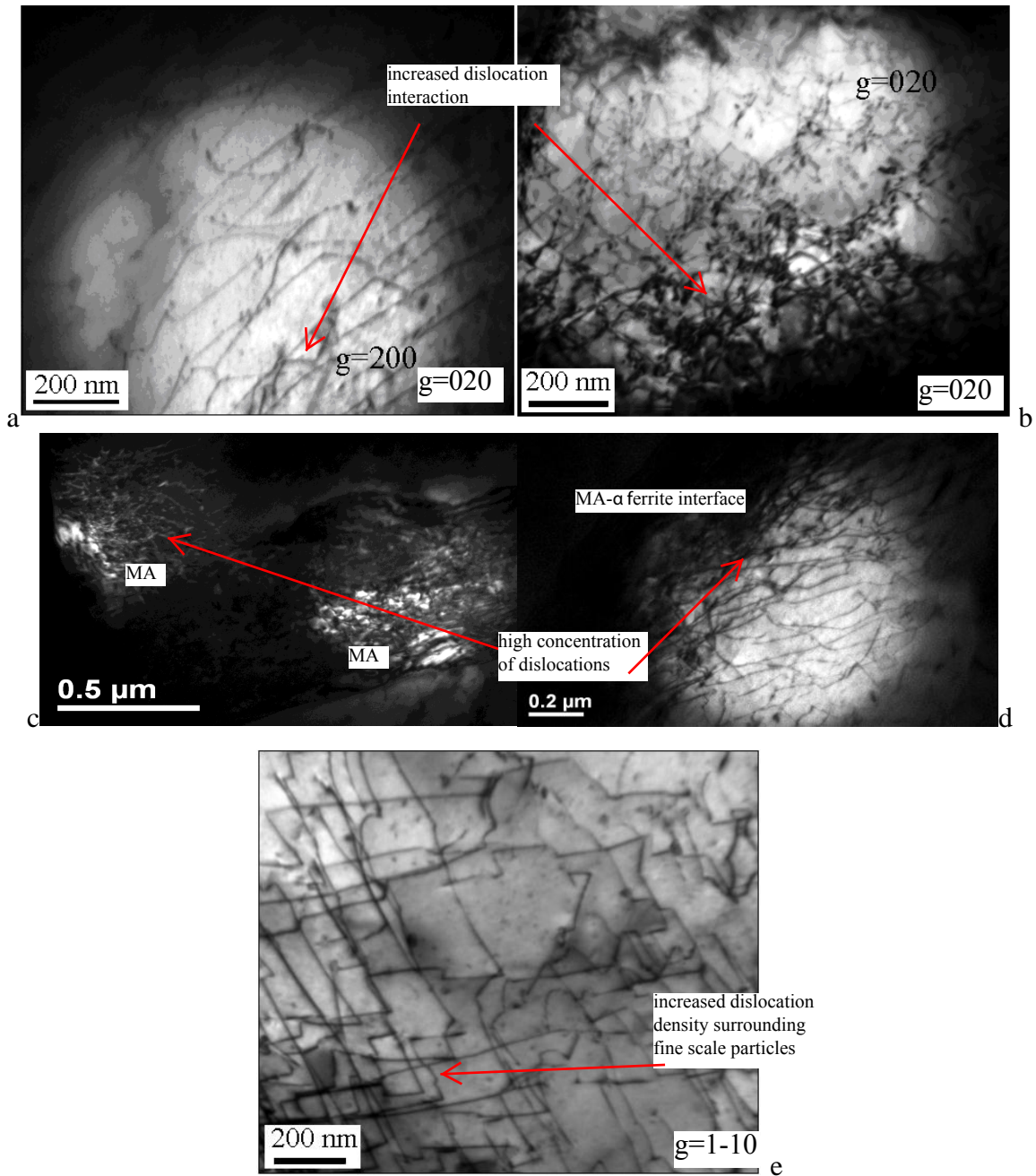
Figure 4.36 TEM micrographs of low-Ni steels after 0.02 strain (a) increased dislocation-dislocation and dislocation-particle interaction in X65 (I), (b) X80 (I) inhomogeneous distribution of dislocations as cell structures and clusters start to develop within ferrite region, (c) dark field image of high density dislocation structure within MA constituent, (d) high dislocation density in the ferrite region immediately adjacent to MA island becoming more widely dispersed in relatively parallel sets in X80 (I) and (e) X65 (III) showing high dislocation density within the immediate area of VC particles
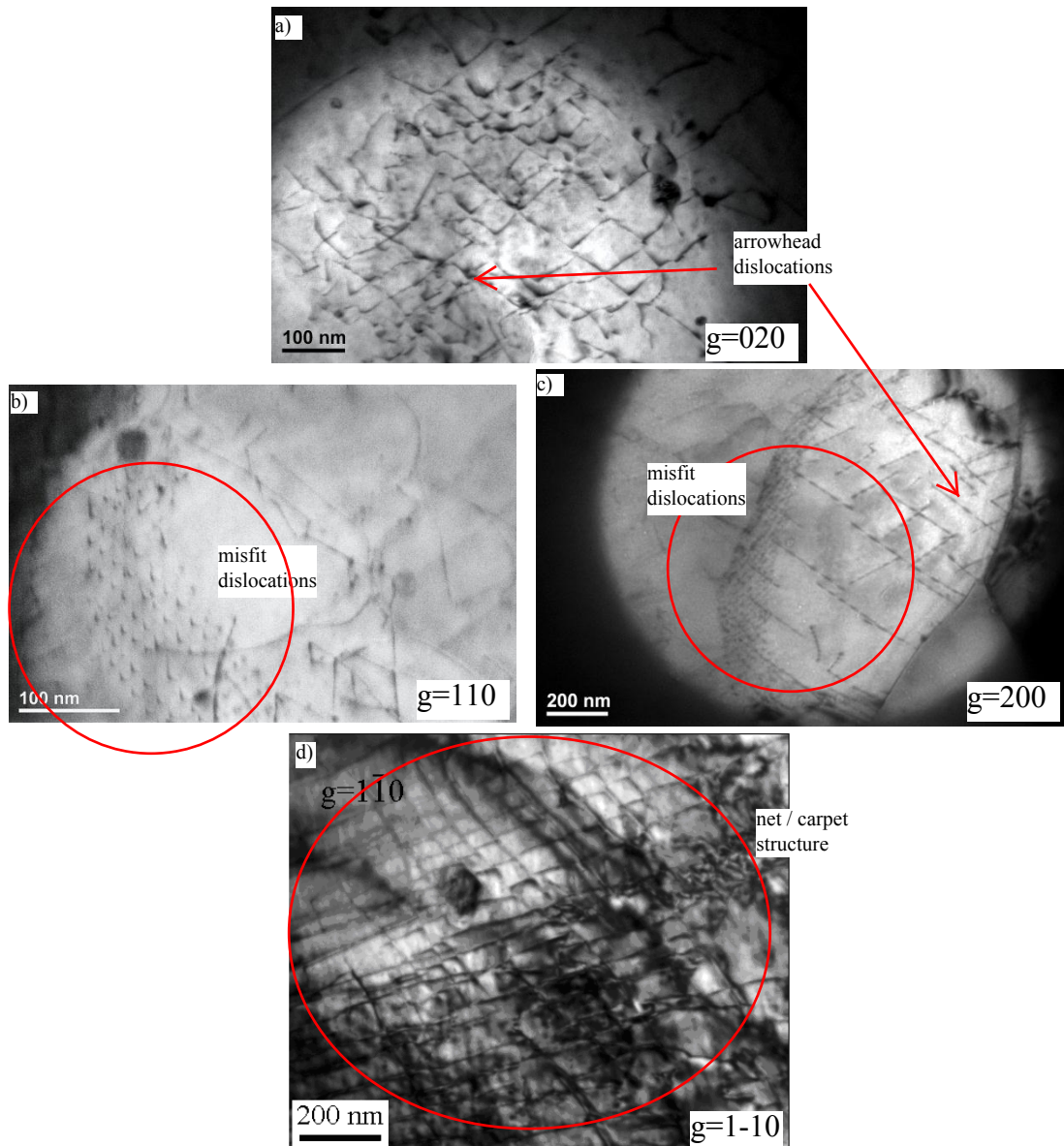
Figure 4.37 TEM micrographs of high Ni steels in the as-received condition showing (a) misfit dislocations / arrowhead configurations near to grain boundaries in X65 (II), (b) misfit dislocations surrounding a (Nb,Ti)(C,N) particle in X80 (II), (c) arrowhead and misfit dislocations near grain boundary in X80 (II) and (d) dislocations in X65 (II) surrounding a coarse (Ti,Nb)-rich carbo-nitride particle arranged in a net structure

After 0.02 strain regular misfit structures were apparent in the form of dislocation walls / pile-ups near to grain boundaries (Figure 4.38 a and b). Dislocation pile-ups were also observed in X65 (II) against large particles in the region of 40 nm in diameter (Figure 4.38 c).
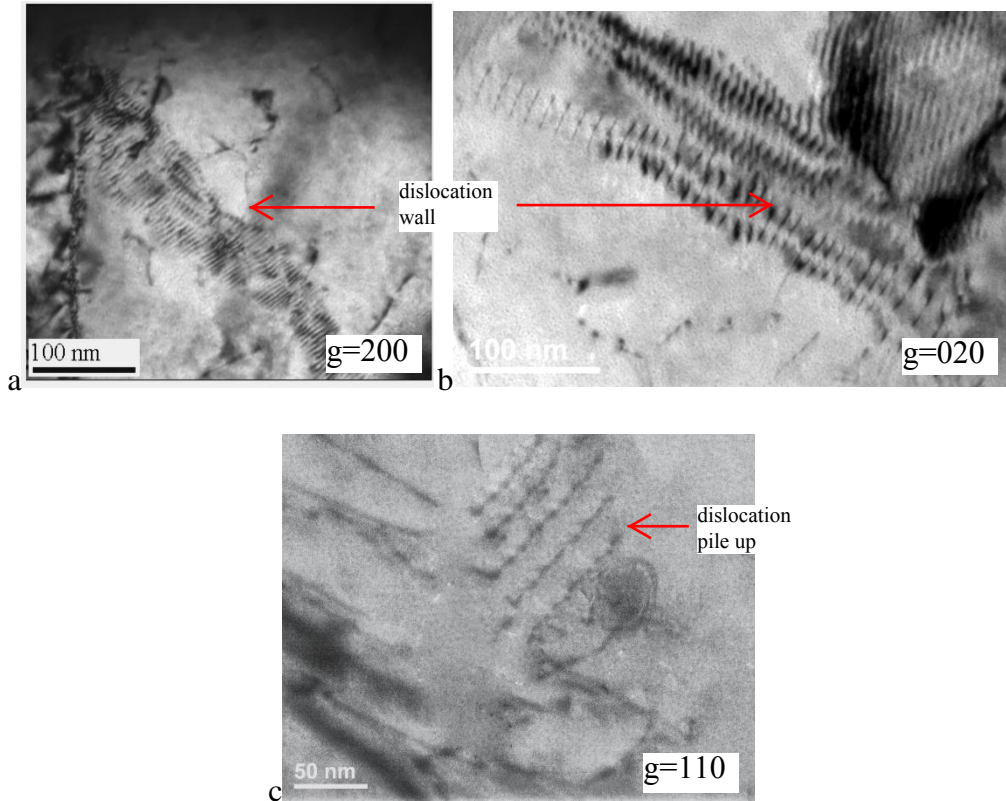
Figure 4.38 TEM micrographs showing (a) dislocation wall near obstacles and grain boundaries in X65 (II) after 0.02 strain, (b) dislocation wall structure within a ferrite grain in X80 (II) after 0.02 strain and (c) dislocation pile-up against large Nb-rich particle in X65 (II) after 0.02 strain

TEM imaging of the vast majority of thin foils showed previously regular structures (0 – 0.02 strain) in non-Ni steels to assume high energy states, i.e. tangles and bowing between other dislocations and particles as seen for X65 (III), after application of increased strain levels (0.04), Figure 4.39 a. Advanced low energy cellular structures were seen to develop in both X80 grade steels after 0.04 strain (Figure 4.39 b and c) with regions of ferrite showing high and low densities of dislocations within the grains. Early onset of cell structures formations was also observed in X65 (II) and (III) but not as frequently or to the same degree of development as in the X80 grade materials. X65 (I) still showed a relatively homogeneous distribution of dislocations in grains with lower dislocation densities, but dislocations in grains with higher densities were seen in large clusters which would have arisen from intersecting dislocations forming nodes which generation sources for new dislocations that quickly become immobilised as per the Frank-Read mechanism (Figure 4.39 d).
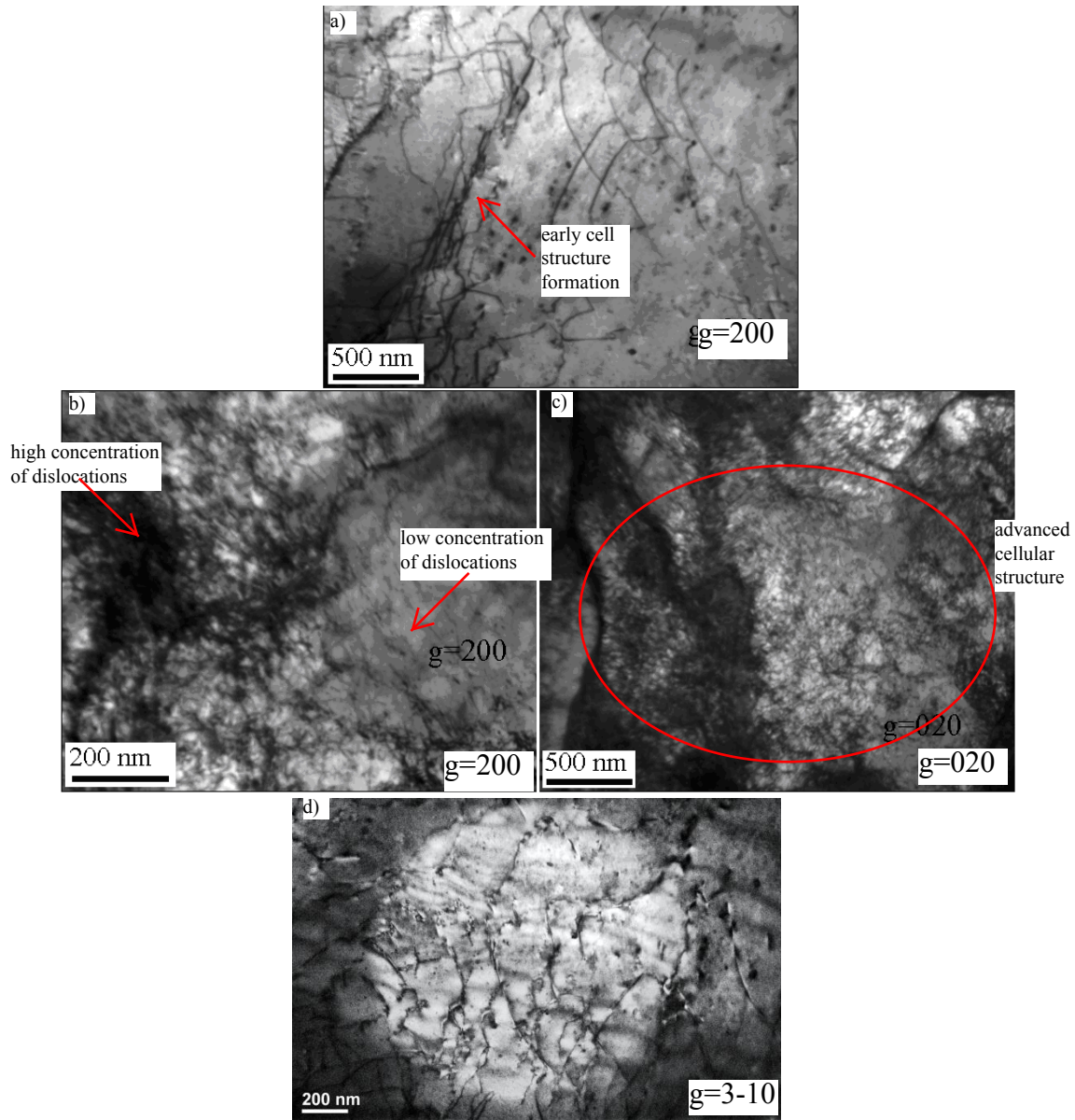
Figure 4.39 TEM micrographs after 0.04 strain (a) X65 (III) accumulation of dislocations in the early stages of cell wall development, (b) advanced cellular structure development in X80 (II) showing a high concentration of dislocations within the cell walls and areas of low dislocation density in the adjacent area, (c) ferrite grain in X80 (I) showing a checkerboard pattern of cellular structures and regions of high and low dislocation density and (d) clustering of dislocations / early stages of cell structure development in a deformed region of X65 (I)

4.4.3 Dislocation / particle interactions

The majority of dislocation / particle interactions were of the Orowan-type in nature (with the exception of pile-ups observed in the Ni-bearing steels, Figure 4.38 c). Frequent examples of pinning and trapping of dislocations were observed throughout the deformation strain range with Nb-rich particles as small as 12 nm (Figure 4.40 a).

Shearing of particles was not directly observed, and dislocations encountering carbides smaller than 5 – 10 nm in diameter were frequently observed in a low energy state (i.e. relatively straight) which would suggest a cutting mechanism is present for this type of interaction. Bowing of dislocations was observed when interacting with particles > 10 nm in diameter in X65 (III) (Figure 4.40 b) which suggests that the effective particle diameter for blocking dislocations is possibly slightly smaller for VC than for NbC (> 10nm and > 12 nm respectively)
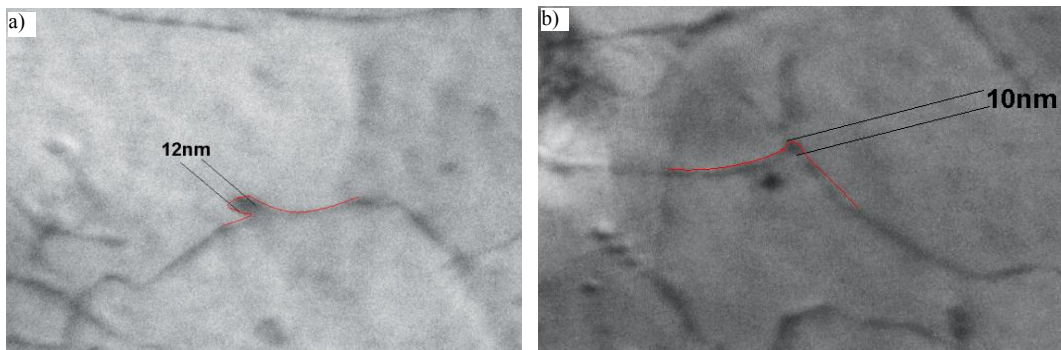
Figure 4.40 TEM micrographs in as received condition showing (a) masking of NbC precipitate in X80 (I) and (b) bowing of dislocation pinned against a 10 nm diameter VC particle in X65 (III)

From TEM micrographs it is possible to measure the average number of interactions with particles per dislocation, which is summarised in Table 4.10. Average dislocation length increases with strain for all studied specimens and these interact with more obstacles as slip continues through the steel matrix, raising the stress. Ni containing specimens had the smallest measured dislocation lengths and the largest average dislocation lengths were recorded in X65 (I) and X65 (III), which have the lowest measured dislocation densities.

Table 4.10 Dislocation-particle interaction parameters for particles > 50 nm

Condition	Steel				
	X65 (I)	X65 (II)	X65 (III)	X80 (I)	X80 (II)
Average Dislocation length per micrograph (nm)					
AR	197	114	243	178	154
0.02 strain	254	139	265	264	236
0.04 strain	319	Not measured	412	cell	cell
Average number of particle interactions per dislocation (measured)					
AR	2	2	4	4	3
0.02 strain	3	5	8	6	6
0.04 strain	not measured				

5 Mechanical behaviour during cold deformation

5.1 Tensile tests

The stress strain curves for the X65 steels are presented in Figure 5.1 a-c. Upper and lower yield points were observed in X65 (I) and (II) but not for X65 (III). X65 (II) and (III) specimens exhibited little to no work hardening / Lüder's strain up to 0.025 strain before the onset of stage II work hardening. X65 (I) demonstrated Lüders banding up to 0.032 accompanied by an apparent decrease in yield stress with increase in strain before work hardening occurred. Once work hardening occurs X65 (I) and (II) showed the highest rate of work hardening and only stage II was apparent up to approximately 0.045 strain. TEM studies showed the dislocation density to increase during Lüder's straining for all three X65 grades (1.1 and 2.0 x10^{14} m^{-2} for X65 (II) and (III) respectively). In the case of X65 (III) a rapid increase in dislocation density is expected due to the number of potential interaction sites from VC particles. A lesser increase in X65 (II) may be attributed to glissile dislocations observed in bainitic phases [135]. X65 (I) showed a very small increase in dislocation density (0.6 x 10^{14} m^{-2}) from 0 – 0.02 strain probably due to the lower number density and volume fraction of particles which give rise to greater dislocation mobility during early stages of deformation.

X65 I

a
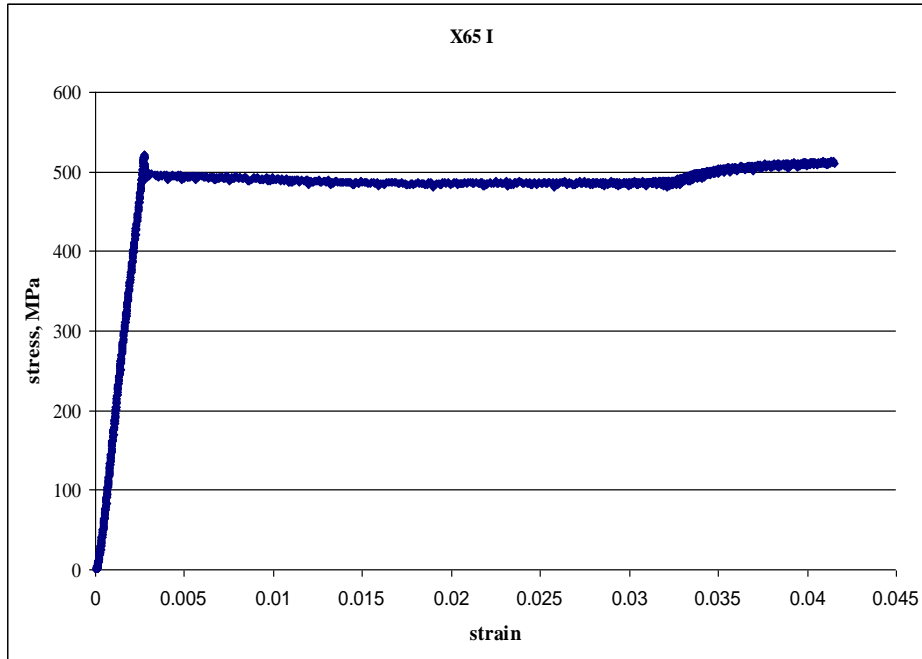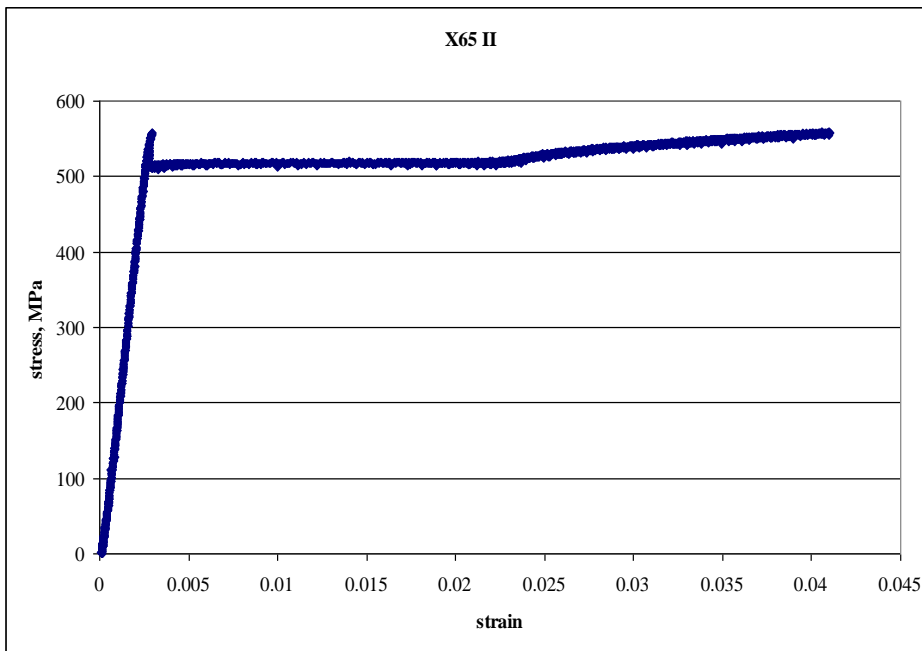
X65 II

b
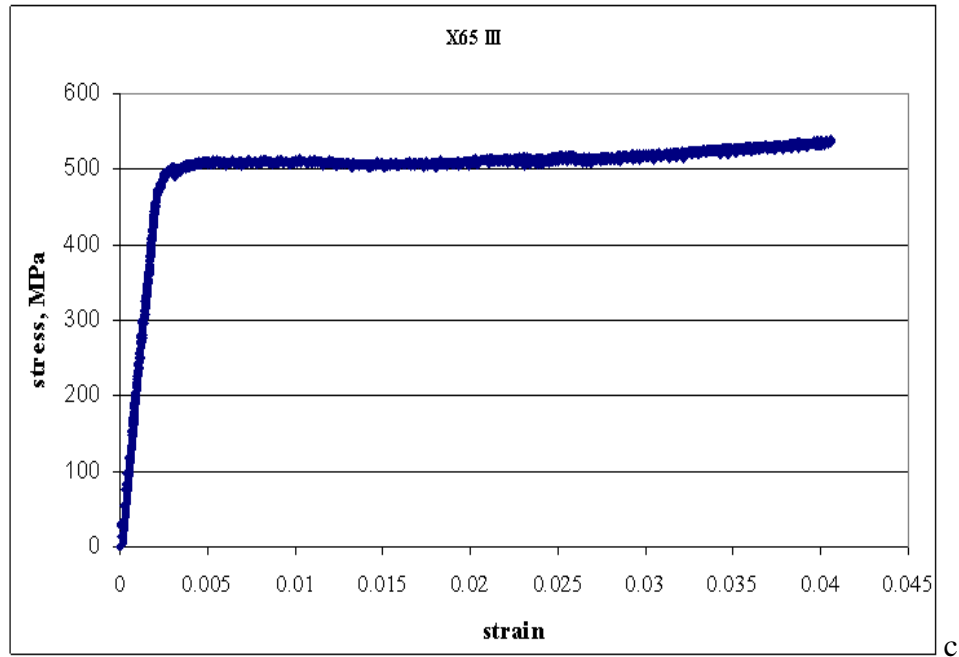
Figure 5.1 Tensile stress strain curves for (a) X65 (I) (b) X65 (II) and (c) X65 (III)

The stress strain behaviour for the X80 specimens is shown in Figures 5.2 a and b. Both steels demonstrated a very small period of transient hardening after yield which lasts for approximately 0.005 strain. A roundhouse curve shape is exhibited as is common for other steels containing MA constituents [166]. Three stages of work hardening are apparent from the curves - the first stage occurs immediately after yielding and is short lived. At 0.01 strain stage II work hardening can be observed and after 0.03 strain parabolic hardening occurs as stage III sets in. The higher rates of hardening are in good agreement with their higher dislocation densities than X65 grades and greater number densities of particles present in the microstructure, the onset of parabolic / stage III hardening is also in good agreement with the onset of cellular structures [85] observed in TEM.
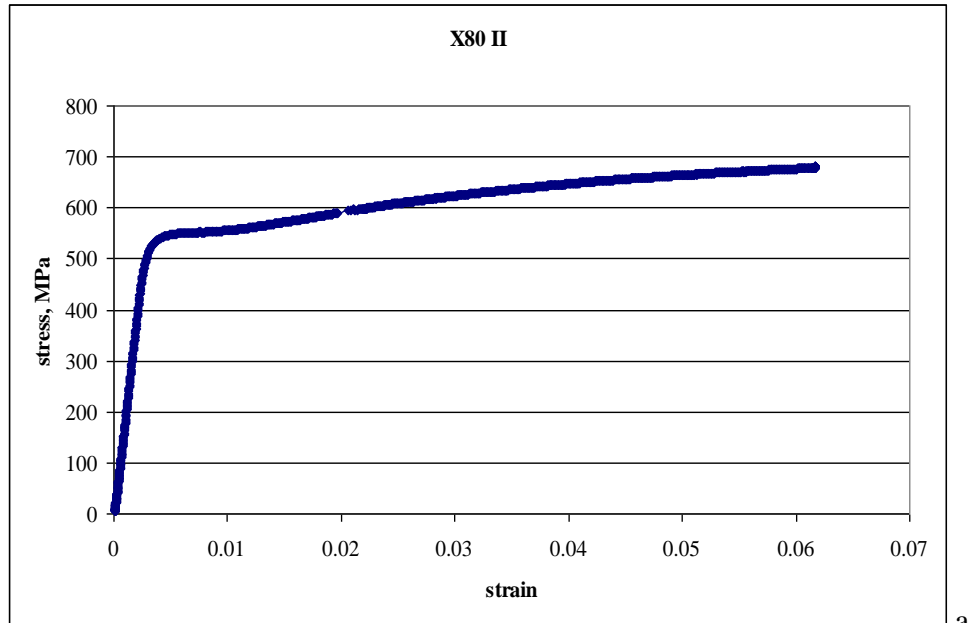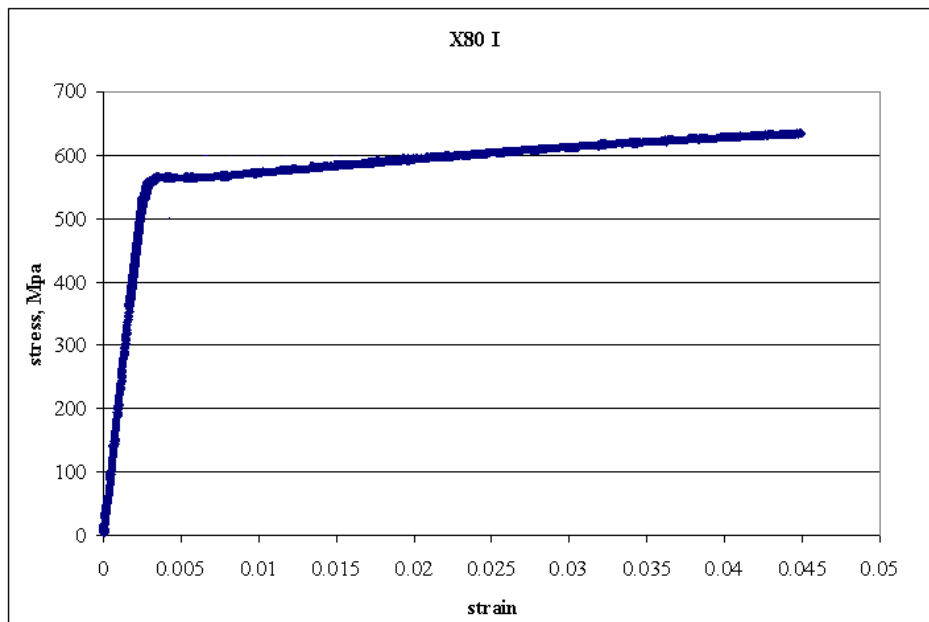
Figure 5.2 Tensile stress strain curves for (a) X80 (I) and (b) X80 (II)

5.2 Compressive stress strain curves

For most of the steels in this study the compressive stress strain behaviour differed slightly from the tensile plots and are shown in Figure 5.3 a-e. Strength differentials for the steels were calculated using equation (24):

$$SD = 2(\sigma_c - \sigma_t) / (\sigma_c + \sigma_t) \tag{24}$$

Where σ_c = compressive yield stress and $\sigma_{t} $ = tensile yield stress.

Stress differential and work hardening behaviour parameters are presented in Table 5.1, below. The Lüders strain region finishes in X65 (I) earlier in compression than tension (0.026 and 0.032 strain respectively) and the stage two work hardening rate n increased from 0.23 in tension to 0.29 in compression. The difference in yield stress was < 3 MPa giving a stress differential (SD) of < 0.01.

X65 (II) showed a slightly higher stress differential of 0.019 due to a difference in yield stress of 10 MPa. Immediately after yield the initial work hardening rate n increased from 0.04 in tension to 0.10 in compression making the yield stress in compression and tension equal at 0.015 strain. Stage II work hardening was also higher increasing the stress at 0.04 strain by about 30 MPa in compression compared to tension. X65 (III) showed near identical behaviour from yielding to stage I work hardening, onset of stage II work hardening starts earlier in compression than in tension which resulted in a difference in stress of +23 MPa at 0.04 strain compared to the tensile stress strain data. Discrepancy is

also observed between the data provided for X80 grade materials which show lower yield stress values than reported by Arcelor Mittal. This can be attributed to the fact that the samples are taken at the quarter thickness region. This may not give a true representation of the steel plate which had a higher percentage of MA constituent at the mid-thickness region and also any prior work hardening at the sub-surface region which would have undergone greater levels of strain during uncoiling adding to the yield stress. X65 grade specimens did not show considerable difference to the data provided by Tata Steel and were within 10 MPa of the reported yield stresses. Previously studied commercial X65 grade steel plates have shown a variation of > 70 MPa between measured and reported yield stress values as seen in studies by Kostryzhev [35] and therefore the variation seen in X80 specimens is not unusual.

a

155

X65 (II)

b

X65 (III)

c

X80 (I)

d

156
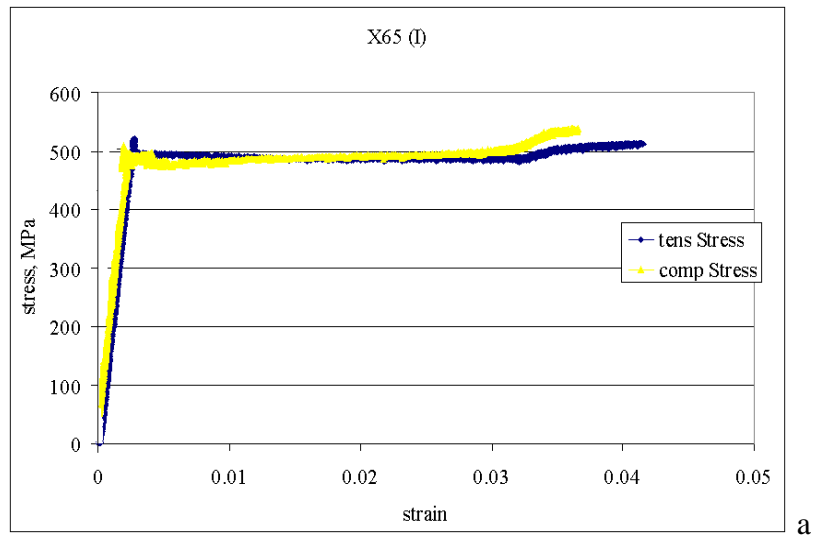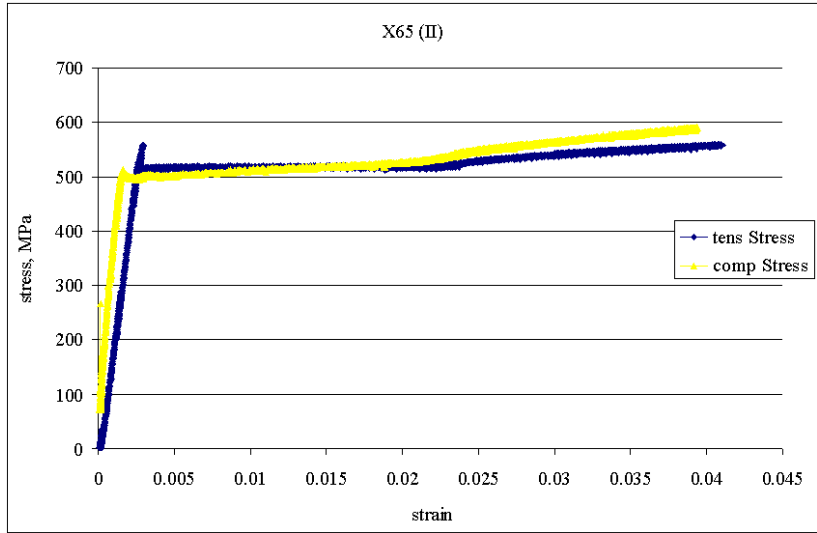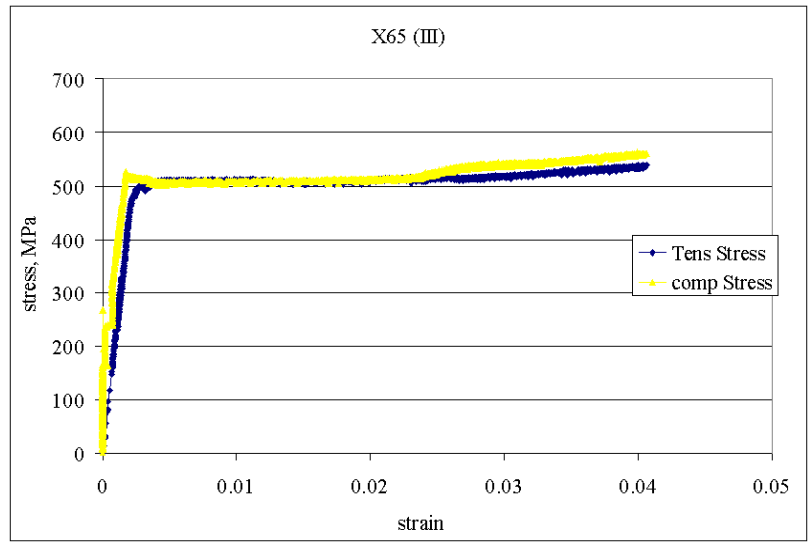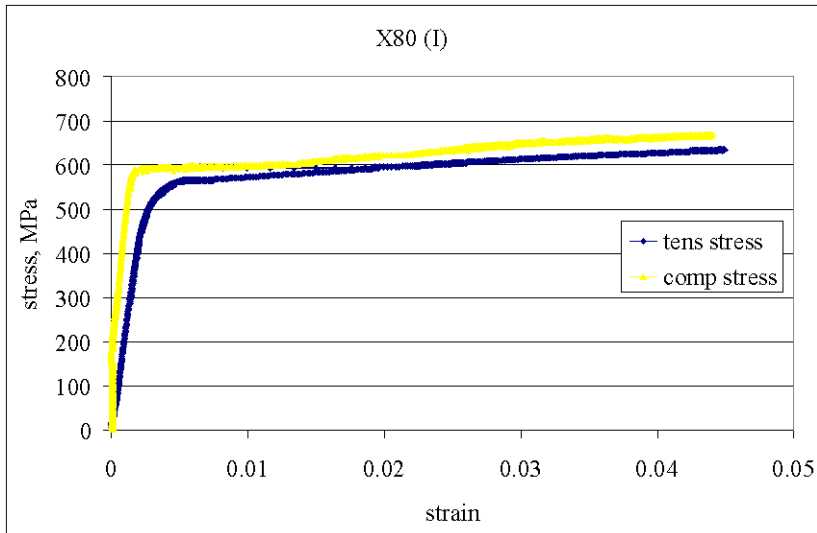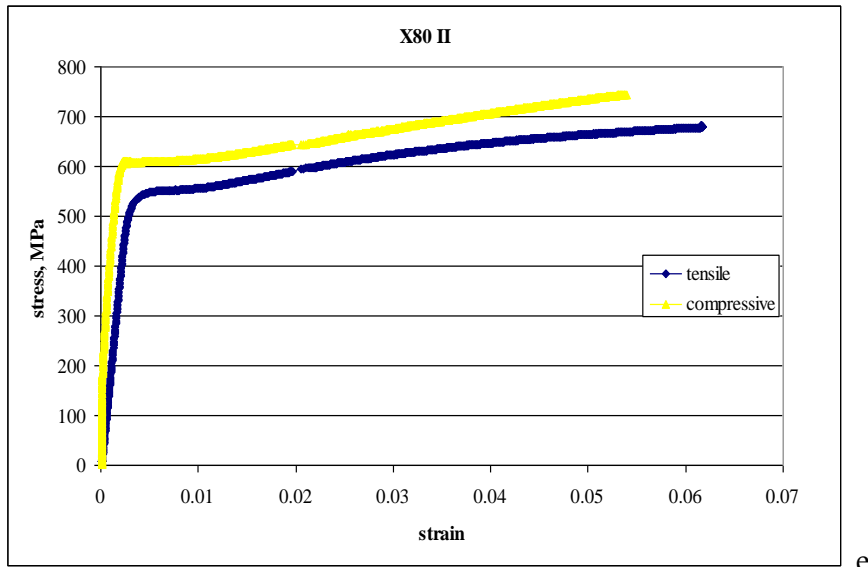
Figure 5.3 Tensile and compressive stress strain plots for (a) X65 (I) (b) X65 (II) (c) X65 (III) (d) X80 (I) and (e) X80 (II)

Table 5.1 Tensile and compressive mechanical properties from compressive and tensile curves

Steel	Tensile yield (MPa)	Compressive yield (MPa)	Strength differential (SD)	Tensile work hardening rate (*n*)			Compressive work hardening rate (*n*)		
				Stage I	Stage II	Stage III	Stage I	Stage II	Stage III
X65 (I)	499	496	-0.006	Lüders strain < 0.032	0.23	-	Lüders strain < 0.026	0.29	-
X65 (II)	509	499	-0.0198	0.04	0.23	-	0.10	0.26	-
X65 (III)	505	501	-0.0079	Lüders strain < 0.02	0.23	-	0.05	0.23	-
X80 (I)	560	590	0.0521	0.03	0.28	0.24	0.03	0.28	0.26
X80 (II)	550	610	0.1034	0.05	0.31	0.26	0.05	0.32	0.30

X80 materials showed a significant difference in compressive and tensile yield stresses; in compression they were 30 MPa and 60 MPa higher than in tension for X80 (I) and X80

157

(II) respectively giving significantly higher SD values than the X65 grade materials. After yielding, initiation of stages (I) and (II) of work hardening were very similar in terms of strain range and work hardening rate but onset of stage (III) in X80 (II) was not observed until 0.035 strain and at a higher rate than in tensile testing (0.26 and 0.30 respecitvely), which gives rise to a stress difference of around 70 MPa between the compressive and tensile plots at 0.04 strain. During stages (I) and (II) the difference in stress is approximately 60 MPa for X80 (II) i.e. the same as the difference in yield stress which would be expected for simliar work hardening rates and strain onset values. For X80 (I) the difference in stress between compressive and tensile plots through the range of strain is 30 MPa, which again, would be expected from the difference in yield stress and similar work hardening rates.

A difference between the compressive and tensile yield stresses has been observed in dual phase steels with up to 25 % martensite and greater strength differences were reported for steels with elongated martensite morphology [186]. It was suggested that the residual stresses are imposed upon ferrite during the formation of martensite from austenite due to the volume differences on transformation. The volume change upon the formation of martensite increases with carbon content and tensile residual stresses are imposed on ferrite and compressive residual stresses remain in the martensite, these residual stresses affect the yielding behaviour in tension and compression as the total volume of ferrite which is plastically activated is lower for tensile loads than for compressive loads [186]. Deformation tests conducted in this research would suggest that volume fraction of martensite plays a role in strength differences as MA constituents are

of similar morphologies in both X80 grade materials but greater yield stress and strength difference were exhibited by X80 (II) which contains the higher volume fraction (12 %) of MA constituents and the strength differences of 5 % and 10 % for X80 (I) and X80 (II) are in reasonable agreement with reported strength differentials of 14 % for steels containing 25 % martensite by Watt et al. [186].

Another reason for the anistropic behaviour demonstrated in the X80 grade specimens could be due to the shape of the tensile yield curve which demonstrates continuous yielding giving a roundhouse shape - similar to those seen in reverse Bauschinger tests. The higher yield stresses given from the compressive curves showed a much more defined yield point as would be expected from low carbons steels which would suggest that the effect of coiling in the specimens has induced some degree of plastic deformation (in good agreement with high intial dislocation densities observed in TEM). Distribution of residual stresses have been shown as non uniform through thickness after the uncoiling process of steel sheet [187] and so the compressive forces imposed during uncoiling have already introduced back stresses to the specimens, aiding the reverse yield stress either in the form of masking of precipitates, dislocation annihilation or relief of high energy dislocation structures (as discussed in section 2.2.3).

X65 grade specimens which were not subject to coiling behave in a more isotropic manner - as the stress differential between the materials was substantially less than the X80 grade specimens. All X65 specimens have well defined yield points for tensile and compressive stress strain curves with the exception of X65 (III) which can be attributed

to a small amount of negative (compressive) residual stress present within the cementite phase after cooling [188].

A high rate of stage II work hardening for X80 (I) and (II) is short lived as parabolic hardening sets in before 0.04 strain which is attributed to the formation of cellular structures. Compression past this point was not carried out so it is not known whether cell size decreased with further strain or whether dislocation annihilation within cell interiors is the reason for the low rate of work hardening in these steels. X65 (III) showed the onset of cellular structures as seen in micrographs; these were at a fairly early stage of development which is in agreement with the end of stage II hardening. Areas with high numbers of VC precipitates frequently had a high number density of dislocations which showed interaction through pinning mechanisms at this stage, this was not accompanied by an increase in work hardening rate (between 0.02 – 0.04 strain) as might be expected from multiplication of dislocations and increased resistance to glide; an alternative explanation could be the dislocations have sheared out of their channels in between particles which has previously been observed in molybdenum crystals. Work by Kuhlman-Wilsdorf (1989) concluded the corresponding increase in dislocation mobility would cause parabolic hardening to occur [112]. Table 5.1 lists the mechanical parameters obtained from the stress strain curves. Parabolic hardening in X80 (I) and X80 (II) can be explained though prior deformation from coiling leading to a more evolved dislocation structure where cellular structures observed at 0.04 strain would cause transient hardening.

5.3 Hardness testing

The average macro hardness values for the five steels are shown in Table 5.2 and in the case of the three X65 grade steels, show only a weak correlation between hardness and grain size which is due to other microstructural factors affecting hardness. X65 (I) which has the most refined grain size for the X65 grade specimens has a comparatively lower hardness value than X65 (III) which had the coarsest grain size, it also shows a lower hardness value than X65 (II). Previous studies on acicular and bainitic microstructures in C-Mn-V microalloyed steels of similar compositions concluded that acicular microstructures showed a reduction in hardness compared with bainitic microstructures as is the case with X65 (I) and (II) which show predominantly acicular and granular bainite microstructures, respectively. X65 (III) has large additions of C, N and V which affect the hardness of the pearlitic region [188] and precipitation hardening of ferrite with increasing C content [190-192].

Despite having a much higher volume fraction of precipitates and presence of second phase pearlite, X65 (III) showed a lower Hv value than that of X65 (II). This could be explained by the smaller grain size and the higher dislocation density observed in X65 (II). The influence of fine carbides associated with VC in X65 (III) and their associated effect on the hardness will compensate for the low dislocation density. Although pearlite is inherently harder than ferrite it does not appear to influence the overall hardness of the X65 (III), which has also been observed in similarly studied steels [35].

The hardness of the X80 grade steels is, as expected, significantly higher than that of the X65 grade materials due to the refined grain size, higher predicted amounts of carbo-nitride phase and presence of MA as the second phase. X80 (II) has a high strength and hardness compared to X80 (I), which is probably mostly due to its higher MA content since its grain size is only slightly finer and it is predicted to contain slightly fewer carbo-nitride precipitates.

Table 5.2 Average macrohardness from the quarter thickness region and overview of microstructural properties

| Steel | Microstructural parameters | | | YS, MPa | Hv20 |
	EBSD / Effective Grain Size (µm)	Second Phase Constituent %	Carbo-nitride volume fraction (Thermo-Calc)		
X65 (I)	5	-	0.00065	496	183 ± 9
X65 (II)	6	-	0.00074	499	192 ± 5
X65 (III)	6.2	10 (pearlite)	0.00148	501	185 ± 5
X80 (I)	4.5	8 (MA)	0.00144	590	220 ± 4
X80 (II)	4.3	12 (MA)	0.00139	610	235 ± 8

Macrohardness was measured at 0.01, 0.02 and 0.04 compressive strain from interrupted tested samples (Figure 5.4) and showed hardness to increase with increasing strain. All steels showed a nearly linear trend of increase averaging 5 H_V per 1 % strain for X65 (II), X65 (III) and X80 (II). X80 (I) showed larger hardening increments of around 10 H_V with each strain increment of 0.01 than other deformed specimens; dislocation density measurements also showed large increases with increasing plastic strain for all specimens

between $1.1 - 2.3 \ 10^{14} \ m^{-2}$ with the exception of X65 (I), which showed an increase in dislocation density from $2.9 \times 10^{14} \ m^{-2}$ in the as-received state to $3.5 \times 10^{14} \ m^{-2}$ at 0.02 strain. When a large increase in H_V was observed (after 0.04 strain), outside of experimental scatter, an increase in dislocation density was also observed in the compressed specimens (to $\sim 6.2 \times 10^{14} \ m^{-2}$) which was a similar increase to that of the remaining steels compressed from as-received to 0.02 strain. From 0.02 to 0.04 strain dislocation density increase was $\sim 5.0 \times 10^{14} \ m^{-2}$ along with the onset of dislocation clusters and cellular structures. This also occurs at the same point on the stress strain curves where Lüders strain finishes and a high rate of work hardening occurs. For the other X65 grades, increase in macrohardness is largely linear across stages I and II and appears to be independent of sudden increases in work hardening rate.
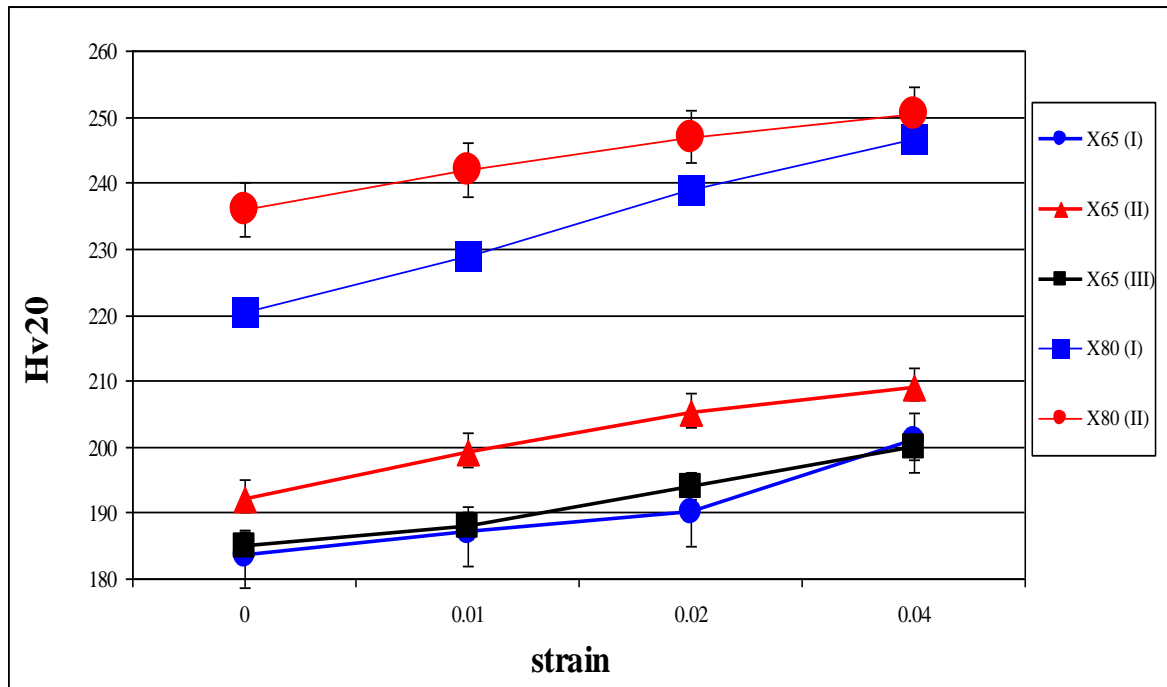
Figure 5.4 Macro-hardness values of studied steels with increasing strain

5.4 Reverse deformation tests

5.4.1 Reverse stress strain curves

All specimens were subjected to 3 separate forward-reverse loading schedules (Bauschinger tests) with 0.01, 0.02 and 0.04 forward pre-strains introduced to the specimens before reverse loading (described in Section 3.2 f). A Bauschinger effect was observed in all specimens i.e. the reverse yield point (on the second stress strain curve) is lower than the initial yield point due to work softening. The reverse stress strain curves for all pre-strain conditions are discussed in detail in this chapter and presented in Figures 5.6 a-e.
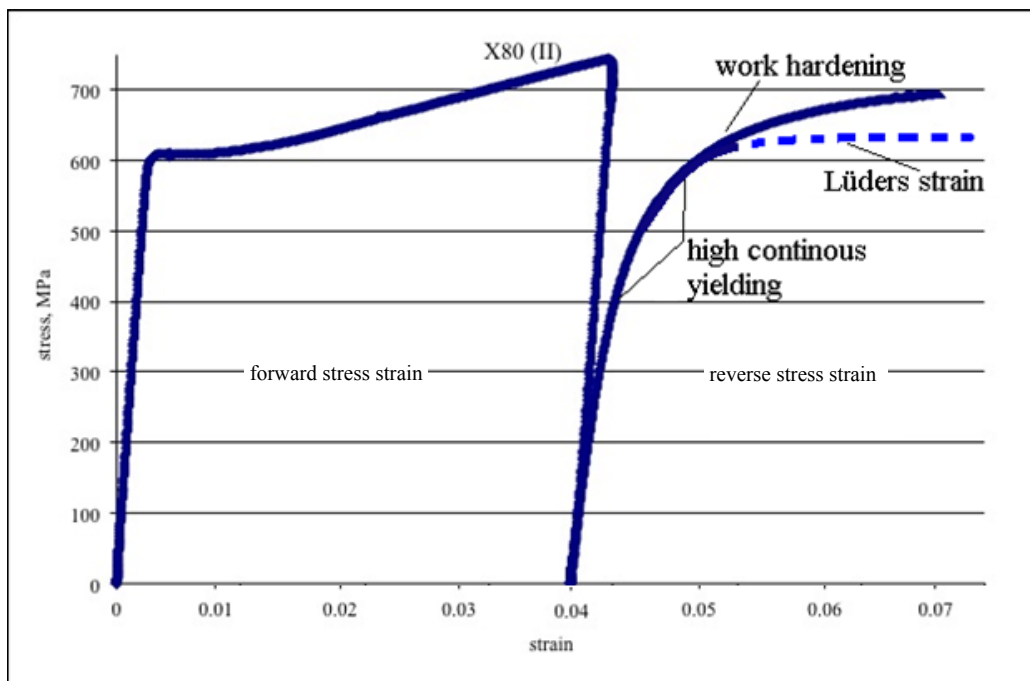
Figure 5.5 Typical reverse stress strain curve from the Bauschinger tests, this graph is for X80 (II) where a pre-strain of 0.04 was applied before reverse straining

All reverse stress strain curves experience a region of elastic strain followed by a region of high continuous yielding behaviour as characterised by a roundhouse curve which then leads to a region of low work hardening or Lüders straining.

The character of deformation stages past the reverse yield point is dependent on the initial microstructural features, mechanical properties and degree of forward pre-strain before reverse loading in the steels which has been reported in previous research [35]. The reverse stress strain curves are shown in Figures 5.6 a-e.

0.01 pre-strained specimens

After reverse yield, a stagnation in work hardening behaviour occurred in all X65 steels, in X65 (I) a period of decreasing stress was observed before Lüders strain, X65 (II) a distinct absence of work hardening after yielding was seen and in X65 (III) an extremely low rate of strain hardening was observed after continuous yielding behaviour finished. It was not possible to capture strain to failure of specimens due to the limitations of the strain gauge equipment but it is assumed that they would not recover i.e. work harden to any significant degree before failure based on similar reverse stress strain curves for low carbon steels in [35, 162]. Plateaus in reverse stress strain curves have been attributed to dislocation particle interactions, dissolution of dislocation sub-structures and saturation of back stress [144,109]. Dislocation substructures were not observed in X65 specimens for < 0.02 pre-strain ruling out the possibility of dissolution of cellular structures. Research by Kostryzhev [35] found that the plateau length increased with a decrease in dislocation density and decreased with an increase in the number of particle / dislocation interactions.

In the case of X65 (III) this holds true as there are a higher number of VC particles acting as potential interaction sites for dislocations and it displayed a lower initial dislocation density than other X65 grade steels in the as received condition. A reduction in reverse stresses during reverse loading (stagnation in reverse work hardening) was only observed during small strains < 0.01 in [35] and in the present study only seen in X65 (I) which has the smallest number of interaction sites in the form of precipitates. This would agree with [144] where dissolution of early dislocation interaction processes such as dislocation-particle bowing and pile-ups (albeit in a homogenously separated fashion) is responsible for stagnation in work hardening and, in the case of the X65 (I), could be the cause of reduction in stresses seen in the reverse stress strain curve.

After 0.01 pre-strain X80 specimens demonstrate roundhouse curves / continuous yielding behaviour during reverse loading up to 0.01 strain in the reverse direction from yield after which point they continue to work harden at a greater rate than seen in any of the X65 grade steels. This is consistent with them having a higher initial dislocation density and greater number of particle / dislocation interaction sites than for the X65 grade steels (with the exception of X65 (III)) and therefore less likely to undergo stagnation of work hardening during reverse loading.

0.02 pre-strained specimens

Following 0.02 pre-strain the parabolic / continuous yield behaviour increased from 0.07 strain in X65 (I) and X65 (III) to 0.01 strain after which the work hardening rate becomes constant (Table 5.3). None of the X65 specimens demonstrated Lüders behaviour or a

decrease in stress during reverse deformation and X65 (III) showed an increase in work hardening following reverse yielding compared with 0.01 pre-strain.

X80 (I) showed similar behaviour to that of X65 (III) i.e. increase in work hardening. The similarity in the discontinuous yielding makes this much easier to observe in Figures 5.6 c and d. X80 (II) showed a similar trend to X65 (II) in that there is no recovery / increase of the reverse yield stress with increased pre-strain. This is shown most clearly in X80 (II) where the reverse stress strain curve for 0.02 is almost identical to that of the 0.01 pre-strained sample. Both these steels have the higher wt % additions of Ni and show very little to no change in reverse flow behaviour with increased pre-strain.

0.04 pre-strained samples

Samples pre-strained to 0.04 strain continued the trends shown in the 0.02 pre-strained samples. The non-Ni bearing steels demonstrated increased work hardening rate in the reverse direction and Ni-bearing steels showed similar reverse deformation curves for 0.02 pre-strained samples (in the case of X65 (II)) and near identical reverse stress strain deformation behaviour in X80 (II) for all pre-strained conditions. This trend has not previously been reported in the literature and when compared against the TEM studies on dislocation arrangements suggest a strong connection between the influence on Ni content on evolution of dislocations and subsequent reverse deformation behaviour.

a

b

X65 (III)

c
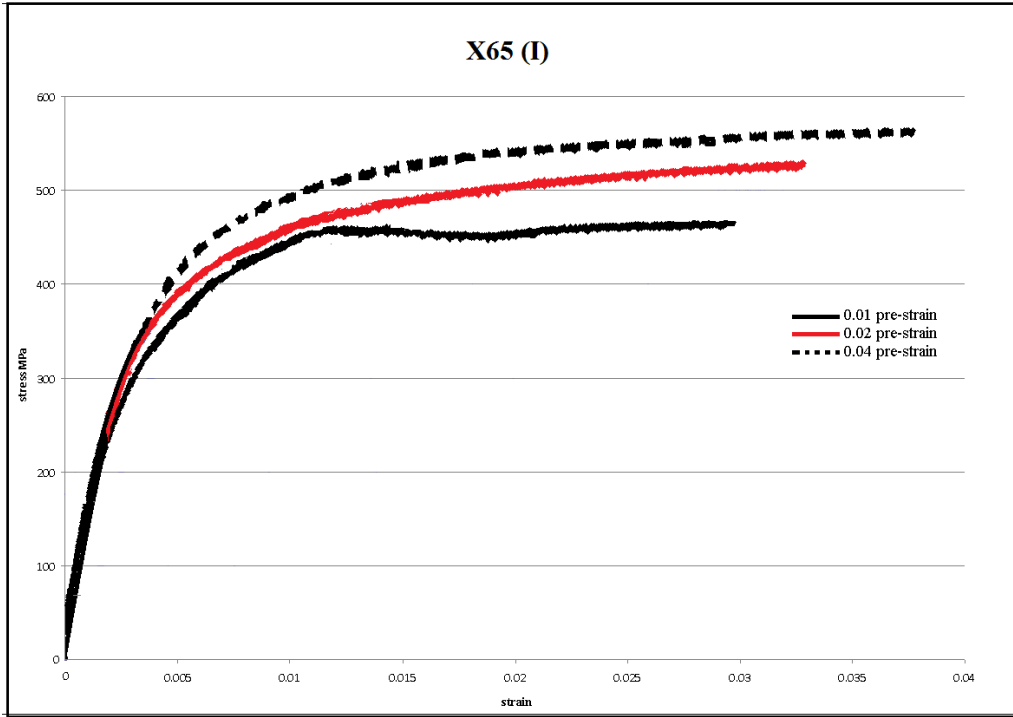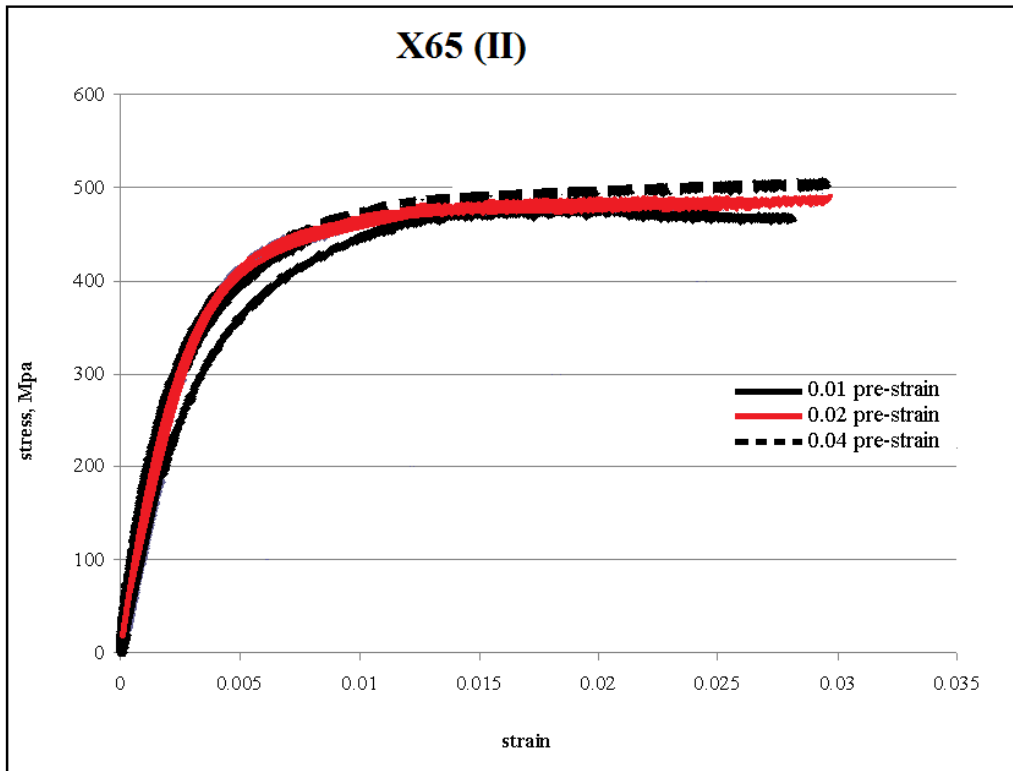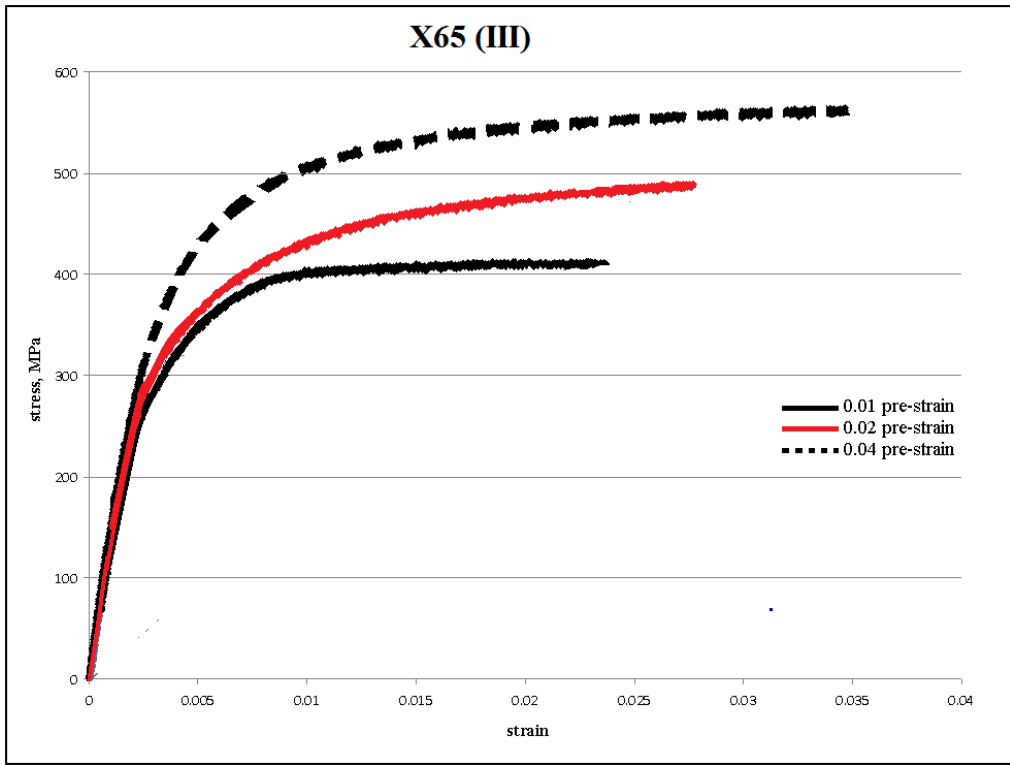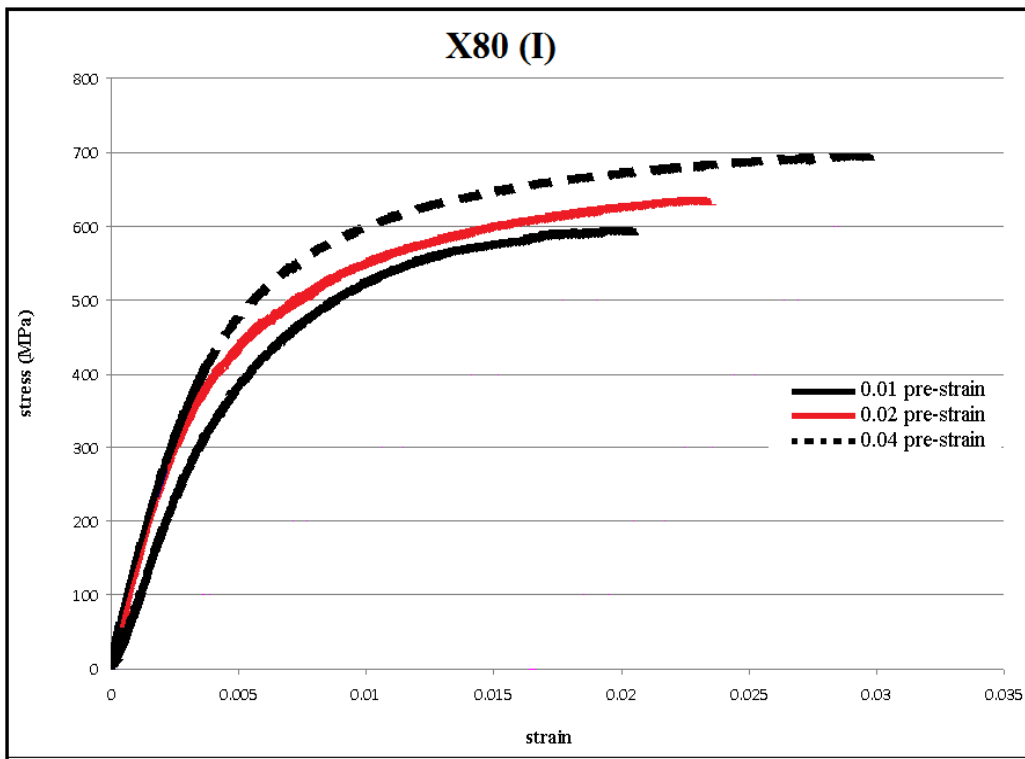
X80 (I)

d
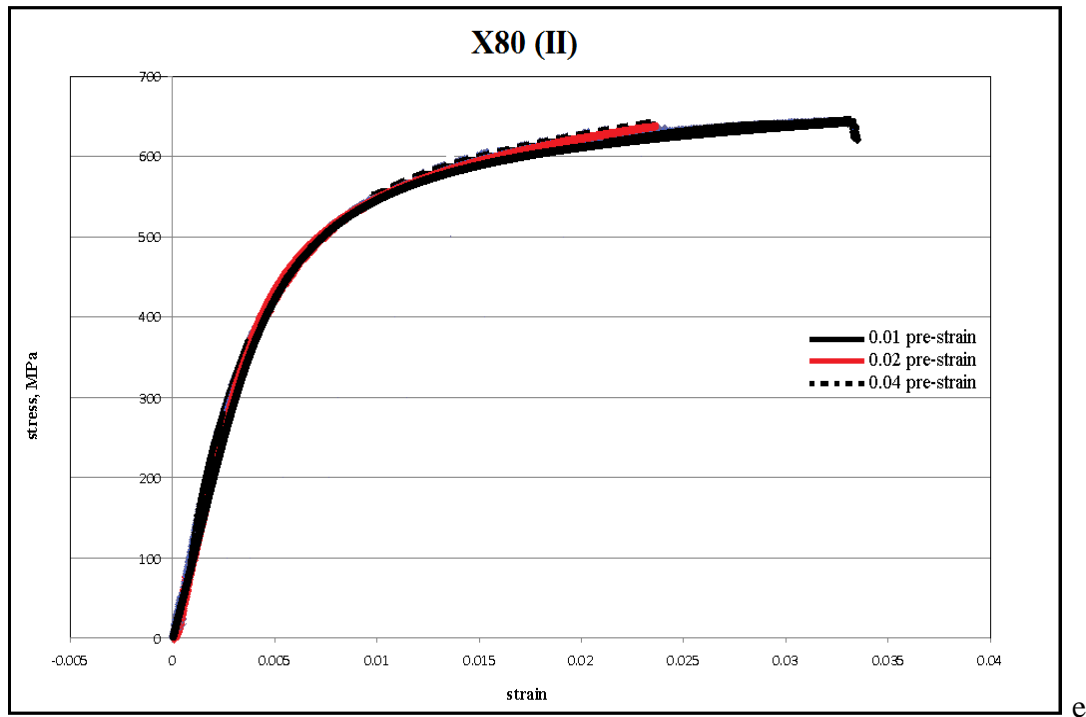
Figure 5.6 Reverse stress strain curves for (a) X65 (I) (b) X65 (II) (c) X65 (III) (d) X80 (I) and (e) X80 (II)

5.4.2   Recovery of original properties past the reverse yield point

Return to constant work hardening was at or just below 0.01 strain for the studied steels. As Bauschinger calculations are concerned with yield immediately after elastic deformation in the reverse direction and at values of 0.001 and 0.005 offset strain this strain regime is not captured in the Bauschinger stress parameters. Recovery (in terms of) yield stress in these steels is a function of long-range interactions between dislocations and particles and internal stresses resulting from elastically deformed second phase present in the matrix [146]. An increase in work hardening exponent was reported in [35]

and attributed to an increase in dislocation density and the number density of interactions between dislocations and obstacles steadily increasing during forward pre-strain.

Figure 5.7 shows the yield stress at 0.01 reverse strain for all specimens at different levels of pre-strain. The non-Ni bearing steels all show a recovery in long range yield stress with increasing pre-strain. Comparing stress values for the 0.01 and 0.04 pre-strained specimens, the higher alloyed X65 (III) and 80 (I) recover their yield stress by 134 MPa and 92 MPa respectively whilst the lower alloyed X65 (III) recovers by 67 MPa. Increased interaction sites for dislocations and particles will increase back stress which will lower the yield stress but once reverse strain exceeds 0.01 and work hardening stabilises the same mechanisms for forward deformation operate and this helps raise the yield stress at this stage. The Ni-bearing steels X65 (II) and X80 (II) showed no recovery of yield stress following increased pre-strain. Given the dissimilar dislocation densities, particle volume fractions and microstructures between both steels, the only factors that can be attributed to this are the additions of Ni and its possible influence on the LEDS observed in TEM studies which inhibit return to original properties.
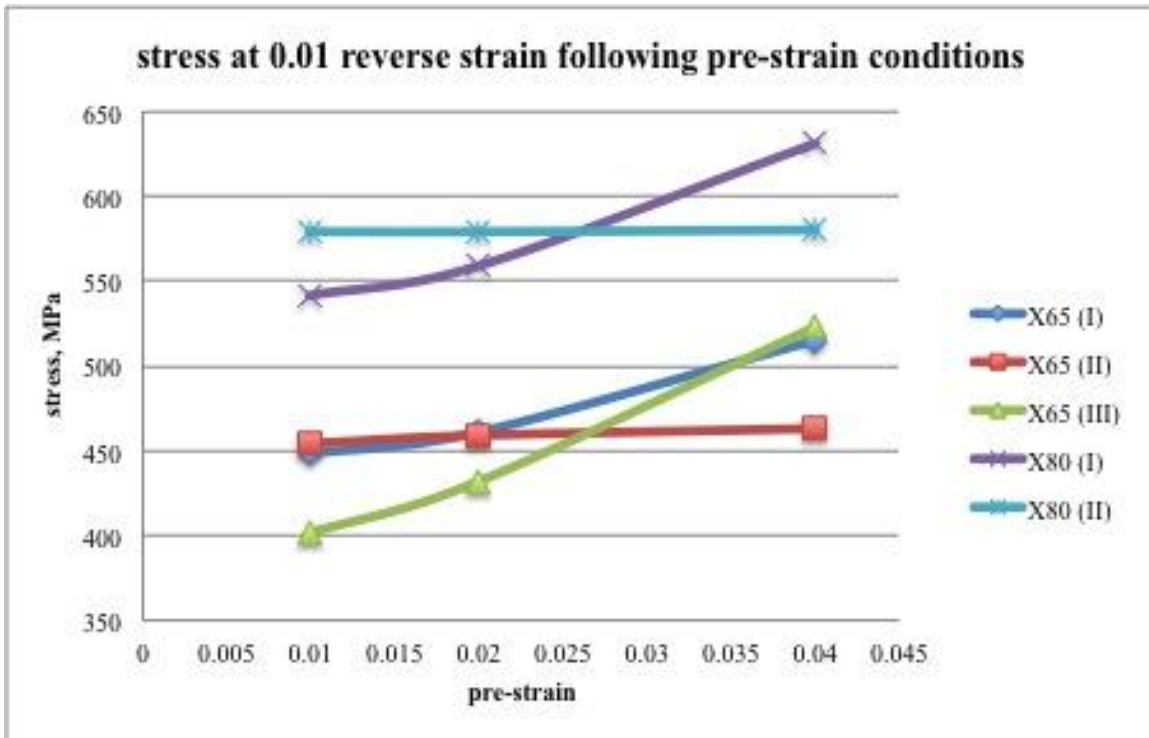
Figure 5.7 Graph showing recovery of stress during reverse loading (taken at 0.01 reverse strain) at different levels of pre-strain

Table 5.3 summarises the work hardening rate n of all studied steels following pre-strain deformation. For all X65 steels compressed to 0.01 pre-strain transient hardening was observed, as pre-strain level reached 0.02 strain the hardening rate increased but appears to reach a maximum value at 0.02 strain for X65 (I) and (III) with a slight increase seen in X65 (II). For both X80 grade steels the work hardening rate n is relatively unaffected by the level of pre-strain deformation as the rate n remains consistent throughout the pre-strain range.

Steels with higher volume fractions of particles appear to recover reverse work hardening rates as opposed to steels with smaller microalloying additions i.e. X65 (I) and (II) but the difference is not significant enough to make a sound conclusion on this as the volume fraction of particles in X65 (III) is far greater than that of the other X65 grades but does not recover work hardening rates in the reverse direction to the same extent as the X80 grades. The most likely possibility is the deformation of second phase MA constituents during reverse loading which cause a yield drop arising from back stresses against the harder phase during the release of dislocations into ferrite. After a short period of discontinuous yielding and back stress diminishing the material properties return to normal and characteristic high levels of work hardening are observed [131] which can explain why these steels show particularly good recovery of their original rates of work hardening.

Table 5.3 Compressive work hardening rates and reverse work hardening rates (taken at 0.01 reverse strain) for different states of pre-strain

Steel	Forward (compressive) work hardening (n)			Reverse work hardening (n) > 0.01 strain		
	Stage I	Stage II	Stage III	0.01 pre-strain	0.02 pre-strain	0.04 pre-strain
X65 (I)	Lüders strain < 0.026	0.29	-	0	0.10	0.08
X65 (II)	0.10	0.26	-	0	0.05	0.08
X65 (III)	0.05	0.23	-	0.04	0.13	0.12
X80 (I)	0.03	0.28	0.26	0.23	0.24	0.23
X80 (II)	0.05	0.33	0.30	0.29	0.29	0.29

5.4.3   The Bauschinger parameters for studied steels

The Bauschinger stress parameters ($\beta\sigma 1$) presented in Figure 5.8 were obtained with an offset yield point of 0.001 strain ($\beta\sigma 1$) which is related to short range work softening i.e. the immediate softening in the material not taking into account any recovery of yield stress from further reverse deformation. Taking an offset of 0.005 strain gives an indication of how much the material has recovered in yield stress / hardened during further reverse loading and therefore gives a lower Bauschinger stress parameter values that are presented later in this section. As expected, all materials experienced a decrease in yield stress upon reverse loading. The overall magnitude of work softening was similar for their respective strength grades but showed distinct variations for which there are three trends.

1. *Small amount of work softening from 0.01 - 0.02 pre-strain followed by a higher amount of work softening after 0.04 pre-strain (as seen in X65 (I))*

2. *Comparatively (for similar strength grades) low work softening at 0.01 pre-strain and large incremental steps for each pre-strain level (as seen in X65 (II) and X80 (II)).*

3. *Comparatively high (for similar strength grades) initial work softening and small incremental increases thereafter (as seen in X65 (III) and X80 (I)).*
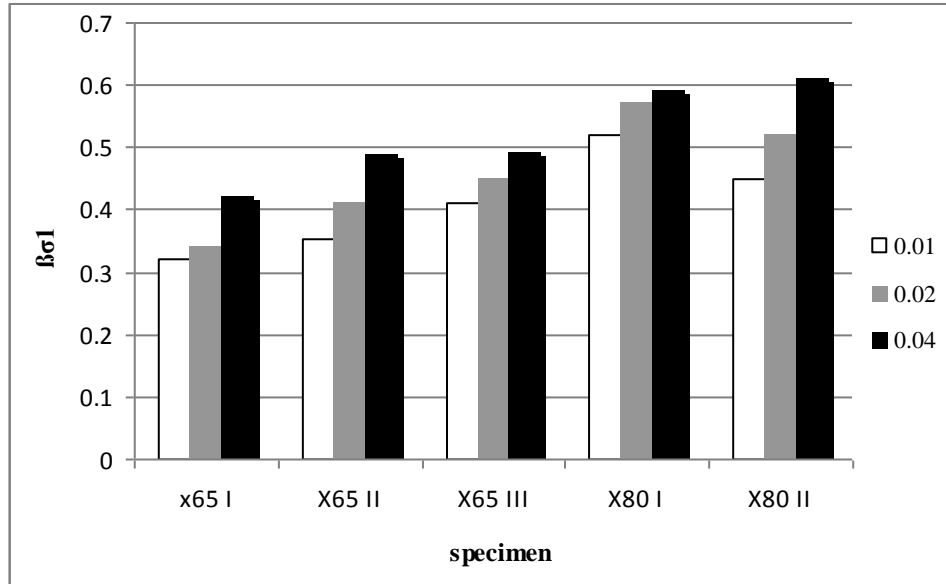
Figure 5.8 Bauschinger stress parameter for all studied steels at 0.01, 0.02 and, 0.04 strain (0.001 offset)

Trend 1:

X65 (I) exhibits prolonged Lüders regions during forward deformation up to 0.03 strain which would appear to suppress high levels of work softening at pre-strains within the Lüders strain region. Work softening does occur when pre-strain is within the Lüders strain region which can be explained by a small increase in the dislocation density in the region of 6 x 10^{13} m^{-2} and early stage interaction between dislocations and particles. When pre-strain levels reach 0.04 strain and work hardening begins the Bauschinger parameter increases in good agreement with a sharp increase in dislocation density (2.7 x 10^{14} m^{-2}) providing more sources of back stress and masking of particles by dislocations

175

during reverse loading. The only comparable low carbon, X65 grade material within the reported literature which demonstrates Lüders strain < 0.03 is found in [35]. The C-Nb-V steel in that study was annealed at 550°C and demonstrated moderately large increments in work softening behaviour within the Lüders strain region similar to that of non-heat treated samples of the same steel that did not display Lüders straining during forward deformation. The reason for this was not reported by the author but this steel did, however, have a higher volume fraction of particles acting as interaction sites (increased from 0.00076 to 0.00374 and dislocation density decreased from 4.0 to 1.6 x 10^{14} m^{-2} after annealing) which may have been offset against any effects of the Lüders strain and therefore an incremental increase was observed in the steel similar to that in the as-received condition.

Trend 2:

An incremental increase in work softening for each level of pre-strain was observed in the Ni-bearing steels. X65 (II) when subject to an initial pre-strain of 0.01 results in a Bauschinger parameter similar to that of X65 (I) but by 0.04 pre-strain the Bauschinger parameter is markedly higher than all X65 (I) values and similar to that of X65 (III) which has a higher Bauschinger parameter at pre-strains < 0.04. X80 (II) shows a similar trend when compared against X80 (I); the Bauschinger parameter is smaller at 0.01 pre-strain and exceeds the Bauschinger parameter for X80 (I) at 0.04 pre-strain. Comparing the volume fractions of particles and the Bauschinger parameters for the steels at 0.01

pre-strain (Figure 5.9) it is seen that a higher Bauschinger parameter is observed with an increase in microalloying content which can explain the lower $\beta\sigma1$ values to those of X65 (III) and X80 (I). When comparing the dislocation density in the as-received condition and the $\beta\sigma1$ parameters at 0.01 strain there is also a correlation between the magnitude of work softening and dislocation density (Figure 5.10). X65 (III) does not fit well into this trend as a disproportionate amount of strengthening is from high microalloying levels of V and Nb which compensate for the dislocation density (measured to be the lowest of all studied steels) and act as a source of back stress.
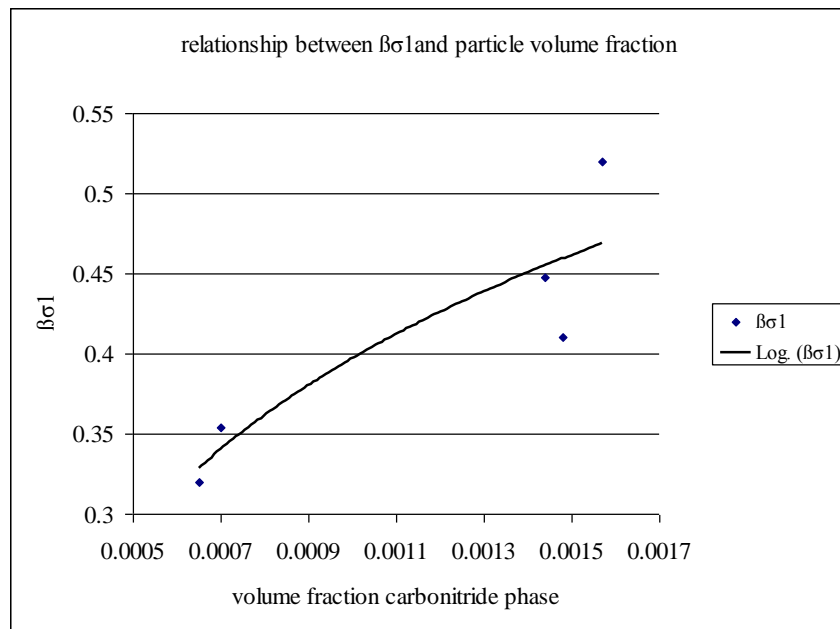
Figure 5.9 Bauschinger parameter plotted against volume fraction of precipitates showing a positive trend of increased particle content leading to a higher Bauschinger parameter
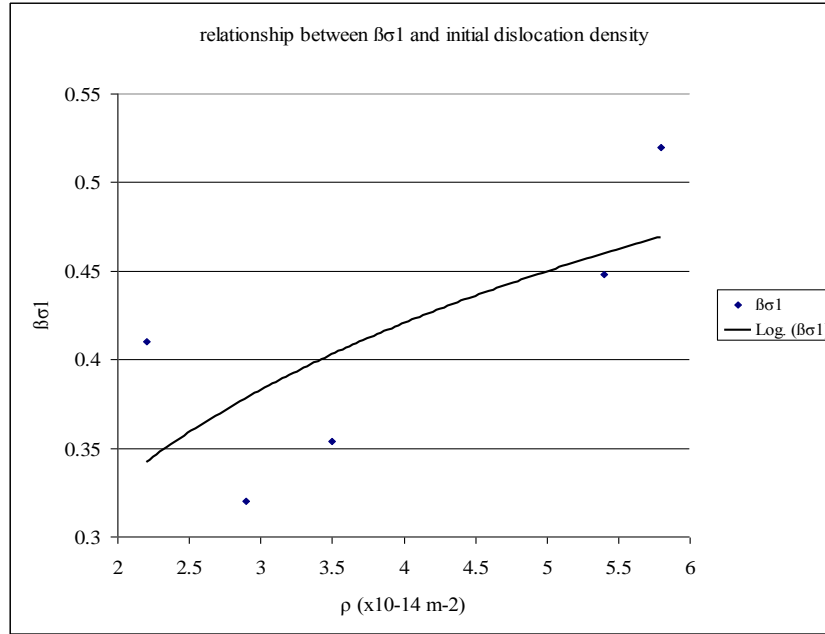
Figure 5.10 Bauschinger parameter plotted against initial dislocation density (ρ) showing increased dislocation density leading to a higher Bauschinger parameter

The large incremental increases in Bauschinger parameter values are discussed with respect to the potential role of nickel later on. This is not typically seen in comparison to other published data which either shows trend 3 work softening behaviour such as in studies by Kostryzhev et al. [35] and Han & Sohn et al. [166], or a plateau in ßσ1 after 0.02 pre-strain as shown in studies by Han et al. [165].

Trend 3:

As mentioned in the previous section, X65 (III) and X80 (I) exhibit large increases in dislocation density during deformation up to 0.04 strain. These steels also have the highest volume fraction of precipitates present for the studied materials within their respective strength grades but do not exhibit the large increases in work softening with

178

increasing pre-strain. A high initial dislocation density would appear to correlate well with a high Bauschinger parameter at 0.01 pre-strain as this is a major difference between the strength grades. X65 (III) is the exception to this as it has the lowest initial dislocation density (2.2 $\times 10^{14}$ m^{-2}) which increases rapidly at 0.02 strain (4.6 $\times 10^{14}$ m^{-2}), possibly from increased dislocation interaction and generation from a high number density of particles. TEM samples were not studied at 0.01 strain so that it was not possible to quantify the dislocation density at this strain, but generally, higher work softening occurs following 0.01 pre-strain in samples with higher volume fractions of particles and higher dislocation densities than specimens of equivalent strength grades as seen in work by Kostryzhev [35]. The low incremental increases in work softening with increased level of pre-strain appear to benefit the steel at higher pre-strains as the Bauschinger parameter is relatively low at this stage compared to the specimens which follow work softening trends 1 and 2.

5.4.4 Comparisons with previous work.

In the literature there have been two studies reported on steels which have very similar microstructures and are the same API grades as the investigated materials: X65 ferrite-pearlite steel and X80 ferrite-MA steels [35,166]. Taking reverse stress strain data and obtaining the Bauschinger parameter for a 0.001 offset strain a comparison can be made between the two steels in this work that are most similar to the previously studied materials (i.e. X65 (III), which has a ferrite-pearlite microstructure and X80 (I) which has a ferritic microstructure with MA constituents) (Figure 5.11). The X65 ferrite-pearlite

steels from the literature both show a high initial Bauschinger parameter and steady increase in work softening up to 0.04 strains. It has been reported that the initial dislocation density (measured to be 2.3 x 10^{14} m^{-3} in the C-Nb microalloyed X65A and 4.0 x 10^{14} m^{-3} in the C-Nb-V microalloyed X65B) in the as-received specimens had a larger influence on work softening than the particle volume fraction (measured to be 0.00011 in the C-Nb microalloyed X65A and 0.00076 in the C-Nb-V microalloyed X65B) both of which were larger in the higher strength (C-Nb-V X65B) material. This is consistent with X65 (III) and both X80 grade steels having higher Bauschinger stress parameters as they have high dislocation densities. The relatively high Bauschinger parameter seen in X65 (III) would therefore be attributed to the high volume fraction of VC particles compensating for the low dislocation density.

The X80 grade steels used in reference [166] labelled X80 A and X80 B have similar yield stresses to the studied X80 steels (610 MPa and 640 MPa respectively), no Lüders banding was observed during deformation, specimens were of similar wt % compositions (0.05C-1.8Mn-0.1Nb) and of similar microstructures consisting of ferrite, granular bainite and MA islands (3.6% and 0.7% for X80 A and X80 B respectively).
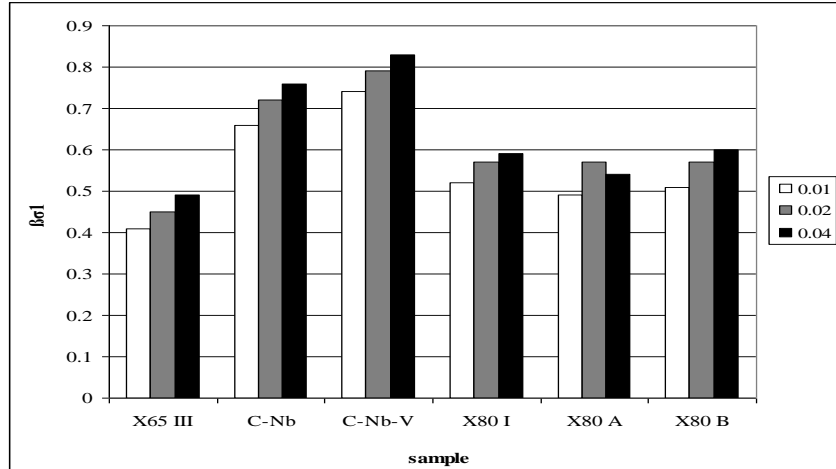
Figure 5.11 Bauschinger parameters from the literature for X65 C-Nb and C-Nb-V ferrite-pearlite steels [35] and X80 C-Nb ferrite-MA steels [166] compared to the X65 (III) and X80 (I) steels from this work

There is a strong similarity between the X80 B material and X80 (I). Although the author presented the MA constituent % present in the microstructure, details of any carbo-nitride phase were not reported. From the composition the greater amounts of Nb present would suggest that the potential volume fraction of precipitates would be similar or greater than that of either two X80 grade materials in this study which would make up for a significant amount of strengthening attributed to the higher levels of MA present in X80 (I) and (II) in the present study. TEM was not conducted on these materials so no comment was made on the dislocation densities. It is generally observed that an increase in strength will result in an increase in the Bauschinger parameter as seen in [35,131,162,164,166]. Comparing the X80 materials from this study and [166] to the X65 grade materials and the corresponding $\beta\sigma 1$ parameters, there is good agreement with a jump in strength grade leading to a greater $\beta\sigma 1$. As the difference in yield strength between materials becomes less pronounced then the variation in $\beta\sigma 1$ is less straight

forward as different pre-strain levels may produce *ßσ1* results which are greater, or less than, a material of similar grade but of lower strength. This is seen in X80 A and B where no obvious trend can be established from the yield stress values, it is also seen in the studied X65 specimens, particularly at 0.01 and 0.04 pre-strains. As discussed in [35] particle and dislocation strengthening play significant roles in the influence on work softening behaviour, unfortunately the results are not comparable to [166] or this study as the *ßσ1* for X65 steels in [35] was reported to be larger than all studied steels which were of higher strength possibly due to sensitivity of a lower strain rate (1.3 x 10^{-4}) or shear strain induced deformation on tensile specimens amplifying the Bauschinger parameter by introducing a strain path change prior to testing.

5.4.5   Long range work softening

The results for the Bauschinger parameter taken at 0.005 offset are present in Figure 5.12 and represent the evolution of yield stress with the initial stages of work hardening in the reverse direction where continuous yielding is occurring (characterised by the roundhouse yield curve) as opposed to the sharply defined yield point in forward loading.
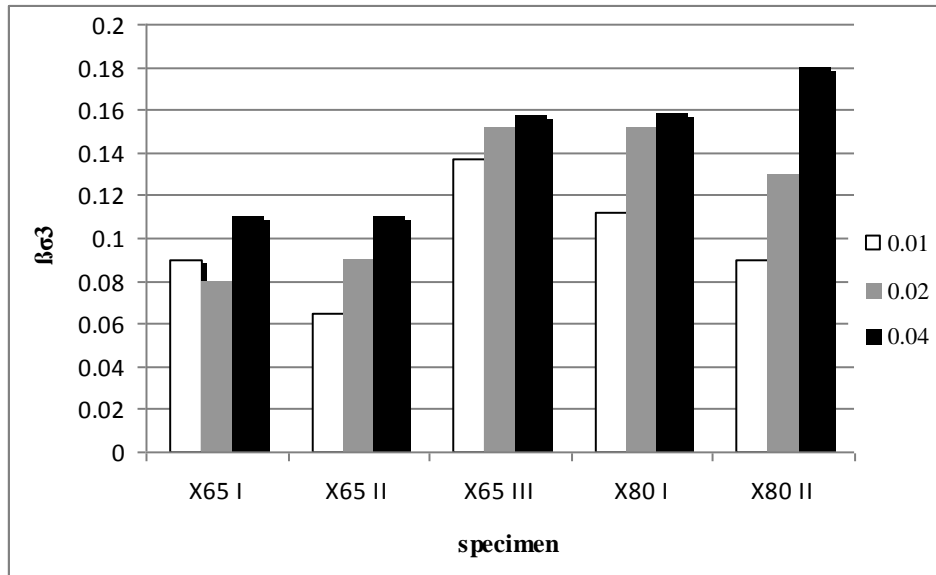
Figure 5.12 Long range (permanent) softening in all studied steels

The results bear similarities to the $\beta\sigma1$ parameters for X65 (II) and X80 (II) in that they have large incremental increases with greater levels of pre-strain. The difference between forward and reverse stress yield stress for 0.05 offset was < 40 MPa for X65 (II) and < 5 MPa for X80 (II) which can explain the large increases in $\beta\sigma3$ as an increase in stress during pre-strain will result in greater stress differences if the reverse yield point is not recovered.

X65 (I) and X65 (II) which have the least amount of precipitation strengthening show a return to their original properties at lower reverse strains than the higher alloyed steels and show a substantial difference when compared against the other steels - all of which have large additions of microalloying elements and higher measured volume fractions of carbo-nitride particles.

183

This trend is consistent with that reported by Kostryzhev [35] who found $\beta\sigma3$ to decrease with increased microalloying contents i.e. increased volume fractions of carbo-nitride phases. This was attributed to immobilisation of dislocations by particles during reverse slip giving rise to an increase in work hardening. This is schematically represented in Figure 5.13 a).
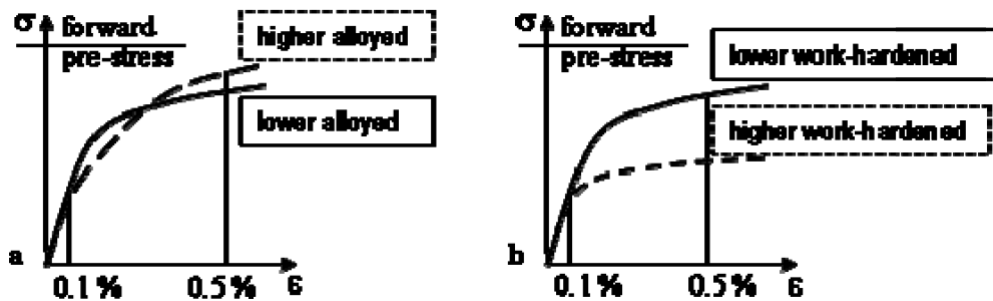
Figure 5.13 Schematic representations of reverse stress strain curves obtained in C-Nb and C-Nb-V steels subject to heat treatment to increase the carbo-nitride phase content [35]

Results obtained from this study suggest that the increase in the work hardening rate during reverse deformation attributed to fine scale particles is over-estimated. In the present study the work hardening rates for X80 (I) and X80 (II) in the reverse direction was greater than for the lower microalloyed X65 (I) and (II) steels, but also substantially greater than X65 (III) which has a greater number density of carbo-nitride particles (mostly VC) than both X80 grade specimens and displayed only marginally higher reverse work hardening rates to that of X65 (I) and (II). This large discrepancy in reverse work hardening may indicate that the effects of particles for this mechanism are higher than expected in the X80 grades and may be attributed to the presence of MA aiding the

184

recovery of forward properties during reverse deformation and emission of dislocations from martensite-ferrite interfaces will ensure high levels of work hardening are resumed.

Results from this study are also not in agreement with the effect of prior work hardening during pre-strain (represented in Figure 5.13 b). Stagnation in work hardening during reverse deformation was attributed by Kostryzhev et al. to dislocation pile-ups on favourable slip planes, this was not observed in the present study; low pre-strains of 0.01 resulted in sharper yield points and lower rates of work hardening after yield in X65 (I) and (III). Increasing the pre-strain increased the reverse work hardening rate n in all steels up to 0.04 pre-strain. TEM studies showed irregular structures and a relatively low dislocation density in X65 (I) and (III) possibly suggesting that dislocation mobility at this stage in these steels is still reasonably high and therefore early stages of reverse work hardening would not be too dissimilar to that in the forward deformation. This does not explain why stagnation of work hardening during reverse loading occurs in these steels and it was not possible to capture data at higher strains to see if the specimens ever recovered during subsequent straining. This phenomenon has been attributed to the annihilation of dislocation structures during reverse loading [142,144] of cellular structures [144] and homogeneously dispersed dislocation - obstacle and dislocation - dislocation interaction [142]. Advanced cellular structures were observed in both X80 grade specimens which accompanied high rates of reverse work hardening behaviour which leads to the conclusion that dissolution of HEDS such as pile-ups and Orowan loops is the most likely mechanism for stagnation of reverse work hardening.

6 Discussion of the effect of microstructural parameters on mechanical behaviour for studied steels

This body of research has collated a large amount of data for the microstructural characteristics of 5 API grade linepipe steels of X65 and X80 grades to establish relationships between strengthening mechanisms and the mechanical behaviour under forward and reverse plastic deformation. Quantification of these microstructural features which are simultaneously contributing to the mechanical properties presents its own problems, particularly in terms of the Bauschinger parameter in that the influence that any one strengthening mechanism may be offset fully or partially by another making deconvolution difficult, particularly in terms of grain size and microstructure.

Theoretical yield stress values were determined from measured data using the relevant equations for solid solution strengthening, grain size refinement, precipitation strengthening and dislocation density contributions to yield stress. Figure 6.1 shows the resulting contributions to yield stress. Phase balance strengthening was omitted as dislocation density was measured for bainitic / acicular microstructures and the proportion of second phase is more likely to affect ultimate tensile stress as opposed to yield stress where ferrite will plastically deform before the harder second phase.

Steels containing dual phase constituents have been previously studied in terms of Bauschinger stress parameters and work hardening behaviour [35,162,164,166]. These studies concluded that steels containing dual phase microstructures will exhibit greater

work softening arising from residual stresses between the softer ferrite phase and harder martensitic / pearlitic phases during plastic deformation. Studies by Kostryzhev, Zhonghua, Kumakura, Han and Sohn [35, 131, 162, 166] do not compare results against other single or dual phase microstructures and studies by Han and Tyne et al [165]. which do compare different microstructures have done so using dissimilar strength grades with no comment on the effect of Orowan strengthening or dislocation structures contributing to the yield stress.

Work hardening behaviour appears to be much more consistent throughout different strength grades regardless of differences in dislocation density and volume fractions of particles. X65 (I) and (II) have high work hardening parameters in the region of 0.25 during stage II work hardening, in X80 specimens the presence of MA constituents seems to greatly increase the work hardening rate in comparison to ferritic and ferrite-pearlite microstructures (around 0.30 during stage II). An increase from 0.8 - 0.12 volume fraction of MA in X80 (I) and (II) accompanies an increase in the work hardening parameter in stage (I) (0.03 and 0.05 respectively) and during stage II (0.28 and 0.31 respectively). This was due to large increases in dislocation density with strain which is typically seen in martensite bearing microstructures which act as sources for dislocations as strain concentrations occur at the martensite-ferrite interface [117,129-131]. The expected trend of increased particle volume fraction leading to increased work hardening appears not be a dominant factor across microstructures as the lowest rate of stage II work hardening was observed in X65 (III) (0.23) which contains the highest volume fraction of particles.
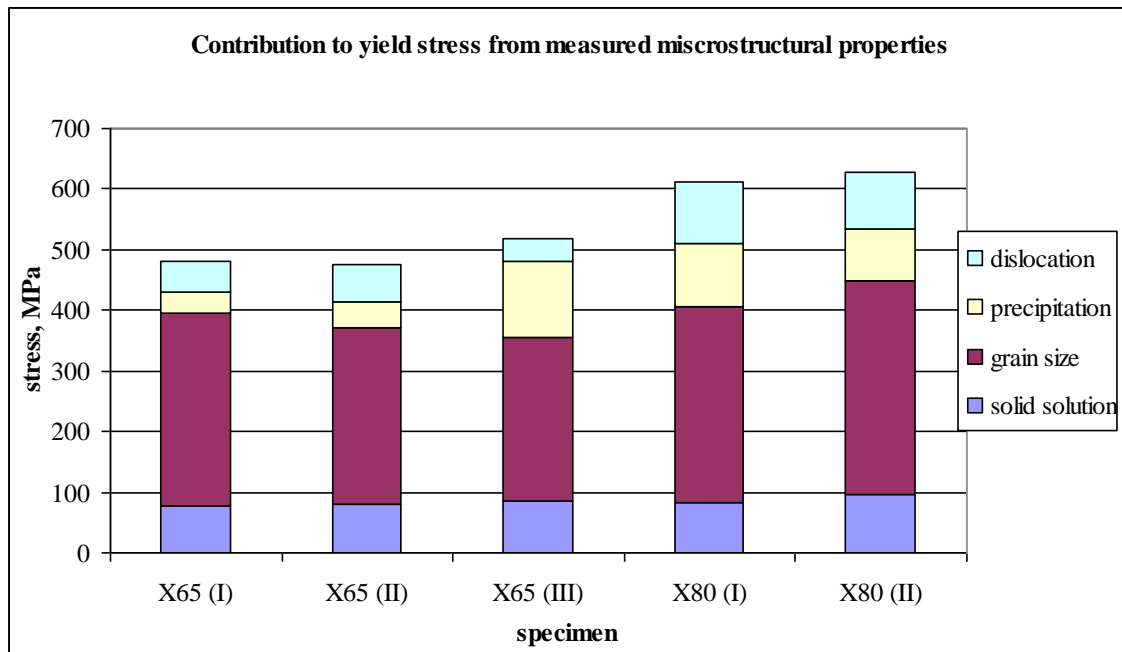
Figure 6.1 Contribution to total yield stress from measured microstructural features from the major strengthening mechanisms in all studied steels.

Taking the effective grain size from EBSD data and an enlargement factor of 2.7 for optical measurements the predicted yield stresses compare well to measured compressive stress strain data for all 5 steels with the largest difference being 6 % for X65 (II). Previous studies determined the grain size to be independent of strain hardening for deformation to > 0.02 strain (i.e. stage II work hardening) [120]. The grain size and solid solution strengthening appears to be independent of the work hardening and Bauschinger parameters for the studied steels; X65 (I), (II) and X80 (I) have similar effective grain sizes yet show noticeably different post yield behaviour; X65 (I) displays Lüders strain after yield and X65 (II) / X80 (I) experienced onset of stage II strain hardening at different strain regions which varied greatly between the two (n = 0.23 and 0.28 respectively). It is proposed that the work hardening rate is more dependent on the

dislocation density which increases with strain (as seen in compressed specimens) as any sharp increase in the work hardening rate was accompanied by changes in dislocation structure such as cellular formation, clusters and interaction with particles seen far from grain boundaries. The initial dislocation density observed in the steels is also a factor of the transformation mechanisms present upon formation of bainite / MA which is displacive and therefore a greater dislocation density would be expected than for a pearlitic bearing steel which is diffusive. Taking this into consideration the lower rates of work hardening exhibited cannot be attributed to a reduction in grain size as the microstructures with the most refined grain size inherently have high dislocation density within the ferrite owing to their TMCR schedules.

In this work the three X65 specimens and two X80 specimens are of comparable strength grades but mechanisms attributed to microstructure such as second phase pearlite, MA, grain size contributing to back stresses are not possible to deconvolute from nano-structures acting simultaneously during loading schedules, contributing to the Bauschinger parameter. The two most comparable grades from literature and the studied steels are X65 (III) and X65B from [35]. Both have similar yield strength, ferrite grain sizes (2.3 μm) and similar amounts of pearlite (10%).

The particle volume fraction and dislocation density for the X65 B material is greater than that of X65 (III) (0.0018 and 0.00148 for their respective particle volume fractions and 2.2 x 10^{14} m^{-2} and 4.0 x 10^{14} m^{-2} respective dislocation densities). Annealing specimens to increase the volume fraction of particles and reduce the dislocation density

indicated that the initial dislocation density and particle volume fraction to influence the magnitude of work softening. Kostryzhev found the dislocation density to be more effective than particle volume fraction by a factor of 2.7 in raising the Bauschinger parameter and by a factor of 3 - 4 times in raising the rate of work hardening. From this, it would be expected that X65 (III) would demonstrate a lower Bauschinger parameter and lower rate of work hardening but not to the extent shown in Figure 5.10.

X65 (I) and (II) do not follow expected trends; despite higher dislocation densities than X65 (III) both have lower Bauschinger stress parameters at the lower pre-strain regimes and despite higher rates of stage II work hardening; X65 (II) shows a similar magnitude of work softening at 0.04 pre-strain. Combining the strength attributed to nano-structures (the predominant source of back stress i.e. particles and dislocations) and plotting these against the Bauschinger parameters for the studied steels (as shown in Figure 6.2) accommodates X65 (III) which falls either side of the trend due to its high volume fraction of particles and low dislocation density. This can give a better explanation as to why higher Bauschinger parameters are not observed in the other X65 grades which have higher dislocation densities as reducing the number of interaction sites, greatly reduces the sources of back stress. Likewise, if a high number of interaction sites are present then even a relatively low number of dislocations will aid back stresses through Orowan mechanisms. This agrees well with the Brown and Stobbs model and work conducted by Queyreau and Devincre [146] which attributes short range back stresses to the bowing of dislocations masking precipitates. X80 grades fit well into this trend as they both show higher Bauschinger stress parameters than the X65 grades which is expected given their

higher particle volume fractions and high dislocation densities. The particle number density also highlights the importance of potential number of interaction sites on short range back stresses, as X65 (III) and X80 (II) have much closer Bauschinger parameters after 0.01 pre-strain (approx. 0.41 and 0.45 respectively) than X80 (I) which has a Bauschinger parameter of 0.51. Both steels have very similar microstructures and this difference can only be attributed to the number density of particles in the three steels (4721, 3652 and 2354 x 10^4 per mm^2 respectively); X65 (III) showing largest number density owing to the formation of VC helping to balance out the small dislocation density and the smallest number density of the three materials in X80 (II) balancing out the high dislocation density and hence the largest Bauschinger parameter is observed in X80 (I) which has both a high number of particles and high dislocation density.
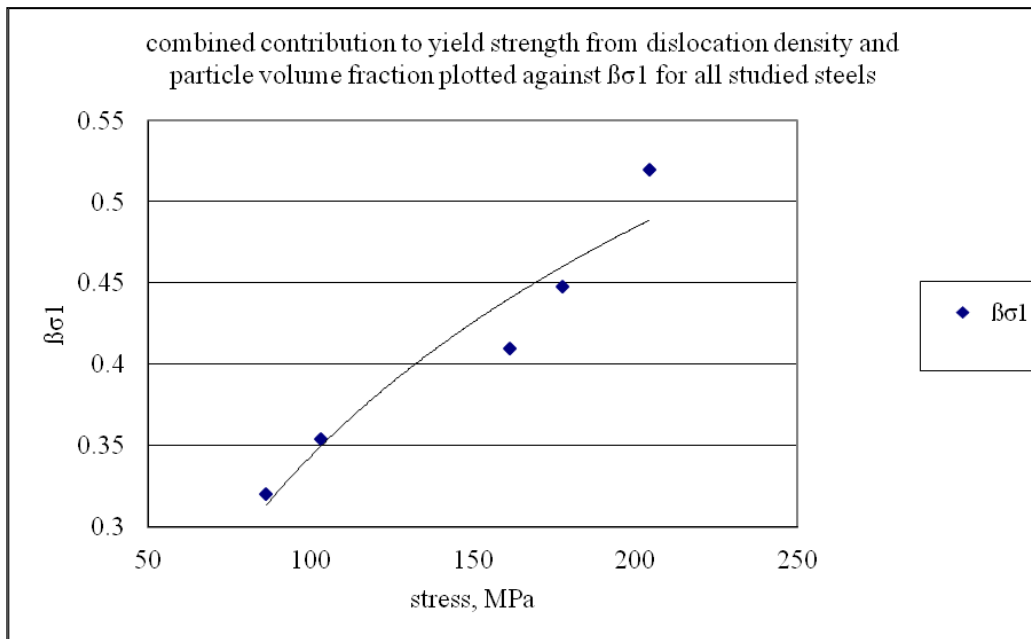
Figure 6.2 Bauschinger stress parameter plotted against the yield strength contribution from dislocation density and particle volume fraction for all studied steels

In terms of fabrication of HSLA steel plate for fabrication of linepipe, this research has shown that consideration into the amount of pre-strain a steel will be exposed to during manufacture of linepipe must be considered in the design as a linear increase in the Bauschinger parameter is not seen in acicular microstructures. For microstructures containing Ni large incremental increases are observed through the strain range which is advantageous for smaller pre-strains (i.e. smaller pipe wall thicknesses) but lead to substantial work softening if this exceeds 0.02 strain. It also highlights the need for further research into mechanisms other than dislocation density and particle interaction as the amount of work softening at small strains may be dependent on number density of precipitates from Orowan interactions but this is not consistent at greater pre-strain levels where further work softening is attributed to dislocation structure.

Stagnation of work hardening in reverse stress strain curves was seen in X65 grade materials where pre-strain was within Lüder's region / stage I work hardening. As cellular structures evolved the reverse work hardening recovered. X80 grade materials did not exhibit any signs of transient hardening during reverse loading despite having higher dislocation densities and more evolved structures i.e. clusters in as-received specimens and cellular structures in strained specimens. This shows that stagnation of work hardening during reverse straining is not necessarily dominated by dissolution of cellular structures but in fact the annihilation of dislocations which are still mobile as reported by Yu et al. [193].

This brings the research to suggest another driver behind the mechanical behaviour during reverse loading which can explain discrepancies in the increments of increased

work softening at different pre-strain levels observed in X65 (II) and X80 (II). Both these steels have much higher additions of Ni than their counterpart strength grades, they also exhibit different dislocation structures observed using TEM. As received specimens and those compressed to 0.02 strain showed dislocations to take on regular straight structures such as nets and pile-ups. It is proposed that the additions of Ni have a profound influence on the dislocation structures in HSLA which give rise to long range stresses from increased mobility of dislocations and subsequent pile-ups. Recent studies into the effects of solute atoms on solid solution softening and dislocation interaction with solute atoms in bcc lattices have shown the local environments caused by W, Cr and Si and Ni solutes to have substantial effects on dislocation mobility and slip paths by acting as lubricants, pinning forces and sources of stress decreases of atomic rows within dislocation cores [193-196]. If such an effect is present in X65 (II) and X80 (II) arising from the high additions of Ni then this can explain the regular structures frequently observed giving rise to additional long range back stresses in the form of pile-ups and increased number of mobile dislocations which will be more susceptible to form HEDS in the form of Orowan loops and bowing. This opens the possibility of new areas of research beyond this body of work and requires further investigation.

7 Conclusions:

Studies into the microstructural and mechanical properties of 5 linepipe steels; 3 X65 grades and two X80 grades have yielded the following conclusions:

In the area of plate / sheet microstructure:

1. Grain size:

Differences in microalloying content between the 5 steels did not show any correlation between wt % and grain size suggesting processing schedules to be the more dominant factor in grain refinement. Linear intercept and EBSD measurements of grain size using a misorientation angle of 1.9^o and 15° showed a consistent hierarchy of grain size when compared to optical measurements. Taking the effective grain size from EBSD data with 15° misorientation between neighbouring grains increased the grain size by a factor of 2.7 for measurements from optical micrographs which agrees well with calculated and measured strength values.

2. Second phase:

Low carbon steels subject to accelerated cooling schedules contained acicular / granular ferrite microstructures and MA islands. Steels with higher carbon contents subject to slower cooling resulted in equaixed ferrite microstructures within prior austenite grains and banding of pearlite. The presence of MA constituents increases the work hardening rate and promote recovery of original material properties during reverse post-yield

loading, but does not appear to influence short range back stresses influencing the $\beta_{\sigma1}$ parameter.

In terms of future trends, dual phase microstructures which can withstand highly abrasive environments owing to their high levels of hardness will benefit the oil and gas industry for applications such as fracking. This is achieved at the expense of an increase in work softening behaviour which places greater demand on fabricators to sufficiently recover the yield stress during reverse deformation through increased O-ing and expansion. Choosing an MA constituent bearing microstructure appears to have a greater consistency in terms of reverse work hardening rates which are not observed to stagnate even at all measured levels of pre-strain as seen in pearlite-bearing microstructures.

3. Second phase carbo-nitride particles:

Measured volume fractions of Ti, Nb and V carbo-nitride particles increased with wt % additions and were in good agreement with Thermo-Calc modelling predictions. Carbo-nitride distribution in X65 (I) and X65 (II) showed fine particles to be more refined in the latter steel which had a microstructure consistent with fast cooling schedules. High alloying additions of VC in X65 (III) yielded the most refinement in particle size of all 5 steels.

Particle number density was greater in regions within and adjacent to pearlite in X65 (III). Precipitates were not present within MA constituents.

Avoidance of high levels of fine scale carbo-nitride precipitates to achieve strength levels enhanced the long term recovery of reverse yield strength ($\beta_{\sigma 5}$) as seen in the most highly alloyed steels X65 (III) and X80 (I) which showed the slowest recovery (i.e. higher $\beta_{\sigma 5}$ parameters). For X65 (III), which had a large proportion of strength attributed to particle volume fraction, the recovery was poor even in comparison to X80 grade materials which showed greater recovery with higher initial dislocation densities up to 0.02 pre-strain.

Dislocations:

Dislocation densities and structures were studied in the as-received condition and after 0.02 and 0.04 compressive strain. Measured dislocation density increased with plastic strain in all steels. Initial dislocation density was higher in the X80 grade steels and was consistently higher than X65 grade steels throughout the range induced plastic strain. Early stages of cell structure development were evident in all steels except X65 (I) where stage II work hardening did not set in until 0.03 strain. Steels containing high microalloying additions of nickel demonstrated regular, low energy dislocation structures determined which were observed at grain boundaries and surrounding large particles > 50 nm. Dislocations showed evidence of pinning and bowing with particles < 10 nm in size, dislocation density increased in particle rich areas and decreased in adjacent areas to large particles < 100 nm.

Dislocations have a synergistic effect with particles on the $\beta_{\sigma 1}$ parameter. LEDS and dislocation mobility during deformation affected by fine scale precipitates, additions of Ni and transformations from austenite – bainite / martensite appear to increase long range

back and short range back stresses as seen by large increments in $\beta\sigma 1$ and $\beta\sigma 5$ parameters with increased pre-strain. This should be considered when selecting wall thicknesses; at lower pre-strains (applicable to the U-ing stage) this is advantageous, but with increased pre-strain (which would be a manifestation of large wall thickness) the Bauschinger stress parameter increases dramatically compared to materials which predominantly have HEDS present (i.e. clusters, tangles and bowing).

In the area of mechanical properties for all studied steels:

1. Work hardening behaviour was found to increase with initial dislocation density and in steels containing MA constituents. Other microstructures showed less stable post-yield behaviour due to Lüders strain,

2. The Bauschinger stress parameter was found to increase with increase in pre-strain for all studied steels. X80 steels demonstrated higher Bauschinger parameters due to the higher dislocation densities and greater particle number densities. Evolution of work softening from 0.01 - 0.04 pre-strain showed greater increments for Ni-bearing steels and for remaining steels showed a plateau > 0.02 pre-strain as a possible result of solute Ni atoms and their effects on stiffness of atomic rows at dislocation cores.

3. Steels subject to warm coiling and cold uncoiling showed more evolved dislocation structures and exhibited a Bauschinger parameter in the as-received condition as shown by significant stress differentials in compression and tensile tests.

8 Future work:

Investigations into the influence of microstructure in linepipe steels has on the mechanical behaviour can be subject to further academic research in the following areas:

In the area of microstructure:

1. Influence of slab reduction on the microstructure of finished plate / sheet in terms of particle size, grain size and dislocation density.

2. Influence of steel chemistry - particularly nickel and other austenite retaining elements on the influence of dislocation structure and subsequent contributions to work softening behaviour / back stresses arising from regular substructures and dislocation pile ups.

In the areas of mechanical properties:

1. Influence of coiling and subsequent stress differences on the Bauschinger parameter - determination as to whether an existing Bauschinger parameter exists giving rise to this phenomenon and whether this has an influence on reverse deformation tests carried out in order of tension-compression and vice versa.

2. Further investigation is required on the role different types of microstructure have to play in the stagnation of work hardening during reverse deformation. In particular MA bearing steels with different microalloying levels to distinguish any trend particle interaction has on stagnation.

3. TEM studies are required in various states during reverse loading to determine the dislocation structures and role of annihilation on reverse stress strain trends particularly at low pre-strains where prior cellular structures are not observed.

4. Wider range of microstructures need to be studied with more variation in macro features i.e. grain size and second phase and less variation of nano-features such as particles to determine how much these are exaggerating / inhibiting the effects of back stress from Orowan mechanisms.

9 References

1. American Petroleum Institute Specification 5L: Line Pipe , 42ND Edition, (2000).

2. H. Hillenbrand, M. Graf, Kalwa. Development and production of high strength pipeline steels, EUROPIPE Niobium, (2001), pp. 1-28.

3. J.Y.Koo, M.J.Luton, N.V.Bangaru, R. A. Petkovic. Metallurgical design of ultra-high strength steels for gas pipelines, Proceedings of the Thirteenth International Offshore and Polar Engineering Conference Honolulu, Hawaii, USA, May 25–30, (2003), pp. 10–18.

4. British Standards Institute, BSI: BS 8010, Code of Practice for Pipeline - Part 3. Pipeline Subsea: Design, Construction and Installation, (1993).

5. H.Y. Liou, S.C. Wang. The influence of microstructure on the hydrogen embrittlement in a low-carbon steel, No. 224, Cossosion/94 (Houston, TX: NACE, 1994), pp. 11.

6. S.U. Koh, J.S. Kim, B.Y. Yang, K.Y. Kim. Effect of line pipe steel microstructure on susceptibility to sulfide stress cracking, NACE Corrosion, Vol. 60, No. 3, (2004) pp. 244-253.

7. C.M. Liao, J.L. Lee. Effect of molybdenum on sulfide stress cracking resistance of low-alloy steels, Corrosion 50, No. 9 (1994): pp. 695 – 705.

8. G.M Pressouyre. Trap theory of hydrogen embrittlement, Acta Metallurgica, Vol. 28, (1978), pp. 895 - 911.

9. NACE Standard MR0175-99, Sulfide stress corrosion cracking resistant metallic materials for oilfield equipment, NACE International, (1999).

10. Irvine, K. Pickering, F. B., and T. Gladman. Grain refined C-Mn steels, Journal of the Iron and Steel Institute 205(2): (1967), pp. 161-182..

11. A. Fatehi, J. Calvo, A.M. Elwazri, S. Yue. Strengthening of HSLA steels by cool deformation, Materials Science and Engineering A 527, (2010), pp. 4233–4240

12. J. Adamczyk. Development of the microalloyed constructional steels Journal of Achievements in Materials and Manufacturing Engineering, Vol. 14, Issue 1-2, (2006), pp. 9-20.

13. C.M. Sellars. The physical metallurgy of hot working, and forming processes, eds. The Metals Society, London, (1979) pp. 3-8.

14. I. Kozasu. Processing, Thermomechanical Controlled Processing, in Constructional and Properties of Steels, F.B. Pickering, Ed., Vol 7, Materials Science and Technology, VCH, Weinheim, (1992), pp 183–217.

15. T. Tanaka. Proc. Int. Conf. Microalloying 95, Iron and Steel Soc., Pittsburg PA, (1995), pp. 165-187.

16. T. Tanaka. Controlled rolling of steel plate and strip International Metals Reviews, Vol. 4, American Society for Metals, Metals Park, OH, (1981), pp. 185– 212.

17. Y. Han, J. Shi, L. Xu, W.Q. Cao, H. Dong. Effect of hot rolling temperature on grain size and precipitation hardening in a Ti-microalloyed low-carbon martensitic steel, Materials Science and Engineering A, Vol. 553, (2012), pp.192– 199.

18. Z. Tang, W. Stumpf. The effect of microstructure and processing variables on the yield to ultimate tensile strength ratio in a Nb–Ti and a Nb–Ti–Mo line pipe steel, Materials Science and Engineering A, Vol. 490, No 1-2, (2008), pp.391-402.

19. H. Sekine, T. Maruyama. effect of hot rolling temperature on grain size and precipitation hardening Trans. Iron Steel Inst. Jpn. 16 (1976), pp.427-438.

20. A. A. B. Sugden, H. K. D. H. Bhadeshia. Lower acicular ferrite, Metallurgical Transactions A, Vol. 20A, (1989), pp. 1811-1818.

21. S.S. Babu, H.K.D.H. Bhadeshia, Stress and the acicular ferrite transformation, Mater. Sci. Eng. A 156 (1992), pp. 1–9.

22. Yokota, T., Garcia-Mateo, C., and Bhadeshia, H. K. D. H., Transformation-induced plasticity for high strength formable steels, Scripta Materialia 51, (2004), pp. 767-772.

23. T. Tanaka, in: Int. Met. Rev. Vol 4, American Society for Metals, Metals Park, OH, (1981) pp. 185 – 212.

24. A. Bakkaloglu, Effect of processing parameters on the microstructure and properties of an Nb microalloyed steel, Materials Letters 56 (2002) pp.200–209.

25. J. Y. Koo, M. J. Luton, N. V. Bangaru. Metallurgical design of ultra high-strength steels for gas pipelines, International Journal of Offshore and Polar Engineering Vol. 14, No. 1, (2004) (ISSN 1053-5381).

26. S.W. Thompson, D.J. Colvin, and G. Krauss. Continuous cooling transformations and microstructures in a low-carbon, high- strength low-alloy plate steel, Metallurgical Transactions A, Vol 21A, (1990), pp 1493–1507.

27. S.N. Prasad, D.S. Sarma. Influence of thermomechanical treatment on microstructure and mechanical properties of a (Nb-V) bearing weather resistant steel, Material Science and Engineering A, Vol. 408, (2005), pp. 53 – 63.

28. M. Esmailian. The effect of cooling rate and austenite grain size on the austenite to ferrite transformation temperature and different ferrite morphologies in microalloyed steels, Iranian Journal of Materials Science & Engineering Vol. 7, Number 1, (2010), pp. 7-10.

29. T.B. Massalski, Massive transformations, in phase transformations, American Society for Metals, (1970), pp 433–486.

30. E.A. Wilson. The γ to α transformation in low carbon irons, ISIJ International, Vol 34, No. 8, (1994), pp. 615–630.

31. Symposium Book. International symposium on new aspects of microstructures in modern low carbon high strength steels, The Iron and Steel Institute of Japan, Tokyo, (1994).

32. J. Cawley, C.F. Harris. and E.A. Wilson, Microstructural studies of low carbon manganese containing alloys, Symposium Book, New Aspects of Microstructures in Modern Low Carbon High Strength Steels, ISIJ, Tokyo, (1994), pp 11–14.

33. W.D. Callister. Material Science and Engineering, John Wiley & Sons, Inc: USA, (2002). Print.

34. S. Allain, O. Bouaziz. Microstructure based modelling for the mechanical behavior of ferrite–pearlite steels suitable to capture isotropic and kinematic hardening, Materials Science and Engineering A 496, (2008) pp. 329–336.

35. A. Kostryzhev. Bauschinger effect in Nb and V microalloyed line pipe steels, Thesis for the degree of Doctor of Philosophy, School of Metallurgy and Materials, University of Birmingham, UK, (2009).

36. F.B. Pickering, T. Gladman. Metallurgical developments in carbon steels, The Iron and Steel Institute, (1963), pp. 10–20.

37. T. Gladman, I.D. McIvor, F.B. Pickering. Some aspects of the structure—property relationships in high-carbon ferrite-pearlite steels Iron Steel Inst. 210 (1972), pp.916–930.

38. H.K. Kouwenhoven, Trans. ASM 26 (1969), pp.437–446.

39. E.S. Davenport, E.C. Bain. Transformation of austenite at constant subcritical temperatures, Transactions AIME, Vol 90, 1930, p 117–144; reprinted as a Metallurgical Classic, with commentary by Harold W. Paxton, in Metallurgical Transactions, Vol. 1, (1970), pp. 3475–353.

40. W.T. Reynolds, Jr., H.I. Aaronson, G. Spanos, A summary of the present diffusionist views on bainite, Materials Transactions, JIM, Vol 32, No. 8, (1991), pp. 737–746.

41. J.W. Christian. The theory of transformations in metals and alloys, (2002), pp. 818-831.

42. Y.E. Smith, A.P. Coldren, R.L. Cryderman. Toward improved ductility and toughness, Climax Molybdenum Company Ltd. (1972), pp. 119–142.

43. G.I. Rees, H.K.D.H. Bhadeshia. Thermodynamics of acicular ferrite nucleation, Mater. Sci. Technol.Vol 10, (1994) pp. 353–358.

44. M. Díaz-Fuentes, I. Gutiérrez. Analysis of different acicular ferrite microstructures generated in a medium-carbon molybdenum steel. Mater Sci Eng A;A363: (2003), pp. 316–324.

45. M.K. Young, H.C. Lee, J. Kim. Transformation behavior and microstructural characteristics of acicular ferrite in linepipe steels, Materials Science and Engineering A 478 (2008), pp. 361–370.

46. M.-C. Zhao, K.Yang, F.-R. Xiao,Y.-Y. Shan, Continuous cooling transformation of undeformed and deformed low carbon pipeline steels, Mater. Sci. Eng.A355 (2003), pp. 126–136.

47. H.Youngchul, M.K. Young, L. Sunghak. Correlation of microstructure and fracture properties of API X70 pipeline steels Metallurgical and Materials Transactions A, March, Vol 36, Issue 3, (2005), pp. 725-739.

48. G. Krauss Steels: Processing, Structure, and Performance, ASM International: USA, (2007). Print.

49. Y.M Kim, S.Y Shin H. Lee, Metall. Mater. Trans. A, Vol. 38A.(2007) pp. 1731 - 1742.

50. S.K. Kim, Y.M. Kim. Mechanical behaviours of materials, Seoul, 15th Conf. On Korea Institute of Metals, (2001), pp. 177-186.

51. Y.H. Seung, Y.S. Sang. Effects of cooling conditions on tensile and charpy impact properties of API X80 linepipe steels. The Minerals, Metals & Materials Society and ASM International Vol 41A, (2010), pp. 329 -340.

52. M. Zhou, L. Du, Y. Zhao, X. Liu. Microstructure characteristics and mechanical properties of X80 pipeline steels, Journal of Wuhan University of Technology-Mater. Sci. Ed. (2012), pp. 252-255.

53. T. Gladman. The physical metallurgy of microalloyed steels, The Institute of Materials, Cambridge University Press, Cambridge, (1997). Print.

54. A. Ghosh, S. Chatterjee. Characterization of precipitates in an ultra low carbon Cu bearing high strength steel: A TEM study, Materials Characterization, Vol. 55, (2005), pp. 298– 306.

55. Kneissl AC, Garcia CI, DeArdo AJ. Characterization of precipitates in HSLA steels. Proc: HSLA steels processing, properties and applications. Warrendale7 TMS Minerals Metals materials Society; (1992). pp. 99– 106.

56. K. Narita. Physical chemistry of the groups IVa (Ti, Zr), Va (V, Nb, Ta) and the rareearth elements in steel, Transactions of ISIJ, Vol. 15, No. 3, (1975), pp. 145 – 152.

57. N.A. Linaza, J.L. Romero, J.M. Rodriguez-Ibabe, J.L. Urcola. Influence of the microstructure on the fracture toughness and fracture mechanism of forging steels microalloyed with titanium with ferrite-pearlite structures, Scripta Metallurgica et Materialla, Vol 29, No. 4, (1993), pp.451-456.

58. R. Soto, W. Saikaly, X. Bano, C. Issartel, G. Rigaut and A. Charai. Statistical and theoretical analysis of precipitates in dual-phase steels microalloyed with titanium and their effect on mechanical properties, Acta Meterialla, Vol. 47, No 12, (1999), pp. 3475-3481.

59. S.P. Ringer, W.B. Li and K.E. Easterling, On the interaction and pinning grain boundaries by cubic shape precipitate particles, Acta Metallurgica, Vol. 37,No. 3, (1989), pp. 831 – 841.

60. T. Niu, Y.L. Kang, H.W. Gu. Precipitation behaviour and its strengthening effect of x100 pipeline steel. Journal of Iron and Steel Research, International. Vol. 17(11); (2010); pp. 73-78.

61. K. Banks, A. Koursaris, F. Verdoorn, A. Tuling. Precipitation and hot ductility of low C–V and low C–V–Nb microalloyed steels during thin slab casting. Mater Sci and Technology, Vol.17, (2001), pp. 1596– 604.

62. E.Valdes and C.M. Sellars. Influence of roughing rolling passes on kinetics of strain induced precipitation of Nb(C,N), Material Science and Technology, Vol. 7, (1991), pp. 622 – 630.

63. J. Irvine and T.N. Baker, The influence of rolling variables on the strengthening mechanisms operating in niobium steels, Material Science and Engineering, Vol. 64, (1984), pp. 123 - 134.

64. W.M. Rainforth, M.P. Black, F. Hofer. Precipitation in a model austenitic steel, Acta Materialia, Vol. 50, (2002), pp. 735 – 747.

65. R. Varughese and P.R. Howell. The application of metallographic techniques to the study of the tempering of HSLA-100 steel, Materials Characterization, Vol. 30, (1993), pp. 261 – 267.

66. T.Gladman, B. Holmes and I.D. McIvor. Effect of second-phase particles on strength, toughness and ductility, Effect of second-phase particles on the mechanical properties of steel, Proceedings of a conference, The Iron and Steel Institute, London, (1971), pp. 68 –78.

67. S. Shanmugan, R.D.K. Misra, T. Mannering, D. Panda, S.G. Jansto. Impact toughness and microstructure relationship in niobium- and vanadium-microalloyed steels processed with varied cooling rates to similar yield strength, Material Science and Engineering A, Vol. 437, (2006), pp. 436 – 445.

68. E. Courtois, T. Epicier, C.Scott. EELS study of niobium carbo-nitride nano-precipitates in ferrite, Micron, Vol. 37, No. 5, (2006), pp. 492 – 502.

69. E.J. Palmiere, C.I. Garcia, A.J. DeArdo. The influence of niobium supersaturation in austenite on the static recrystallisation behaviour of low carbon microalloyed steels, Metallurgical and Materials Transactions A, Vol. 27, No.4, (1996), pp. 951 – 960.

70. A.J. Craven, K. He, L.A. Garvie, T.N. Baker, Complex heterogeneous precipitation in Ti–Nb microalloyed Al-killed HSLA steels-II. non-titanium based particles, Acta Materialia, Vol. 48, (2000), pp. 3869 – 3878.

71. Pandit, A. Murugaiyan, A. Saha Podder, A. Haldar, D. Bhattacharjee, S. Chandra, R.K. Ray. Strain induced precipitation of complex carbo-nitrides in Nb–V and Ti–V microalloyed steels, Scripta Materialia, Vol. 53, (2005), pp. 1309 – 1314.

72. B.Dutta, E.Valdes and C.M. Sellars. Mechanism and kinetics of stain induced precipitation of Nb(C,N) in austenite, Acta Metallurgica et Materialia, Vol.40, No. 4, (1992), pp. 653 – 662.

73. R. Lagneborg, T. Siwecki. The Role Of Vanadium In Microalloyed Steels, The Scandanavian Journal of Metallurgy, (1999).

74. H.W. Yen, P.Y. Chen, C.Y. Huang. Interphase precipitation of nanometer-sized carbides in a titanium–molybdenum-bearing low-carbon steel, Acta Materialia 59, (2011) pp. 6264–6274.

75. R. Okamoto, A. Borgenstam, J. A'gren. Interphase precipitation in niobium-microalloyed steels, Acta Materialia, Vol.58 (2010), pp. 4783–4790.

76. T. Furuhara, H. I. Aaronson. On the mechanisms of interphase boundary carbide precipitation, Scripta Metallurgica, Vol. 22, (1988), pp. 1635-1637.

77. J.C. Cao, Q.L Yong. Precipitation of MC phase and precipitation strengthening in hot rolled Nb-mo and Nb-Ti steels, Journal of Materials Science, Vol.42, No. 24 (2007), pp.180.

78. B. Dutta, E.Valdes, C. M. Sellars. Mechanism and kinetics of strain induced precipitation of nb(c, n) in austenite, Acta Metall, Mater. Vol. 40, No. 4, (1992), pp. 653-662.

79. Z.Wanga, X.P. Maoc, Z. Yanga. Strain-induced precipitation in a Ti micro-alloyed HSLA steel, Materials Science and Engineering A 529 (2011), pp.459– 467.

80. A.Pandit, A.Murugaiyan, A.Podder, A.Haldar, D. Bhattacharjee, Strain induced precipitation of complex carbo-nitrides in Nb–V and Ti–V microalloyed steels, Scripta Materialia 53 (2005), pp. 1309–1314.

81. A.J. Deardo. Niobium in modern steels, International Materials Reviews, Vol. 28, No. 6, (2003), pp. 371-402.

82. R. W. K. Honeycombe. Proceedings of International Conference in HSLA Steels: Metallurgy and Applications, ASM International, (1986), pp. 243-258.

83. A.M.Sage, D.M. Hayes, C.C. Early, E.A. Almond. Effects of some variations in composition on mechanical properties of controlled-rolled and normalized vanadium steel 12 mm plate, Metals Technology, Vol. 19, (1976), pp. 293 - 302.

84. M. Prikryl, A. Kroupa, G.C Weatherly, S.V. Subramanian, Precipitation behaviour in a medium carbon, Ti–V–N microalloyed steel. Metall Trans A Phys Metall Mater Science, 27A, (1996), pp. 1149–1165.

85. A. Luft. microstructural processes of plastic instabilities in strengthened metals, Progress in Materials Science Vol. 35, (1991), pp. 97-204.

86. B. Verlinden, J. Driver, I. Samajdar. Thermo-Mechanical Processing of Metallic Materials, First Ed, Elsevier: Oxford, (2007). Print.

87. H.Kestenbach, J. Gallego. On dispersion hardening of microalloyed hot strip steels by carbo-nitride precipitation in austenite, Scripta Mater. Vol. 44, No. 5, (2001), pp. 791–796.

88. A.Melander, P.Persson. Acta Metall 20, (1972), pp. 267-278.

89. J, L. Mihelich. Ciimax Molybdenum Co, Controlled rolled steels for offshore pipeline, Journal of Petroleum Technology, (1977) pp. 730-736.

90. S. Kyriakides, Mechanics of offshore pipelines Vol 1: buckling and collapse, Elsevier, Oxford, (2007). Print.

91. W.B. Morrison. The effect of grain size on the stress-strain relationship in low carbon steel. Trans. ASM, Vol. 59 (1966), pp. 824-846.

92. K.J. Irvine. The development of high-strength steels. Journal of Iron and Steel Institute, Vol.200, (1962), pp. 820-836.

93. T. Kasugai. Journal of Japan Welding Society, 3, No.8, (1975), pp. 220-234.

94. G. Titherand M. Lavite. Journal of Metals, 27, (1975), pp. 15-32.

95. M.H. Ha, M. Hung. The effect of chromium and molybdenum on the susceptibility to sulfide stress cracking of api x70 grade linepipe steels, NACE Corrosion, (2004), No. 04107, pp. 1-13.

96. F.S. Jaberi, A.H. Kokabi. Influence of nickel and manganese on microstructure and mechanical properties of shielded metal arc-welded API-X80 steel, Journal of Materials Engineering and Performance, (2010).

97. W.O. Alexander, G.J. Davies, K.A. Reynolds, E.J. Bradbury. Essential metallurgy for engineers, Van Nostrand Reinhold (UK) Co. Ltd. ISBN: 0-442-30624-5, (1985), pp. 63-71.

98. X. Wu, H.Lee, M.K. Young. Effects of processing parameters on microstructure and properties of ultra high strength linepipe steel , Journal of Material Science and Technology, 28(10), (2012), pp. 889–894.

99. J.R. Bowen, A. Gholinia, S.M. Roberts. Analysis of billet deformation behaviour in equal-channel angular extrusion, Materials Science and Engineering A, Vol. 287, (2000), pp. 87-99.

100.   R.D. Dohert, D.A. Hughes, F.J. Humphreys, J.J. Jonas. Current issues in recrystallization: a review, Materials Science and Engineering A238, (1997), pp. 219–274.

101. A. Cracknell, N.J. Petch, Frictional forces on dislocation arrays at the lower yield point in iron, Acta Metallurgica, Vol. 3, (1955), pp. 186 – 189.

102. B.W. Christ , G.V. Smith. Comparison of the Hall-Petch parameters of zone-refined iron determinated by the grain size and extrapolation methods, Acta Metallurgica, Vol.15, (1967), pp. 809 – 816.

103. H. Conrad, G. Schoeck. Cottrell locking and the flow stress in iron, Acta Metallurgica, Vol. 8, (1960), pp. 791 – 796.

104. N.J.Petch. The upper yield stress of polycrystalline iron, Acta Metallurgica, Vol. 12, (1964), pp. 59 – 65.

105. H.K.D.H. Bhadeshia, R. Honeycombe. Steels: Microstructure and Properties, Third Edition, Elsevier: Oxford , (2006). Print.

106. K.K. Ray, V. Toppo 1, S.B. Singh. Influence of pre-strain on the wear resistance of a plain carbon steel, Materials Science and Engineering A 420, (2006) pp. 333–341.

107. G.I. Taylor, H. Quinney. The latent energy remaining in a metal after cold working. Proceedings of the Royal Society of London 143, (1934), pp. 307–326.

108. G.T. Van Rooyen. Basic factors which influence the Lüders strain during discontinous yielding, Mater, Sci, Eng, (1971) p. 37-48.

109. N. Tsuchida, Y. Tomota, K. Nagai, K. Fukaura. A simple relationship between Lüders elongation and work-hardening rate at lower yield stress, Scripta Mater. 54, (2006), pp. 57–60.

110. J.F. Butler. Lüders front propagation in low carbon steels J. Mech. Phys. Solids 10, (1962), pp. 313–334.

111. U.F. Kocks. Laws for work-hardening and low-temperature creep. J Eng Mater Technol ASME 98: (1976), pp.76–85.

112. D. Kuhlmann-Wilsdorf. Theory of plastic deformation: properties of low energy dislocation structures, Materials Science and Engineering, All3, (1989) pp. 1-41.

113. F.C. Frank, W.T. Read. Multiplication process for slow moving dislocations, Physical Review Letters, Vol. 79, (1950), pp. 722 – 723.

114. M. Nabil Bassim, R. J. Klassen. Variation in dislocation cell size with

local strain in a low alloy steel, Materials Science and Engineering, Vol.81, (1986) pp. 163-167.

115. T. Ungar and M. Zehetbauer. Stage IV work-hardening in cell forming materials, part II: a new mechanism, Scripta Materialia, Vol. 35, No. 12, (1996), pp. 1467-1473.

116. J. T. Evans, R. Rawlings. Work hardening in low-carbon steel deformed at room temperature, Mater. Sci. Vol. 4 (1969), pp. 297-303.

117. M.B. Chul, J.N Won. Effects of Microstructural parameters on work hardening of pearlite at small strains, Met Trans A, Vol. 31A, (2000), pp.2665 – 2669.

118. A.K. Sachdev. Effect of retained austenite on the yielding and deformation behavior of a dual phase steel, Acta Meterialla. Vol. 31, No. 12, (1983), pp. 2037-2042.

119. M. Gaško1, G. Rosenberg. Correlation between hardness and tensile properties in ultra-high strength dual phase steels – Short Communication, Materials Engineering - Materiálové inžinierstvo, Vol. 18, (2011), pp. 155-159.

120.   M. Calcagnotto, D. Ponge, D. Raabe. Effect of grain refinement to 1 micron strength and toughness of dual-phase steels, Materials Science and Engineering A 527, (2010), pp.7832–7840.

121. L. Yumen. Dislocation structures in a ferrite steel, Materials Science and Engineering, Vol.81, (1986), pp.451-455.

122. J. Pal'a, O. Stupakov, J. Bydzovsky, I. Tomas and V. Novak. Magnetic behaviour of low carbon steel in parallel and perpendicular directions to tensile deformation, Journal of Magnetism and Magnetic Materials, Vol. 310, (2007), pp. 57 – 62.

123. D.J. Dingly, D. McLean. Components of the flow stress of iron, Acta Metallurgica, Vol. 15, (1967), pp. 885 – 901.

124. T. Ungar, H. Mughrabi, D. Ronnpagel, M. Wilkens, X-ray line-broadening study of the dislocation cell structure in deformed [001]-orientated copper single crystals, Acta Metallurgica, Vol. 32, No 3, (1984), pp. 333 – 342.

125. E.M. Viatkina, W.A.M. Brekelmans, M.G.D. Geers. Modeling the evolution of Dislocation structures upon stress reversal, International Journal of Solids and Structures, Vol. 44, (2007), pp. 6030 – 6054.

126. A. Zare, A. Ekrami. Influence of martensite volume fraction on tensile properties of triple phase ferrite-bainite-martensite steels, Materials Science and Engineering A 530, (2011), pp. 440–445.

127. R. Li, X. Zuo, Y. Hu, Z, Dingxu Hu. Microstructure and properties of pipeline steel with a ferrite/martensite dual-phase microstructure, Materials Characterisation, 62, (2011), pp. 801–806.

128. J. Pesicka, A. Dronhofer, G. Eggeler. Free dislocations and boundary dislocations in tempered martensite ferritic steels Materials Science and Engineering A 387–389 (2004), pp.176–180.

129. D. L. Bourell, A. Rlzk, Influence of martensite transformation strain on the ductility of dual-phase steels, Acta Metallurgica., Vol. 31. No. 4. (1983), pp. 609-617.

130. A.K. Sachdev. Effect of retained austenite on the yielding and deformation behavior of a dual phase steel, Acta Metallurgica, Vol. 31, No. 12, (1983), pp. 2037-2042.

131. L. Zhonghua, G. Haicheng. Bauschinger Effect and residual phase stresses in two ductile-phase steels: Part 1. The influence of phase stresses on the Bauschinger Effect, Metallurgical Transactions A, Vol. 21a, (1990), pp. 717-723.

132. W. Wang, Y. Yin, S. Yanga. Study of high strength pipeline steels with different microstructures, Materials Science and Engineering A, Vol.502, (2009) pp.38–44.

133. P. Poruks, I. Yakubtsov, J.D. Boyd. Martensite–ferrite interface strength in a low-carbon bainitic steel, Scripta Materialia, Vol. 54 (2006) pp.41–45.

134. J.H. Yang, Q.Y. Liu. Microstructure and transformation characteristics of acicular ferrite in high niobium bearing microalloyed steel, Journal Of Iron And Steel Research,International, Vol. 17, No.6, (2010), pp.53-59.

135. H. Mathy, J. Gouzou, T. Gréday, in: R.A. Kot, B.L. Bramfitt (Eds.). Fundamentals of Dual-phase Steels, The Metallurgical Society of AIME, New York, 1981, pp. 413–426.

136. A.K. Roy, S. Bandyopadhyay, S.B. Suresh, D. Maitra, P. Kumar, D. Wells, L. Ma. Relationship of residual stress to dislocation density in cold-worked martensitic alloy, Material Science and Engineering A, Vol. 416, (2006), pp. 134 – 138.

137. J. Pesicka, R. Kuzel, A. Dronhofer, G. Eggeler. The evolution of dislocation density during heat treatment and creep of tempered martensite, Acta Mater. 51 (2003), pp.4847–4862.

138. Y.I. Son, Y.K. Lee, K.T. Park. Dynamic Torsional Deformation Behavior of Ultra-Fine-Grained Dual-Phase Steel Fabricated by Equal Channel Angular Pressing Acta Mater. 53 (2005), pp. 3125–3134.

139. W.F. Cuia, S.X. Zhanga, Y. Jiang. Mechanical properties and hot-rolled microstructures of a low carbon bainitic steel with Cu–P alloying, Materials Science and Engineering A 528 (2011), pp.6401– 6406.

140. S.S. Nayaka, R.D.K. Misraa, J. Hartmannb, F. Siciliano. Microstructure and properties of low manganese and niobium containing HIC pipeline steel, Materials Science and Engineering A, Vol.494, (2008), pp. 456–463.

141. G, Shiflet. Low energy dislocation structures caused by phase transformations, Materials Science and Engineering, Vol. 81, (1986), pp. 61-100.

142. T. Hasegawa, T. Yakou, S. Karashima. Deformation behavior and dislocation structures upon stress reversal in polycrystalline aluminium, Material Science and Engineering, Vol. 20, (1975), pp. 267 – 276.

143. E.M. Viatkina, W.A.M. Brekelmans, M.G.D. Geers. Modelling the evolution of dislocation structures upon stress reversal, International Journal of Solids and Structures Vol.44, (2007), pp. 6030–6054.

144. G. Vincze, E.F. Rauch, J.J. Gracio, F. Barlat, A.B. Lopes. A comparison of the mechanical behavior of an AA1050 and a low carbon steel deformed upon strain reversal, Acta Materialia, Vol. 53, (2005), pp. 1005 – 1013.

145. B. Gardey, S. Bouvier, B. Bacroix. Correlation between the macroscopic behavior and the microstructural evolutions during large plastic deformation of a dual-phase steel, Metallurgical Transactions A, Vol. 36A, (2005), pp.2937 – 2945.

146. S. Queyreau,B. Devincre. Bauschinger effect in precipitation-strengthened materials: A dislocation dynamics investigation, Philosophical Magazine Letters, Vol. 89, No. 7, (2009), pp. 419–430.

147. S. Kyriakides, E. Corona. Mechanics of offshore pipelines, Elsevier: Oxford, (2007). Print.

148. NKK Corporation, NKK LINE PIPE, Cat. No. 141-012-01, 1993.

149. Establishment of commercial production for high strength UOE linepipe up to X120, Proceedings of the Nineteenth International Offshore and Polar Engineering Conference, (2009), pp. 86-91.

150. A. Palmer, R. King, Subsea Pipeline Engineering, 2nd Edition, PennWell Corp, USA, (2006). Print.

151. D.K. Han, S.J. Kim. Effect of pipe forming on hydrogen permeation behaviour of linepipe steel in sour environment, Proceedings of the Twenty-second International Offshore and Polar Engineering Conference, Rhodes, Greece, (2012), pp. 17–22.

152. H.-G. Hillenbrand, M.K. Graef. Development of linepipe for deep-water applications, Proceedings of The Twelfth International Offshore and Polar Engineering Conference, Japan, (2002) pp. 287-297.

153. S.U. Koh, H.G. Jung, K.Y. Kim KY. Effect of microstructure on hydrogen diffusion in high strength low alloyed steels, Proceedings of the 16th International Corrosion Congress, Beijing, (2005), Paper No. 10-H-03.

154. T.C. Harrison, R.T. Weiner and G.D. Fearnehough. Influence of the Bauschinger effect, Journal of Iron and Steel Institute, (1972), pp. 334 - 336.

155. J. P. Ormandy. Plate to pipe tensile property variation in UOE processed line pipe steels, Thesis for the degree of Master of Philosophy, School of Metallurgy and Materials, University of Birmingham, UK, (2000).

156. D.G. Stalheim, K.R. Barnes, D.B. McCutcheon. Alloy designs for high strength oil and gas transmission linepipe steels, Presentation at the International Symposium on Microalloyed Steels for the Oil and Gas Industry, CBMM-TMS, Araxa, Brazil, (2006), pp. 23-25.

157. K. Nakajima, W. Mizutani, T. Kikuma and H. Matumoto. The Bauschinger effect in pipe forming, Transactions, ISIJ, Vol. 15, (1975), pp. 1 – 10.

158. D.Harris. British Steel Internal Memo: SL/WEM/R/S2670/17/97/D, (1997).

159. D. Harris, D.J. Senogles. British Steel Internal Memo: SL/WEM/R/S2670/21/98/D, (1998).

160. L.M. Brown, Orowan's explanation of the Bauschinger effect. Scripta Metallurgica, Vol.11, (1977), pp. 127 – 131.

161. A. Abel and H. Muir. The Bauschinger effect and discontinuous yielding, Philosophical Magazine, Vol. 26, (1972), pp. 489 – 504.

162. S. Kumakura. The Bauschinger effect in carbon steels, Bulletin of JSME, Vol. 11, No. 45, (1968), pp. 426 – 434.

163. S. Danilov, Metallovedenie. Effect of grain size on the Bauschinger effect, Termicheskaya Obrabotka Metallov, No. 9, (1964), pp. 38-41.

164. D.S. Balint, V.S. Deshpande, A. Needleman, E. Van der Giessen. Discrete dislocation plasticity analysis of the grain size dependence of the flow strength of polycrystals, International Journal of Plasticity, Vol. 24 (2008), pp.2149–2172.

165. K. Han, C.J. Van Tyne, B.S. Levy. Effect of strain and strain rate on the Bauschinger effect response of three different steels, Metallurgical and Material Transactions A, Vol. 36, Sept. (2005), pp. 2379 – 2384.

166. S.Y. Han, S.S. Sohn, S.Y. Shin. Effects of microstructure and yield ratio on strain hardening and Bauschinger effect in two API X80 linepipe steels, Materials Science and Engineering A, (2012), pp. 192-199.

167. B. Hutchinson and N. Ridley. On dislocation accumulation and work hardening in Hadfield Steel, Scripta Materiala, Vol. 55, (2006), pp.299-302.

168. X.G. Qiao, M.J. Starink, N. Gao. Hardness inhomogeneity and local strengthening mechanisms of an Al1050 aluminium alloy after one pass of equal channel angular pressing, Materials Science and Engineering A 513–514 (2009), pp.52–58.

169. G.H. Zahid 1, Y. Huang, P.B. Prangnell. Microstructure and texture evolution during annealing a cryogenic-SPD processed Al-alloy with a nanoscale lamellar HAGB grain structure, Acta Materialia, Vol. 57, (2009), pp.3509–3521.

170. Sangho Kim, Sunghak Lee, Bong Sang Lee. Effects of grain size on fracture toughness in transition temperature region of Mn-Mo-Ni low-alloy steels, Materials and Engineering A359, (2003), pp.198-209.

171. D. Williams, C.B. Carter. Transmission electron microscopy, II – Diffraction, Plenum Press, New York, (1996). Print.

172. J.R. Yang, H.K.D.H Bhadeshia, The dislocation denisty of acicular ferrite in steel welds, Journal of Welding Research, Vol. 305-S, (1990). pp.305-307.

173. B. Sundman. Thermo-Calc. Users' Guide, Royal Institute of Technology, Stockholm,(1999).

174. A. Kundu. Grain structure development during casting, reheating and deformation of Nb-microalloyed steel, Thesis for the degree of Doctor of Philosophy, School of Metallurgy and Materials, University of Birmingham, UK, (2011).

175. S. Zajac, T. Siwecki and M. Korchynsky. Low-carbon steels for the 90's, (ed. R. Asfahani and G. Tither), (1993), pp. 139–149.

176. Y. Li1, J. A. Wilson, A. J. Craven, P. S. Mitchell. Dispersion strengthening in vanadium microalloyed steels processed by simulated thin slab casting and direct charging Part 1 – Processing parameters, mechanical properties and microstructure, Materials Science and Technology, Vol. 23, No. 5, (2007), pp.509.

177. S.G. Hong, H.J. Jun, K.B. Kang. Evolution of precipitates in the Nb–Ti–V microalloyed HSLA steels during reheating, Scripta Materialia, Vol. 48, (2003), pp. 1201–1206.

178. G.Fourlaris, A.Baker. A Microscopic Investigation of the precipitation phenomenon of vanadium carbide in steel, Materials Science and Engineering A, Vol. 111, (1989), pp. 189 -199.

179. D. Bhattacharjee , C.L. Davis. Influence of processing history on mesotexture and microstructure-toughness relationship in control-rolled and normalised steels, Scripta Materialia 47, (2002), 825–831.

180. H.G. Hillenbrand, M. Graf and C. Kalwa, Development and production of high strength pipeline steels, EUROPIPE, GmbH, www.europipe.de, (2001).

181. J.M. Zhang, W.H. Sun, H. Sun. Mechanical properties and microstructure of x120 grade high strength pipeline steel, Journal of Iron and Steel Research, Vol. 17, No.10, (2010), pp.63-67.

182. F. Louchet, Thermally activated dislocation sources in silicon, Journal of Physics C: Solid State Physics, Vol. 13, (1980), pp. 847 – 849.

183. J. Friedel and P. Feltham, The mechanism of work-hardening and slip-band formation, Proceedings of the Royal Society of London, Series A, Mathematical and Physical Sciences, Vol. 242, No. 1229, (1957), pp. 147 – 159.

184. W.M. Quach, J.G. Teng, K.F. Chung. Residual stresses in steel sheets due to coiling and uncoiling: A closed form analytical solution. Engineering Structures, Vol. 26 No.9, (2004), pp.1249–59.

185. R.B. Cruise, L. Gardner. Residual stress analysis of structural stainless steel sections, Journal of Constructional Steel Research, Vol. 64 (2008), pp. 352–366.

186. D.F.Watt. Effect of martensite morphology on the strength differential effect in dual phase steels. Scripta Metallurgica, Vol.18, (1984), pp 1379-1382.

187. W.M. Quacha, J.G. Teng, K.F. Chung. Residual stresses in press-braked stainless steel sections, I: Coiling and uncoiling of sheets, Journal of Constructional Steel Research 65, (2009), pp.1803-1815.

188. H. Ruppersberg, Stress fields in the surface region of pearlite, Materials Science and Engineering A224, (1997), pp. 61-68.

189. L.M. Panfilova, LA. Smirnov, Unique properties of new steels microalloyed with vanadium and nitrogen, Steel in Translation, Vol.40, No.5, (2010), pp.495-500.

190. S. Zajac, T. Siwecki and W. B. Hutchinson. Precipitation phenomena in V-microalloyed 0.15-0.22%C structural steels, Swedish Institute for Metals Research, Internal Report IM-3453, (1996).

191. S. Zajac, T.Siwecki, W. B. Hutchinson, R. Lagneborg. Strengthening mechanisms in vanadium microalloyed steels intended for long products, ISIJ Int., 38 (1998), pp. 1130-1139.

192. S. Zajac. The role of nitrogen and carbon in precipitation strengthening of V-microalloyed steels, Swedish Institute for Metals Research, Internal Report (1997).

193. H.Yu, Y.Kang, H. Dong. Comparison and analysis of dislocation density, morphology and evolution in microstructure of low-carbon steel produced using different technologies, Materials Science and Engineering, Vol.13, No.5, (2006), pp. 406-410.

194. D. R. Trinkle, C. Woodward. The chemistry of deformation: how solutes soften pure metals, Science 310, Issue 5754, (2005), pp.1665–1667.

195. D. Caillard. A TEM in situ study of alloying effects in iron, I-Solid solution softening caused by low concentrations of Ni, Si and Cr. Acta Materialia, Vol. 61, (2013) pp. 2793-2807.

196. N.G. Kioussis, N.M/ Ghoniem, Modelling of dislocation interaction with solutes, nano-precipitates and interfaces: a multiscale challenge. Journal of Computational and Theoretical Nanoscience,Vol.7, (2010) pp. 1-30.